Springer Series in Materials Science 339

Rolf Sandström

Basic Modeling and Theory of Creep of Metallic Materials

Springer

Springer Series in Materials Science

Volume 339

The Springer Series in Materials Science covers the complete spectrum of materials research and technology, including fundamental principles, physical properties, materials theory and design. Recognizing the increasing importance of materials science in future device technologies, the book titles in this series reflect the state-of-the-art in understanding and controlling the structure and properties of all important classes of materials.

Rolf Sandström

Basic Modeling and Theory of Creep of Metallic Materials

Springer

Rolf Sandström
Material Science and Engineering
Royal Institute of Technology
Stockholm, Sweden

ISSN 0933-033X ISSN 2196-2812 (electronic)
Springer Series in Materials Science
ISBN 978-3-031-49506-9 ISBN 978-3-031-49507-6 (eBook)
https://doi.org/10.1007/978-3-031-49507-6

This Springer imprint is published by the registered company Springer Nature Switzerland AG
The registered company address is: Gewerbestrasse 11, 6330 Cham, Switzerland

Paper in this product is recyclable.

Preface

The computation of mechanical properties is of increasing importance. The fast development of software has enabled many new possibilities. Unfortunately, the development of basic modelling of mechanical properties has not taken place at the same rate. This should be contrasted with other scientific areas. Prediction of physical properties with the help of quantum mechanics methods (ab initio) has made great progress in recent years and thousands of papers have been published. Also in the field of computational thermodynamics (Calphad), rapid progress has taken place. Phase components in the microstructure and their composition can often be predicted with good accuracy, which is basic information for the understanding of the development of the microstructure.

The results of ab initio and Calphad computations are often referred to as basic or fundamental since they do not involve adjustable parameters to predict property values. Considering mechanical properties, on the other hand, computations are commonly performed with empirical models with a number of adjustable parameters. The progress in the ab initio and Calphad area has inspired me to try to find out if it is possible to predict mechanical properties from physically based models without adjustable parameters with results that are sufficiently accurate to be used in industrial and scientific work. To be precise, models that satisfy these requirements are referred to as basic or fundamental (synonyms) in this book. It is evidently a challenging task because the properties depend on the behaviour of the dislocations, which is in turn a sensitive function of the microstructure.

The use of basic models is essential not least due to a number of limitations with empirical models.

1. Models involving adjustable parameters are often quite flexible. It is common experience that with say three or more adjustable parameters a wide range of data sets can be fitted. Thus, a precise fit does not automatically mean that the model represents the physics of the data.
2. For the same reason as given in 1, it would be very risky to use a model with fitting parameters to identify operating mechanisms. Many models could describe the same data.

3. When properties are modelled, there is almost invariably a desire to generalise and extrapolate the results. That would obviously be very dangerous with empirical models, since almost arbitrary values can be obtained. The exception is when the model is fitted to a large data set. The criterion is that the number of adjustable parameters must be very much smaller than the number of experiments. A well-known case is the extrapolation of creep rupture data with the help of time temperature parameters such as Larson–Miller. It is well established that consistent values can be obtained, which is demonstrated in Chap. 14.

The limitations listed above are well-established and easy to understand. However, there are subtler effects as well. Scientists want to get a good agreement between model and observations as possible. If a model with adjustable parameters is involved, a good agreement is usually easily fixed. In this situation, there is obviously a risk that the most flexible model available is chosen or that observations in agreement with the model are preferred. In most cases, such decisions are likely to be taken intuitively and not on purpose.

The success of the ab initio and Calphad modelling has been an inspiration for me to try to avoid the limitations mentioned above and to try to collect and develop basic models also for mechanical properties. With basic models, a number of phenomena can be investigated in a more precise way. This will be exemplified next.

The Bird, Mukherjee and Dorn (BMD) equation that describes the influence of the stress and temperature on the stationary creep rate has been very important for creep research. It is a semi-empirical model with a physical background. It involves at least three adjustable parameters: a proportionality constant, an activation energy and a stress exponent. The BMD equation can describe a large fraction of available creep rate data and is consequently very valuable. In two early papers, Weertman suggested that dislocation climb would give a stress exponent of about five and dislocation glide an exponent of three. Even before, modelling of diffusional creep gave a stress exponent of one. Unfortunately, these suggestions made people believe that the creep mechanism could be identified from the stress exponent. Consequently, much of the early creep research focused on the measurement of the stress dependence of the secondary creep rate. Nowadays, there are both experiments and modelling results that show that dislocation climb can give stress exponents from 1 to 50 making it impossible to use the stress exponent to identify the creep mechanism. This is discussed in Chaps. 2 and 5. Although it is not accepted by everyone, dislocation glide is always faster than dislocation climb and the former process cannot control the creep rate, Chap. 2.

As mentioned in the previous paragraph, the stress exponent as well as the activation energy have frequently been determined for the secondary creep rate. However, the corresponding values during primary creep have more rarely been measured. It turns out that both types of values are lower in the primary stage, which has been demonstrated both by observations and models. This is in practice quite important because if the secondary stage has not been fully reached, both the activation energy and the stress exponent can be under-estimated. These findings are particularly important at low stresses since it can be quite time-consuming to reach the secondary stage.

It has been known for a long time that at low stresses, the variation of the creep rate during primary creep can be quite helpful in identifying the creep mechanism, but this fact has largely been ignored in the literature, Chap. 5.

A number of the creep models presented in the book are based on a dislocation model. Although the dislocation model is properly derived, it is essential that the predictions are verified against experiments. From the dislocation model, formulae for primary, stationary and tertiary creep as well as stress strain curves are derived. The validity of these formulae and a number of others has been demonstrated by comparison to experimental data. The basic models for primary and secondary creep were first verified for Cu at fairly high stresses close to ambient temperatures. Later, it has been demonstrated that the models also work for Al, Ni and, for example, austenitic stainless steels. It has been shown that the models also can handle very high temperatures and low stresses under conditions that are assumed to be typical for diffusion-controlled creep. This verifies that the models can cope with a wide range of applications. Moving from high stresses to low stress can involve a change in the creep rate by 10 orders of magnitude, which is very strong support for the validity of the basic models, Chap. 5.

This change in stress level can thus imply an effective extrapolation by 10 orders of magnitude. This should be contrasted to extrapolation with empirical models that are commonly assumed to be able to handle of factor of 3 in time. The extrapolation capabilities of basic models are of great technical importance. Modern nuclear plants are often designed for a lifetime of 60 years. Considering that the longest creep tests are typically performed for about 10 years, an extrapolation by a factor of 3 is not enough. A more extreme case is copper canisters for storage of spent nuclear fuel in the Swedish KBS-3 system. The canisters should stay intact for 100000 years. Without basic creep models such time spans would never be possible to handle. Since the author has been working with copper canisters for many years, this was an additional reason for the interest in developing basic creep models.

Stockholm, Sweden Rolf Sandström
rsand@kth.se

Contents

Chapter 1
The Role of Fundamental Modeling

Abstract The difference between empirical and basic modeling and its significance is explained. The types of basic models that have been possible to develop and that are describe in the book are summarized. The starting point is a basic model for the dislocation density that is used to derive expression for tensile and creep properties. It is described how the accuracy of the basic models can be verified. For the creep models it is described that they are applicable over a wide range of temperatures and stresses that is of great value to identify operating mechanisms.

1.1 Background

Modeling and prediction of materials properties have had a rapid development in recent years. Ab initio methods are used to compute the electronic structure of crystals based on quantum mechanical methods. The full multi particle problem is not possible to solve but a number of first principle procedures such as Density Functional Theory (DFT) are available to handle the problem. By minimizing the total energy of the system, lattice parameters and the most stable crystal and surface structures can be established. A range of physical parameters such as thermal expansion coefficient, heat capacity, electric and thermal conductivity can be computed. Interface energies and elastic constants can be derived. This type of modeling is referred to as fundamental because it is based on physically well founded algorithms and no parameters are fitted to experimental data.

Computational thermodynamics (CTD) is another area where great progress has taken place in recent decades. Its base is unique. Expressions for the free energy are fitted to a range of thermophysical properties as a function of alloy content, which is referred to as the Calphad approach. The functions determined in this way can then be used to find the equilibrium phases for specific amounts of alloying elements. Phase diagrams can be generated. By using data also for interface energies and diffusion constants the development of microstructure can be predicted, which is the basis of much research in materials science. The variation of the interface energies and diffusion coefficients with alloying elements can also be derived with CTD, which is

R. Sandström, *Basic Modeling and Theory of Creep of Metallic Materials*, Springer Series in Materials Science 339,
https://doi.org/10.1007/978-3-031-49507-6_1

usually referred to as fundamental in spite of the fitting of the free energy functions to experimental data, because once this process is completed no further fitting is involved.

Mechanical properties are of great technical and scientific interest. In spite of this, the amount of fundamental modeling that has been performed for mechanical properties is much more limited than for ab initio methods and CTD. Mechanical properties are primarily controlled by the motion of dislocations and this has created a barrier for more fundamental modeling.

Probably the most common way of measuring mechanical properties is the tensile test. It gives a stress strain curve that can be used to assess the yield and tensile strengths as well as the ductility in the form of elongation or reduction of area. To describe stress strain curves almost exclusively empirical models are used. Some of the most well-known models are Hollomon, Ludwik, Voce and Swift. These models do not have any physical background. They are simply mathematical expressions with a number of adjustable parameters that can be fitted to the data. Only the Voce model can readily be derived from basic physical principles. This will be described in Chap. 3.

Also for creep, mainly empirical models are used. The development of them has taken place over many decades. A major event was when Norton in his book from 1929 gave an equation for the stress dependence of the creep rate [1]. This relation is now often referred to as the Norton equation. It was the only equation in the book. The stress dependence of the creep rate has played a profound role in the development. An important result by Bird, Mukherjee and Dorn (BMD) in the 1960ties gave an explicit expression for the temperature dependence in the Norton equation [2]. The creep rate was assumed to be proportional to an Arrhenius equation of the self-diffusion coefficient which is natural when climb is the controlling dislocation mechanism. This implies that the activation energy for creep is the same as that for self-diffusion, a relation that has been experimentally confirmed for a number of pure metals. Some temperature dependence was also incorporated by explicitly taking into account the temperature dependence of the shear modulus. This generalization of the Norton equation is referred to as the BMD equation.

The BMD equation can be considered as a semi-empirical equation. The inclusion of the self-diffusion constant was based on physical thinking, but the equation still has at least two adjustable parameters: a proportionality constant and the stress exponent n_N. In spite of these limitations the equation is frequently used till this day. The value of n_N was assumed to be related to the operating mechanisms. Weertman suggested that climb control would give $n_N \approx 5$ and glide control $n_N \approx 3$ [3, 4]. Together with the knowledge that diffusion control gives $n_N \approx 1$, it was thought that the value of n_N could be used to identify the operating mechanism. For this reason much focus in creep research in the coming decades was on measuring the secondary creep rate and determining the stress exponent. This seemed logical at the time but has turned out to be unfortunate. It gradually became apparent that the stress exponent was not automatically related to the rate controlling creep mechanism [5]. With the fundamental models that are presented in this book, it is shown that climb controlled creep can be associated with stress exponents from 1 to 50, demonstrating that a

specific range of stress exponents does not necessarily make it possible to identify the creep mechanism.

For a more detailed modeling of creep deformation, it must be possible to describe how the dislocation density is evolving with time and strain. Initially models were semi-empirical in nature, but later it has been possible to derive and verify some of these models. There are three contributions to the changes in the dislocation density. Work hardening involves the generation of dislocation that raises the strength. In the 50ties and 60ties numerous scientists were engaged in developing models for work hardening. For creep of polycrystalline materials, a simple expression derived from the Orowan equation has turned out to be useful. This was first utilized by Lagneborg [6]. Two recovery processes that reduce the dislocation density are central aspects of creep: dynamic recovery that is strain controlled and static recovery that is time controlled. The expression for dynamic recovery was first presented by Bergström [7]. It was also given in a well-known paper by Kocks [8]. The role of static recovery was initially emphasized by Lagneborg [6].

What has been described so far is the empirical and semi-empirical modeling of creep. Before entering fundamental modeling, it is worth-while to specify what we mean by the different types of modeling. These definitions are not supposed to be general, but it is essential to clarify what we mean in this book.

- Empirical models. Models that have limited or no physical basis. They are mathematical expressions that are used to fit experimental data. For that purpose a number of adjustable parameters are involved. Example, the Norton equation.
- Semi-empirical models. Models that are at least partially derived from physical facts. They include adjustable parameters or constants that are not well defined and it is not clear how the constants could be derived in a precise way. Example, the BMD equation.
- Fundamental (or basic) models. The models are fully based on physical facts and a scientific derivation is available. No adjustable parameters are involved. All the constants can be derived in a precise way. Fundamental and basic models will be used as synonyms in this book. Example, ab initio modeling.

When fundamental models exist they are more valuable tools because they can be used to make predictions and generalize results. However, empirical models can be quite useful as well. A classic example is the empirical Bohr model for the hydrogen atom, where an electron circles around the nucleus as a particle. The Bohr model inspired a large number of scientists to perform experiments and to develop models. The Bohr model is now superseded by the quantum mechanical description of the hydrogen atom.

Empirical models are usually the first ones to be established for a specific phenomenon. The Norton equation is an example of that. It created the understanding about some basic facts about creep. It took about three decades before semi-empirical improvements started to appear and even further decades before fundamental versions were available. There is always a risk to focus too much on empirical or semi-empirical models. With the help of adjustable parameters, it is usually possible to get a good fit to experimental data and that can easily create the impression that

good understanding of the phenomenon has been established. But it is important to recall that it is very difficult to make predictions, generalizations and to identify operating mechanisms with empirical and semi-empirical models. The use of the BMD equation is unfortunately an example of that in a number of cases.

The starting point for development of basic creep models concerns *diffusion creep*. In these models the deformation is assumed to take place by diffusion of atoms inside the grains [9] or along the grain boundaries [10]. These models are quite simple and easy to understand intuitively. They both predict a stress exponent of 1. It was thought that these models would be easy to verify experimentally. But this has not turned out to be the case. The interpretation of many earlier tests has also been questioned [11–13]. One of the main reasons for the difficulty is the assumption that only diffusion creep is associated with a stress exponent of 1. It has more recently been shown that dislocation creep can give a stress exponent of 1 at low stresses. This has been found for aluminum at very high temperatures [14, 15]. In the past a stress exponent of 1 was observed. But by carrying out the testing until sufficiently high strains were reached, a stress exponent of 3 was obtained. Low stress exponents for dislocation creep have also been observed for the martensitic 9Cr1Mo steel P91 and for the austenitic stainless 17Cr12Ni2Mo steel 316H [16, 17]. Although the tests for these steels were performed till 1000 h, the secondary stage was far from reached. If the stress exponent is determined in the primary rather than in the secondary stage it can give a low value of about unity.

It is evident from these experimental results and also from modeling findings in the present book that dislocations can be of importance at high temperatures and low stresses and that contribution from them can even be much larger than that from diffusion. When studying diffusion creep it is consequently important to check the amount of dislocation creep that is present. A simple way to do that is to observe if primary creep occurs, which would be a clear sign that dislocation creep is present. In addition, the creep exponent must be unity and the measured creep rate should agree with the formulae for diffusion creep. Unfortunately, it is not easy to find studies fulfilling these requirements in the literature. This does not mean that diffusion creep is not a real effect. However, it seems to be masked by other mechanisms in many cases.

1.2 Description

Basic modeling of *dislocation creep* can be said to be started by the formulation of the climb mobility by Hirth and Lothe [18]. Climb is by far the most important mechanism for controlling the creep rate. This climb mobility has been implemented in the expression for static recovery proposed by Lagneborg [6]. Also the parameters in his expression have been derived and the expression validated. The first to give a basic modeling of dynamic recovery was Roters et al. [19]. This item is not fully settled yet because the modeled dynamic recovery constant ω is not always in agreement with experiments. With these achievements a basic differential equation

for the development of the dislocation density could be established. The equations are derived in Chap. 2.

From the differential equation for the dislocation density, the stationary creep rate can be derived. In this way the *Norton equation* is obtained where all the parameters are well defined with given values. In the past many attempts have resulted in expressions with poorly defined back stresses, activation energies or activation areas. This is now avoided. The new formulation gives a stress exponent of three or four in its simplest form. This is sometimes referred to as the "natural creep law" because it is a direct consequence of the balance between work hardening and recovery during stationary creep [20, 21].

It is well established that the stress exponent is raised when higher stresses and lower temperatures are considered. A dramatic increase from the values of n_N = 4–7 in power-law creep is observed, which is often referred to as *power-law break down*. The increase in the stress exponent has been possible to be fully explained by taking strain enhanced formation of vacancies into account [22]. This effect is now integrated in the expression for the creep mobility and it is taken into account in the Norton equation. This will be described in Chap. 2.

It is natural to assume that stress controlled, load controlled as well as rate controlled plastic deformation are governed by the same mechanisms and equations. To follow this principle, stress strain curves are described with the same dislocation models as for creep. For fcc alloys, the stress strain curves obey the Voce model in the most direct derivation. This can give an as accurate representation as empirical models for stress strain curves. The dynamic recovery constant ω plays a special role because it controls the work hardening behavior of an alloy. The value of this parameter as well as stress strain curves are covered in Chap. 3.

Basic expressions for *primary creep* have not been derived until recently. In [23] a formulation was presented for 9–12%Cr steels and in [24, 25] for copper. In these papers, the primary creep rate is derived from dislocation equations without introducing new quantities. For copper the observed exponential decrease in creep rate with increasing strain can be reproduced. With a satisfactory description of primary creep, the behavior at very low stresses can be modeled. As discussed below this is of importance for analyzing data for diffusion creep. In addition, an accurate representation is important in many cases in design at high temperatures. Empirical equations for primary creep are typically difficult to generalize and transfer to suitable expressions for stress analysis. However, from basic equations this is readily possible. Primary creep will be covered in Chap. 4.

Creep at low stresses and with low stress exponents has always created a special interest amongst scientists due to the simple expressions for diffusion creep. With the event of basic formulae for primary dislocation creep, it is possible to analyze its role at low stresses. Since stationary conditions are rarely reached at very low creep stresses, it is essential to take primary creep into account. It is shown in the book that dislocation creep can give stress exponents of 1 and that situation is thus not restricted to diffusion creep. Examples are given for an austenitic stainless steel, for aluminum and for copper. Both for aluminum and copper, the basic creep model can accurately represent creep measurements at high temperatures and low stresses

as well as at low temperatures and high stresses. Thus, the model can handle a wide range of conditions in temperature and stress. These findings can be considered as a direct verification of the basic creep model. The results are presented in Chap. 5.

For *solid solution hardening* (SSH) already Hirth and Lothe [18] derived expressions for slowly diffusion elements. Surprisingly enough, the expressions have not been used extensively in the literature. The author has shown that the expressions can reproduce experimental results quite well. For fast diffusing elements the mechanism is different [26]. The dislocations have to break away from their Cottrell atmospheres of elements to move. The most well characterized case is phosphorus in copper where ppm quantities have a pronounced effect on the creep strength. SSH will be discussed in Chap. 6.

Precipitation hardening (PH) is a potent method to increase the creep strength of alloys. This was realized early on and many scientists were engaged to try to model the magnitude of the contributions. They worked from the assumption that there is a barrier against climb when the dislocations pass the particles. A number of estimates of the size of the barrier were made. However, eventually the values became so low that they had no technical interest anymore [27]. With the lack of a proper model for a long time, in many papers PH contribution to the creep strength was estimated with the Orowan strength, which strongly overestimates the PH contribution and in addition gives the wrong temperature dependence. Later, it was assumed that the controlling factor was the time it takes for a dislocation to climb across a particle [28, 29]. This mechanism was used to describe the creep strength of austenitic stainless steels [30–32]. These studies had unfortunately the situation that the PH was only a smaller part of creep strength. To verify the model, Co particles in Cu were studied [33]. The Cu–Co alloys had the advantage that PH was a major part of the creep strength and the validity of the model could be verified. The influence of composition and heat treatment could be reproduced. PH is analyzed in Chap. 7.

Cells or subgrains are formed in virtually all materials during plastic deformation and are collectively referred to as substructure. If the substructure can be locked with the help of particles, it can give a significant contribution to the creep strength. A well-known example is the martensitic steel P91 where $M_{23}C_6$ particles can be used to stabilize the substructure [23]. Models for the formation of substructure during creep and during plastic deformation at near ambient temperatures are presented. Unbalanced dislocations can be formed where the presence of opposite Burgers vector is absent. This has the consequence that static recovery does not occur and the substructure can build up a significant contribution to the creep strength. This is an important mechanism for how the creep strength can be raised after cold work [25]. The model can accurately describe how cold work can raise the rupture time by several orders of magnitude. This can be considered as an additional verification of the basic creep models. Substructures are analyzed in Chap. 8.

Grain boundary sliding (GBS) is assumed to be the main mechanism for initiation of creep cavities. The grain boundary displacements have been quantified with the help of finite element analysis (FEM) [34, 35]. The displacement is proportional to the creep strain with a proportionality constant C_s that can be assessed from the FEM results [36, 37]. The amount of data on GBS in the literature is limited. However,

for copper three types of measurements have been performed, and these measured values for C_s are in agreement with the theoretical value. GBS is also believed to be the main mechanism for superplasticity. The results for GBS are used to derive a basic model for superplasticity. The model can reproduce literature data for Al22Zn. GBS is discussed in Chap. 9.

Nucleation, growth and linkage of *creep cavities* are the source of crack initiation in many cases and are therefore of considerable technical interest. *Nucleation of cavities* can be well described by assuming that it is controlled by GBS. In particular, it gives the number of cavities that is proportional to the creep strain in a way that is in quantitative agreement with observations [38]. Cavities are mainly nucleated at particles or subboundary junctions in the grain boundaries. In the past, attempts have been made to base cavity nucleation on classical nucleation theory. However, it suggests a strong stress and temperature dependence that is at variance with observations.

Models for diffusion *growth of creep cavities* have been available for a long time, but the original expressions overestimated the observed growth. This was solved by requiring that the growth rate should not be faster than the creep rate (constrained growth). However, these modeled growth rates are still higher than the experimental values. By analyzing the balance between the cavity growth rate and the creep rate with the help of finite element methods (FEM), further improvements have been achieved and now the data can be described in a satisfactory way [39]. Strain controlled growth of cavities is also analyzed. A number of models can be found in the literature. However, several of these models give a very low growth rate if the normal size of cavity nuclei is assumed. That makes it difficult to use them for prediction of growth rates. In addition, some models do not take constrained growth into account. On the other hand for larger initial cavity sizes, the predicted growth rates can exceed the observed ones in a pronounced way. One approach that relates the growth rate directly to the amount of GBS avoids these problems [40]. Cavitation is discussed in Chap. 10.

Cavitation during cyclic loading is expected to play the same important role for rupture prediction as during static creep. To describe the nucleation of cavities, the amount of creep during creep-fatigue interaction must be possible to predict. The basic models for static creep can be taken over when describing the stress strain loops during cycling with one important change. The dynamic recovery parameter ω must be increased. The reason is that dislocations encounter each other much more frequently during cycling than during static loading, leading to an enhanced annihilation of dislocations. The principles for nucleation and growth of cavities can essentially be taken over from static loading. This is verified by comparison to experiments for 1Cr0.5Mo steel, which is handled in Chap. 11.

Numerous empirical models for *tertiary creep* can be found in the literature. They are used to describe the creep damage for example during the analysis of residual lifetime of components with the help of the continuum damage mechanics (CDM). There are many mechanisms that can contribute to tertiary creep such as cavitation as well as particle and substructure coarsening. However, recent investigations suggest that another mechanism is often the dominating one [41]. The true stress during a constant load test increases rapidly with strain. During primary and secondary creep,

the increase rate in the dislocation stress matches that of the true stress. However during tertiary creep this is no longer the case and the creep rate increases. For a more complete picture, the role of the substructure must be taken into account as well. The model results suggest that necking starts to form right at the beginning of the tertiary stage, but the neck is not fully developed until very close to rupture. These findings are consistent with available observations [41]. Findings on tertiary creep are presented in Chap. 12.

Modeling of *creep ductility* is natural to divide between brittle and ductile rupture because the failure mechanisms are different. For common creep resistant alloys brittle rupture is initiated by cavitation. When the cavitated area fraction in the grain boundaries reaches a critical factor, cracking and rupture are initiated. The general behavior of the ductility of austenitic steels has been modeled, where the ductility decreases with increasing temperature and rupture time. For ductile rupture, the modeling suggests that necking activates the failure. So far this has been demonstrated for copper and for steels that obey the Omega model, where the logarithm of the strain rate is linear in the strain in the tertiary stage. These materials include low alloy steels, martensitic 9–12%Cr steels and some austenitic stainless steels. Creep ductility is covered in Chap. 13.

Extrapolation of creep rupture data to longer times is technologically most important due to the extended design life of modern high temperature plants of 30 years or more. Extrapolation is in most cases performed with empirical statistical methods. In particular, time-temperature parameters (TTP) are commonly used. To obtain accurate results a large number of data points must be available and careful post assessment tests must be performed. It is shown that the results are found in a safer way if requirements are placed on the derivatives of the creep rupture curves in the analysis. A method for the assessment of the errors in the extrapolated values is presented. An example is also given of the use of neural networks (NNs) in the assessment of creep rupture data. NNs are straightforward to use but stringent requirements on the analyses must be fulfilled to get meaningful results. Fundamental models have reached a sufficient degree of development that they can be used to predict creep rupture data. This is demonstrated for austenitic stainless steels. The results of fundamental models can be generalized and extrapolated. In conventional empirical *extrapolation* with statistical methods, recently safe extrapolation can reach a factor of 3–5 in time [42]. This should be contrasted with the use of the basic model for primary and secondary creep of copper. It has been demonstrated that the model can describe experimental data at low stresses even after extrapolating the creep rate by many orders of magnitude [24]. For copper canisters for spent nuclear fuel, the canisters should stay intact for 100000 years. In such a situation the use of fundamental models is absolutely essential. Even such a large time scale can be covered. Extrapolation is discussed in Chap. 14.

1.3 Objectives

The starting point for the study of creep can be one of the excellent text books by Ilschner [43], Evans and Wilshire [44], Kassner [45] or Zhang [46]. There are also many high quality review articles about creep, for example: Sherby and Burke [47], Lagneborg [6], Nix and Ilschner [48], Orlova and Cadek [49], Kassner and Pérez-Prado [50], and Blum [51].

It is not the aim to review the complete literature on creep modeling. It would neither be possible nor meaningful. Instead the book is concentrated to models that can be derived from physical principles and can give results in quantitative agreement with observations. Such models have mainly been presented in recent years.

The *purpose* of this book is fourfold

- To show that it is quite possible to derive models for properties for plastic deformation that are based on physical principles and that avoid the use of adjustable parameters. Such models are referred to as fundamental (or basic).
- To demonstrate that the use of fundamental models has and will give useful contributions to creep research and that they can give quantitative predictions of properties.
- To illustrate that there are many situations where the use of fundamental models is essential.
- To stimulate more scientists to get involved in the development of fundamental models. There are many areas where further efforts are needed.

1.4 Layout

The author has taken a number of steps to make it easier for the reader to understand the models that are presented:

- Each chapter is started with an and abstract and an introduction that describes the content of the chapter without using any formulae.
- In Section 2 of most chapters, common empirical models are summarized and applied. The aim is to make the reader find models that he/she is familiar with and to illustrate how the empirical and fundamental models are related.
- In the remaining section(s), basic models are derived, their use is illustrated and predictions are compared with experimental data.
- At the end of each chapter a summary of the findings is given.

1.5 Supplementary Material

It is planned to provide supplementary material to the book text. The supplementary material will contain values of material constants and other information that would simplify repeating some of the computations in the book. This material will be placed at the author's home page.

https://www.kth.se/profile/rsand

Or as an SKB report at

https://skb.se/publications

The title of the book will be included in the name of the supplementary material.

Acknowledgements Financial and research support from the Swedish Nuclear Fuel and Waste Management Co (SKB) is gratefully acknowledged. The author would like to thank Christina Lilja, SKB, and Jun-Jing He, KTH, for checking the manuscript and for contributing with many valuable suggestions.

References

1. F.H. Norton, *The Creep of Steel at High Temperatures* (McGraw-Hill Book Co., New York, 1929)
2. J.E. Bird, A.K. Mukherjee, J.E. Dorn, Quantitative relation between properties and microstructure, in A.R. D.G. Brandon (ed.) (Israel Universities Press, 1969), p. 255
3. J. Weertman, Steady-state creep through dislocation climb. J. Appl. Phys. **28**, 362–364 (1957)
4. J. Weertman, Steady-state creep of crystals. J. Appl. Phys. **28**, 1185–1189 (1957)
5. B. Wilshire, Observations, theories, and predictions of high-temperature creep behavior. Metall. Mater. Trans. A **33**, 241–248 (2002)
6. R. Lagneborg, Dislocation mechanisms in creep. Int. Metall. Rev. **17**, 130–146 (1972)
7. Y. Bergström, A dislocation model for the stress-strain behaviour of polycrystalline α-Fe with special emphasis on the variation of the densities of mobile and immobile dislocations. Mater. Sci. Eng. **5**, 193–200 (1970)
8. U.F. Kocks, Laws for work-hardening and low-temperature creep. J. Eng. Mater. Technol. Trans. ASME, Ser H **98**, 76–85 (1976)
9. C. Herring, Diffusional viscosity of a polycrystalline solid. J. Appl. Phys. **21**, 437–445 (1950)
10. R.L. Coble, A model for boundary diffusion controlled creep in polycrystalline materials. J. Appl. Phys. **34**, 1679–1682 (1963)
11. O.A. Ruano, J. Wadsworth, J. Wolfenstine, O.D. Sherby, Evidence for Nabarro-Herring creep in metals: fiction or reality? Mater. Sci. Eng. A **165**, 133–141 (1993)
12. J. Wolfenstine, O.A. Ruano, J. Wadsworth, O.D. Sherby, Refutation of the relationship between denuded zones and diffusional creep. Scr. Metall. Mater. **29**, 515–520 (1993)
13. O.A. Ruano, O.D. Sherby, J. Wadsworth, J. Wolfenstine, Rebuttal to "In defense of diffusional creep." Mater. Sci. Eng. A **211**, 66–71 (1996)
14. P. Kumar, M.E. Kassner, W. Blum, P. Eisenlohr, T.G. Langdon, New observations on high-temperature creep at very low stresses. Mater. Sci. Eng. A **510–511**, 20–24 (2009)
15. M.E. Kassner, P. Kumar, W. Blum, Harper-dorn creep. Int. J. Plast **23**, 980–1000 (2007)
16. L. Kloc, V. Sklenička, J. Ventruba, Comparison of low stress creep properties of ferritic and austenitic creep resistant steels. Mater. Sci. Eng. A **319–321**, 774–778 (2001)

17. L. Kloc, V. Sklenička, Confirmation of low stress creep regime in 9% chromium steel by stress change creep experiments. Mater. Sci. Eng. A **387–389**, 633–638 (2004)
18. J.P. Hirth, J. Lothe, *Theory of Dislocations* (McGraw-Hill, New York, 1967)
19. F. Roters, D. Raabe, G. Gottstein, Work hardening in heterogeneous alloys—A microstructural approach based on three internal state variables. Acta Mater. **48**, 4181–4189 (2000)
20. S. Straub, W. Blum, Does the "natural" third power law of steady state creep hold for pure aluminium? Scr. Metall. Mater. **24**, 1837–1842 (1990)
21. W. Blum, On the validity of the natural creep law at low stresses, Materialia, **15** (2021)
22. R. Sandström, Fundamental models for the creep of metals, in Creep, inTech (2017)
23. H. Magnusson, R. Sandstrom, Creep strain modeling of 9–12 pct Cr steels based on microstructure evolution. Metall. Mater. Trans. A **38A**, 2033–2039 (2007)
24. R. Sandstrom, Basic model for primary and secondary creep in copper. Acta Mater. **60**, 314–322 (2012)
25. R. Sandström, The role of cell structure during creep of cold worked copper. Mater. Sci. Eng. A **674**, 318–327 (2016)
26. R. Sandstrom, H.C.M. Andersson, The effect of phosphorus on creep in copper. J. Nucl. Mater. **372**, 66–75 (2008)
27. W. Blum, B. Reppich, Creep of particle-strengthend alloys, in *Creep Behaviour of Crystalline Solids*. ed. by B. Wilshire, R.W. Evans (Pineridge Press, Swansea, U.K., 1985), p.83
28. H. Magnusson, R. Sandstrom, The role of dislocation climb across particles at creep conditions in 9–12 pct Cr steels. Metall. Mater. Trans. A **38A**, 2428–2434 (2007)
29. J. Eliasson, A. Gustafson, R. Sandstrom, Kinetic modelling of the influence of particles on creep strength. Key Eng. Matter. **171–1**, 277–284 (2000)
30. R. Sandström, M. Farooq, J. Zurek, Basic creep models for 25Cr20NiNbN austenitic stainless steels. Mater. Res. Innov. **17**, 355–359 (2013)
31. R. Sandström, Creep strength of austenitic stainless steels for boiler applications, in *Coal Power Plant Materials and Life Assessment: Developments and Applications*, pp. 127–146 (2014)
32. R. Sandström, Fundamental models for creep properties of steels and copper. Trans. Indian Inst. Met. **69**, 197–202 (2016)
33. F. Sui, R. Sandström, Creep strength contribution due to precipitation hardening in copper–cobalt alloys. J. Mater. Sci. **54**, 1819–1830 (2019)
34. F. Ghahremani, Effect of grain boundary sliding on steady creep of polycrystals. Int. J. Solids Struct. **16**, 847–862 (1980)
35. R. Raj, M.F. Ashby, On grain boundary sliding and diffusional creep, metallurgical. Transactions **2**, 1113–1127 (1971)
36. R. Sandström, R. Wu, J. Hagström, Grain boundary sliding in copper and its relation to cavity formation during creep. Mater. Sci. Eng. A **651**, 259–268 (2016)
37. J. He, R. Sandström, Modelling grain boundary sliding during creep of austenitic stainless steels. J. Mater. Sci. **51**, 2926–2934 (2016)
38. J. He, R. Sandström, Formation of creep cavities in austenitic stainless steels. J. Mater. Sci. **51**, 6674–6685 (2016)
39. J. He, R. Sandström, Growth of creep cavities in austenitic stainless steels, in *8th European Stainless Steel & Duplex Stainless Steel Conference, ASMET*, pp. 561–570 (2015)
40. R. Sandström, Basic creep-fatigue models considering cavitation. Trans. Indian National Acad. Eng. (2021)
41. F. Sui, R. Sandström, Basic modelling of tertiary creep of copper. J. Mater. Sci. **53**, 6850–6863 (2018)
42. S. Holdsworth, The European creep collaborative committee (ECCC) approach to creep data assessment. J. Press. Vessel Technol. Trans. ASME **130**, 0240011–0240016 (2008)
43. B. Ilschner, *Hochtemperatur-Plastizitaet: Warmfestigkeit und Warmverformbarkeit metallischer und nichtmetallischer Werkstoffe* (Springer Berlin; Heidelberg, New York, 1973)
44. R.W. Evans, B. Wilshire, *Creep of Metals and Alloys* (Institute of Metals, Swansea, 1985)
45. M.E. Kassner, *Fundamentals of Creep in Metals and Alloys*, 3rd edn. (Butterworth-Heinemann, Boston, 2015)

46. J.-S. Zhang, *High Temperature Deformation and Fracture of Materials* (Woodhead Publ; Science Press, Oxford, Beijing, 2010)
47. O.D. Sherby, P.M. Burke, Mechanical behavior of crystalline solids at elevated temperature. Prog. Mater Sci. **13**, 323–390 (1968)
48. W.D. Nix, B. Ilschner, Mechanisms controlling creep of single phase metals and alloys, in *Strength of Metals and Alloys* (Pergamon, 1979), pp. 1503–1530
49. A. Orlová, J. Čadek, Dislocation structure in the high temperature creep of metals and solid solution alloys: a review. Mater. Sci. Eng. **77**, 1–18 (1986)
50. M.E. Kassner, M.T. Pérez-Prado, Five-power-law creep in single phase metals and alloys. Prog. Mater. Sci. **45**, 1–102 (2000)
51. W. Blum, P. Eisenlohr, F. Breutinger, Understanding creep—A review. Metall. Mater. Trans. A **33**, 291–303 (2002)

Chapter 2
Stationary Creep

Abstract An introduction to creep and its main characterstics are given. Stationary creep has been studied extensively in the literature. Stationary creep is a result of a balance between work hardening and recovery processes, which allows for a continues plastic deformation without raising the stress. The starting point for the basic modeling of creep is a differential equation for the dislocation density that describes how it varies with strain or time. The model explains how the dislocation density is influenced by work hardening and recovery. From the dislocation model, a basic equation for the creep rate is derived that is in many respects similar to the classical Bird, Mukherjee and Dorn (BMD) formula but with the values of the parameters given. By taking the role of strain induced vacancies into account, the applicability of the BMD equation is widely expanded because the basic model can also handle low temperatures and high stresses that is usually referred to as the power-law break down regime. It is illustrated that the creep model can represent the creep rate for pure metals such as Al and Ni.

2.1 The Creep Process

Creep deformation is in general assumed to take place by the motion of dislocations. At very low stress and high temperatures creep can also occur by the diffusion of individual atoms, which is referred to as diffusion creep. The framework for diffusion creep and the competing dislocation creep at very low stresses are discussed in Chap. 5. In this chapter the focus will be on dislocation creep.

Let us consider a specimen in a soft annealed condition. During a creep test the few dislocations present initially will rapidly multiply and form a network. This network will strengthen the material, which is referred to as *work hardening*. In a polycrystalline metal, the initial phase of the work hardening is characterized by an increase in the strength from the dislocations that is proportional to the strain. Gradually the dislocation density becomes sufficiently high that more stable and energy efficient dislocation structures are formed that reduce the increase in strength. During this stage also some dislocations are eliminated due to the interaction with

R. Sandström, *Basic Modeling and Theory of Creep of Metallic Materials*, Springer Series in Materials Science 339,
https://doi.org/10.1007/978-3-031-49507-6_2

other dislocations. Thus there is a process that balances the work hardening and removes and stabilizes some dislocations. We will refer to this process as *dynamic recovery*. It is strain controlled in the same way as the work hardening. The stages described so far are similar for creep and rate controlled tensile tests.

Specific for creep is that there is an additional process called *static recovery*. Dislocations with opposite burgers vectors attract each other and if the dislocations are free to move, they will eventually eliminate each other. At low temperatures dislocations can only move in their glide planes, which is referred to as glide. At high temperatures the dislocations can also move perpendicular to the glide planes. For edge dislocations this is possible if atoms can diffuse to and from the dislocation cores. This mechanism is called climb. The main difference between plastic deformation at low and at high temperatures is that climb of dislocations can take place. This enables that dislocations can move both parallel and perpendicular to the glide planes. This is crucial during static recovery since the dislocations that are influenced by attracting forces can reach each other. This makes it possible for dislocations to annihilate each other and that is the basis of static recovery.

When the dislocation density has reached a certain level during a creep test due to work hardening, the static recovery starts to be of importance. There is work hardening that raises the dislocation density and recovery that reduce the density. The rates of recovery increase faster with time than the rate of work hardening. This means that eventually there will be a balance between work hardening and recovery. The whole process becomes stationary and the dislocation density becomes constant. This is referred to as stationary creep. In the traditional way of describing a creep strain versus time curve ("creep curve"), stationary creep is the second stage and therefore it is referred to as secondary creep as well. Although stationary and secondary creep does not always be exactly the same thing, no distinction between the terms will be made in the present book.

The presence of a stationary stage implies that a specimen can continue to deform at constant stress or load, which is one of the most characteristic features of creep, and any basic creep model must be able to describe how the stationary stage is reached. In creep strain tests, the secondary creep rate is usually measured as the minimum creep rate. Even in the secondary stage, the creep rate is not fully constant. The extent of the secondary stage is rarely precisely defined and it is up to the one analyzing the creep data to determine that.

Two types of recovery, dynamic and static, are introduced above. In fact, in most papers where recovery during creep is discussed no distinction is made between dynamic and static recovery. In addition, the nomenclature varies. In this book dynamic recovery is strain controlled and static recovery time controlled. This means that dynamic recovery only takes place when a specimen is strained whereas static recovery can occur even without external load. To describe both tensile and creep tests with the same models, both dynamic and static recovery must be taken into account. In addition, there are a number of phenomena such as the role of cell structure and the influence of cold work on creep that would be very difficult to describe without taking both types of recovery into account.

In Sect. 2.2 empirical models for the secondary creep rate are presented. The dislocation model that is the basis for the description of both stress controlled (creep) and rate controlled (stress strain curves) deformation is derived in Sect. 2.3. Some constants that are needed in the creep models are analyzed in Sect. 2.4. The basic formula for the secondary creep rate is given in Sect. 2.5. The dislocation mobility plays a central role in the modeling, Sect. 2.6. Finally in Sect. 2.7, the analysis is applied to aluminum and in Sect. 2.8 to nickel.

2.2 Empirical Models of Secondary Creep

It was early on recognized that the creep rate in the secondary stage could be described with simple relations. Norton found that stress dependence of the creep rate $\dot{\varepsilon}_{\text{sec}}$ could be described with an exponential expression [1]

$$\dot{\varepsilon}_{\text{sec}} = A_{\text{N}}\sigma^{n_{\text{N}}} \tag{2.1}$$

where σ is the applied stress A_{N} is a constant. n_{N} is referred to as the stress or Norton exponent. Equation (2.1) was later extended by including the temperature and grain size dependence [2, 3]

$$\dot{\varepsilon}_{\text{sec}} = \frac{A_{\text{N}} D_{\text{self}} G b}{k_{\text{B}} T}\left(\frac{b}{d}\right)^{p}\left(\frac{\sigma}{G}\right)^{n_{\text{N}}} \tag{2.2}$$

D_{self} is assumed to be the self-diffusion coefficient represented with an Arrhenius expression $D_{\text{s0}} \exp\left(-Q_{\text{self}}/R_{\text{G}}T\right)$ where D_{s0} is a frequency factor, Q_{self} an activation energy, and R_{G} the gas constant. G is the shear modulus, b the Burgers vector, k_{B} the Boltzmann's constant, T the absolute temperature, d the grain size, σ the applied stress, and A_N a constant. The constant p is the grain size exponent that is usually close to zero but takes positive values for fine grained materials. A_{N}, p and n_{N} are usually considered as adjustable parameters and fitted to experimental data. Unless the activation energy is close to that for self-diffusion, it is an additional adjustable parameter. Equation (2.2) is often referred to as the Bird, Mukherjee and Dorn (BMD) equation. The equation has been much used in creep research in the past decades. It has been assumed that from the values of the stress exponent, the activation energy and the grain size exponent, the active mechanisms could be identified. This will first be analyzed for the stress exponent below.

Another reason for the importance of Eq. (2.2) is that the creep rate can roughly be related to the rupture time with the help of the Monkman-Grant relationship [4]

$$\dot{\varepsilon}_{\text{sec}}^{m_{MG}} t_R = C_{MG} \tag{2.3}$$

where t_{R} is the time to rupture and m_{MG} and C_{MG} are constants. The relation works

best when the secondary stage is a fairly large fraction of the creep life. An alternative way of writing Eq. (2.3) is

$$\dot{\varepsilon}_{\text{sec}} t_R = \varepsilon_{R_{\text{sec}}} \tag{2.4}$$

where $\varepsilon_{R\text{sec}}$ is the total creep strain in the secondary stage. Equation (2.4) is often easier to apply than (2.3).

The understanding of dislocation creep is mainly based on modeling. The prime interest has been on secondary creep. The reason is that the stress dependence of the rate in the secondary stage has been assumed to reflect the operating creep mechanism. In two papers Weertman suggested that stress exponent was about 5 if climb of dislocations and about 3 if glide of dislocations was controlling [5, 6]. This resulted in the anticipation that the value of the stress exponent could be used to identify the controlling microstructure mechanism. This was further emphasized by the predictions of the diffusion creep models that gave a stress exponent of 1.

Creep investigations concerning metals have often been performed above half the absolute melting point T_{m}. In Fig. 2.1, the stress dependence of the creep rate is illustrated for 0.5Cr0.5Mo0.25V steel at 565 °C over a wide range of stresses.

The slope of the curve gives the stress exponent n_{N}. At intermediate stresses (and temperatures) the stress exponent is usually in the range 3–8. The value in Fig. 2.1 is 4. The stress exponent is much higher at high stresses (and at low temperatures), in the Figure illustrated with $n_{\text{N}} = 12$. The creep rate varies exponentially with stress at still higher stresses, which is referred to as power-law breakdown. This can give very high stress exponents. At very low stresses, the n_{N} value takes values down to unity or even below unity [7]. The steel 0.5Cr0.5Mo0.25V is a precipitation hardened material. Other precipitation hardened alloys can show much higher stress exponents than in Fig. 2.1.

Climb of dislocations has in general been considered as the operating mechanism at intermediate exponents (3–8). However, glide has also been proposed to control the

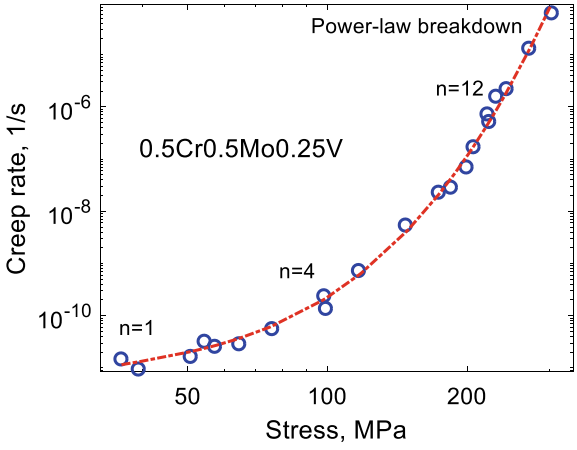

Fig. 2.1 Creep rate versus stress for 0.5Cr0.5Mo0.25V steel at 565 °C. The *n* value is the stress exponent in the power-law creep law, Eq. (2.2). At large stresses the creep rate increases exponentially with the stress, which is called power-law breakdown. Some of the data points are extrapolated. After Wilshire [7]. Reprinted from [8] with permission of intechopen

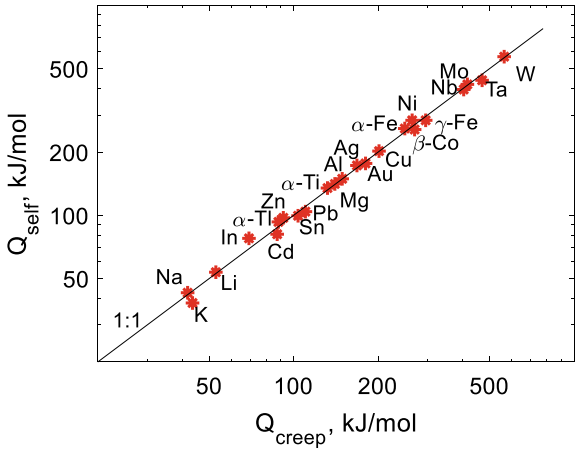

Fig. 2.2 Activation energy for self-diffusion Q_{self} versus the activation energy for creep Q_{creep}. Q_{creep} is obtained by fitting the Q value in Eq. (2.2) to creep strain rate data. After Sherby and Miller [3]

deformation for certain alloy types. The dominating mechanism at high stresses has been suggested as glide. The main mechanism at low stress exponents approaching 1 has been considered to be diffusion creep. This consistent change of operating mechanism with stress has been challenged, see for example [7]. Recent research supports that this challenge is relevant. This will be discussed in Sect. 2.6.4.

It was early on recognized that when the activation energy in Eq. (2.2) was fitted to creep strain data for pure metals a value close to the activation energy for self-diffusion Q_{self} was obtained. This was the reason for having the self-diffusion coefficient in Eq. (2.2). The fitted value is referred to as the activation energy for creep Q_{creep}. The relation between Q_{creep} and Q_{self} is illustrated in a classical picture in Fig. 2.2 [2, 3].

The natural explanation of the close relation between Q_{creep} and Q_{self} is that creep is controlled by climb. Since climb requires the diffusion of vacancies, the climb rate of pure metals is proportional to the constant for self-diffusion. However, for alloyed steels the activation energy for creep can be significantly higher than for self-diffusion due to solid solution hardening. There are other mechanisms that give a creep rate that is related to the self-diffusion constant. The most well-known one is diffusion creep.

2.3 Dislocation Model

The most characteristic feature of creep is that there is a continuous deformation at constant load or stress. This requires that extensive recovery of dislocations takes place that balances the strengthening effect of dislocations due to work hardening. Basic creep models must be able to describe this feature. This is the basis of creep recovery theories [9]. To provide creep models that can make general predictions, the models must be based on basic physical principles and the use of adjustable

parameters must be avoided. In this chapter such a creep recovery model will be presented.

To describe plastic deformation, the development of the dislocation structure must be known. Only recently quantitative basic models have been established that fulfill the requirements in the previous paragraph. Such a model will now be presented. In later sections and chapters it will be used in a number of applications.

During plastic deformation three main processes take place. Work hardening raises the strength by generation of new dislocations and thereby increases their density. The increase of the dislocation density raises the energy content of the material. There is a driving force to reduce the energy content. The mechanism that makes this possible is called recovery. During recovery dislocations of opposite signs combine to form low energy configuration or annihilate each other, which reduces the density of dislocations. There are two types of recovery: dynamic recovery that is strain dependent and static recovery that is time dependent.

2.3.1 Work Hardening

The work hardening of polycrystalline materials can be described with the help of the following equation for the dislocation density ρ

$$\frac{d\rho}{d\varepsilon} = \frac{m_\mathrm{T}}{bL_\mathrm{s}} \qquad \text{(work hardening)} \tag{2.5}$$

ε is the strain, m_T the Taylor factor, b Burger's vector and L_s the "spurt" distance which the dislocation moves in each elementary release during deformation for example from a Frank-Read source. Equation (2.5) can be derived from the Orowan equation

$$\dot{\varepsilon} = b\rho v/m_\mathrm{T} \tag{2.6}$$

$\dot{\varepsilon}$ is the creep rate and v the velocity of the dislocations. If Eq. (2.6) is integrated, one obtains

$$\varepsilon = b\rho L_\mathrm{s}/m_\mathrm{T} \tag{2.7}$$

This equation describes how much strain is generated when the dislocations have spurted a distance L_s. If we derivate Eq. (2.7) and keep the spurt distance L_s constant, we get Eq. (2.5). The Orowan Eq. (2.6) is based only on a geometrical argument and not on a specific mechanism, and this applies to Eqs. (2.5) and (2.7) as well. In this way these equations have a general applicability. In Eq. (2.5), L_s can be related to the barriers in the materials such as grains or subboundaries. The simplest assumption is that the spurting dislocations are stopped by the grain boundaries. L_s would then be the grain size d_g. This would give a grain size dependence in the creep rate that

is not observed except in special cases. The most common assumption is that L_s is controlled by the forest of dislocations, i.e. it is related to the average distance between the dislocations $1/\rho^{1/2}$.

$$L_s = \frac{c_L}{\rho^{1/2}} \tag{2.8}$$

c_L is a constant that is much larger than unity. How to find the size of c_L will be discussed below. If the dislocations are stopped by the subboundaries instead it gives an L_s value that is not very different from that in Eq. (2.8) as will be seen below. If Eq. (2.8) is inserted into Eq. (2.5) one finds that

$$\frac{d\rho}{d\varepsilon} = \frac{m_T \rho^{1/2}}{b c_L} \qquad \text{(work hardening)} \tag{2.9}$$

This form of the work hardening equation appears in many models including empirical ones, see for example [10, 11]. As will be seen below, this model can describe the initial stages of work hardening in fcc alloys.

2.3.2 Dynamic Recovery

When two dislocations during plastic deformation are nearer to each other than a critical distance d_{int} a low energy configuration may be formed or annihilation occurs reducing the dislocation density. This process is referred to as dynamic recovery. It is commonly taken into account with the help of the following equation

$$\frac{d\rho}{d\varepsilon} = -\omega\rho \tag{2.10}$$

where ω is a constant. This equation was first proposed by Bergstrom and co-workers [12, 13]. Roters et al. [14] gave a basic derivation of Eq. (2.10). They used the following argument. During a time increment dt a dislocation travels a distance v dt and has to find a suitable dislocation within the distance $2d_{int}$. This gives an annihilation rate of

$$d\rho = -\rho v dt 2d_{int}\rho = -\frac{\dot{\varepsilon} m_T}{b} dt 2d_{int}\rho \tag{2.11}$$

In the last step, the Orowan Eq. (2.6) has been applied. This gives an equation of the same form as Eq. (2.10). By taking the role of slip planes, dislocation locks and dislocation dipoles into account, the following expression for the constant ω was obtained [14]

$$\omega = \frac{m_T}{b} d_{int} \left(2 - \frac{1}{n_{slip}} \right) \tag{2.12}$$

n_{slip} is the number of independent slip systems (=12 for fcc metals). Roters et al. [14] suggested a high value for d_{int}. But in fact d_{int} is quite small [15]. The simplest way to estimate d_{int} is to assume that it is equal to twice the dislocation core radius. For example, ab initio calculations for copper give a core radius of $r_0 = 1.3\ b$ [16], and thus $d_{int} = 2.6\ b$. This gives $\omega = 15$ which is quite a good value for copper in agreement with observations. To represent dynamic recovery, Eq. (2.10) is a common equation to use. Together with Eq. (2.9), work hardening of many materials can be described [10, 11]. Equation (2.10) has been used in many papers for representing stress strain curves. A list of such papers can be found in [17].

2.3.3 Static Recovery

Dislocations of opposite burgers vector attract each other. Static recovery takes into account how climbing (and gliding, see below) dislocations of opposite signs move towards each other and finally annihilate. This can be described by the following equation

$$\frac{d\rho}{dt} = -2\tau_L M \rho^2 \tag{2.13}$$

t is the time, τ_L the dislocation line tension, and M the dislocation climb mobility. The idea behind this equation was suggested by Friedel [18], but he never gave any derivation of it in his book. The equation was first used extensively by Lagneborg and co-workers [9]. To derive the equation, let us consider a network of dislocations with an average spacing of R, which corresponds to a dislocation density of $\rho = 1/R^2$. With the help of the dislocation mobility, the velocity of the dislocations can be estimated

$$\frac{dR}{dt} = -Mb\sigma = -Mb\frac{Gb}{2\pi R} \ln\left(\frac{R}{r_0}\right) = -\frac{M\tau_L}{R} \tag{2.14}$$

G is the shear modulus. In the second equality, the expression for the stress from a neighboring screw dislocation is introduced. In the third equality, an expression for the line tension of a screw dislocation has been applied. If equations for edge dislocations or mixed screw and edge dislocations are used instead, the end result is the same. The time to eliminate the dislocation pair t_{elim} is obtained by integrating Eq. (2.14) with respect to time

$$t_{elim} = \frac{R^2}{2M\tau_L} \tag{2.15}$$

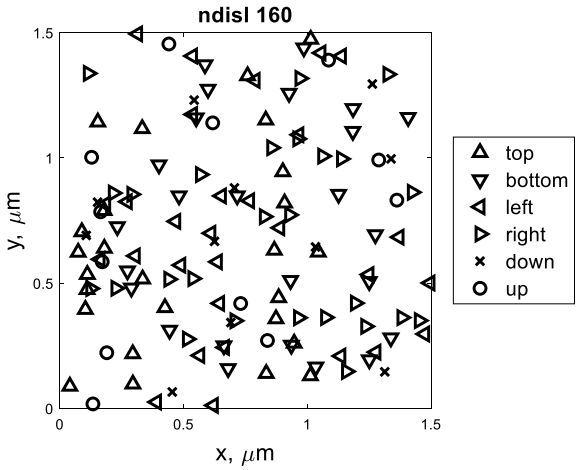

Fig. 2.3 Dislocation dynamics simulation in 2D of static recovery. There are edge dislocations with four Burgers vectors (in the directions top, bottom, left, right) and screw dislocations with two Burgers vectors (in the directions down, up). 160 dislocations remain in the simulation

The average distance between the dislocations changing with time during the recovery is obtained from Eq. (2.15)

$$\frac{dR}{dt} = \frac{M\tau_{\mathrm{L}}}{R} \tag{2.16}$$

If now the relation $R = 1/\sqrt{\rho}$ is applied to Eq. (2.16), (2.13) is recovered.

The derivation of the rate for static recovery, Eq. (2.13), is obviously simplified since it considers only a pair of dislocations. To analyze static recovery in a more general situation, dislocation dynamic simulations have been performed. Randomly distributed parallel dislocations with six different Burgers vectors have been studied, see Fig. 2.3. Four of the sets were edge dislocations and two screw dislocations. Dislocations of opposite signs attract each other (top, bottom or left, right or down, up) and eventually annihilate.

The result of the analysis is illustrated in Fig. 2.4. In this case 1300 dislocations were used in the simulation. In Fig. 2.4 the values from Eq. (2.13) are scaled to the same number of initial dislocations.

It is evident from Fig. 2.4 that the validity of Eq. (2.13) is not restricted to a single pair of dislocations.

Equation (2.13) is based on the annihilation of forest dislocations, i.e. dislocations in the subgrain interiors. If the static recovery is based on subgrain coarsening instead, the recovery rate can be derived with the help of the results in [19]. In fact, the same results as before are obtained, i.e. Eq. (2.13) is reproduced. Thus, the role of the subgrains cannot be determined from the form of Eq. (2.13). Blum has suggested that taking substructure into account would change the recovery process [20]. This obviously depends on the details of the assumptions.

Both dynamic and static recovery are based on the annihilation of dislocations of opposite Burgers' vector or orientation that come close to each other. Although the

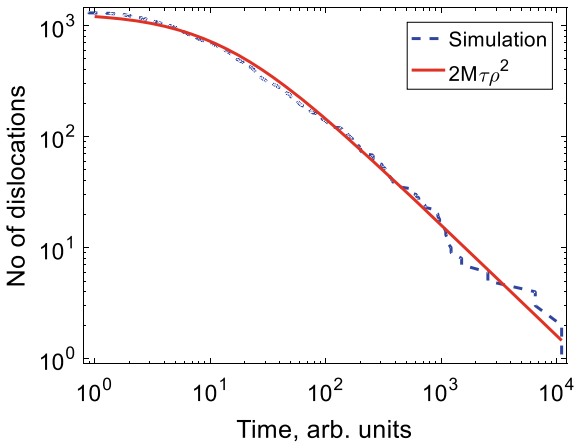

Fig. 2.4 Number of dislocations versus time during static recovery. Dislocation simulation results are compared with Eq. (2.13)

modelling of dynamic and static recovery are strain and time controlled, respectively, and they are based on the different derivations, the two recovery mechanisms are not completely unrelated. For some processes, it is essential to take both types of recovery into account, for example, for stress strain curves for large strains and for primary creep. For more limited strain ranges, dynamic recovery is enough to consider for stress strain curves. On the other hand, the stationary creep rate is based on static recovery. In some cases, it is even assumed that the two recovery mechanisms can give the same results. This is the case in one derivation of the c_L parameter. Dynamic and static recovery should be considered as different appearances of the same phenomenon, and their relative importance depends on the application. Their final role should always be verified by comparison to experiments. The varying influence of the two types of recovery could be compared with phenomena in quantum mechanics, which could be explained in terms of particles or wave packages or both.

2.3.4 Accumulated Dislocation Model

To describe how the dislocation density ρ develops during plastic deformation, the contributions from work hardening (2.5), dynamic recovery (2.10), and static recovery (2.13) are added.

$$\frac{d\rho}{d\varepsilon} = \frac{m_T}{bc_L}\rho^{1/2} - \omega\rho - 2\tau_L M\rho^2/\dot{\varepsilon} \tag{2.17}$$

Notice that we have strain derivatives in (2.5) and (2.10) but a time derivative in (2.13). By multiplying or dividing by $\dot{\varepsilon}$, one can make a transformation from one type of derivative to the other. Equation (2.17) represents a general basic equation

for the development of the dislocation density during plastic deformation. We have seen above that all parts of Eq. (2.17) have a good basis.

The validity of the two first two terms on the right hand side (RHS) of Eq. (2.17) has been verified by comparison to the work hardening in tensile tests. This will be further discussed in Chap. 3. The experimental verification of the last term, the static recovery term is done with the help of creep tests. Examples will be given below.

In many papers in the literature either dynamic or static recovery is taken into account but not both. However, there are cases where it is absolutely essential to include both. For example, this is the case for the influence of cold working on creep properties, which will be treated in Sect. 8.3 [21]. In addition, if the same equation is to be used to describe both strain rate and stress controlled tests, both dynamic and static recovery must be included. Equation (2.17) has to be expanded for some types of materials. A well-known case is martensitic 9 and 12% Cr-steels. For example, to describe primary creep more than one type of dislocation density must be taken into account [22]. This will be described in Sect. 4.5.

2.4 The c_L Parameter

The value of the c_L parameter can be found from the following analysis. The maximum dislocation density ρ_x that is derived from Eq. (2.17) plays an important role because it gives the dislocation contribution to the creep strength during stationary conditions and the amount of work hardening during tensile tests.

The main alternative to derive the value of c_L. is to make reference to the substructure. The spurt distance L_s in Eq. (2.5) can be related to the subgrain or cell diameter d_{sub}.

$$L_s = n_{sub} d_{sub} \tag{2.18}$$

where the constant n_{sub} is close to 3 [23, 24]. It is well established that the subgrain or cell size can be related to the dislocation stress

$$d_{sub} = \frac{K_{sub} G b}{\sigma_{disl}} \tag{2.19}$$

K_{sub} is a constant typically in the range 10–20 [25]. The dislocation stress σ_{disl} is given by Taylor's equation

$$\sigma_{disl} = \alpha m_T G b \rho^{1/2} \tag{2.20}$$

where σ_{disl} is the strength contributions from the dislocations. This equation gives the relation between the strength contribution from the dislocations and the dislocation density where $\alpha \approx 0.19$ is a constant. Experimentally α takes typically values in

the range 0.2–0.6 [26]. In this book a computed value $\alpha \approx 0.19$ applicable to high temperatures will be used, Eq. (3.17). Equation (2.18) can now be rewritten as

$$L_s = \frac{n_{sub} K_{sub} G b}{\sigma_{disl}} = \frac{n_{sub} K_{sub}}{m_T \alpha \rho^{1/2}} \tag{2.21}$$

Equation (2.21) has the same form as Eq. (2.8) so a c_L value can be obtained directly

$$c_L = \frac{n_{sub} K_{sub}}{m_T \alpha} \tag{2.22}$$

A simple estimate of the c_L value can be obtained in the following way. It is assumed that the maximum dislocation density ρ_x is either controlled by the dynamic recovery term (ρ_{xdr}) or the static recovery term (ρ_{xsr}) in Eq. (2.17)

$$\rho_{xdr} = \left(\frac{m_T}{b c_L \omega}\right)^2 \qquad \rho_{xsr} = \left(\frac{m_T \dot{\varepsilon}}{2 b c_L \tau_L M}\right)^{2/3} \tag{2.23}$$

At ambient temperatures, the stress dependence of the recovery terms is such that the dynamic recovery term dominates. This means that first of Eq. (2.23) is the one that is applicable and can be used to obtain an estimate of c_L.

$$c_L = \frac{m_T}{b \omega \rho_x^{1/2}} = \frac{m_T^2 \alpha G}{\omega \sigma_{dislx}} \approx \frac{m_T^2 \alpha G}{\omega (R_m - \sigma_y)} \tag{2.24}$$

where R_m is the tensile strength and σ_y the yield strength at room temperature. In the second equality, Taylor's Eq. (2.20) has been applied. In the final equality in Eq. (2.24), the maximum value of σ_{disl} has been estimated as the difference between the tensile strength R_m and the yield strength σ_y for a material without significant contributions from precipitation and solid solution hardening. The ratio between the expressions for static and dynamic recovery, Eqs. (2.13) and (2.10), is given by

$$\frac{2 \tau_L M \rho}{\omega \dot{\varepsilon}}$$

Apart from constants this is the same ratio as in the creep Eq. (2.28), see below, if the ratio is multiplied by $\rho^{1/2}$. This means that the following ratio is at least approximately temperature and stress independent

$$\frac{2 \tau_L M}{\omega \dot{\varepsilon}} \rho^{3/2}$$

To make Eq. (2.24) valid at higher temperature, we have to multiply it by $(\rho(T)/\rho(T_{RT}))^{1/2}$ which gives

$$c_{\mathrm{L}} = \frac{m_{\mathrm{T}}}{b\omega\rho(T)^{1/2}}\left(\frac{\rho(T)}{\rho(T_{\mathrm{RT}})}\right)^{1/2} = \frac{m_{\mathrm{T}}}{b\omega\rho(T_{\mathrm{RT}})^{1/2}} \tag{2.25}$$

where T_{RT} is the room temperature. This expression is identical to Eq. (2.24). This means that Eq. (2.24) is valid at elevated temperatures as well. Consequently, c_{L} is a temperature independent constant. Eq. (2.22) represents a more physically based value than Eq. (2.24), but the values are of the same order.

Another argument can in a number of cases give a more accurate estimate of c_{L}. It is well-known that tensile stress strain tests can give rise to a stationary stress level if sufficiently large strains can be reached. This stress level is comparable to the creep stress that gives the same strain rate that was used in the tensile test. For many creep tests the contribution from the static recovery is dominating that of dynamic recovery. On the other hand for stress strain curves, the situation is reversed: dynamic recovery is more important than static recovery. But the comparison between the results from the tensile and the creep tests gave the same stationary results. A possible assumption is then that dynamic recovery and static recovery should generate the same findings. Putting it in mathematical terms this means that the two last terms in Eq. (2.17) should be the same, which gives

$$\omega\dot{\varepsilon} - 2\tau_{\mathrm{L}}\rho_{\mathrm{s}}M_{\mathrm{cl}}(\rho_{\mathrm{s}}) \tag{2.26}$$

Since the climb mobility M_{cl} in general depends on the dislocation density, Eq. (2.26) has to be solved by iteration to find the stationary dislocation density ρ_{s}. This argument is only valid if only one of the dynamic or the static recovery term is taken into account. If the dynamic recovery term is considered, the first two terms on the RHS of Eq. (2.17) have the same value under stationary conditions and the c_{L} value can be determined.

$$c_{L=}\frac{m_{\mathrm{T}}}{b\omega}\rho_{\mathrm{s}}^{1/2} \tag{2.27}$$

This relation will be used in Sect. 3.3 for stress strain curves.

2.5 Secondary Creep Rate

The recovery theory is the basis of our understanding of the creep process [9]. For secondary creep to take place the recovery rate must be sufficiently fast that the dislocation density can be kept constant. In the presence of a continuously rising dislocation density, the creep rate will gradually be reduced and eventually vanish, which is not in accordance with observations. Thus, the balance between the generation and the annihilation of dislocations is a crucial feature. The strain derivative in Eq. (2.17) vanishes if we assume stationary conditions. The secondary strain rate can then be expressed as

$$\dot{\varepsilon}_{\text{sec}} = \frac{2\tau_{\text{L}} b c_{\text{L}}}{m_{\text{T}}} M_{\text{climb}} \rho^{3/2} \tag{2.28}$$

In Eq. (2.28) only static recovery is taken into account, not dynamic recovery to make the equation agree with observations. This was discussed at the end of Sect. 2.3.3.

If other contributions than the dislocation stress is part of the applied stress, Eq. (2.20) has to be rewritten as

$$\sigma_{\text{disl}} = \alpha m_{\text{T}} G b \rho^{1/2} = \sigma - \sigma_i \tag{2.29}$$

σ_{disl} is the dislocation stress. σ_{i} is an internal stress that was the yield strength above. In addition, contributions from solid solution hardening and particle hardening can be included. They will be discussed in Chaps. 6 and 7. Equation (2.28) can be transformed to stresses with the aid of Taylor's Eq. (2.29),

$$\dot{\varepsilon}_{\text{sec}} = h_{\text{sec}}(\sigma - \sigma_i) \text{ where } h_{\text{sec}}(\sigma) = \frac{2\tau_{\text{L}} b c_{\text{L}}}{m_{\text{T}}} M_{\text{climb}}(T, \sigma) \frac{\sigma^3}{(\alpha m_{\text{T}} G b)^3} \tag{2.30}$$

The mobility M will be given below. At low stresses this expression is almost independent of stress, and Eq. (2.28) approximately gives a power-law expression with a stress exponent of 3 if there is no internal stress. This is sometimes referred to as the natural creep law [27]. This stress exponent is often observed at high temperatures for austenitic stainless steels [28]. There are many factors that influence the value of the stress exponent n_{N}. If diffusion takes place along dislocations (pipe diffusion) instead of in the grains, the stress exponent is increased by 2 [29]. If the dislocation network consists of dipoles instead of single dislocations the stress exponent is raised by 2, but limited experiments are available to support that [20]. But the most dramatic effect is from strain induced vacancies that will be analyzed in detail below.

According to Eq. (2.29), the applied stress σ is equal to the sum of the strength contributions from dislocations σ_{disl} and from other parts σ_{i} (solid solution and particle hardening). At low temperatures σ_{i} can also include the yield strength. Thus, for a pure metal the applied stress is equal to the dislocation strength if the yield strength is not taken into account. There are other formulations of the creep-recovery theory that also involve an effective stress σ_{eff}, see for example [30]. This means that Eq. (2.29) is replaced by

$$\sigma = \sigma_{\text{eff}} + \sigma_{\text{disl}} - \sigma_i \tag{2.31}$$

Physical arguments have been given for the existence of an effective stress [31]. However, the effective stress is a problematic quantity. It has been suggested that σ_{eff} could be measured in stress drop tests. If the dislocation structure is intact after a stress drop, the strain rate would disappear after a sufficiently large stress drop, because the back stress from dislocations would be much larger than for the stationary

level at the new lower stress. However, it is known now from dislocation dynamics simulations (DDS) that the forest dislocations adapt to the new stress level within milliseconds [32]. The substructure is also likely to partially adapt to the new stress level but not completely. So the back stress that is measured is from the unchanged part of the substructure. Unfortunately, no detailed studies on the momentary effect on the substructure seem to exist. It is evident that what is measured in a stress drop test is something that is quite different from what is supposed to be the effective stress. Stress drop tests at different laboratories have not in general given consistent results [33]. This is not surprising considering the dynamic nature of stress drop tests, which makes them very sensitive to the exact experimental setup [34]. In the present text, the effective stress will not be considered, since there seems to be no well-defined way to measure or model the quantity.

$$\sigma_{\text{eff}} = 0 \tag{2.32}$$

From the results that are presented in this text it will be evident that precise creep models can be formulated without introducing an effective stress.

2.6 Dislocation Mobility

2.6.1 Climb Mobility

The dislocation mobility M in Eq. (2.17) describes the velocity v of moving dislocations

$$v = Mb\sigma \tag{2.33}$$

where σ is the applied stress. Glide of dislocations takes place in their slip planes and climb perpendicular to the slip planes. Climb is associated with the emission and absorption of vacancies by diffusion. Climb is a slower process than glide. Hirth and Lothe [35] derived a basic expression for the climb mobility of pure metals at high temperatures (>0.4 T_{m} where T_{m} is the melting temperature)

$$M_{\text{climb0}} = \frac{D_{\text{s0}} b}{k_{\text{B}} T} e^{\frac{\sigma b^3}{k_{\text{B}} T}} e^{-\frac{Q_{\text{self}}}{R_{\text{G}} T}} \tag{2.34}$$

where T is the absolute temperature, σ the applied stress, D_{s0} the pre-exponential coefficient for self-diffusion, Q_{self} the activation energy for self-diffusion, k_{B} Boltzmann's constant, and R_{G} the gas constant.

At lower temperatures, plastic deformation raises the number of vacancies above the equilibrium value. A climbing dislocation will either emit or absorb vacancies. Jogs in the form of steps of the length of a Burgers vector are formed on gliding

dislocations when they cut each other. In general jogs move by climb and hence they also emit or absorb vacancies. Since the climb rate is proportional to the number of vacancies per unit volume, it is influenced by the excess vacancy concentration.

Mecking and Estrin [36] have developed a model that describes how the number of vacancies is influenced by plastic deformation. They estimated the number of vacancies produced mechanically in a unit volume per unit time as

$$P = 0.5\frac{\sigma\dot{\varepsilon}}{Gb^3} \tag{2.35}$$

The quantities in this equation have been explained above. The constant in Eq. (2.35) was estimated to 0.1 in [36]. A detailed derivation gives the value 0.5. For the excess vacancies the annihilation rate A was found to be

$$A = \frac{D_{\text{vac}}}{\lambda^2}(c - c_0) \tag{2.36}$$

where c_0 is the equilibrium vacancy concentration, $\Delta c = c - c_0$ the excess concentration, D_{vac} the diffusion constant for the vacancies, and λ the spacing between vacancy sinks. Following [36], λ can be related to the cell or subgrain size d_{sub}, Eq. (2.19) if a substructure is present. Combining Eqs. (2.19), (2.35) and (2.36), an expression for the excess vacancy concentration is obtained

$$\frac{\Delta c}{c_0} = 0.5\frac{\sqrt{2}K_{\text{sub}}^2\dot{\varepsilon}b^2}{D_{\text{self}}}\frac{G}{\sigma} \tag{2.37}$$

In finding Eq. (2.37), a relation for the self-diffusion coefficient has been applied

$$D_{\text{self}} = c_0\Omega D_{\text{vac}} \tag{2.38}$$

where Ω is the atomic volume. In the same way as in [36], the climb rate is assumed to be proportional to the total vacancy concentration. Equation (2.37) then gives the increase in the climb rate g_{climb} due to the presence of excess vacancy concentration

$$g_{\text{climb}} = 1 + \frac{\Delta c}{c_0} \tag{2.39}$$

The total climb mobility M_{climb} is obtained by multiplying Eq. (2.34) by g_{climb}.

$$M_{\text{climb}} = M_{\text{climb0}}g_{\text{climb}} \tag{2.40}$$

2.6.2 The Glide Mobility

The glide mobility is very high in a dislocation free crystal. A glide mobility of $M_0 = 1 \times 10^4$ 1/Pa/s was measured for a copper single crystal by Edington [37]. The mobility is much lower in an alloy where a forest of dislocations is present. As discussed above, jogs will be formed on the dislocations during deformation. Often the jogs will have to move perpendicular to their glide planes. This implies that they are sessile, and they have to move by climb [35], and this is a slow process. The motion of the jogs is likely to control the glide rate. This will be assumed and this is also what Hirth and Lothe did [35].

The starting point for the glide mobility is Eq. (2.40), since the jogs are moving by climb. However, there is another aspect that must be considered. Jogs are only present on a small part of a dislocation. Due to the slow movement of the jogs, the forces on the dislocations are localized to the jogs. The average distance between jogs can be related to the dislocation density ρ as $l_{\text{jog}} = 1/\sqrt{\rho}$. The Peach-Koehler formula $F = b\sigma l$ where l is the length of the dislocation gives the force F on a dislocation. F will be the force on each jog if l is chosen as l_{jog}. Thus, the stress on the jogs is raised by

$$g_{\text{glide}} = \frac{l_{\text{jog}}}{b} = \frac{1}{b\sqrt{\rho}} \tag{2.41}$$

where the length of a jog is set as the burgers vector. Equation (2.41) can be expressed in terms of the stress σ with the help of Taylor's equation

$$\sigma = \sigma_{\text{y}} + \alpha m_{\text{T}} G b \sqrt{\rho} \tag{2.42}$$

where σ_{y} is the yield strength

$$g_{\text{glide}} = \frac{\alpha m_{\text{T}} G}{\sigma - \sigma_{\text{y}}} \tag{2.43}$$

Multiplying the climb mobility by g_{glide} gives the glide mobility

$$M_{\text{glide}} = M_{\text{climb0}} g_{\text{climb}} g_{\text{glide}} \tag{2.44}$$

Equation (2.44) is applicable to both edge and screw dislocations. It is evident that the climb and glide mobility are closely related with the assumptions made. g_{glide} is approximately equal to the ratio between the shear modulus G and the applied stress σ. g_{glide} is always much larger than unity, since G is considerably larger than σ. As a consequence, the glide mobility is always larger than the climb mobility. When modeling creep, this is also a common starting point.

2.6.3 Cross-Slip Mobility

With the help of cross-slip, screw dislocations can change glide plane. This can increase the annihilation of dislocations with opposite Burgers vectors and raise the rate of recovery. There is an additional activation energy E_{cs} for cross-slip. Püschl gave the following values of E_{cs} [38].

$$E_{cs} = 0.012Gb^3 \frac{d_{SFE}}{b} \ln\left(\frac{2d_{SFE}}{b}\right) \tag{2.45}$$

d_{SFE} is the width of a stacking fault [35]

$$d_{SFE} = \frac{Gb^2}{8\pi\gamma_{SFE}} \frac{(2-\nu_P)}{(1-\nu_P)} \tag{2.46}$$

where γ_P is Poisson's ratio and γ_{SFE} the stacking fault energy. Taking copper and aluminum as examples with stacking fault energies of 45 mJ/m^2 and 166 mJ/m^2, respectively [39], Eq. (2.45) gives for E_{cs} values of 560 and 40 kJ/mol. This indicates strong temperature dependence for copper. Equation (2.45) is derived with the help of elasticity theory, which can give imprecise values at the atomic level. However, ab initio calculations have recently been carried out with similar results. Du et al. found E_{cs} values of 210 to 270 kJ/mol for Ni–Al alloys and Nöhring and Curtin 60 kJ/mol for Al–Mg, 160 kJ/mol for Cu–Ni and 180 kJ/mol for Ni–Al [40, 41]. Lower energy values have also been obtained in ab initio calculations. Rao et al. found values in the range 50–70 kJ/mol for Cu and Ni [42]. The effect of cross-slip on the mobility can be expressed as

$$g_{\text{cross-slip}} = \exp(-\frac{E_{cs}}{R_G T}) \tag{2.47}$$

$$M_{\text{cross-slip}} = M_{\text{climb0}} g_{\text{climb}} g_{\text{glide}} g_{\text{cross-slip}} \tag{2.48}$$

The role of cross-slip in dynamic recovery will be analyzed in Sect. 3.4.

2.6.4 The Climb Glide Mobility

The results for the dislocation mobilities are recent [8]. It has been known for a long time that the climb mobility in Eq. (2.34) underestimated the creep rates at low temperatures and high stresses by a wide margin. The main assumption was that glide would be the controlling mechanism under these conditions. To handle this situation a combined climb and glide mobility was formulated [43]

$$M_{\text{climb}} = M_{\text{climb0}} f_{\text{clglide}} \tag{2.49}$$

where f_{clglide} is given by

$$f_{\text{clglide}} = \exp\left(\frac{Q_{\text{self}}}{R_{\text{G}}T}\left(\frac{\sigma}{R_{\text{max}}}\right)^2\right) \tag{2.50}$$

R_{max} is the true tensile strength at ambient temperatures. It was work of Kocks et al. [44] that suggested the form of Eq. (2.50). They presented an empirical expression for the glide mobility. However, the expression had five unknown parameters and could therefore not be used directly. According to a suggestion by Nes, an integrated climb and glide mobility could be introduced [45]. In this way some of the unknown parameters could be found. With the aid of work by Chandler, the other parameters could be fixed [46].

The introduction of Eq. (2.50) has a number of important implications at low temperatures. First, the activation energy for creep is reduced. Second, the creep rate is increased by a large factor. Third, the stress exponent is raised in a dramatic way. These findings are in excellent accordance with experiments [15, 47].

Ideally, to describe creep, the basic models for the dislocation mobilities derived above should be used when modeling creep and other types of plastic deformation. However, since g_{climb} involves the strain rate, it is difficult to apply directly. Instead, the equations for the mobilities will be used to verify the validity of Eq. (2.50). This equation can then be applied to compute the creep rate. g_{climb} and f_{clglide} are compared in Figs. 2.5 and 2.6 for pure aluminum.

In Fig. 2.5, a continuous set of parameters for temperature and strain rate are used whereas in Fig. 2.6 experimental values are applied. It can be seen that the enhancement in vacancy concentration due to plastic deformation can fully explain the increase in creep rate in relation to the high temperature climb mobility. A second

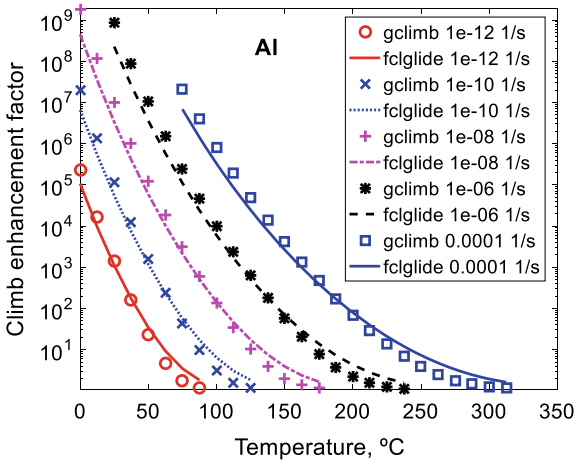

Fig. 2.5 Climb enhancement factor versus temperature at five strain rates for aluminum. The increase in vacancy concentration due to plastic deformation, Eq. (2.39) is compared to the climb-glide enhancement factor, Eq. (2.50). Redrawn from [8] with permission of intechopen

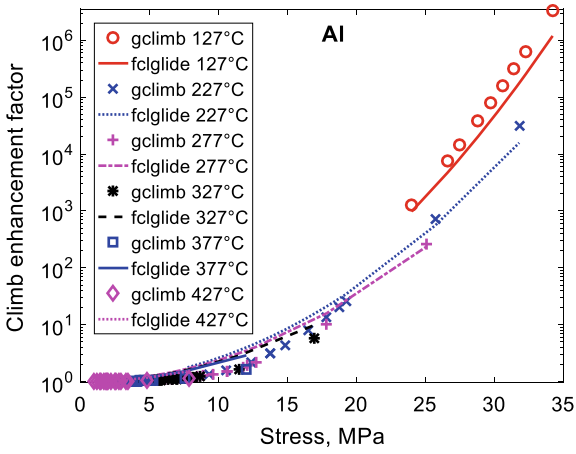

Fig. 2.6 Climb enhancement factor versus stress at six temperatures for aluminum. The increase in vacancy concentration due to plastic deformation, Eq. (2.39) is compared to the climb-glide enhancement factor, Eq. (2.50). Experimental data from [48]. Redrawn from [8] with permission of intechopen

example of the comparison is given in Figs. 2.7 and 2.8 for copper with 50 ppm P (Cu-OFP).

The two sets of models show an excellent agreement over many orders of magnitude of strain rate. The dependence of temperatures, stress and strain rate is well covered. It verifies that the expression for the climb-glide enhancement in Eq. (2.50) can be fully explained by the increase in vacancy concentration. Since its stress and temperature dependence is explicit, it is straightforward to apply. The total formula for the climb mobility, Eq. (2.49), with the equations for high temperature climb mobility M_{climb0}, Eq. (2.34), and the climb glide factor, Eq. (2.50) is now

$$M_{\text{climb}}(T,\sigma) = \frac{D_{\text{s0}}b}{k_{\text{B}}T} e^{\frac{\sigma b^3}{k_{\text{B}}T}} e^{-\frac{Q_{\text{self}}}{R_{\text{G}}T}} f_{\text{clglide}}(T,\sigma) \tag{2.51}$$

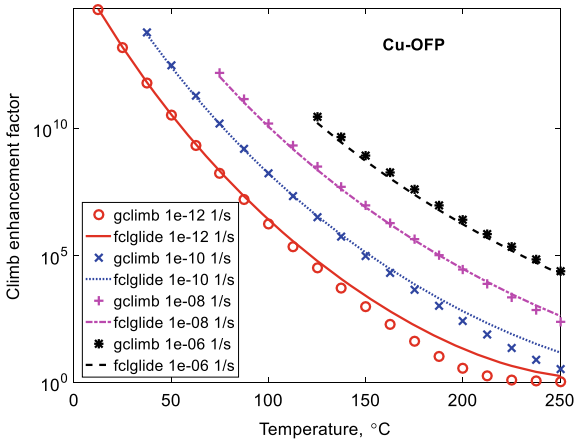

Fig. 2.7 Climb enhancement factor versus temperature at four strain rates for copper alloyed with 50 ppm P (Cu-OFP). The increase in vacancy concentration due to plastic deformation, Eq. (2.39) is compared to the climb-glide enhancement factor, Eq. (2.50)

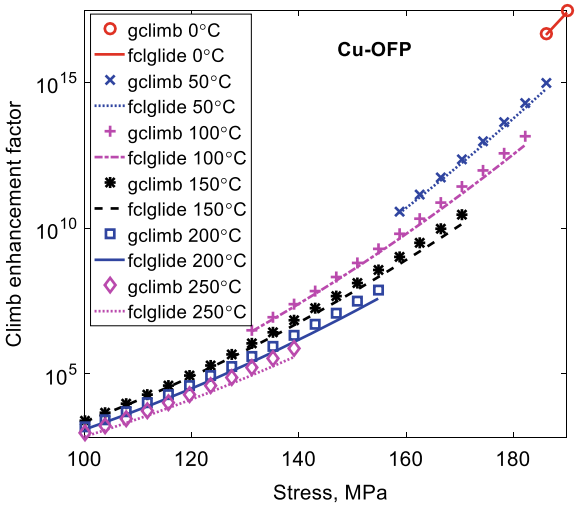

Fig. 2.8 Climb enhancement factor versus stress at six temperatures for copper alloyed with 50 ppm P (Cu-OFP). The increase in vacancy concentration due to plastic deformation, Eq. (2.39) is compared to the climb-glide enhancement factor, Eq. (2.50). Redrawn from [8] with permission of intechopen

This is the expression that should be inserted in the equation for the secondary creep rate (2.30)

$$\dot{\varepsilon}_{\text{sec}} = h_{\text{sec}}(\sigma - \sigma_i) \quad \text{where} \quad h_{\text{sec}}(\sigma) = \frac{2\tau_{\text{L}} b c_{\text{L}}}{m_{\text{T}}} M_{\text{climb}}(T, \sigma) \frac{\sigma^3}{(\alpha m_{\text{T}} G b)^3} \tag{2.52}$$

The derivation of the factor f_{clglide}, Eq. (2.50), was originally based on the assumption that it took the effect of glide into account. But the derivation now considers only climb. The result is that creep is fully climb controlled even at lower temperatures and higher stresses in the power-law breakdown regime.

2.7 Application to Aluminum

According to what we know today, static recovery is in general controlled by climb. This was analyzed in Sect. 2.3.3. This implies that Eq. (2.40) for the climb mobility should be applied in Eq. (2.30). Furthermore it was found that the enhancement factor for the climb mobility g_{climb} due to the increased vacancy concentration in Eq. (2.39) agreed with the climb glide enhancement factor f_{clglide} in Eq. (2.50). Further support to the use of Eq. (2.40) is found from the successful application of f_{clglide} to model experimental data.

An application of Eq. (2.30) will now be demonstrated for pure aluminum. In bcc metals dislocations are exposed to a friction stress, called the Peierls stress. The Peierls stress is usually not thought to be of significance for fcc alloys. However, it has recently been demonstrated by ab initio calculations that the Peierls stress is non-negligible for aluminum. A Peierls stress will be applied for σ_{i}. The following

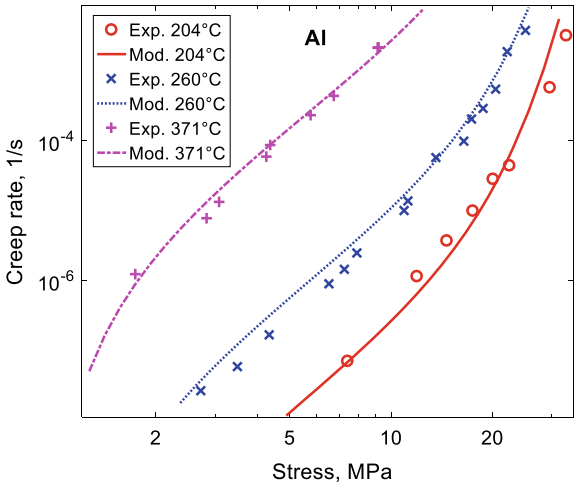

Fig. 2.9 Secondary creep rate versus stress for pure aluminum. Equation (2.30) is compared to experimental data from [50]. Reprinted from [8] with permission of intechopen

value for the Peierls stress of edge dislocations σ_{pe} was found by Shin and Carter [49].

$$\sigma_{\mathrm{pe}} = 4.9 \times 10^{-5} G \tag{2.53}$$

Screw dislocations gave much smaller values. The application of Eq. (2.30) is illustrated in Fig. 2.9.

The slope of the curves is about 4.5 at intermediate stresses in Fig. 2.9. The slope is the value of the stress exponent. The slope increases at higher stresses, indicating power-law breakdown. An increase of the stress exponent is also observed at low stresses. This is due to the presence of the Peierls stress. It can be seen that the model in Eq. (2.30) can obviously handle the experimental data quite well.

2.8 Application to Nickel

The factor f_{clglide} in Eq. (2.50) has been found to work with good precision for Al and Cu. It is used successfully in many places in this book for example also for austenitic stainless steels. It is an expression that is fitted to g_{climb} in Eqs. (2.37) and (2.39) and it may not be completely general. In fact, it has been found for nickel that a different expression has to be applied [51]. In this case, the starting point is to use the function for the secondary creep rate, Eq. (2.30) without the factor f_{clglide}.

$$\dot{\varepsilon}_{\mathrm{sec}} = 2\frac{bc_L\tau_{\mathrm{L}}}{m_{\mathrm{T}}} M_{\mathrm{climb0}}(T,\sigma) f_{\mathrm{SFE}} \frac{\sigma^3}{(\alpha m_{\mathrm{T}} G b)^3} \tag{2.54}$$

This formula for the creep rate is inserted into Eq. (2.37)

$$f_{\text{clglide}} = 1 + \frac{\Delta c}{c_0} = 1 + \frac{\sqrt{2} K_{\text{sub}}^2}{k_{\text{B}} T} \frac{b c_{\text{L}} \tau_{\text{L}}}{(\alpha m_{\text{T}})^3 m_{\text{T}}} f_{\text{SFE}} \frac{\sigma^2}{G^2} e^{\frac{\sigma b^3}{k_{\text{B}} T}} \tag{2.55}$$

For Ni, pipe diffusion, i.e. diffusion along dislocations is important. To the bulk diffusion coefficient in M_{climb0}, the pipe diffusion coefficient has to be added [29]

$$D_{\text{eff}} = D_{\text{self}} + \rho A_{\text{d}} D_{\text{d}} \tag{2.56}$$

where ρ is the dislocation density, A_{d} is the core area of the dislocations, and D_{d} the dislocation diffusion coefficient. For the core radius of the dislocations, a value of 6×10^{-10} m has been chosen. The values of the activation energy and pre-factor for the dislocation diffusion coefficient are 152.4 kJ/mol and 1.56×10^{-4} m^2/s [51, 52]. The creep rate can now be predicted using Eqs. (2.51), (2.52) and (2.55). Results are illustrated in Fig. 2.10.

There are important differences between Eqs. (2.50) and (2.55). At high stresses, Eq. (2.50) gives a stress exponent that increases with decreasing temperature that is a characteristic feature of creep in the power-law break down regime. On the other hand, Eq. (2.55) is associated with an essentially temperature independent stress exponent. In Fig. 2.10, the stress exponent is $n_{\text{N}} = 7$. Equation (2.54) in its basic form gives $n_{\text{N}} = 3$. Since pipe diffusion is dominant there is a contribution of 2 from the second term in Eq. (2.56), since ρ is proportional to the stress squared according to Taylor's Eq. (2.29). There is also a stress exponent contribution of 2 from Eq. (2.55). These contributions to the stress exponent add up to $n_{\text{N}} = 7$.

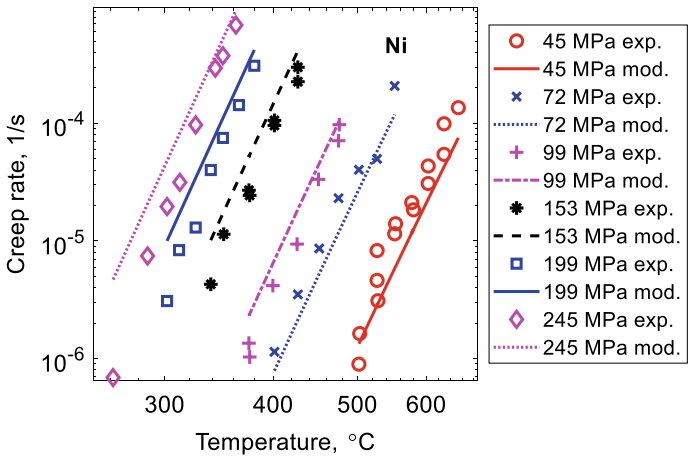

Fig. 2.10 Secondary creep rate versus temperature at six stresses for pure nickel. Predictions using Eqs. (2.51), (2.52) and (2.55) are compared to experimental data from [53]. Redrawn from [51] with permission of ASME

2.9 Summary

- In the past much creep research has been based on the Bird, Mukherjee and Dorn (BMD) equation. It describes the creep rate in the secondary stage as a function of temperature and stress. With the three to four adjustable parameters, most results for the creep rate can be described. It was for a long time assumed that the stress exponent and the activation energy would fall in a narrow range for specific creep mechanisms and that knowledge could be used to identify the operating mechanisms. However that assumption is challenged by more recent findings.
- The most important quantity in the modeling of creep is the dislocation density because it gives a large contribution to the creep strength. There are three main processes that control the development of the dislocation density: work hardening, dynamic recovery and static recovery. Models for the contribution from these three processes are derived. Differential equations for the time and strain derivative for the dislocation density are formulated. These equations are the starting point for much basic modeling of creep. From the equations, an expression for the secondary creep rate can be derived.
- Dislocation creep is assumed to be controlled by climb. The climb mobility is an important quantity in this respect. At low stresses the climb mobility is essentially stress independent and is only a function of the temperature. In this situation the models suggest a stress exponent of about three. During creep, strain induced vacancies appear. At higher stresses they have a dramatic effect on the stress exponent. Strain induced vacancies can quantitatively explain the high stress exponents at least up to 50 during power-law breakdown. This has been demonstrated for aluminum and copper.

References

1. F.H. Norton, *The creep of steel at high temperatures* (McGraw-Hill Book Co., New York, 1929)
2. J.E. Bird, A.K. Mukherjee, J.E. Dorn, Quantitative relation between properties and microstructure, in ed. by A.R.D.G. Brandon (Israel Universities Press, 1969), p. 255
3. O.D. Sherby, A.K. Miller, Combining phenomenology and physics in describing the high temperature mechanical behavior of crystalline solids. J. Eng. Mater. Technol. Trans. ASME **101**, 387–395 (1979)
4. F.C. Monkman, N.J. Grant, An empirical relationship between rupture life and minimum creep rate in creep-rupture tests. ASTM Proc. **1956**(56), 593–620 (1956)
5. J. Weertman, Steady-state creep through dislocation climb. J. Appl. Phys. **28**, 362–364 (1957)
6. J. Weertman, Steady-state creep of crystals. J. Appl. Phys. **28**, 1185–1189 (1957)
7. B. Wilshire, Observations, theories, and predictions of high-temperature creep behavior. Metall. Mater. Trans. A **33**, 241–248 (2002)
8. R. Sandström, Fundamental models for the creep of metals, in Creep, inTech (2017)
9. R. Lagneborg, Dislocation mechanisms in creep. Int. Metallur. Rev. **17**, 130–146 (1972)
10. U.F. Kocks, Laws for work-hardening and low-temperature creep. J. Eng. Mater. Technol. Trans. ASME, 98 Ser H, 76–85 (1976)

11. W. Roberts, Y. Bergström, The stress-strain behaviour of single crystals and polycrystals of face-centered cubic metals—A new dislocation treatment. Acta Metall. **21**, 457–469 (1973)
12. Y. Bergström, A dislocation model for the stress-strain behaviour of polycrystalline α-Fe with special emphasis on the variation of the densities of mobile and immobile dislocations. Mater. Sci. Eng. **5**, 193–200 (1970)
13. Y. Bergström, W. Roberts, A dislocation model for dynamical strain ageing of α-iron in the jerky-flow region. Acta Metall. **19**, 1243–1251 (1971)
14. F. Roters, D. Raabe, G. Gottstein, Work hardening in heterogeneous alloys—A microstructural approach based on three internal state variables. Acta Mater. **48**, 4181–4189 (2000)
15. R. Sandstrom, Basic model for primary and secondary creep in copper. Acta Mater. **60**, 314–322 (2012)
16. R. Wang, S. Wang, X. Wu, Edge dislocation core structures in FCC metals determined from ab initio calculations combined with the improved Peierls-Nabarro equation. Phys. Script. **83** (2011)
17. S. Mohamadnejad, A. Basti, R. Ansari, Analyses of dislocation effects on plastic deformation. Multiscale Sci. Eng. **2**, 69–89 (2020)
18. J. Friedel, *Dislocations* (Addison-Wesley, Reading (MA), USA, 1964)
19. R. Sandstrom, Subgrain growth occurring by boundary migration. Acta Metall. Mater. **25**, 905–911 (1977)
20. W. Blum, P. Eisenlohr, Dislocation mechanics of creep. Mater. Sci. Eng. A **510–511**, 7–13 (2009)
21. R. Sandström, The role of cell structure during creep of cold worked copper. Mater. Sci. Eng. A **674**, 318–327 (2016)
22. H. Magnusson, R. Sandstrom, Creep strain modeling of 9–12 pct Cr steels based on microstructure evolution. Metall. Mater. Trans. A **38A**, 2033–2039 (2007)
23. D. Francke, W. Pantleon, P. Klimanek, Modelling the occurrence of disorientations in dislocation structures. Comp. Mater. Sci. **5**, 111–125 (1996)
24. P. Ambrosi, C. Schwink, Slip line length of copper single crystals oriented along [100] and [111]. Scr. Metall. **12**, 303–308 (1978)
25. M.R. Staker, D.L. Holt, The dislocation cell size and dislocation density in copper deformed at temperatures between 25 and 700 °C. Acta Metall. **20**, 569–579 (1972)
26. H. Wiedersich, Hardening mechanisms and the theory of deformation. JOM **16**, 425–430 (1964)
27. W. Blum, P. Eisenlohr, F. Breutinger, Understanding creep—A review. Metall. Mater. Trans. A **33**, 291–303 (2002)
28. S. Vujic, R. Sandstrom, C. Sommitsch, Precipitation evolution and creep strength modelling of 25Cr20NiNbN austenitic steel. Mater. High Temp. **32**, 607–618 (2015)
29. O.A. Ruano, A.K. Miller, O.D. Sherby, Influence of pipe diffusion on the creep of fine-grained materials. Mater. Sci. Eng. **51**, 9–16 (1981)
30. H. Magnusson, R. Sandstrom, The role of dislocation climb across particles at creep conditions in 9 to 12 pct Cr steels. Metall. Mater. Trans. A **38A**, 2428–2434 (2007)
31. P. Ostrom, R. Lagneborg, Recovery-athermal glide creep model. J. Eng. Mater. Technol. Trans. ASME 98 Ser H, 114–124 (1976)
32. A.H. Delandar, R. Sandström, P. Korzhavyi, The role of glide during creep of copper at low temperatures. Metals **8** (2018)
33. M. Biberger, J.C. Gibeling, Analysis of creep transients in pure metals following stress changes. Acta Metall. Mater. **43**, 3247–3260 (1995)
34. B. Wilshire, M. Willis, Mechanisms of strain accumulation and damage development during creep of prestrained 316 stainless steels. Metall. Mater. Trans. A: Phys. Metallur. Mater. Sci. **35 A**, 563–571 (2004)
35. J.P. Hirth, J. Lothe, *Theory of dislocations* (Krieger, Malabar, Florida, 1982)
36. H. Mecking, Y. Estrin, The effect of vacancy generation on plastic deformation. Scr. Metall. **14**, 815–819 (1980)
37. J.W. Edington, The influence of strain rate on the mechanical properties and dislocation substructure in deformed copper single crystals. Phil. Mag. **19**, 1189–1206 (1969)

38. W. Püschl, Models for dislocation cross-slip in close-packed crystal structures: a critical review. Prog. Mater. Sci. **47**, 415–461 (2002)
39. X.-Z. Wu, R. Wang, S.-F. Wang, Q.-Y. Wei, Ab initio calculations of generalized-stacking-fault energy surfaces and surface energies for FCC metals. Appl. Surf. Sci. **256**, 6345–6349 (2010)
40. J.-P. Du, C.-Y. Wang, T. Yu, Cross-slip process in model Ni(Al) solid solution: an embedded-atom method study. Comp. Mater. Sci. **91**, 192–199 (2014)
41. W.G. Nöhring, W.A. Curtin, Dislocation cross-slip in fcc solid solution alloys. Acta Mater. **128**, 135–148 (2017)
42. S.I. Rao, D.M. Dimiduk, T.A. Parthasarathy, J. El-Awady, C. Woodward, M.D. Uchic, Calculations of intersection cross-slip activation energies in fcc metals using nudged elastic band method. Acta Mater. **59**, 7135–7144 (2011)
43. R. Sandstrom, H.C.M. Andersson, Creep in phosphorus alloyed copper during power-law breakdown. J. Nucl. Mater. **372**, 76–88 (2008)
44. U.F. Kocks, Argon A.S., Ashby, M.F., Thermodynamics and kinetics of slip. Prog. Mater. Sci. **19**, 1 (1975)
45. E. Nes, K. Marthinsen, Modeling the evolution in microstructure and properties during plastic deformation of f.c.c.-metals and alloys—An approach towards a unified model. Mater. Sci. Eng.: A **322**, 176–193 (2002)
46. H.D. Chandler, Effect of unloading time on interrupted creep in copper. Acta Metall. Mater. **42**, 2083–2087 (1994)
47. R. Sandström, Fundamental models for creep properties of steels and copper. Trans. Indian Inst. Met. **69**, 197–202 (2016)
48. H. Mecking, A. Styczynski, Y. Estrin, *Steady state and transient plastic flow of aluminium and aluminium alloys, in strength of metals and alloys (ICSMA 8)* (Pergamon, Oxford, 1989), pp.989–994
49. I. Shin, E.A. Carter, Possible origin of the discrepancy in Peierls stresses of fcc metals: first-principles simulations of dislocation mobility in aluminum. Phys. Rev. B—Condensed Matter Mater. Phys. **88** (2013).
50. I.S. Servi, N.J. Grant, Creep and stress rupture behaviour of aluminium as a function of purity. Trans. AIME **191**, 909–916 (1951)
51. R. Sandström, J. Zhang, Modeling the creep of nickel. J. Eng. Mater. Technol. **143** (2021)
52. S. Soltani, N. Abdolrahim, P. Sepehrband, Mechanism of intrinsic diffusion in the core of screw dislocations in FCC metals—A molecular dynamics study. Comp. Mater. Sci. **144**, 50–55 (2018)
53. E.C. Norman, S.A. Duran, Steady-state creep of pure polycrystalline nickel from 0.3 to 0.55 Tm. Acta Metall. **18**, 723–731 (1970)

Chapter 3
Stress Strain Curves

Abstract Traditionally, stress strain curves for example from tensile testing are described with empirical models with a number of adjustable parameters such as Hollomon, Ludwik, Voce and Swift. With such models it is difficult or impossible to generalize and extrapolate. A model in the form of Voce equation is derived from the same basic dislocation model used for the creep models with the values of constants computed. The derived model is used to describe stress strain curves for Cu including their temperature and strain rate dependence. The dynamic recovery constant ω plays a central to show how the work hardening deviates from a linear behaviour. The temperature dependence of ω is analyzed and shown to be related to that of the shear modulus. In the literature it is frequently assumed that dynamic recovery is controlled by cross-slip. However, the measured activation energy for dynamic recovery is many times smaller than the energy required to make partial dislocations brought together and form a constriction, which is necessary to enable cross-slip, so this is an unlikely possibility.

3.1 General

Stress strain curves are usually generated with the help of tensile tests. In a tensile test a specimen is exposed to a constant length expansion rate at the same time as the force is recorded. The expansion rate is transferred to strain by dividing it by the initial specimen gauge length. The stress is obtained by dividing the force by the initial specimen cross section. In this way a stress versus strain curve is generated for the material, which is also referred to as a flow curve.

Tensile tests are performed on a large scale since the test is used to check the properties of batches during metal production. From the stress strain curves the strength and ductility of the material can be determined. The strength that is a measure of the initiation of plastic deformation, the yield strength, is taken at the linear offset by 0.2% strain for most material. The maximum load in the flow curve gives the maximum stress a material can take, the tensile strength. It is often thought that the strength is the most important property of a material. However, that is not necessarily

R. Sandström, *Basic Modeling and Theory of Creep of Metallic Materials*, Springer Series in Materials Science 339,
https://doi.org/10.1007/978-3-031-49507-6_3

the case. In fact, in order to allow for a more flexible use of a material, it must have a certain amount of formability. In a tensile test, the formability can be measured as the (total) elongation, which is determined as the strain at failure. In scientific work, also the uniform elongation is used, which is the strain at the maximum load in the tensile test. The elongation is also referred to as the ductility that can be said to be another word for formability. Elongation is not the only way to measure the ductility in a tensile test. Another way is to determine the reduction in the specimen cross section after failure, reduction of area.

The ductility is quite an important property. For example, a low ductility makes the material sensitive to overloads, fatigue loads and scratches and other marks on the surface. This can be exemplified for many ceramic materials that have virtually nil ductility. Special design procedures are required to avoid premature failures with low ductility. For example, tensile stresses, sharp corners and rough surfaces must be avoided.

In materials production, stress strain curves from tensile tests are recorded but not usually modeled. If they are, empirical methods are used. Examples of empirical methods for analyzing stress strain curves will be given in Sect. 3.2. In the same way as for creep tests, basic modeling is needed to safely determine the operating mechanisms. This applies also to flow curves from tensile tests. Unfortunately, scientific efforts to formulate such models have been quite limited. However, some models will be presented in Sect. 3.3. The results from tensile tests and creep tests can be assumed to be controlled by the same plastic deformation mechanisms. Thus, the data from tensile tests can significantly supplement the information recorded from creep tests. The dynamic recovery parameter ω plays an important role for the work hardening behavior. In particular, it describes how fast the deviation from a linear stress strain curve takes place. Its value and temperature dependence are discussed in Sect. 3.4.

3.2 Empirical Methods to Describe Stress Strain Curves

To describe stress strain curves, there are many empirical methods in the literature. Some of the classical approaches are listed in Eqs. (3.1–3.4). Ludwik's equation is by far the oldest, but the other three have been around since about 1950. References to the original papers can be found in [1]

$$\sigma = a_1 \varepsilon^{m_1} \quad \text{Hollomon} \tag{3.1}$$

$$\sigma = a_1 + a_2 \varepsilon^{m_1} \quad \text{Ludwik} \tag{3.2}$$

$$\sigma = a_1 - a_2 e^{-\Omega \varepsilon} \quad \text{Voce} \tag{3.3}$$

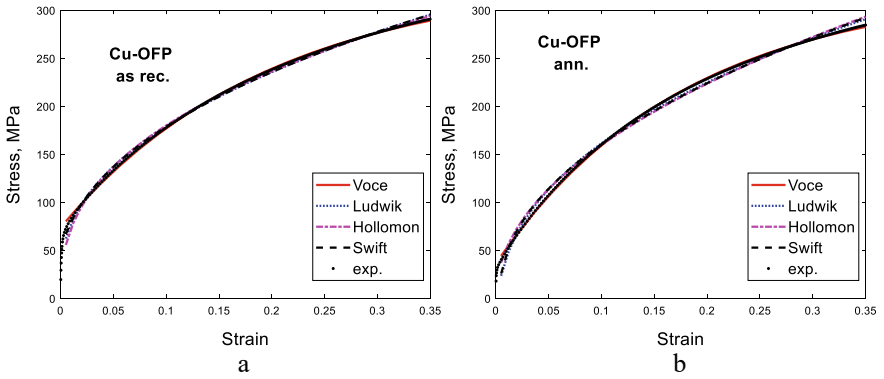

Fig. 3.1 Stress versus strain for Cu-OFP at room temperature; comparison between four empirical models and experimental data; **a** as received condition (forged); **b** annealed condition (450 °C, 3 h) (unpublished data)

$$\sigma = a_1(\varepsilon_0 + \varepsilon)^{m_1} \quad \text{Swift} \tag{3.4}$$

σ is the stress and ε is the strain. The other quantities are adjustable parameters that are fitted to the data. The use of the equations will be illustrated for copper and for a stainless steel. In Fig. 3.1 data for phosphorus alloyed pure copper (Cu-OFP) is shown in two conditions and compared with fitted curves using Eqs. (3.1)–(3.4).

The two conditions give quite similar curves. However, there are some small differences. In the annealed condition the data have a slightly larger curvature and the yield strength is lower in comparison to the as received condition. The reason is that a small amount of cold working remains after the forging in the as received state.

In general an acceptable fit to the data is obtained. There are some slight deviations though. The Ludwik and the Swift equations do not fit the data fully in the annealed condition. At small strains below 0.02 there are significant deviations for both conditions. For the as received condition the Ludwik and the Swift equations seem to work best whereas the situation is the opposite for the other condition where the Voce and Hollomon methods seem to be somewhat better.

The situation at small strains can readily be improved by extending the Eqs. (3.1)–(3.4) somewhat, A direct way is to combine the Ludwik and Voce expressions, Eq. (3.5)

$$\sigma = a_1 + a_2\varepsilon^{m_1} + a_3 e^{-\Omega_2\varepsilon} \quad \text{Ludwik} + \text{Voce} \tag{3.5}$$

Another way is to duplicate the fitting terms. This is illustrated in Eqs. (3.6) and (3.7)

$$\sigma = a_1 + a_2\varepsilon^{m_1} + a_3\varepsilon^{m_2} \quad \text{Ludwik } 2m \tag{3.6}$$

$$\sigma = a_1 + a_2 e^{-\Omega_1 \varepsilon} + a_3 e^{-\Omega_2 \varepsilon} \quad \text{Voce } 2\Omega \tag{3.7}$$

In the literature Ludwigson's Eq. (3.8) has been cited many times [2]. It is the same as Eq. (3.5) but without the constant term. Unfortunately, this turns it out to make it more difficult to use the equation.

$$\sigma = a_1 \varepsilon^{m_1} + a_2 e^{-\Omega_1 \varepsilon} \quad \text{Ludwigson} \tag{3.8}$$

The application of Eqs. (3.5)–(3.7) to copper is illustrated in Figs. 3.2 and 3.3.

It can be seen that with the extended Eqs. (3.5)–(3.7) the fit at low strains can be much improved. To see any deviation one has to go to the enlargements in Figs. 3.2 and

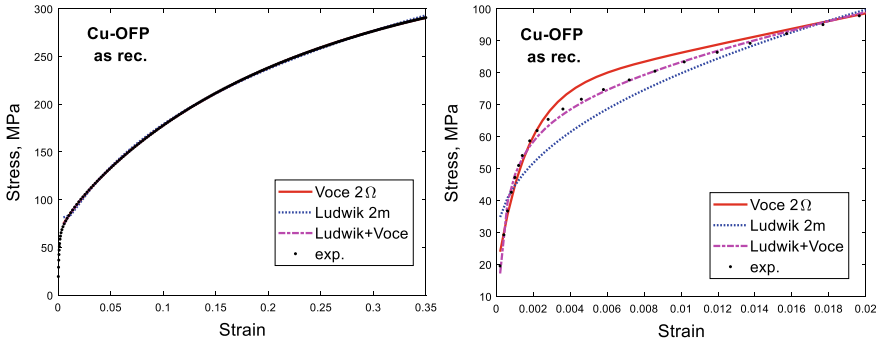

Fig. 3.2 Stress versus strain for Cu-OFP at room temperature in as received condition; **a** fit to Eqs. (3.5)–(3.7); **b** enlargement of the low strain part of (**a**)

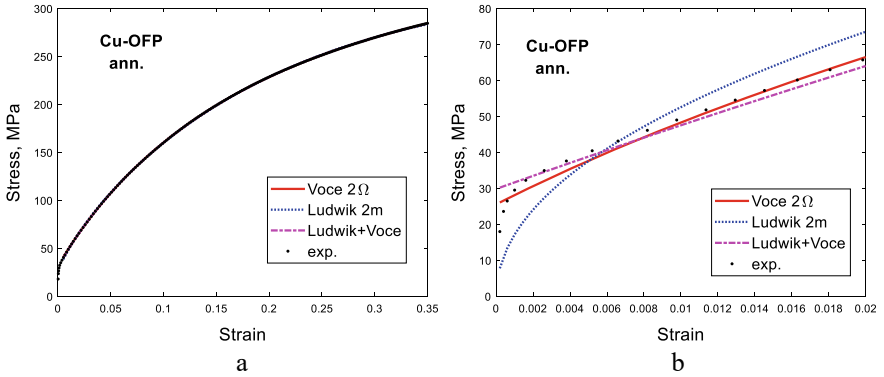

Fig. 3.3 Stress versus strain for Cu-OFP at room temperature in the annealed condition; **a** fit to Eqs. (3.5)–(3.7); **b** enlargement of the low strain part of (**a**)

3.3. There it can be seen that the best result is obtained for the Voce + Ludwik method in the as-received condition and the Voce 2Ω method in the annealed condition.

In Fig. 3.4, data for the austenitic stainless steel 17Cr12Ni2Mo0.08C (316H) at room temperature and 800 °C are illustrated.

From Fig. 3.4a it is evident that the Hollomon equation does not work very well in this case. At 800 °C, Eqs. (3.1), (3.2) and (3.4) are satisfactory but not the Voce equation. Handling of low strains is less problematic than for the copper alloys. However, if a higher precision is needed the extended equations can be applied for the stainless steels as well. This is shown in Figs. 3.5 and 3.6.

It is evident from Figs. 3.5a and 3.6a, the three extended methods work well for the stainless steel both at room temperature and at 800 °C: In Fig. 3.5b, the Voce

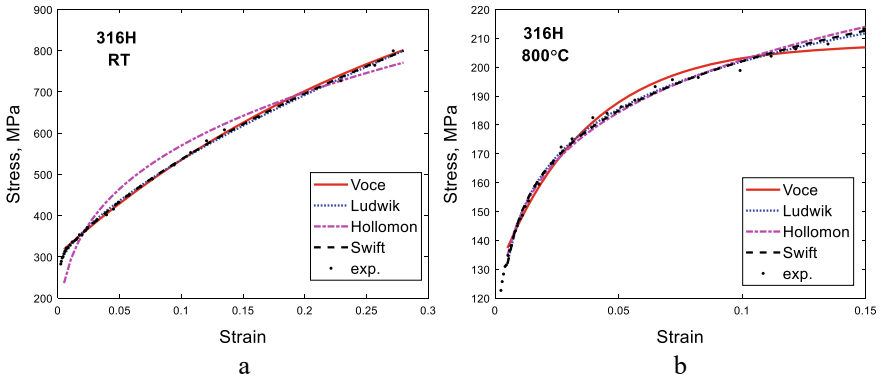

Fig. 3.4 Stress versus strain for the austenitic stainless steel 17Cr12Ni2Mo0.08C (316H); **a** at room temperature; **b** at 800 °C. Equations (3.1)–(3.4) are compared to experimental data from [1]

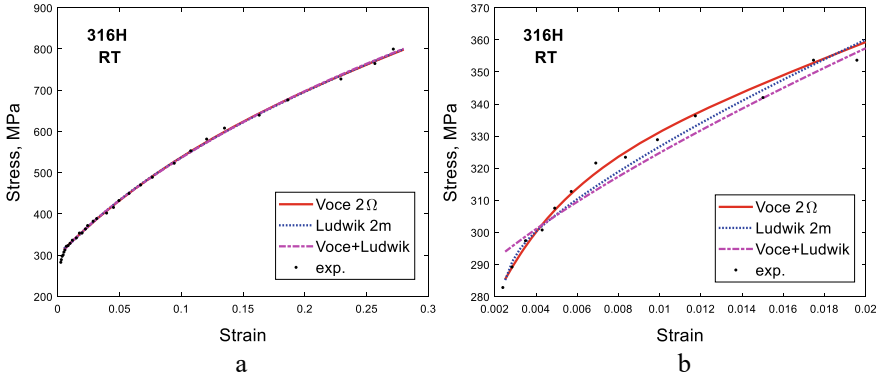

Fig. 3.5 Comparison to the extended Eqs. (3.5)–(3.7) for the same data for 316H at room temperature as in Fig. 3.4a; **a** full curve; **b** enlargement of the low strain part of (**a**)

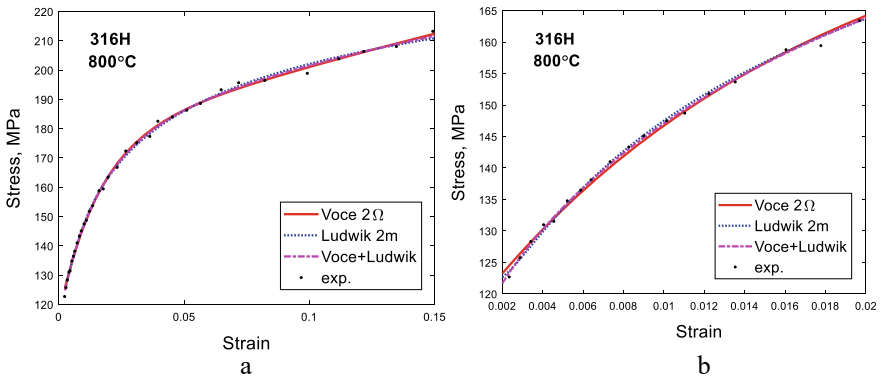

Fig. 3.6 Comparison to the extended Eqs. (3.5)–(3.7) for the same data for 316H at 800 °C as in Fig. 3.4b; **a** full curve; **b** enlargement of the low strain part of (**a**)

2Ω method seems to be the best alternative. At the high temperature all the extended methods are satisfactory also at low strains, Fig. 3.6.

There is a general experience that it is not simple to decide in advance which empirical relation would give the best fit. This has also been illustrated by the examples above. Most of Eqs. (3.1)–(3.7) are purely empirical and cannot be derived from basic physical principles. The exception is the Voce equation. This will be demonstrated in detail in the next section. The other methods are purely empirical. This means that they are flexible expressions that are suitable for data fitting. One of the risks with empirical expressions is that when you get a good fit to the data it is tempting to draw the conclusion that is has physical significance, but that should clearly be avoided.

In Eqs. (3.1)–(3.8) above 2–5 adjustable parameters are present that are to be fitted to the experimental data. There are many types of software that can handle that task. However, it has been found that the fitting process can be slow in particular when the number of adjustable parameters is large. In addition one cannot automatically be sure that the parameters converge to the desired result. The situation is different if there is only a linear dependence of the parameter. An example of that is the determination of constants when a time temperature parameter is used to extrapolate creep rupture data. The problem can be formulated in such a way that the function to be fitted is linear in the adjustable parameters. In such a case the parameter values can be found by solving a linear equation, which is instant. Equations (3.1)–(3.8) are linear in a_1, a_2 and a_3, whereas m_1, m_2, Ω_1 and Ω_2 are nonlinear parameters. By fitting the nonlinear parameters by the optimization software and the linear parameters by solving a linear equation, the accuracy and efficiency of the process can be much improved.

3.3 Basic Model

3.3.1 The Model

Tensile tests are performed at a constant expansion rate or approximately constant strain rate. Creep strain and rupture tests are carried out at constant load or stress. In spite of the difference in testing conditions it is assumed that the same mechanisms are controlling the plastic deformation in both cases. This means that the equations developed in Chap. 2 should be valid also for stress strain curves. The basic expression for the development of the dislocation density ρ is given by Eq. (2.17)

$$\frac{d\rho}{d\varepsilon} = \frac{m_T}{bc_L}\rho^{1/2} - \omega\rho - 2\tau_L M_{cl}\rho^2/\dot{\varepsilon} \tag{3.9}$$

where ε is the strain and $\dot{\varepsilon}$ the strain rate, m_T the Taylor factor, b burgers vector, c_L a dimensionless factor, ω the dynamic recovery factor, τ_L the dislocation line tension, and M_{cl} the dislocation climb mobility. These quantities are further explained in Sect. 2.3. The three terms on the right hand side (RHS) of Eq. (3.9) represent the contributions from work hardening, dynamic recovery and static recovery. At low strains the work hardening term dominates. Thus at this stage the dislocation density ρ increases with increasing strain. Due to different dependence on ρ of the three terms in Eq. (3.9), the dynamic recovery term increases faster with strain than the work hardening term, and the static recovery term faster than the dynamic recovery term. This means that the rate of increase in ρ drops with increasing strain. Eventually the recovery terms are so large that there is a balance between these terms and the work hardening. This balance cannot always be observed in a tensile test, because an instability might occur before the balance is reached and the specimen fails. This instability will be discussed below.

For stress strain curves, the last term in Eq. (3.9), the static recovery term is often small and can be neglected. The role of this term will still be analyzed below. If the static recovery term is ignored, Eq. (3.9) can be integrated directly

$$\rho = \left(\frac{m_T}{b\omega c_L}\right)^2 (1 - \exp(-\omega\varepsilon/2))^2 \tag{3.10}$$

We find as expected that ρ increases with strain and reaches saturation value at large strains. The Taylor equation is used to transfer the dislocation density to strength

$$\sigma = \sigma_y + \sigma_{disl} = \sigma_y + m_T \alpha G b \rho^{1/2} \tag{3.11}$$

where σ_{disl} is the strength contribution from the dislocations, σ_y the yield strength, $\alpha \approx 0.19$ a constant, and G the shear modulus. If Eq. (3.10) is inserted into Eq. (3.11), the strain dependence of the strength is obtained

$$\sigma = \sigma_y + \frac{\alpha G m_T^2}{\omega c_L}(1 - \exp(-\omega\varepsilon/2)) \tag{3.12}$$

It is convenient to introduce the saturation stress σ_{sat}

$$\sigma_{sat} = \sigma_y + \frac{\alpha G m_T^2}{\omega c_L} \tag{3.13}$$

By introducing the saturation stress, Eq. (3.12) can be rewritten as

$$\sigma = \sigma_y + (\sigma_{sat} - \sigma_y)(1 - \exp(-\omega\varepsilon/2)) \tag{3.14}$$

In Eq. (3.14), the yield strength depends on the temperature and the strain rate. A model for this dependence is presented in [3].

$$\sigma_y(T, \dot{\varepsilon}) = \sigma_y(T_0, \dot{\varepsilon}_0)\frac{G(T)}{G(T_0)}\left(\frac{\dot{\varepsilon}}{\dot{\varepsilon}_0}\right)^{(1/n_N)} \tag{3.15}$$

The yield strength is first given at a reference temperature T_0 and reference strain rate $\dot{\varepsilon}_0$ that are usually taken as 20 °C and 1×10^{-4} 1/s, respectively. The change in the yield strength with temperature is assumed to follow that of the shear modulus G. The strain rate dependence is described with a Norton equation. The stress exponent n_N is determined at the temperature and strain rate in question from the equation for the secondary creep rate, Eq. (2.30). The shear modulus $G(T)$ is assumed to be approximately linear in temperature. Equations (3.12) and (3.14) have exactly the form of the Voce Eq. (3.3) with

$$a_1 = \sigma_{sat} \quad a_2 = \sigma_{sat} - \sigma_y \quad \Omega_1 = \omega/2 \tag{3.16}$$

Equation (3.9) has been used for many years to derive the Voce equation, see for example [4–6]. In these papers, a number of the constants were used as adjustable parameters. This is no longer necessary. All the constants in Eq. (3.16) are given except σ_y that is taken as an experimental value. σ_y varies significantly for different material batches and cannot be accurately predicted at present. But the full strain dependence can be described. The constant α requires a comment. The contribution to α can be split into a short range part α_S and a long range part α_G [7, 8]. The long range part has been explicitly derived [8]

$$\alpha_G = \frac{1}{2\pi}\frac{(1 - \nu_P/2)}{(1 - \nu_P)} \tag{3.17}$$

where ν_P is Poisson's ratio. With $\nu_P = 0.3$, $\alpha_G = 0.19$. At elevated temperatures, $\alpha \approx \alpha_G$ [7]. As a consequence, $\alpha = 0.19$ is used in this book.

At the end of Sect. 2.4, a special procedure was described for finding the value of the work hardening parameter c_L based on the assumption that dynamic and static

recovery give the same result. An expression for the maximum dislocation density ρ_s in this situation was given in Eq. (2.26). This is equation is now expressed in stress instead of the dislocation density with the help of the Taylor Eq. (3.11)

$$\omega\dot{\varepsilon} = \frac{2\tau_L b c_L}{(\alpha G b m_T)^2} M_{cl}(T, \sigma_{sat} - \sigma_i)(\sigma_{sat} - \sigma_i)^2 \tag{3.18}$$

τ_L is dislocation line tension, M_{cl} the climb mobility and σ_i the contribution from particle and solid solution hardening including the yield strength. In general, Eq. (3.18) has to be iterated to find the value of the saturation stress, but the iteration usually converges quickly. With Eq. (3.13), the value of c_L is obtained

$$c_L = \frac{\alpha G m_T^2}{\omega(\sigma_{sat} - \sigma_i)} \tag{3.19}$$

A plastic instability in a tensile test takes place when Considère's criterion is satisfied

$$\frac{d\sigma}{d\varepsilon} = \sigma \tag{3.20}$$

Applying Considère's criterion to Eq. (3.14), the maximum stress σ_{max} in a tensile test can be obtained as well as the strain at this position, which is referred to as the uniform elongation ε_u.

$$\sigma_{max} = \sigma_{sat} \frac{\omega}{\omega + 2} \tag{3.21}$$

$$\varepsilon_u = \frac{2}{\omega} \ln\left(\frac{(\omega + 2)(\sigma_{sat} - \sigma_y)}{2\sigma_{sat}}\right) \tag{3.22}$$

With $\omega \approx 15$ for copper and some stainless steels [1], the maximum stress σ_{max} is about 10% less than the saturation stress σ_{sat}. The uniform elongation ε_u is often measured. ε_u is an important property because it is much easier to predict than the total elongation where the role of specimen necking must be taken into account. This will be considered in Chap. 12 for tertiary creep.

3.3.2 Application to Parent Metal

In Fig. 3.7 tensile data for Cu-OFP at 75 °C are presented. A comparison is made to the model that is obtained by integrating Eq. (3.9) and combining it with the Taylor equation, Eq. (3.11). To investigate the significance of the static recovery term (the last term in Eq. (3.9)), results are shown both with and without this contribution. It is evident that static recovery has a negligible influence in this case.

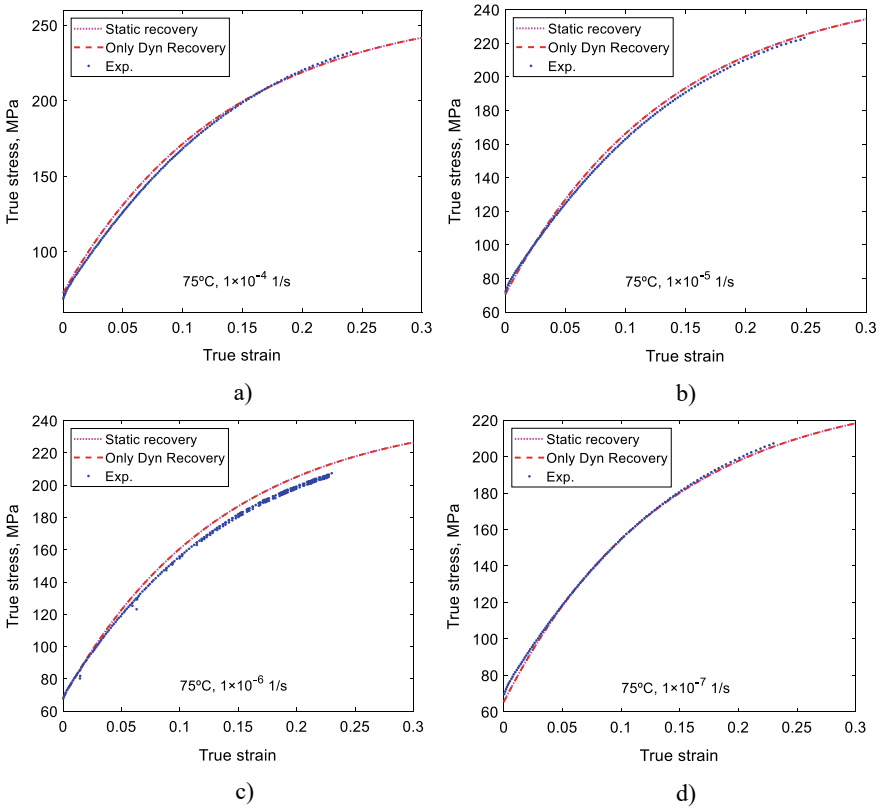

Fig. 3.7 Stress versus strain for Cu-OFP at 75 °C comparing the model in Eqs. (3.9) and (3.11) with experiments. Data from [3]. To analyze the role of static recovery (last term in Eq. (3.9)), results with and without this term are shown; **a** 1×10^{-4} 1/s; **b** 1×10^{-5} 1/s; **c** 1×10^{-6} 1/s; **d** 1×10^{-7} 1/s

In Fig. 3.8 results at 125 °C are given. The model results in this case involve all the terms in Eq. (3.9) including the static recovery term.

In Fig. 3.9 experimental and model results for Cu-OFP at 175 °C are given. Only predicted values for the parameters in Eqs. (3.9) and (3.11) are used. The exception is the yield strength. Its value at 75 °C and 1×10^{-4} 1/s is taken from experiments. The yield strength value at other conditions are derived using the Eq. (3.15).

3.3.3 Application to Welds

Equations (3.9) and (3.11) have also been applied to friction stir welds in phosphorus alloyed oxygen copper Cu-OFP. To describe welds is always challenging since the properties can locally vary significantly. The same parameters as for the parent metal

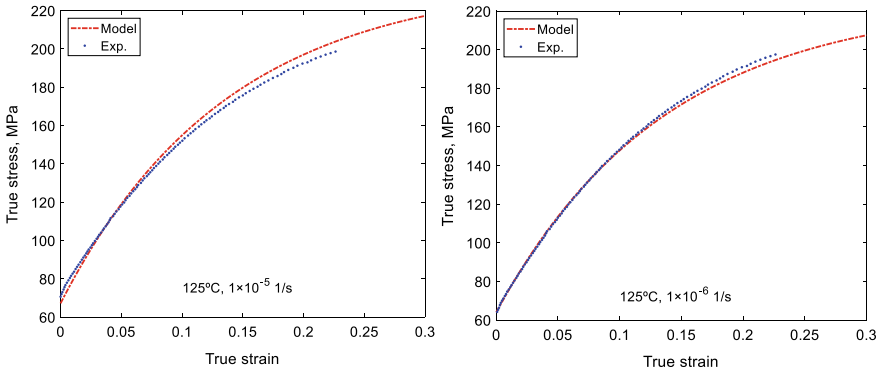

Fig. 3.8 Stress versus strain for Cu-OFP at 125 °C comparing the model in Eqs. (3.9) and (3.11) with experiments. Data from [3]; **a** 1×10^{-5} 1/s; **b** 1×10^{-6} 1/s

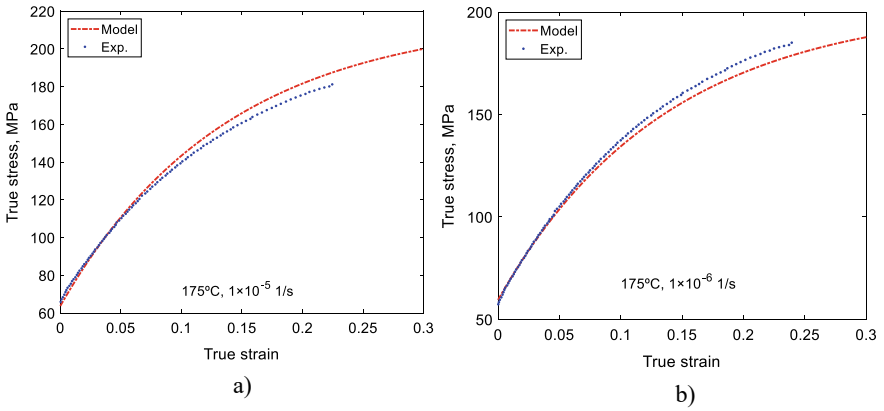

Fig. 3.9 Stress versus strain for Cu-OFP at 175 °C comparing the model in Eqs. (3.9) and (3.11) with experiments. Data from [3]; **a** 1×10^{-5} 1/s; **b** 1×10^{-6} 1/s

have been used except for ω (= 12) and the yield strength where one value has been taken from the experiments at 75 °C and 1×10^{-4}. Why the ω value had to be reduced is not understood. In Fig. 3.10 examples are given for the weld zone.

The heat affected zone (HAZ) has also been studied. Examples are presented in Fig. 3.11. The behavior of the whole weld (the cross weld) usually has to be derived from the properties of the weld zone and the HAZ. However, since the properties of the weld are essentially the same and close to those of the parent metal, it is reasonable to think that the weld can be handled in the same way and that has been assumed. Examples for cross welds are shown in Fig. 3.12.

It can be concluded that the dislocation model in (3.9) and (3.11) can represent stress strain curves for both parent metals and welds of Cu-OFP in quite a reasonable

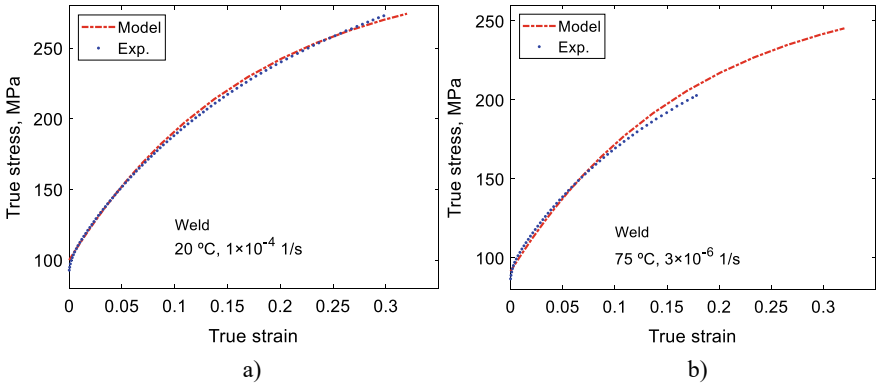

Fig. 3.10 Stress versus strain for the weld zone in friction stir welds in Cu-OFP comparing the model in Eqs. (3.9) and (3.11) with experiments. Data from [9]; **a** 20 °C, 1×10^{-4} 1/s; **b** 75 °C, 3×10^{-6} 1/s

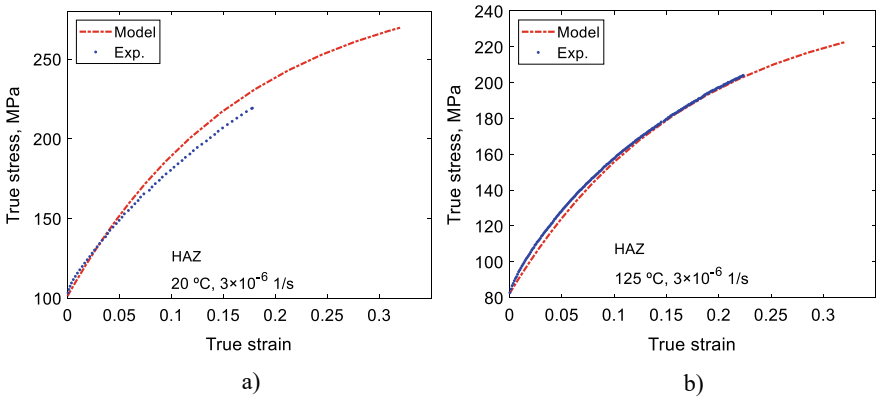

Fig. 3.11 Stress versus strain for the heat affected zone (HAZ) in friction stir welds in Cu-OFP at 75 °C comparing the model in eqs. (3.9) and (3.11) with experiments. Data from [9]; **a** 20 °C, 3×10^{-6} 1/s; **b** 125 °C, 3×10^{-6} 1/s

way essentially without the use of adjustable parameters. The analysis above is likely to be valid for other fcc alloys as well. However, some parameters and in particular ω will take other values. This will analyzed in the next section.

3.4 The ω Parameter in Dynamic Recovery

As was emphasized in Sect. 2.3, two types of recovery (dynamic and static) are

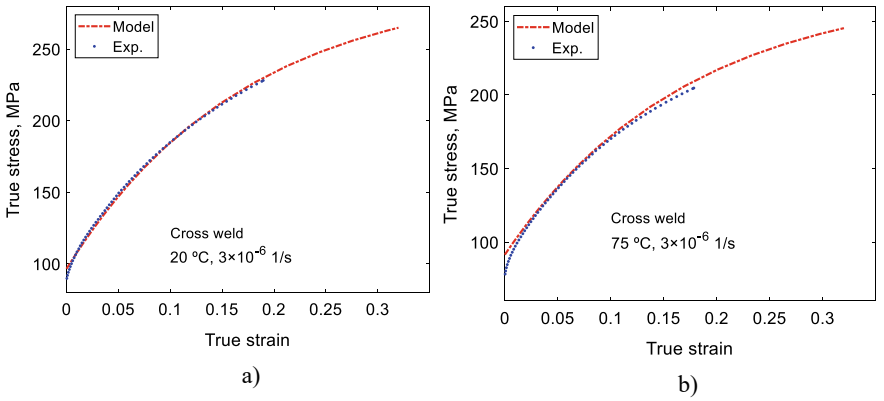

Fig. 3.12 Stress versus strain for cross welds in friction stir welds in Cu-OFP comparing the model in Eqs. (3.9) and (3.11) with experiments. Data from [9]; **a** 20 °C, 3×10^{-6} 1/s; **b** 75 °C, 3×10^{-6} 1/s

important to take into account when discussing creep. It is also important to distinguish between the two types of recovery. The primary role of dynamic recovery is to provide the reduction of the work hardening rate with increasing strain in stress strain curves. Static recovery reduces the dislocation content during creep, which makes it possible for creep deformation to continue at constant load or stress. Static recovery must be considered to be well understood. At high temperatures static recovery is assumed to control the creep rate and the temperature and stress dependence of the creep rate has been studied for many alloys. In this way detailed knowledge about static recovery has been gathered indirectly. The models for static recovery are based on expressions for a basic model of the climb mobility, which was established many years ago.

Unfortunately, the modeling of dynamic recovery is not at all at the same level. This is surprising since it has been seen earlier in this chapter that dynamic recovery is an essential part of the description of plastic flow curves at ambient and intermediate temperatures. As can be seen for example in Fig. 3.7, the slope of the curve which is referred to as the work hardening rate is continuously decreasing with increasing strain that is the effect of dynamic recovery. This slope can directly be obtained from Eq. (3.12) if the Voce equation is satisfied

$$\frac{d\sigma}{d\varepsilon} = \frac{\alpha G m_{\mathrm{T}}^2}{2c_L} \exp(-\omega\varepsilon/2) \tag{3.23}$$

The initial work hardening rate which is the constant in front of the exponential is found to take a value of about $G/20$ for polycrystalline fcc alloys [4]. The work hardening rate in Eq. (3.23) can also be expressed in terms of the stress. By using Eqs. (3.12) and (3.13), Eq. (3.23) can be transformed to

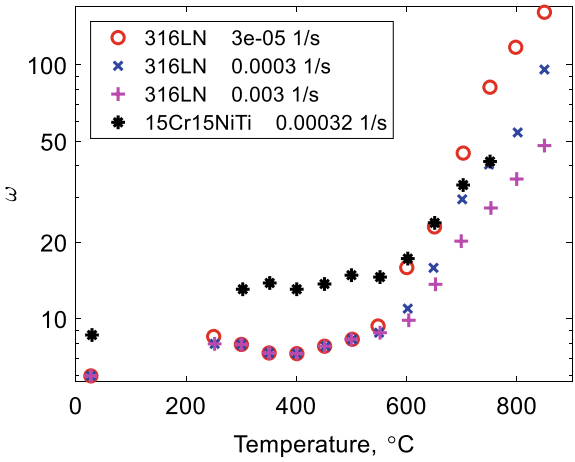

Fig. 3.13 The dynamic recovery parameter ω as a function of temperature for two austenitic stainless steels. Data from [1, 11]

$$\frac{d\sigma}{d\varepsilon} = \frac{\omega}{2}(\sigma_{sat} - \sigma) \tag{3.24}$$

This linear behavior of the work hardening rate as a function of stress has been demonstrated in many papers, see for example [10].

According to Eq. (3.9), the amount of dynamic recovery is directly proportional to the parameter ω. Consequently, the value of ω is of main importance for understanding dynamic recovery. For example, it is evident from Eqs. (3.23) and (3.24) that ω has major influence on the work hardening rate. Unfortunately, only limited data for ω is available in the literature. Data for austenitic stainless steels are shown in Fig. 3.13.

Different designations for ω can be found in the literature. For stress strain curves Ω and n_V are often used. They are related to ω in the following way

$$\Omega = -n_V = \omega/2 \tag{3.25}$$

It is not uncommon that values for ω and Ω are mixed up so it is wise to check the data.

It is evident from Fig. 3.13 that one should distinguish between two ranges for the temperature dependence of ω. At high temperatures in the creep range, the ω values are strongly dependent on both temperature and strain rate. For austenitic stainless steels, the creep range starts at about 550 °C. At lower temperatures, ω is weakly temperature dependent and the strain rate has quite a small effect. This is called the work hardening range, because the flow curves are primarily controlled by the work hardening rate. This behavior has also been found for aluminum [12].

When mechanisms are considered the work hardening and creep range are defined in the following way

$$\sigma_{sat} < \sigma_{creep} \quad \text{Work hardening range} \tag{3.26}$$

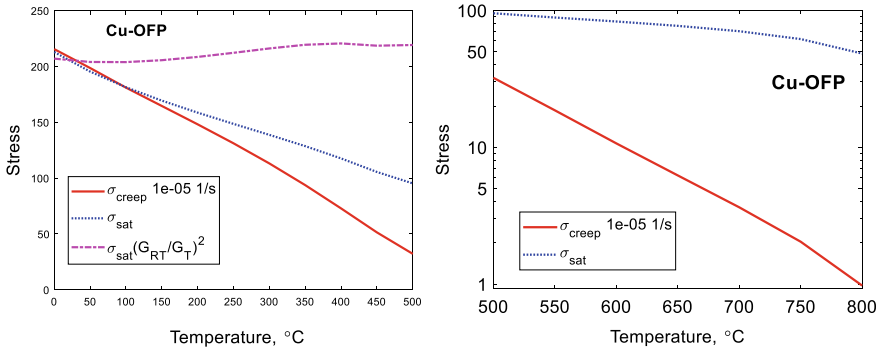

Fig. 3.14 Saturation and creep stress as a function of temperature for Cu-OFP at a strain rate of 1 $\times$ 10^{-5} 1/s. A third curve gives the saturation stress multiplied by $(G_{RT}/G_T)^2$ where G_{RT} and G_T are the shear modulus at room temperature and temperature, respectively

$$\sigma_{sat} > \sigma_{creep} \quad \text{Creep range} \tag{3.27}$$

σ_{sat} is the maximum flow stress in a stress strain curve. For a material satisfying the Voce equation, σ_{sat} is given by Eq. (3.13). σ_{creep} is the stress in a creep test that gives the same strain rate as for the stress strain flow curve. This division is illustrated in Fig. 3.14.

Below about 100 °C, $\sigma_{sat} < \sigma_{creep}$ and we are in the work hardening range in Fig. 3.14. The situation is reversed above this temperature. Below 400 °C (T_m/2 for Cu, T_m the absolute melting point) both σ_{sat} and σ_{creep} decrease linearly with increasing temperature but with different slope. Above 400 °C, σ_{creep} decreases exponentially with increasing temperature, a behavior that is frequently observed for creep resistant steels. It is natural to distinguish between three temperature ranges: the high temperature range ($T > T_m/2$), the intermediate range ($0.3T_m < T < T_m/2$, 130–400 °C for Cu) and the low temperature range ($T < 0.3T_m$). The high temperature range is the classical region for studying creep. Dynamic recovery is the dominating recovery process only in the low temperature range.

There is not a sharp transition between the low and intermediate temperature ranges. In fact, we can have $\sigma_{sat} > \sigma_{creep}$ in spite σ_{creep} being above the experimental data range in a flow curve in the lower part of the intermediate range. In Fig. 3.15a, ω values are shown for Cu-OFP at the transition from the work hardening to the creep range. There is temperature dependence but only a weak influence of the strain rate.

According to Eq. (3.13), there is a close relation between ω and the saturation stress σ_{sat}.

$$\omega = \frac{\alpha G m_T^2}{c_L(\sigma_{sat} - \sigma_y)} \tag{3.28}$$

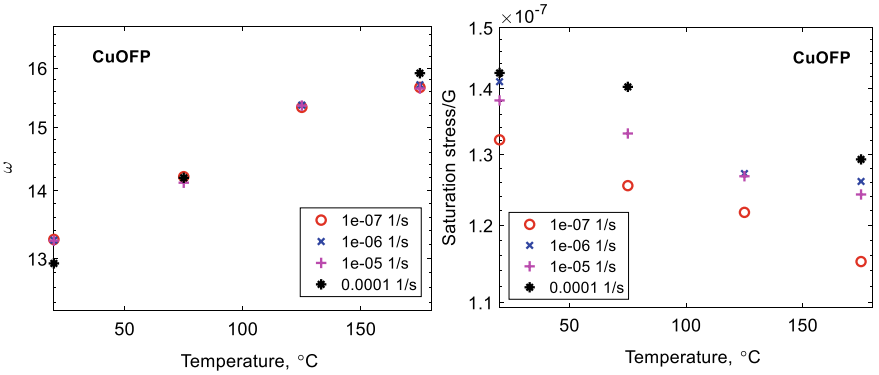

Fig. 3.15 Voce parameters for tensile stress strain curves of Cu-OFP as a function of temperatures for four strain rates; **a** dynamic recovery parameter ω; **b** saturation stress σ_{sat} divided by the shear modulus *G*. Data from [3]

Many times the yield strength σ_y is only a small fraction of σ_{sat} and then ω is roughly inversely proportional to σ_{sat}. As can be seen for Cu-OFP in Fig. 3.15b the temperature dependence of σ_{sat} is inverted in comparison to that of ω. However, the strain rate effect is much larger for σ_{sat} in comparison to that of ω. The reason is that the yield strength depends on the strain rate and that has a direct influence on σ_{sat}.

In the literature σ_{sat} has been studied more frequently than ω. In principle, this should not make much difference since σ_{sat} and ω are related according to Eq. (3.28). However, in a number of cases it has not been checked whether the data points are in the work hardening or in the creep range. If attempts to determine σ_{sat} are made in the creep range, it is in fact σ_{creep} that has been measured, the value of σ_{sat} would be strongly underestimated and the role of dynamic recovery cannot be assessed. Data from [13] have been used in several influential papers to discuss the temperature dependence of dynamic recovery [10, 14]. However, most of the data in [13] are in the creep range and a significant fraction even in the high temperature range. This has probably contributed to the misconception that dynamic recovery is strongly temperature and strain rate dependent.

Even with the modest temperature dependence of ω that has been observed, Figs. 3.13 and 3.14, it is natural to assume that dynamic recovery is a thermally activated process, and an Arrhenius expression is formulated

$$\omega = \omega_{RT} \exp\left(-\frac{Q_\omega}{R_G T}\left(\frac{1}{T} - \frac{1}{T_{RT}}\right)\right) \tag{3.29}$$

ω_{RT} is the ω value at room temperature that is determined with the help of Eq. (3.28). Q_ω is an activation energy and T_{RT} room temperature. Expression (3.29) is compared to the available experiments for fcc alloys for ω in Fig. 3.16.

By fitting Eq. (3.29) to the experimental data, a value of $Q_\omega = 1$ kJ/mol was found that is two orders of magnitude smaller than typical activation energies for

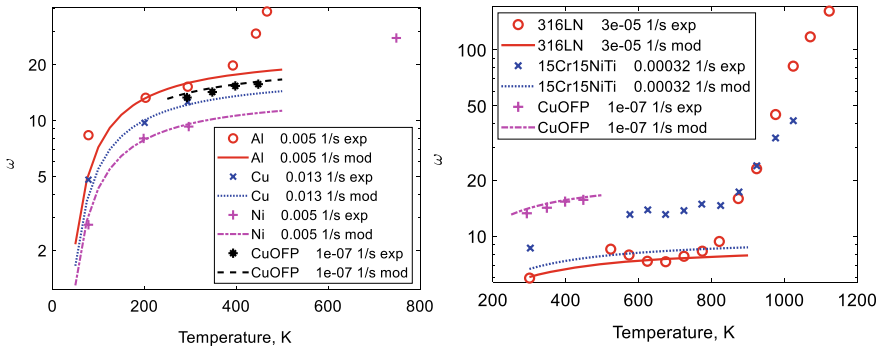

Fig. 3.16 The dynamic recovery parameter ω as a function of temperature for fcc materials. Data from [1, 11, 15]

self-diffusion. Values for the pure elements Al, Cu and Ni are included in Fig. 3.16a from [15]. The values from [15] had to be corrected due to numerical errors in the paper, which makes the values uncertain. The same value of Q_ω could be used for the six materials in Fig. 3.16. The expression in Eq. (3.29) is of course only valid below the creep range.

Since the 1950ties there has been an almost unanimous opinion in the literature that cross-slip is the controlling mechanism for dynamic recovery, see for example [10, 16, 17]. Notable exceptions are [18, 19]. Cross-slip has been observed many times during work hardening. However, cross-slip is associated with high activation energies. Modern ab initio calculations give values from 50 to 300 kJ/mol, see Sect. 2.6.3. High energies are required to form the constrictions that are necessary to make the extended screw dislocations in fcc alloys cross-slip. Such high activation energies are clearly at variance with the low value of Q_ω found above.

Attempts to quantitatively model cross-slip are rare and apparently not very successful [18]. The role of cross-slip for dynamic recovery should not be completely ruled out. It is well-known that cross-slip takes place in deformation stage I in fcc single crystals. In this stage the stresses are very low and if high activation energies would be required, cross-slip would simply not take place [18, 19]. Another possible mechanism for dynamic recovery is the formation of dislocation tangles on secondary glide planes which is known to take place in early stages of work hardening [10]. Argon has suggested an entirely different mechanism for dynamic recovery [19]. As discussed in Sect. 2.4, gliding dislocations are expected to pass through about two cell boundaries when they are released. When moving through cell boundaries, they would remove dislocation locks and other dislocations configurations from the cell boundaries thus reducing the dislocation content.

If cross-slip of extended dislocations is active it is natural that the stacking fault energy plays a major role. Argon and Moffatt have derived an expression for how much the climb rate for extended dislocations is slowed down in comparison to perfect dislocations [20]

$$g_{\text{SFE}} = 2\left(\frac{8\pi(1-\nu_{\text{P}})}{2+\nu_{\text{P}}}\right)^2\left(\frac{\gamma_{\text{SFE}}}{Gb}\right)^2 \tag{3.30}$$

γ_{SFE} is the stacking fault energy. The main factor in this expression is the dimensionless quantity $\left(\frac{\gamma_{\text{SFE}}}{Gb}\right)^2$. The factor 8 was originally 24, but has been changed due to an error in [20]. The influence on gliding dislocations is the same as for climbing ones since it is the jogs on the dislocations that control their speed, see Sect. 2.6.2. The three elements in Fig. 3.16 have quite different values of γ_{SFE}. No effect of γ_{SFE} is thus observed in the Figure. However, the shear modulus seems to have an impact. In Fig. 3.14, the predicted ω value is also divided by the shear modulus squared following Eq. (3.30). As can be seen ω is approximately proportional to one over the shear modulus squared at least below the creep range. This means that the temperature dependence of ω is of the same type as that of G. The influence of temperature on the shear modulus can be modeled with ab initio methods taking the role of phonons into account. The value of ω during cyclic loading is discussed in Chap. 11.

3.5 Summary

- Stress strain curves are mostly described by well-known empirical models such as Hollomon, Ludwik, Voce and Swift. With the available parameters in these models, there is in general little problem to obtain a good fit to the data. As with most empirical models, it is difficult or impossible to generalize the results. Only the Voce model has been possible to derive from basic principles.
- With the basic models for dislocation creep, accurate descriptions of the stress strain curves can be obtained. This is natural since the basic models should be applicable whether the deformation is load, stress or strain rate controlled.
- The dynamic recovery parameter ω plays a special role because it describes how the increase in the dislocation stress deviates from a linear behavior and tends to a saturation value. The temperature dependence of ω has been analysed. Although the amount of data is limited, it suggests that ω has the same temperature dependence as the inverse of the shear modulus squared.
- It has been proposed in many places in the literature that dynamic recovery is controlled by cross-slip. However, this requires that partial dislocations can be brought together and form a constriction. This would require an activation energy of about 50 kJ/mol or more that would give the dynamic recovery parameter a strong temperature dependence. However, this is in direct conflict with observations, see previous bullet. The role of cross-slip remains unexplained.

References

1. B.K. Choudhary, E.I. Samuel, K. Bhanu Sankara Rao, S.L. Mannan, Tensile stress–strain and work hardening behaviour of 316LN austenitic stainless steel. Mater. Sci. Technol. **17**, 223–231 (2001)
2. D.C. Ludwigson, Modified stress-strain relation for FCC metals and alloys. Metall. Trans. **2**, 2825–2828 (1971)
3. R. Sandström, J. Hallgren, The role of creep in stress strain curves for copper. J. Nucl. Mater. **422**, 51–57 (2012)
4. U.F. Kocks, Laws for work-hardening and low-temperature creep. J. Eng. Mater. Technol. Trans. ASME, 98 Ser H, 76–85 (1976)
5. Y. Bergström, A dislocation model for the stress-strain behaviour of polycrystalline α-Fe with special emphasis on the variation of the densities of mobile and immobile dislocations. Mater. Sci. Eng. **5**, 193–200 (1970)
6. Y. Bergström, W. Roberts, A dislocation model for dynamical strain ageing of α-iron in the jerky-flow region. Acta Metall. **19**, 1243–1251 (1971)
7. F.F. Lavrentev, The type of dislocation interaction as the factor determining work hardening. Mater. Sci. Eng. **46**, 191–208 (1980)
8. A. Orlová, On the relation between dislocation structure and internal stress measured in pure metals and single phase alloys in high temperature creep. Acta Metall. Mater. **39**, 2805–2813 (1991)
9. R. Sandstrom, S. Waqas Ahmad, K.T. Pasupuleti, M. Mahdavi Shahri, Slow strain rate tensile testing of friction stir welded Cu-OFP. Constitutive equations for creep, Swedish Nuclear Waste Management Company Report R-13-33 (2017)
10. U.F. Kocks, H. Mecking, Physics and phenomenology of strain hardening: the FCC case. Prog. Mater Sci. **48**, 171–273 (2003)
11. P.V. Sivaprasad, S. Venugopal, S. Venkadesan, Tensile flow and work-hardening behavior of a Ti-modified austenitic stainless steel. Metall. Mater. Trans. A **28**, 171–178 (1997)
12. W.J. Poole, J.D. Embury, D.J. Lloyd, Work hardening in aluminium alloys, in *Fundamentals of Aluminium Metallurgy: production, Processing and Applications* (2010), pp. 307–344.
13. H. Mecking, B. Nicklas, N. Zarubova, U.F. Kocks, A "universal" temperature scale for plastic flow. Acta Metall. **34**, 527–535 (1986)
14. E. Nes, K. Marthinsen, Modeling the evolution in microstructure and properties during plastic deformation of f.c.c.-metals and alloys—An approach towards a unified model. Mater. Sci. Eng.: A **322**, 176–193 (2002)
15. H. Hallén, A theory of dynamic recovery in F.C.C. metals. Mater. Sci. Eng. **72**, 119–123 (1985)
16. P.J. Jackson, Dislocation modelling of shear in f.c.c. crystals, Progress in Mater. Sci. **29**, 139–175 (1985)
17. E. Nes, Modelling of work hardening and stress saturation in FCC metals. Prog. Mater. Sci. **41**, 129–193 (1997)
18. M. Zaiser, P. Hähner, Stage-III hardening revisited, philosophical magazine a: physics of condensed matter. Struct. Defects Mech. Prop. **77**, 1515–1529 (1998)
19. A. Argon, *Strengthening Mechanisms in Crystal Plasticity* (Oxford University Press, Oxford, 2008)
20. A.S. Argon, W.C. Moffatt, Climb of extended edge dislocations. Acta Metall. **29**, 293–299 (1981)

Chapter 4
Primary Creep

Abstract For many materials, primary creep can be described with the phi (ϕ) model and tertiary creep with the Omega (Ω) model (discussed in Chap. 12). According to the phi model, the creep rate is linear in strain and time in a double logarithmic diagram. When using empirical descriptions of the creep curves, these models are recommended. Several basic models for primary creep are derived. They are based on the creep rate in the secondary stage. This means that primary creep can be derived without any new data. The primary creep models are in agreement with the phi model and can describe experimental data. For the martensitic 9–12% Cr steels at least two dislocation densities are needed to represent primary creep because the initial dislocation density is high contrary to the situation for annealed fcc materials.

4.1 General

The classical form of a creep strain versus time curve ("creep curve") is that there is first a primary stage where the creep rate increases but with a continuously decreasing rate, a secondary stage where the creep rate is approximately constant and a tertiary stage with a continuously increasing strain rate. Surprisingly many materials show this behavior but there are many exceptions. In this chapter the primary stage will be analyzed.

The primary stage is technically very important. If there is a limit on the amount of strain that a product can accept, primary creep must be considered. Well-known examples are blades of gas and steam turbines. If the strain is too large the blades will get in contact with other parts of the structure resulting in disaster. Another case is where the strains can never become very large. One example is copper canisters for nuclear waste. Inside the copper tube there is a cast iron insert. Between the copper tube and the iron insert there is only a small gap. Due to the external pressure the copper tube creeps towards the insert and when it is reached, creep stops in this part of the structure. For some materials the total strain is larger in the primary stage than in the secondary stage. If only secondary creep is considered in design which is not uncommon, there is a risk that the creep deformation is significantly underestimated.

R. Sandström, *Basic Modeling and Theory of Creep of Metallic Materials*, Springer Series in Materials Science 339,
https://doi.org/10.1007/978-3-031-49507-6_4

Primary creep is also of importance during creep at very low stresses since stationary conditions are rarely reached. This is discussed in Chap. 5.

Secondary creep has been studied much more extensively than primary creep in the literature. The reason is that for a long time it was believed that the stress exponent in the secondary stage could be used to identify the controlling creep mechanisms. As was discussed in Chap. 2 and will be further discussed in Chap. 5, this connection is not always true and examples where people are likely to have drawn the wrong conclusions are easy to find.

Primary creep has almost exclusively been analyzed with empirical models. Only in recent years, basic models have been presented in the literature. Already in the 1930'ties, Bailey presented a model for the time dependence of the strain in primary creep. This model is still the first hand choice when describing the primary stage. The model has later been generalized [1]. We will refer to it as the phi or ϕ model. It gives an exponential decrease in creep rate with increasing time or strain. As will be illustrated in the next section several types of materials follow this behavior.

There are a large number of empirical models for representing creep curves. Only a few of them give a reasonable description of primary and tertiary creep separately and we will focus on them. For tertiary creep, the correspondence to the phi (ϕ) model is the Omega (Ω) model. These two models can accurately represent primary and tertiary creep for the well investigated 9CrMo steels.

Basic models for primary creep have been developed in recent years. Three of these models will be presented in Sects. 4.3–4.5. The first two models are applicable to fcc alloys whereas the third one is suitable for CrMo-steels. In some of the models it is necessary to distinguish between more than one type of dislocation density. In general these models give the same time dependence of the strain as the phi (ϕ) model. Expressed in other words, the phi (ϕ) model can be derived from basic physical principles, which has not been shown for any other of the empirical model for primary creep. So this is an additional reason why we concentrate on the phi (ϕ) model, when discussing empirical models for primary creep.

4.2 Empirical Models for Creep Strain Curves

In this section models for both primary and tertiary creep will be considered. The reason is that many models are designed to handle the entire creep curve rather than primary and tertiary creep separately. A large number of empirical models have been proposed. Reviews can be found in [2, 3]. Some of the more frequently used methods are summarized in Table 4.1. The model that probably has got most attention in the literature was developed by the Wilshire group. They referred to it as θ projection. In Table 4.1 it is called the θ model. The assumptions in the model are that both the primary and the tertiary creep rates are linear in the creep strain. This gives a creep rate that decreases exponentially with time in the primary stage and increases exponentially in the tertiary stage. To describe the whole creep curve the primary and tertiary parts are simply added. Thus, it is not necessary to have a separate contribution

from secondary creep. However, if primary and tertiary data are analyzed separately, the θ model does typically not give a good representation of data.

Instead the ϕ model should be used for primary creep data and the Omega (Ω) model for tertiary data. This will be illustrated below. The phi (ϕ) model for primary creep gives the following strain rate dependence as a function of strain

$$\dot{\varepsilon}_{\text{prim}} = \phi_1 \varepsilon^{-\phi_2} \qquad \text{phi model} \tag{4.1}$$

The creep rate decreases exponentially with increasing strain. Its time dependence has the same mathematical form. The Ω model for tertiary creep takes the form

$$\dot{\varepsilon}_{\text{tert}} = \Omega_3 e^{\Omega_4 \varepsilon} \qquad \text{Omega model} \tag{4.2}$$

In Eq. (4.2) the creep rate increases exponentially with strain. This gives a time dependence with a singularity, see Table 4.1. The time at this singularity is close to the rupture time.

The three models in Table 4.1 have one term for primary creep and one for tertiary creep. In each term there are two adjustable parameters. So for describing a creep curve four adjustable parameters are needed.

Equations (4.1) and (4.2) are illustrated for the 9Cr1Mo steel P91 in Figs. 4.1, 4.2, 4.3 and 4.4. The steel P91 is common in modern fossil fired power plants.

Table 4.1 Empirical models for describing single creep curves (reproduced from [4] with permission of Elsevier)

Model	Parameters	Strain rate versus strain	Strain rate versus time	Strain versus time	Refs.
θ model, primary	θ_1, θ_2	$\dot{\varepsilon}_{\text{prim}} = \theta_2(\theta_1 - \varepsilon)$	$\dot{\varepsilon}_{\text{prim}} = \theta_1\theta_2 e^{-\theta_2 t}$	$\theta_1(1 - e^{-\theta_2 t})$	[5, 6]
θ model, tertiary	θ_3, θ_4	$\dot{\varepsilon}_{\text{tert}} = \theta_4(\varepsilon + \theta_3)$	$\dot{\varepsilon}_{\text{tert}} = \theta_3\theta_4 e^{\theta_4 t}$	$\theta_3(e^{\theta_4 t} - 1)$	[5, 7]
ϕ model, primary	ϕ_1, ϕ_2	$\dot{\varepsilon}_{\text{prim}} = \phi_1 \varepsilon^{-\phi_2}$	$\dot{\varepsilon}_{\text{prim}} = \phi_1(\phi_1(1+\phi_2)t)^{-\phi_2/(1+\phi_2)}$	$(\phi_1(1+\phi_2)t)^{1/(1+\phi_2)}$	[1, 8]
ϕ model, tertiary	ϕ_3, ϕ_4	$\dot{\varepsilon}_{\text{tert}} = \phi_3 \varepsilon^{\phi_4}$	$\dot{\varepsilon}_{\text{tert}} = \phi_3(\phi_3(1-\phi_4)t)^{\phi_4/(1-\phi_4)}$	$(\phi_3(1-\phi_4)t)^{1/(1-\phi_4)}$	[8]
Ω model, primary	Ω_1, Ω_2	$\dot{\varepsilon}_{\text{prim}} = \Omega_1 e^{-\Omega_2 \varepsilon}$	$\dot{\varepsilon}_{\text{prim}} = \frac{\Omega_1}{\Omega_1\Omega_2 t+1}$	$\frac{\ln(\Omega_1\Omega_2 t+1)}{\Omega_2}$	[9]
Ω model, tertiary	Ω_3, Ω_4	$\dot{\varepsilon}_{\text{tert}} = \Omega_3 e^{\Omega_4 \varepsilon}$	$\dot{\varepsilon}_{\text{tert}} = \frac{\Omega_3}{1-\Omega_3\Omega_4 t}$	$-\frac{\ln(1-\Omega_3\Omega_4 t)}{\Omega_4}$	[10–12]

ε is the creep strain, $\dot{\varepsilon}$ the strain rate, t the time

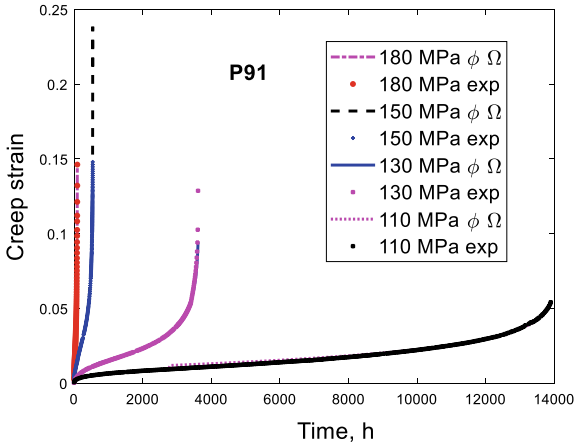

Fig. 4.1 Creep strain versus time curves for the 9Cr1Mo steel P91 at 600 °C at the four stresses 110, 130, 150 and 180 MPa fitted with the ϕ and Ω models, Eqs. (4.1) and (4.2). Data from [1]. Reprinted from [13] with permission of MDPI

By using double logarithmic scale for a creep rate versus strain curve, a straight line should result in the primary stage if Eq. (4.1) is valid. That this is the case is shown in Fig. 4.2.

The same behavior can be illustrated if the creep rate is plotted versus time. From Table 4.1 it can be seen that also the time dependence of the creep rate in the primary stage is exponential. It should give a straight line in Fig. 4.3. This is approximately the case. However, this way of presenting the data is more sensitive to the scatter in the data.

In the tertiary stage a semi logarithmic scale with the creep rate versus strain diagram is appropriate to make a comparison to the Omega (Ω) model in Eq. (4.2).

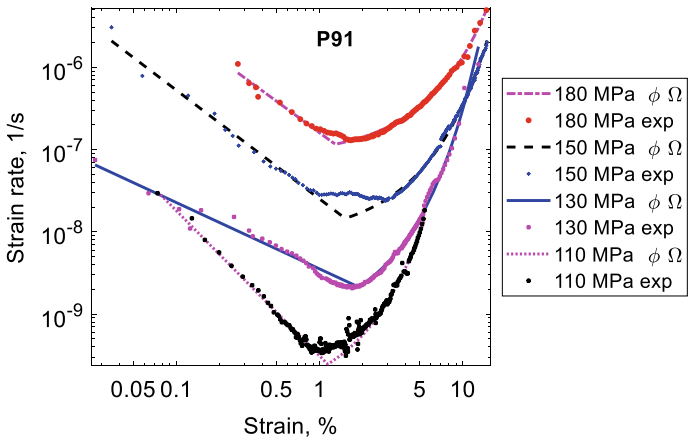

Fig. 4.2 Creep rate versus strain curves for the 9Cr1Mo steel P91 at 600 °C for the same tests as in Fig. 4.1. Double logarithmic scale. Reprinted from [13] with permission of MDPI

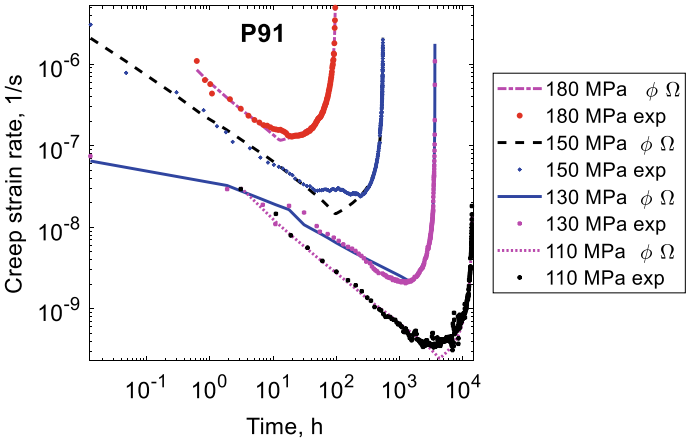

Fig. 4.3 Creep rate versus time curves for the 9Cr1Mo steel P91 at 600 °C for the same tests as in Fig. 4.1. Double logarithmic scale

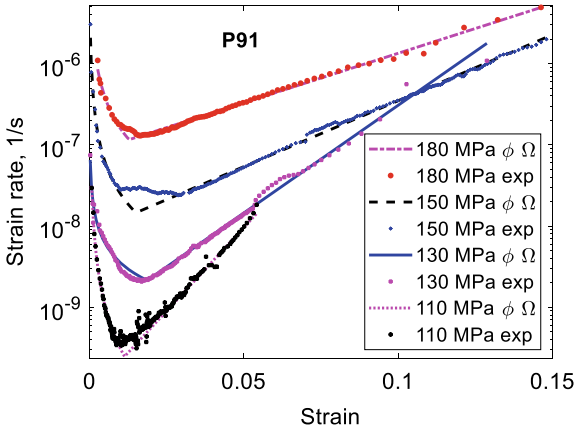

Fig. 4.4 Creep rate versus strain curves for the 9Cr1Mo steel P91 at 600 °C for the same tests as in Fig. 4.1. Semi logarithmic scale. Data from [14]. Reprinted from [13] with permission of MDPI

This is illustrated in Fig. 4.4. Indeed, straight lines give a good representation of the data. Some deviations around the minimum creep rate can be observed.

In Figs. 4.2, 4.3 and 4.4 the contributions from both Eqs. (4.1) and (4.2) are included. The maximum value of them is shown. It can be seen that the whole curves are quite well represented in this way.

Also the strain versus time curve in Fig. 4.1 can be handled in this way. For the primary stage Eq. (4.1) is used and for the tertiary stage Eq. (4.2). If an even better fit is required for the strain versus time curve all the parameters ϕ_1, ϕ_2, Ω_3 and Ω_4 can be fitted simultaneously to the data. In fact, if four parameters are fitted many combinations of models for primary and tertiary can be used, for example different combinations in Table 4.1 such as the θ model or the Ω model for both primary and tertiary creep. However, such an approach is not recommended because

the expressions for the primary and tertiary stages will not be able to describe the primary and the tertiary stages separately.

It is well established that high chromium steels like P91 follows the ϕ model in the primary stage and the Ω model in the tertiary stage at least approximately. This is well documented in the literature. For example, Abe has written several papers about it [15–18]. The phi (ϕ) and Omega (Ω) models are also applicable to other types of materials. This will be illustrated in Figs. 4.5, 4.6, 4.7 and 4.8 for the high alloyed creep resistant austenitic stainless steel Sanicro 25 (22Cr25Ni4W1.5Co3CuNbN) developed by Sandvik.

Creep strain versus time curves are shown in Fig. 4.5. It can be noticed that the appearance of the creep curves is quite different from those of P91. The amount of primary creep is quite small and tertiary creep starts early on and dominates the creep curve.

In Fig. 4.6, strain rate versus time curves with a double logarithmic scale are given. The presence of the straight lines in the primary stage illustrates that the phi (ϕ) model is satisfied for three of the stresses.

Also in creep rate versus time curves the validity of the ϕ model can be demonstrated, see Fig. 4.7. Due to scatter in the experimental data the agreement is not complete.

For the primary stage only a limited number of data points on the creep curves are available in [19]. For the tertiary stage the data situation is much better. It is evident in Fig. 4.8 that the tertiary is well represented by the Omega (Ω) model.

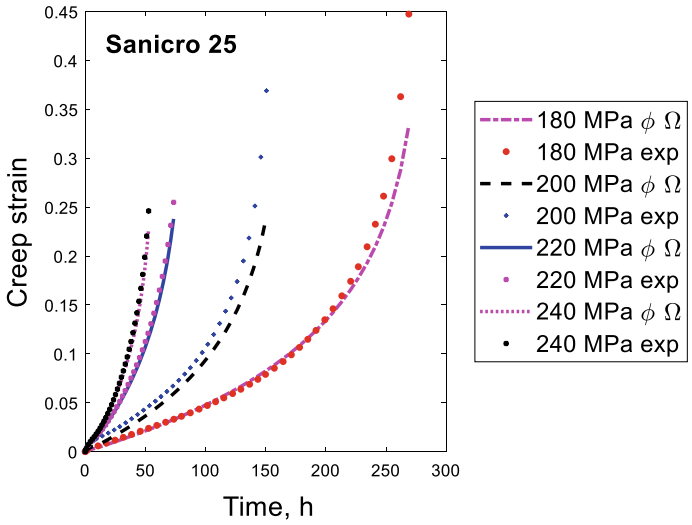

Fig. 4.5 Creep strain versus time curves for the 22Cr25Ni4W1.5Co3CuNbN austenitic stainless steel Sanicro 25 at 750 °C at the four stresses 180, 200, 220 and 240 MPa fitted with the ϕ and Ω models, Eqs. (4.1) and (4.2). Data from [19]. Reprinted from [13] with permission of MDPI

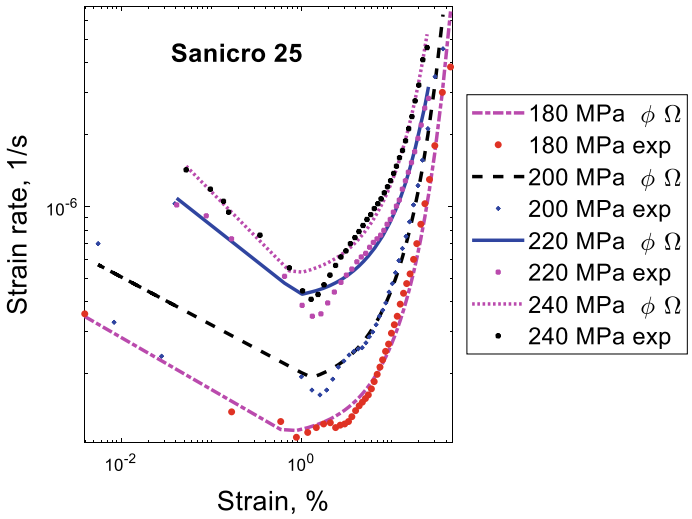

Fig. 4.6 Creep rate versus strain curves for the 22Cr25Ni4W1.5Co3CuNbN austenitic stainless steel Sanicro 25 at 750 °C for the same tests as in Fig. 4.5. Double logarithmic scale

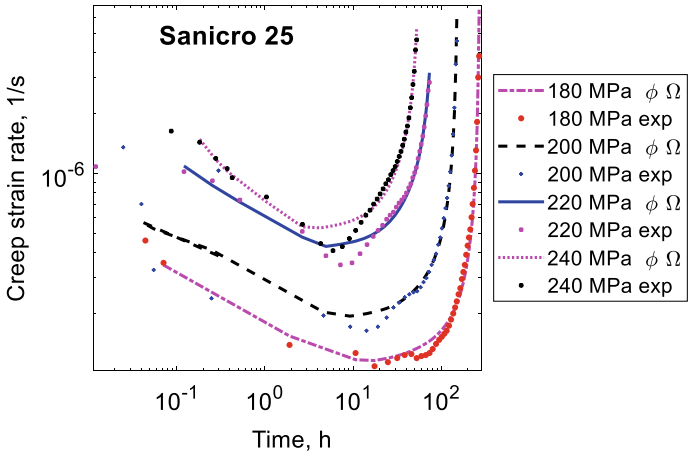

Fig. 4.7 Creep rate versus time curves for the 22Cr25Ni4W1.5Co3CuNbN austenitic stainless steel Sanicro 25 at 750 °C for the same tests as in Fig. 4.5. Double logarithmic scale. Reprinted from [13] with permission of MDPI

The creep rates in Figs. 4.6, 4.7 and 4.8 show deviations to phi (ϕ) and Omega (Ω) model around the minimum creep rate. This is a common effect for many creep curves. The experimental values in the range are lower than the model values. These deviations are not large enough to show up in the creep strain curves in Fig. 4.5.

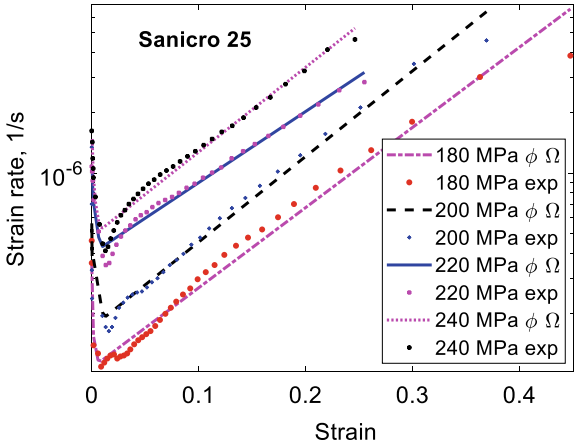

Fig. 4.8 Creep rate versus strain curves for the 22Cr25Ni4W1.5Co3CuNbN austenitic stainless steel Sanicro 25 at 750 °C for the same tests as in Fig. 4.5. Semi logarithmic scale. Redrawn from [14] with permission of Taylor & Francis

The reason of modeling creep strain is in general to try to extrapolate the results to other conditions. This is typically very difficult with empirical methods. The background is that the fitting parameters practically always vary in a complex way that is challenging to analyze. Instead, the basic models that are described in the next three sections are readily useful to generalize the results to new conditions.

4.3 Dislocation Controlled Primary Creep

In Chap. 2, an expression for the creep rate in the secondary stage was derived, Eqs. (2.30) and (2.29)

$$\dot{\varepsilon} = h(\sigma - \sigma_i) \quad \text{with} \quad h(\sigma) = \frac{2\tau_L b c_L}{m_T} M(T,\sigma) \frac{\sigma^3}{(\alpha m_T G b)^3} \tag{4.3}$$

$$\sigma_{disl} = \alpha m_T G b \rho^{1/2} = \sigma - \sigma_i \tag{4.4}$$

where $\dot{\varepsilon}$ is the strain rate, σ the applied stress, m_T the Taylor factor, b burgers vector, G the shear modulus, c_L and α dimensionless factors, ω the dynamic recovery constant, τ_L the dislocation line tension and M the dislocation mobility. σ_{disl} is the dislocation stress, ρ the dislocation density, σ_i is an internal stress that will be discussed below. Contributions from solid solution hardening and particle hardening can be included in σ_i. The validity of these equations was demonstrated in Chap. 2.

To derive the time dependence of the creep strain, the corresponding time dependence of the dislocation density must be known. Eq. (2.17) describes this variation

$$\frac{d\rho}{d\varepsilon} = \frac{m_T}{bc_L}\rho^{1/2} - \omega\rho - 2\tau_L M\rho^2/\dot{\varepsilon} \tag{4.5}$$

where ε is the strain. The other quantities were explained above.

The common behavior in the primary creep stage is that there is a continuously decreasing creep rate with increasing time until the secondary stage is reached. At the same time it is assumed that there is a gradually increasing density of dislocations. This is a natural assumption since the dislocation density is low at the start of the creep test for soft hot worked materials. The density reaches a stationary value in the secondary stage. There are many possible alternative scenarios for example with a hard cold worked material or continuous precipitation in the primary stage. However, we will only consider the main one.

To describe primary creep several assumptions are made [20]:

- The stress dependence of the creep rate is the same in the primary and in the secondary stage. This means that the function $h(\sigma)$ in Eq. (4.3) should be applicable.
- The development of the dislocation density can be described with the same equation, Eq. (4.5) that was used to derive the equation for the secondary creep rate.
- When starting from a low dislocation density at the start of the creep, Eq. (4.5) gives an increasing dislocation density. This density is assumed to generate a dislocation back stress according to Eq. (4.4).
- The creep rate in the primary stage is given by

$$\dot{\varepsilon} = h(\sigma + \sigma_{\text{disl sec}} - \sigma_{\text{disl}} - \sigma_i) \tag{4.6}$$

  where $\sigma_{\text{disl sec}}$ is the stress due to the dislocations (dislocation stress) in the secondary stage. In comparison to Eq. (4.3), the effective stress in Eq. (4.6) is raised by what we can call the primary stress σ_{prim}

$$\sigma_{\text{prim}} = \sigma_{\text{disl sec}} - \sigma_{\text{disl}} \tag{4.7}$$

The presence of σ_{prim} in Eq. (4.6) raises the creep rate in comparison to the secondary stage, which is a characteristic feature of primary creep. When the secondary stage is reached, the dislocation stress σ_{disl} is equal to $\sigma_{\text{disl sec}}$ and σ_{prim} vanishes as it should. σ_{prim} is a help quantity which makes it possible to model the creep rate in the primary stage. The applied stress σ is still constant.

- In the secondary stage there is a balance between the applied stress σ and the back stress from the dislocations σ_{dislsec} plus the internal stress σ_i

$$\sigma = \sigma_{\text{disl sec}} + \sigma_i \tag{4.8}$$

  If Eq. (4.8) is applied, Eq. (4.6) can be rewritten as

$$\dot{\varepsilon} = h(2(\sigma - \sigma_i) - \sigma_{disl}) \tag{4.9}$$

The internal stress σ_i has several contributions

$$\sigma_i = \sigma_y(T, \dot{\varepsilon}) + \sigma_{SSH} + \sigma_{PH} \tag{4.10}$$

where σ_y is the temperature and strain rate dependent yield strength, σ_{SSH} and σ_{PH} the contributions from solid solution hardening and precipitation hardening that will be discussed in Chaps. 6 And 7.

It is important to recognize that the five assumptions do not involve any new functions or new parameters. It is simply assumed that the same basic dislocation mechanisms control both the primary and the secondary stage. A number of quantities such as the dislocation stresses σ_{disl} and $\sigma_{dislsec}$ and contributions to the internal stress σ_{SSH} and σ_{PH} are mathematical quantities that are useful in the modeling. These quantities can be defined in different ways. It is important to recognize that these quantities cannot be measured and they are not meaningful unless they are precisely defined. For example, there are many ways of defining a back or internal stress. A general discussion about a back stress without a proper definition does not make sense.

In the contribution to the internal stress in Eq. (4.10), the yield strength has been included. It is possible to make exactly the same analysis about primary creep without taking the yield strength into account. It is material dependent if the yield strength should be taken into account.

The use of the model will now be illustrated for two creep tests of Cu-OFP. In Fig. 4.9 the development of the dislocation density, Eq. (4.5) and the dislocation stress, Eq. (4.4) are shown.

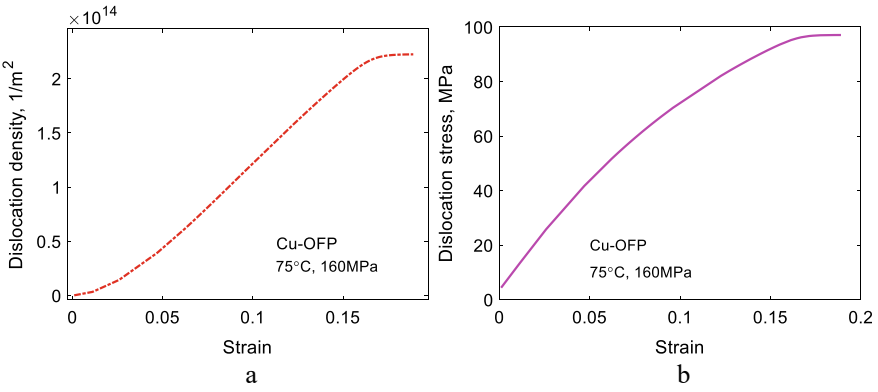

Fig. 4.9 Creep test of Cu-OFP at 75 °C and 160 MPa. The creep test was interrupted after 12000 h; **a** dislocation density versus strain according to Eq. (4.5); **b** dislocation stress versus strain for the dislocation density in **a** according to Eq. (4.4)

The dislocation density increases approximately linearly with increasing strain over most of the strain range considered. When the dislocation density has reached a sufficiently high level, the third (static recovery) term gives a contribution. Eventually there is a balance between the two contributions. The secondary stage has been reached. At this stage the dislocation density becomes independent of strain. The dislocation stress, Eq. (4.4) is also continuously raised until a plateau in the secondary stage is reached. In the secondary stage the dislocation stress is the difference between the applied stress, 160 MPa, and the internal stress, Eq. (4.8). The internal stress consists of the yield strength and the solid solution hardening due to phosphorus and these quantities take the values 57 and 6 MPa, respectively at the temperature and strain rate of the test. The used model for solid solution hardening is presented in Chap. 6. In Fig. 4.9 the maximum dislocation stress is 97 MPa. These three values add up to the applied stress as they should according to Eq. (4.8).

In Fig. 4.10a the creep strain versus time curve for the same test is shown. It can be seen that the model can reproduce the observations even for the fast initial stage of the test.

The creep rate versus time is given in Fig. 4.10b. Also in this Figure it is evident that the model can describe the measurements. When the strain had reached a sufficiently high value in the test, the test had to be reloaded several times to avoid that the dead weights hit the floor. This is the reason for the spikes in the experimental curves.

In Fig. 4.10b with a double logarithmic scale, the data lie along a straight line in the primary stage. This indicates that copper in addition to P91 and Sanicro 25 follows the ϕ model, Eq. (4.1). It is evident that also the model, Eq. (4.9), shows this behavior.

The results for another creep test that has run until rupture are given Fig. 4.11. The general appearance of creep strain and creep rate curves is not very different from that in Fig. 4.10. Both the primary and secondary stages are reproduced by the model. The modeling of the tertiary stage which is not taken into account here will

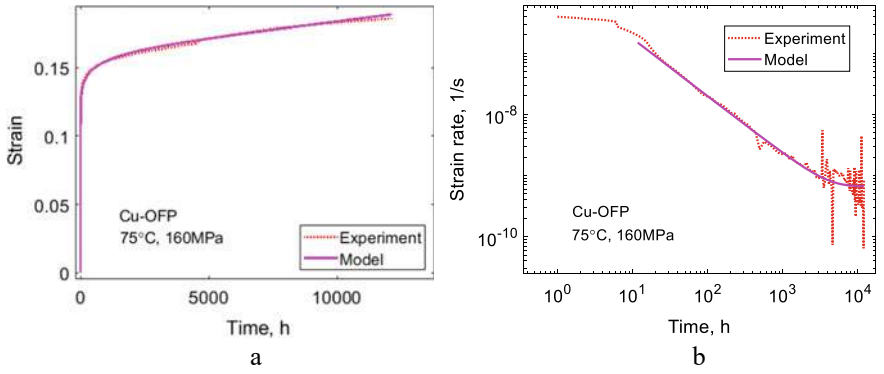

Fig. 4.10 Creep test of Cu-OFP at 75 °C and 160 MPa. The creep test was interrupted after 12000 h; **a** creep strain versus time; **b** creep rate versus time; Eq. (4.9). Redrawn from [20] with permission of Elsevier

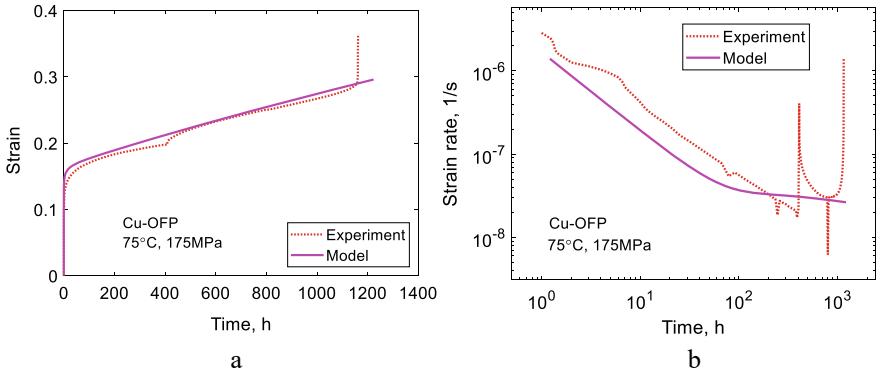

Fig. 4.11 Creep test of Cu-OFP at 75 °C and 175 MPa. The creep test was run until rupture; **a** creep strain versus time; **b** creep rate versus time; Eq. (4.9)

be discussed in Chap. 12. Again the data and the model follow closely the phi (ϕ) model in the primary stage.

4.4 Stress Adaptation

4.4.1 Model

In Sect. 3.3 it was demonstrated that a stress strain curve which had the form of a Voce equation could be derived from Eq. (4.5)

$$\sigma = \sigma_y + (\sigma_{sat} - \sigma_y)(1 - \exp(-\omega\varepsilon/2)) \tag{4.11}$$

This relation can be rewritten as

$$\sigma_{sat} = \sigma_y + \frac{\sigma - \sigma_y}{1 - e^{-\omega\varepsilon/2}} \tag{4.12}$$

The saturation stress σ_{sat} is closely related to the stationary creep stress. With this background, Eq. (4.12) is now generalized and transformed and considered as the driving stress for primary creep [4]

$$\sigma_{primSA} = \sigma_y(T, \dot{\varepsilon}) + \frac{\sigma - \sigma_y(T, \dot{\varepsilon})}{1 - e^{-\Omega\varepsilon/2}} \tag{4.13}$$

This expression is then inserted in Eq. (4.3) for the secondary creep rate

$$\frac{d\varepsilon}{dt} = h(\sigma_y(T, \dot{\varepsilon}) + \frac{\sigma - \sigma_y(T, \dot{\varepsilon})}{1 - e^{-\Omega\varepsilon/2}}, T) \tag{4.14}$$

The Ω value was originally identical to the dynamic recovery constant ω. However, it has been found that at situation far from stationary conditions, Ω might have to be chosen in a different way and that is discussed below. For this reason ω is replace by Ω in Eqs. (4.13) and (4.14). In Eq. (4.14) the yield strength depends on the temperature and the strain rate. The following dependence is assumed, Eq. (3.15).

$$\sigma_y(T, \dot{\varepsilon}) = \sigma_y(T_0, \dot{\varepsilon}_0)\frac{G(T)}{G(T_0)}\left(\frac{\dot{\varepsilon}}{\dot{\varepsilon}_0}\right)^{(1/n_N)} \tag{4.15}$$

T_0 is a reference temperature and $\dot{\varepsilon}_0$ a reference strain rate that are usually taken as 20 °C and 1×10^{-4} 1/s, respectively. The temperature dependence of the yield strength follows that of the shear modulus *G*. The strain rate dependence is described with a Norton equation. n_N is the stress exponent determined at the temperature and strain rate in question from the equation for the secondary creep rate, Eq. (2.30).

The expression for σ_{primSA} is quite different from that of σ_{prim} given in Sect. 4.3. Two features of Eq. (4.13) are important to recognize. When the strain increases σ_{primSA} tends towards the applied stress and Eq. (4.14) is back to the expression for secondary creep. At small strains σ_{primSA} can be expanded in the strain. If a Norton expression with a stress exponent is assumed, it can be shown that Eq. (4.14) takes the same form as Eq. (4.1) for the ϕ model. This means that if the ϕ model is valid for very small strains, Eq. (4.14) may be applicable. Equation (4.14) cannot be expected to be as general as the model in Sect. 4.3. Special assumptions are made and eq. (4.14) is based on the Voce equation that is not valid for all alloys. The strain rate and temperature dependence of the yield strength must be taken into account and they are not always known.

4.4.2 Numerical Integration

Equation (4.14) is numerically complicated to integrate. The reason is that the yield strength depends on the strain rate. Thus in each integration step an iteration has to be performed. This way of direct integration is quite feasible. It is referred to as *stress adaptation* since to determine the stress σ_{primSA} iteration is required in each step.

There are alternative ways to perform the integration. A brief summary is given here. For further details, see [21]. One way is to represent the function $h(\sigma, T)$ by a Norton equation

$$\frac{d\varepsilon}{dt} = h(\sigma, T) = A_N(T)\sigma^{n_N} \tag{4.16}$$

Using Eqs. (4.15) and (4.16), Eq. (4.14) can be rewritten as

$$\left(\frac{\dot{\varepsilon}}{A_{\mathrm{N}}}\right)^{1/n_{\mathrm{N}}} = \sigma_{\mathrm{y}}(T,\dot{\varepsilon}_0)\frac{G(T)}{G(T_0)}(\frac{\dot{\varepsilon}}{\dot{\varepsilon}_0})^{(1/n_{\mathrm{N}})} + \frac{\sigma - \sigma_{\mathrm{y}}(T,\dot{\varepsilon}_0)\frac{G(T)}{G(T_0)}(\frac{\dot{\varepsilon}}{\dot{\varepsilon}_0})^{(1/n_{\mathrm{N}})}}{1-e^{-\Omega\varepsilon/2}} \tag{4.17}$$

The following abbreviations are introduced

$$a_{\mathrm{N}} = A_{\mathrm{N}}^{1/n_{\mathrm{N}}} \qquad b_{\mathrm{N}} = \sigma_{\mathrm{y}}(T,\dot{\varepsilon}_0)\frac{G(T)}{G(T_0)}/\dot{\varepsilon}_0^{1/n_{\mathrm{N}}} \tag{4.18}$$

Using these abbreviations and solving for $\dot{\varepsilon}$ gives

$$\dot{\varepsilon}^{1/n_{\mathrm{N}}} = \frac{1}{1/a_{\mathrm{N}} - b_{\mathrm{N}} + \frac{b_{\mathrm{N}}}{1-e^{-\Omega\varepsilon/2}}}\ \frac{\sigma}{1-e^{-\Omega\varepsilon/2}} \tag{4.19}$$

From this expression, the formula for the yield strength can be obtained directly

$$\sigma_{\mathrm{y}}(T,\dot{\varepsilon}) = \sigma_{\mathrm{y}}(T,\dot{\varepsilon}_0)\frac{G(T)}{G(T_0)}\left(\frac{\dot{\varepsilon}}{\dot{\varepsilon}_0}\right)^{1/n_{\mathrm{N}}} = b_{\mathrm{N}}\dot{\varepsilon}^{1/n_{\mathrm{N}}} = \frac{\sigma}{(\frac{1}{a_{\mathrm{N}}b_{\mathrm{N}}}-1)(1-e^{-\Omega\varepsilon/2})+1} \tag{4.20}$$

The strain rate has now been eliminated so the integration of Eq. (4.14) can be performed directly. This procedure is referred to as *expansion integration.*

Another problem in the numerical integration is the singularity for small strains in Eqs. (4.14) and (4.20). This singularity can be eliminated by modifying the model in the following way [22]. In Eq. (4.13) the strain rate dependence is extracted

$$\sigma = \left[\sigma_{\mathrm{y}}(T) + K(T)(1-\mathrm{e}^{-\omega\varepsilon/2})\right](\frac{\dot{\varepsilon}}{\dot{\varepsilon}_{\mathrm{k}}})^{1/n_{\mathrm{N}}} \tag{4.21}$$

σ_{y} and K are assumed to have the same strain rate dependence, which is approximately the case. The reference strain rate $\dot{\varepsilon}_{\mathrm{k}}$ is only known for the maximum stress, which also defines K

$$\dot{\varepsilon}_{\mathrm{k}} = A_{\mathrm{N}}(\sigma_{\mathrm{y}}(T) + K(T))^{n_{\mathrm{N}}} \tag{4.22}$$

A_{N} and n_{N} are determined from the total stress σ_{primSA} in Eq. (4.13) in the same way as in the previous integration alternative. From Eq. (4.21) an expression for the strain rate can be obtained

$$\frac{\dot{\varepsilon}}{\dot{\varepsilon}_{\mathrm{k}}} = \left\{\frac{\sigma}{\sigma_{\mathrm{y}}(T) + K(T)(1-\mathrm{e}^{-\Omega\varepsilon/2})}\right\}^{n_{\mathrm{N}}} \tag{4.23}$$

Equations (4.22) and (4.23) give

$$\dot{\varepsilon} = A_{\mathrm{N}}\left\{\frac{\sigma(\sigma_{\mathrm{y}}(T) + K(T))}{\sigma_{\mathrm{y}}(T) + K(T)(1-\mathrm{e}^{-\Omega\varepsilon/2})}\right\}^{n_{\mathrm{N}}} \tag{4.24}$$

The Norton Eq. (4.24) can be replaced by an equation of the original form, Eq. (4.14)

$$\dot{\varepsilon} = h\left(\frac{\sigma(\sigma_y(T) + K(T))}{\sigma_y(T) + K(T)(1 - e^{-\Omega\varepsilon/2})}, T \right) \tag{4.25}$$

In Eq. (4.25) the singularity at small strains has been removed. This procedure is referred to as *max stress integration.*

A simplistic variant of Eq. (4.25) will be given to illustrate how the model works [23]. The formula in Eq. (4.25) will be expressed as a Norton equation with the constants A and n. Considering small strains ($\Omega\varepsilon/2 < 1$), the exponential can be expanded

$$\dot{\varepsilon}_{\text{prim}} = A\left\{ \frac{\sigma(1 + \sigma_y/K)}{\sigma_y/K + \Omega\varepsilon/2)} \right\}^n \tag{4.26}$$

Equation (4.26) is integrated with respect to time t. Assuming the initial strain to be zero, one finds that

$$\varepsilon = \{(1+n)A\}^{1/(n+1)} \left\{ \frac{2\sigma(1 + \sigma_y/K)}{\Omega} \right\}^{\frac{n}{n+1}} t^{\frac{1}{n+1}} - \frac{2\sigma_y}{K\Omega} \tag{4.27}$$

The time derivative of Eq. (4.27) is

$$\frac{d\varepsilon}{dt} = \frac{\{(1+n)A\}^{1/(n+1)}}{n+1} \left\{ \frac{2\sigma(1 + \sigma_y/K)}{\Omega} \right\}^{\frac{n}{n+1}} t^{-\frac{n}{n+1}} \tag{4.28}$$

Although Eqs. (4.26) and (4.28) are both derivatives of Eq. (4.27), they are not identical because Eq. (4.26) is a function of strain and Eq. (4.28) a function of time.

According to the simplistic model, the stress exponent is $n/(n+1)$, i.e. close to 1 provided n is not small. The time dependence is also of importance. The ϕ model is valid for many materials in the primary stage

$$\dot{\varepsilon}_{\text{prim}\phi} = A_\phi t^{-\phi} \tag{4.29}$$

where t is the time and A_ϕ and ϕ are parameters. Further details about the ϕ model can be found in Sect. 4.2 and in [22]. From (4.28) it can be seen that the simplistic model agrees with the ϕ model where $\phi = n/(n+1)$. This requires that the last term in (4.27) is small is relation to the value of the strain. This can be expressed in terms of the following criterion

$$\frac{\sigma_y}{K} < \frac{\Omega\varepsilon}{2} \tag{4.30}$$

It can be shown that this criterion must also be fulfilled for the full model in Eq. (4.25).

If the primary creep is near its end and approaching stationary conditions, Ω can be replaced with the dynamic recovery constant ω. The temperature correction for ω introduced in Sect. 3.4, $(G(\mathrm{RT})/G(T))^2$, where $G(T)$ and $G(\mathrm{RT})$ are the shear modulus at temperature and room temperature respectively, should be considered. However, if the primary creep is far from stationary conditions, Ω has to be determined in an other way [22]. At low strains the work hardening can be found from Eq. (3.12)

$$\frac{d\sigma_{\mathrm{disl}}}{d\varepsilon} = \frac{\alpha G m_{\mathrm{T}}^2}{2c_{\mathrm{L}}} \tag{4.31}$$

The dislocation stress can never be larger than the applied stress. When the dislocation stress is approaching the applied stress, a semi-stationary condition may be said to be reached. The strain has then the value

$$\varepsilon_{\mathrm{semi\ stat}} = (\sigma - \sigma_{\mathrm{i}})\frac{2c_{\mathrm{L}}}{\alpha G m_{\mathrm{T}}^2} \tag{4.32}$$

At this stage the exponential in Eq. (4.25) must be small, say 0.05, which gives

$$\Omega \approx \frac{3}{\varepsilon_{\mathrm{semi\ stat}}} = \frac{3\alpha G m_{\mathrm{T}}^2}{2c_{\mathrm{L}}(\sigma - \sigma_{\mathrm{i}})} \tag{4.33}$$

where σ_{i} includes strength contributions, for example, from solid solution and precipitation hardening. The applicability of Eq. (4.33) is shown for example in Sect. 5.8 and [22] for applications at a wide range of temperatures for copper.

4.4.3 Applications

The use of Eq. (4.14) will now be illustrated. Two examples for creep tests of Cu-OFP at 75 °C are shown. The results for a test at a stress of 180 MPa are shown in Fig. 4.12.

It can be seen that the creep strain and creep strain rate versus time are approximately reproduced. The three integration methods stress adaptation, expansion integration and max stress integration give closely the same result. The straight line in Fig. 4.12b indicates that the phi (ϕ) model is followed down to fairly short times.

Another example is presented in Fig. 4.13. Again the experimental results for the creep strain and the creep rate are modeled in a general way. It is clear that the model in the present section gives a less precise description of the data than the model in Sect. 4.3. However, the model is useful to describe results at very low stresses, Chap. 5.

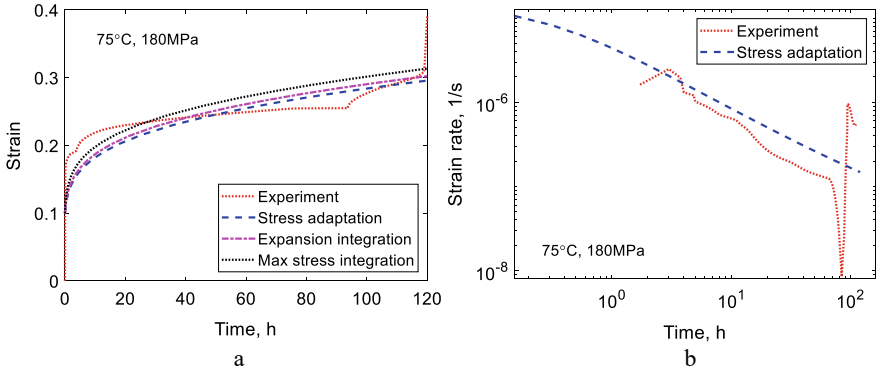

Fig. 4.12 Creep test of Cu-OFP at 75 °C and 180 MPa. The creep test was run until rupture; **a** creep strain versus time; **b** creep rate versus time; Eq. (4.14)

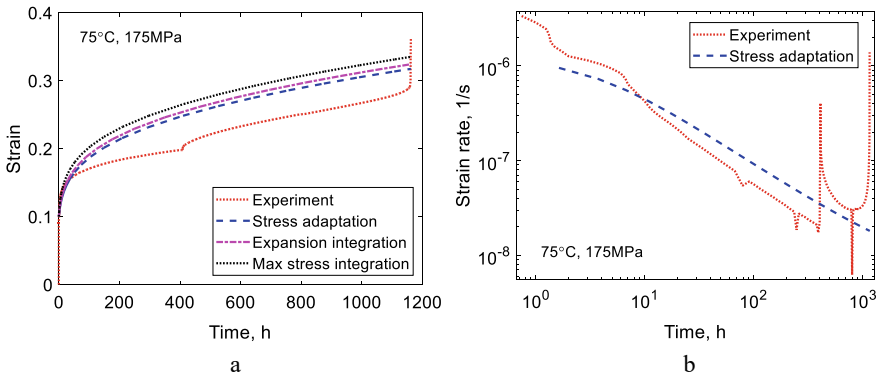

Fig. 4.13 Creep test of Cu-OFP at 75 °C and 175 MPa. The creep test was run until rupture; **a** creep strain versus time; **b** creep rate versus time; Eq. (4.14)

4.5 12% Cr Steels

4.5.1 Dislocation Model

The creep models presented in Sects. 4.3 and 4.4 as well as in Chap. 2 are based on a single dislocation density. However, there are materials for which more than one type of dislocation density must be introduced to fully take into account the role of the substructure. For the type of material, 9–12% Cr steels, that will be analyzed in this section, this is essential. In models with a single dislocation density, it is increased gradually from low values in the primary stage until it reaches the stationary value in the secondary stage. For 9–12% Cr steels, the initial microstructure is an annealed martensitic structure. It is characterized by well-developed subgrains with

subboundaries full of dislocations. This implies that the initial dislocation density is high. But the creep behavior of the 9–12% Cr steels in the primary stage is not very different from that in the fcc-alloys.

To handle this situation, a distinction is made between free and immobile dislocations. The free dislocations are located in the subgrain interiors and the immobile ones primarily in the subboundaries. The following equations are formulated for the densities of the free dislocations ρ_f and the immobile dislocations ρ_{im} [24, 25]

$$\frac{d\rho_f}{d\varepsilon} = \frac{1}{L_s}\frac{m_T}{b} - (\omega_1 + \omega_2)\rho_f \tag{4.34}$$

$$\frac{d\rho_{im}}{d\varepsilon} = \omega_2\rho_f - 2M\tau_L\rho_{im}^2/\dot{\varepsilon} \tag{4.35}$$

ε is the strain, $\dot{\varepsilon}$ the creep rate, L_s the mean spurt distance of dislocations, m_T the Taylor factor, b Burgers vector, M the climb mobility, and τ_L the dislocation line tension. The first term on the right hand side of Eq. (4.34) gives the work hardening. Only the free dislocations contribute to the work hardening. There are two types of dynamic recovery. A free dislocation will interact with a dislocation of opposite Burgers creating a dipole with a spacing d_{dip} that can annihilate each other

$$d_{dip} = \frac{m_T}{8\pi(1-\nu_P)}\frac{Gb}{\sigma} \tag{4.36}$$

This gives a recovery constant ω_1

$$\omega_1 = \frac{2m_T}{b}\frac{d_{dip}}{n_{slip}} \tag{4.37}$$

n_{slip} is the number of active slip systems. Dislocations can also form locks, when dislocations with different Burgers vector at a distance of d_{lock} interact. d_{lock} has about the same size as d_{dip}. This is another recovery effect that transfers the free dislocations to immobile ones.

$$\omega_2 = \frac{4m_T}{b}\frac{d_{lock}\left(n_{slip}-1\right)}{n_{slip}} \tag{4.38}$$

Thus this type of recovery reduces the free dislocation density and increases the immobile dislocation density. It gives no net change in the total dislocation density. The immobile dislocations can only be removed by static recovery. The static recovery term is the last term in Eq. (4.35) and it has the same form as in Eq. (4.5).

Only the immobile dislocations are included in Eq. (4.39) for the dislocation stress

$$\sigma_{disl} = \alpha m_T G b \rho_{im}^{1/2} \tag{4.39}$$

It is now possible to describe what happens during primary creep. Initially, ρ_f has a high value and ρ_{im} a low value. This gives a high total dislocation density, but the dislocation stress is low. To compute the strain rate, σ_{disl} should be inserted in Eq. (4.9). With a low value of σ_{disl}, the creep rate will be high. With increasing strain, the free dislocations are transferred to immobile ones, σ_{disl} is increased and the creep rate reduced. With Eqs. (4.34) and (4.35) the established features of primary creep are reproduced.

The internal stress is an important quantity for 9–12% Cr-steels. Particles increase the creep strength in two ways. Fine carbo-nitrides give a direct increase in the creep strength. Coarse $M_{23}C_6$ carbides stabilize the subboundaries and thereby reduce the recovery rate of the immobile dislocations. This implies a high value of the dislocation strength can be kept that decreases the creep rate. Only the role of the fine carbo-nitrides will be discussed briefly here. Further details are given in Chap. 7 on precipitation hardening. Only particles with a radius larger than a critical size contribute to the creep strength, Eq. (7.12)

$$r_{crit} = M_{climb}(T, \sigma) b^2 \sigma \lambda_s \frac{\rho_f}{\dot{\varepsilon}_{sec} m_T} \tag{4.40}$$

where λ_s is the interparticle spacing for all the carbo-nitrides. The particles give the following contribution to the internal stress

$$\sigma_i = \sigma_{part} = \frac{C_O G b m_T}{\lambda_{crit}} \tag{4.41}$$

where $C_O = 0.8$ and λ_{crit} is the interparticle spacing for particles larger than r_{crit}. Equation (4.41) is the expression for the Orowan strength except that λ_s is replaced by λ_{crit}. Together with σ_{disl}, σ_i should be inserted in Eq. (4.9) to find the creep rate.

4.5.2 Simulated Creep Curves

Results for creep strain curves of 12Cr1MoV steels (X20) will be presented. The creep curves have been published in [9]. Two heats CL and CT are considered. The particles in this steel are primarily $M_{23}C_6$ carbides. M stands mainly for Cr and Fe. The size distribution of the carbides has been measured [26]. The result is presented in Fig. 4.14.

In the semi logarithmic scale in Fig. 4.14, the size distributions are approximately linear except for small particle sizes. The deviation for small particles is often due to the difficulty to make accurate measurements for such particles. Otherwise the Figure shows that the number of particles per unit area n_{part} decreases exponentially with increasing carbide radius r_{part}

$$n_{part} = n_0 e^{-\beta r_{part}} \tag{4.42}$$

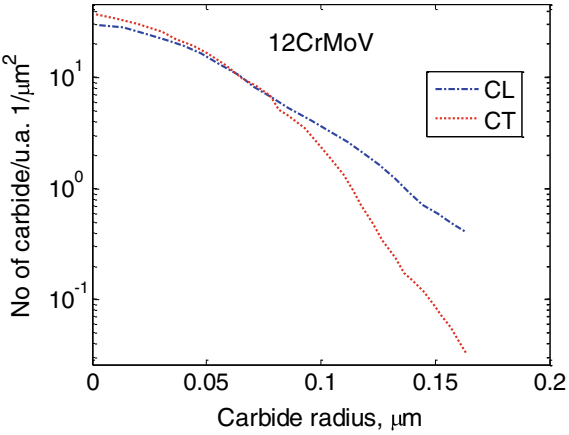

Fig. 4.14 Number of $M_{23}C_6$ carbides per unit area versus carbide radius for two heats CL and CT for a 12Cr1MoV steels. From [27]

where n_0 and β are constants. The values of β for the heats CL and CT in Fig. 4.14 are 3.2×10^7 and 6.0×10^7 1/m, respectively.

The initial values of the dislocation densities ρ_f and ρ_{im} have been taken as 8×10^{13} and 1×10^{11} 1/m^2 from two doctorial theses from Erlangen on 9 to 12% Cr-steels (Polcik 1998; Sailer 1998).

Experimental creep strain versus time curves are compared to the model in Figs. 4.15 and 4.16. The model curves only include primary and secondary creep since tertiary creep is not considered. In the primary and the secondary stages the experimental data is reasonably well reproduced.

This is further illustrated in Fig. 4.17 where the experimental and modeled minimum creep rates are compared. The Figure shows that the deviation is about a factor of two, which can be considered as acceptable. Again it is shown that primary creep can be accurately modeled without the use of adjustable parameters

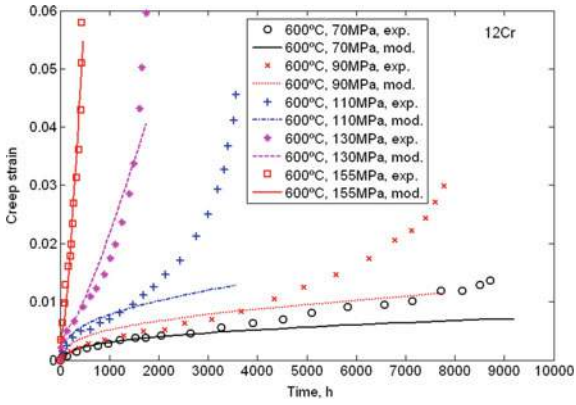

Fig. 4.15 Creep strain versus time curves for 12CrMoV steel at 600 °C for stresses between 70 and 155 MPa. Experimental data from [9]. Heat CT. From [27]

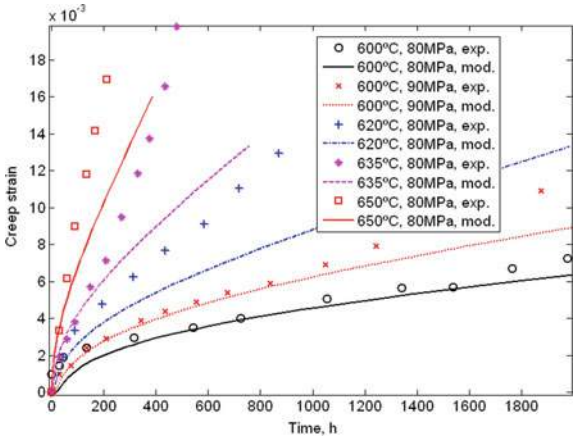

Fig. 4.16 Creep strain versus time curves for 12CrMoV steel at 600–650 °C for a stress of 80 or 90 MPa. Experimental data from [9]. Heat CL. From [27]

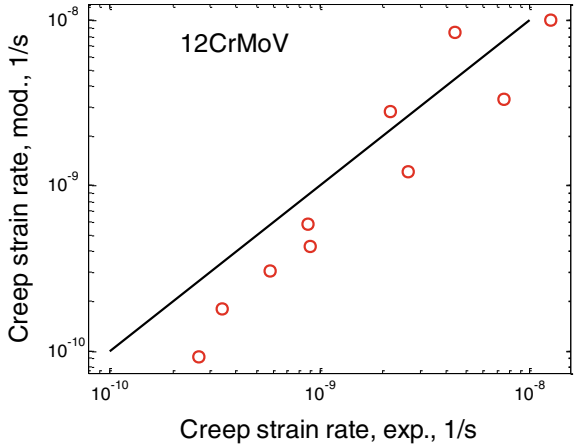

Fig. 4.17 Comparison of minimum creep strain rates between the experimental and model curves in Figs. 4.15 and 4.16. From [27]

4.6 Summary

- Many empirical models exist for representing creep curves, i.e. creep strain versus time curves. With four or more parameters almost any of these models can give a good fit to the curves. To get a better basis for selection of models, primary and tertiary creep should be handled separately. Then it is enough to involve just two parameters for primary creep and two for tertiary. For many types of steels primary creep can be represented with the phi model and tertiary creep with the Omega model. The phi model gives a linear curve in a double logarithmic strain rate versus time diagram. The Omega-model provides a linear curve when the logarithmic of the strain rate is shown as a function of the strain. The two models can be added to describe the whole creep curve. It is usually not necessary to have a separate term for secondary creep.

- Several basic models for primary creep are derived in the chapter. The modeling is based on the assumption that the dislocation density has initially a low value that increases during the primary stage until a stationary value is reached in the secondary stage that can be described with the basic dislocation models. The dislocation density is associated with a dislocation stress according to Taylor's equation. In one of the models an effective creep stress is introduced which is twice the applied stress minus the dislocation stress. This effective stress can be introduced in the expression for the secondary creep rate to find the creep rate in the primary stage. The expression can be generalized to include also tertiary creep, see Sect. 12.4.
- The use of the basic models for primary creep demonstrates that they can describe experimental creep curves. These modelled creep curves follow the phi model.
- For martensitic 9–12% Cr steels the situation is somewhat more complicated. Due to the martensitic microstructure the initial dislocation density is high. To handle this case at least two types of dislocation densities must be introduced; free and immobile. As a consequence, the development of both types of dislocations must be taken into account but the principles are the same.

References

1. R. Wu, R. Sandstrom, F. Seitisleam, Influence of extra coarse grains on the creep properties of 9% CrMoV (P91) steel weldment. J. Eng. Mater.-T ASME **126**, 87–94 (2004)
2. S.R. Holdsworth, F. Abe, T.-U. Kern, R. Viswanathan, 14-Constitutive equations for creep curves and predicting service life, in *Creep-Resistant Steels* (Woodhead Publishing, 2008), pp. 403–420
3. S.R. Holdsworth, M. Askins, A. Baker, E. Gariboldi, S. Holmstrom, A. Klenk, M. Ringel, G. Merckling, R. Sandstrom, M. Schwienheer, S. Spigarelli, Factors influencing creep model equation selection. Int J Pres Ves Pip **85**, 80–88 (2008)
4. R. Sandstrom, Basic model for primary and secondary creep in copper. Acta Mater. **60**, 314–322 (2012)
5. R.W. Evans, B. Wilshire, in *Creep of Metals and Alloys* (Institute of Metals, Swansea, 1985)
6. P.G. McVetty, Factors affecting the choice of working stresses for high temperature service. Trans ASME **55**, 99 (1933)
7. D. McHenry, A new aspect of creep in concrete and its application to design. Proc. ASTM **43**, 1069 (1943)
8. A. Graham, K.F.A. Walles, Relations between long and short time properties of commercial alloys. J. Iron Steel Inst. **179**, 105–120 (1955)
9. R. Wu, R. Sandstrom, J. Storesund, Creep strain behavior in a 12%-Crmov steel. Mater. High Temp. **12**, 277–283 (1994)
10. R. Sandstrom, A. Kondyr, Creep deformation, accumulation of creep rupture damage and forecasting of residual life for three Mo- and CrMo-steels. VGB Kraftwerkstechnik **62**, 802–813 (1982)
11. R. Sandstrom, A. Kondyr, Model for tertiary Creep in Mo and CrMo steels, in *ICM 3* (Pergamon Press, 1979), pp. 275–228
12. M. Prager, Development of the MPC omega method for life assessment in the creep range. J. Pressure Vessel Technol. Trans. ASME **117**, 95–103 (1995)
13. R. Sandström, Basic analytical modeling of creep strain curves. Materials **16** (2023)

14. R. Sandström, J.-J. He, Prediction of creep ductility for austenitic stainless steels and copper. Mater. High Temp. *39*(6), 427–435 (2022)
15. F. Abe, Analysis of creep rates of tempered martensitic 9%Cr steel based on microstructure evolution. Mater. Sci. Eng. A **510–511**, 64–69 (2009)
16. F. Abe, Bainitic and martensitic creep-resistant steels. Curr. Opin. Solid State Mater. Sci. **8**, 305–311 (2004)
17. F. Abe, T. Horiuchi, M. Taneike, K. Sawada, Stabilization of martensitic microstructure in advanced 9Cr steel during creep at high temperature. Mater. Sci. Eng. A **378**, 299–303 (2004)
18. F. Abe, Coarsening behavior of lath and its effect on creep rates in tempered martensitic 9Cr–W steels. Mater. Sci. Eng. A **387–389**, 565–569 (2004)
19. Y. Zhang, H. Jing, L. Xu, L. Zhao, Y. Han, J. Liang, Microstructure and texture study on an advanced heat-resistant alloy during creep. Mater. Charact. **130**, 156–172 (2017)
20. R. Sandström, The role of cell structure during creep of cold worked copper. Mater. Sci. Eng. A **674**, 318–327 (2016)
21. R. Sandstrom, S. Waqas Ahmad, K.T. Pasupuleti, M. Mahdavi Shahri, Slow strain rate tensile testing of friction stir welded Cu-OFP. Constitutive equations for creep. Swedish Nuclear Waste Management Company Report R-13-33 (2017)
22. R. Sandström, Primary creep at low stresses in copper. Mater. Sci. Eng.: A (2023)
23. R. Sandström, Creep at low stresses in aluminium (Harper-Dorn) and in an austenitic stainless steel with a stress exponent of 1. Mater. Today Commun. **36** (2023)
24. F. Roters, D. Raabe, G. Gottstein, Work hardening in heterogeneous alloys—A microstructural approach based on three internal state variables. Acta Mater. **48**, 4181–4189 (2000)
25. H. Magnusson, R. Sandstrom, Creep strain modeling of 9–12 pct Cr steels based on microstructure evolution. Metall. Mater. Trans. A **38A**, 2033–2039 (2007)
26. R. Wu, R. Sandstrom, Carbide coarsening during creep in 12% CrMoV steel. J. Eng. Mater.-T ASME **118**, 485–492 (1996)
27. R. Sandstrom, H. Magnusson, Basic model for creep deformation in 12Cr1MoV steels, in *12th International Conference on Creep and Fracture of Engineering Materials and Structures Japan Institute of Metals* (2012)

Chapter 5
Creep with Low Stress Exponents

Abstract Primary creep models predict that at low stresses a stress exponent of 1 can be obtained for dislocation creep. Also experimentally this has been observed for an austenitic stainless steel. The time dependence of the primary creep verifies that it is dislocation creep. An other example is for Al at very high temperatures (Harper-Dorn creep), where at sufficiently low stresses, the stress exponent approaches 1. For both materials higher stresses give larger stress exponents as expected for dislocation creep. Obviously, diffusion and dislocation creep can be competing processes. The validity of creep models at low stresses and high temperatures as well as at high stresses and low temperatures demonstrates their wide range of usage. Since this in reality represents an extensive extrapolation, it can be consider as a direct verification of the basic creep models. In cases for Cu and stainless steels, the predicted creep rate by diffusion creep (Coble) exceeds the observed creep rate as well as the predicted one by dislocation creep by an order of magnitude. The likely explanation is that constrained boundary creep is taken place, i.e. the grain boundary creep rate cannot be essentially faster than that of the bulk.

5.1 General

Creep at low stresses has generated great interest amongst scientists for a long time. Expressions for diffusional creep that do not involve dislocations were developed at an early stage. First an expression based on bulk diffusion was formulated [1]. This is now referred to as Nabarro-Herring creep. The creep takes place by diffusion from grain boundaries with low stresses to boundaries located perpendicular to the loading direction. An alternative expression was given by Coble [2] where the diffusion is assumed to take place in the grain boundaries instead of in the bulk. The difference in diffusion mechanism means that Nabarro-Herring creep is proportional to the bulk diffusion coefficient and Coble creep to the grain boundary diffusion coefficient. The grain size dependence is also different. With bulk diffusion the creep rate is inversely proportional to the square of the grain size. With grain boundary diffusion

R. Sandström, *Basic Modeling and Theory of Creep of Metallic Materials*, Springer Series in Materials Science 339,
https://doi.org/10.1007/978-3-031-49507-6_5

the proportionality is instead to the inverse cube of the grain size. Models for diffusion creep is summarized in Sect. 5.2.

The derivations for diffusional creep gave the first basic equations for the creep rate. The expressions do not involve any arbitrary or adjustable parameters and the equations are fully predictable. For both types of diffusional creep, the rate is proportional to the stress, which means that the stress exponent is 1. Thus diffusional creep has a number of characteristic features: well defined dependence of the grain size, stress and temperature (through the diffusion coefficient). For a long time it was also assumed that a stress exponent of 1 should always be associated with diffusional creep. Authors have suggested observations of Herring-Nabarro or Coble creep in many metals: Cd, Co, Cu, Fe, Mg and Zr. Kassner has given an excellent review of diffusional creep [3] and details about the observations and references can be found there.

Observations of diffusional creep have often been controversial. One reason is that observed creep rates have not been in agreement with predicted ones in a number of studies [4]. In for examples the excellent studies on βCo and αFe [5, 6], the observed creep rate was about two orders of magnitude higher than the predicted ones. The identification of diffusional creep is not necessarily based only on the observed creep rates. There are also metallographic techniques to distinguish between dislocation and diffusional creep. Langdon proposed that if scratches are made parallel to the loading direction, the markings would be still continuous across the grain boundaries after the test for dislocation creep but not for diffusional creep [7]. This requires that no grain boundary sliding occurs along the considered boundaries. Another proposal is that diffusional creep gives denuded zones in particle hardened alloys or grooves around grain boundaries [8, 9]. For example, McKnee et al. have used these techniques to support observations of diffusional creep [10, 11]. The role of denuded zones has been questioned in the literature [12]. Ample evidence is now available that demonstrates that denuded zones can be formed also during dislocation creep. Wadsworth et al. suggest that denuded zones are created at grain boundaries that are sliding and migrating simultaneously [13].

When recording creep rates during diffusional creep, it is assumed that stationary conditions have been reached. In creep testing at higher stress, the deformation can be allowed to continue until rupture takes place. Then it is straightforward to determine when the stationary stage has been reached. During dislocation creep, a distinct primary stage is expected. If such a stage is observed it is an indication that the operating mechanism is not diffusional creep. However, as will be discussed in this chapter, it is possible that diffusional creep can also show primary creep. It is evident that in many cases it is quite difficult to decide when stationary conditions have been achieved. If the creep rate is assessed during the primary stage, the measured creep rate would typically be much higher than in the secondary stage. In addition, the stress exponent can be low also for dislocation creep often approaching a value of 1. This makes it easy to mistake it for diffusional creep. Modeling can be quite helpful in understanding non-stationary conditions. In this chapter, modeling is presented that can assess and interpret creep rates that are measured in the primary stage, Sect. 5.5.

Harper and Dorn tested aluminum very close to the melting point at very low stresses looking for diffusional creep [14]. Their results gave a stress exponent of 1 but the creep rate was two orders of magnitude higher than the diffusional creep models predicted. They draw the conclusion that the mechanism was dislocation creep with a stress exponent of 1. This phenomenon is referred to as Harper-Dorn creep. It has created large interest. The work in the area is summarized in a paper by Kassner et al. [15]. Some authors were able to reproduce the results of Harper and Dorn [16, 17], others were not [18]. It was early on suspected that in many cases stationary conditions had not been reached. This has been confirmed in a paper by Kumar et al. [19] where the testing was carried to somewhat larger strains. The stress exponent now took the value of 3. They also found that Harper and Dorn had introduced a threshold stress, which Kumar et al. could not find any justification for. If the threshold stress is removed also the Harper and Dorn data are consistent with a stress exponent of 3 so the whole effect disappears. In Sect. 5.7, creep at very low stresses in aluminum is modeled. It is shown that deviations from a stress exponent of 3 can be explained by taking non-stationary effects into account. Thus, creep at very low stresses at high temperature can be fully accounted for with ordinary dislocation creep models and there is no need to refer to Harper-Dorn creep as a special effect.

Tests at very low stresses for the austenitic stainless steel 316H and the martensitic steel P91 have given a stress exponent of 1 [20]. Since distinct primary creep is observed and stress change experiments gave a stress exponent of 4.5 [21], it is concluded that the operation mechanism is dislocation creep. The tests for 316H are analyzed with a primary creep model in Sect. 5.6. The non-stationary model can quantitatively explain the behavior at low stresses (and at higher stresses). This clearly demonstrates that dislocation creep can be of importance also at very low stresses.

Creep tests that have claimed to demonstrate diffusional creep for Cu [9, 22], have been analyzed in Sect. 5.8. It is shown that the part of the experimental data that has been investigated is possible to reproduce with non-stationary dislocation creep. There are pros and cons whether these observations represent diffusional or dislocation creep. Further details are given in Sect. 5.8.

Results for previously unpublished results on creep in Cu between and 1 and 2 MPa at 600° C are presented. The tests are unusual for low stress experiments since the testing times exceed 12000 h. The results clearly represent dislocation creep, since the stress exponent is 3 and distinct primary creep is observed. Furthermore the results are in good agreement with the basic model for stationary creep, so any non-stationary model is not needed. The surprising feature is that the Coble creep model suggests a creep rate that exceeds the observations by an order of magnitude or more. Although mechanisms have been proposed in the literature that can reduce the Coble creep rate, it is difficult to identify such a mechanism in this case that can explain the effect. This is further discussed in Sect. 5.8.1. Also for the investigated case for 316H, Coble creep overestimates the observed creep rates at low stresses (by about one order of magnitude).

The classical diffusional models are briefly derived and summarized in Sect. 5.2. To explain the effect of alloying elements on the diffusional creep rate, several authors

assume that mobile grain boundary dislocations are a prerequisite for diffusional creep. For this reason a recovery creep model for grain boundary dislocations is formulated in Sect. 5.3. It is demonstrated that the grain boundary dislocations can give rise to quite a high creep rate, a phenomenon that does not seem to be covered in the literature. Some results suggest that creep along the grain boundaries must be accompanied with simultaneous deformation in the grains. This is covered in Sect. 5.4. It is referred to as constrained grain boundary creep. In Sect. 5.5, the primary creep model that is used to describe non-stationary dislocation creep at low stresses is summarized. Applications of the primary creep model at low stresses for an austenitic stainless steel are given in Sect. 5.6, for aluminum in Sect. 5.7, and for copper in Sect. 5.8.

5.2 Model for Diffusional Creep

Detailed models for diffusional creep were already presented in the original papers for Nabarro-Herring and Coble creep [1, 2]. Here, only a simplified derivation will be given. During Nabarro-Herring creep in tension, matter is transported to grain boundaries oriented perpendicular to the loading direction from grain boundaries parallel to the loading direction. This is possible by migration of vacancies in the opposite direction. It is assumed that the sources and sinks of the vacancies are at the grain boundaries. This is opposite to dislocation creep where the sinks and sources are primarily at the dislocations. The difference in vacancy concentration Δc_v between the boundaries that are exposed to a stress σ and the others is

$$\Delta c_\mathrm{v} = \exp\left(-\frac{Q_\mathrm{F}}{k_\mathrm{B}T}\right)\left(\exp\left(\frac{\sigma v_\mathrm{atom}}{k_\mathrm{B}T}\right) - 1\right) \tag{5.1}$$

Q_F is the vacancy formation energy and v_atom the atomic volume. The first factor in Eq. (5.1) is the thermal equilibrium concentration of vacancies. The second factor describes the increase in vacancy concentration due to the presence of the stress. Since only low stresses are considered, Eq. (5.1) can be rewritten as

$$\Delta c_\mathrm{v} = c_\mathrm{v0}\frac{\sigma v_\mathrm{atom}}{k_\mathrm{B}T} \tag{5.2}$$

A notation c_v0 has been introduced for the equilibrium vacancy concentration. The flow of vacancies J can be expressed as

$$J = -\frac{D_\mathrm{v}}{v_\mathrm{atom}}\frac{\Delta c_\mathrm{v}}{d_\mathrm{eff}} = -D_\mathrm{v}\frac{c_\mathrm{v0}}{d_\mathrm{eff}}\frac{\sigma}{k_\mathrm{B}T} \tag{5.3}$$

D_v is the vacancy diffusion coefficient and d_eff the effective diffusion distance. For a simple grain structure, d_eff can be estimated. Let us assume that we have coordinates

x and y on perpendicular grain boundaries in a quadratic grain

$$d_{\text{eff}} = \frac{1}{d_{\text{grain}}^2} \int_0^{d_{\text{grain}}/2} \int_0^{d_{\text{grain}}/2} \sqrt{x^2 + y^2} dx dy = 0.1 d_{\text{grain}} = \frac{d_{\text{grain}}}{A_{\text{NH}}} \tag{5.4}$$

The constant A_{NH} has been introduced to mark that its value depends on the geometry of the grains. The vacancy flux gives rise to a change in the grain size along the loading direction

$$\frac{d d_{\text{grain}}}{dt} = -J v_{\text{atom}} \tag{5.5}$$

This corresponds to a creep rate $\dot{\varepsilon}_{\text{NH}}$ of

$$\dot{\varepsilon}_{\text{NH}} = \frac{1}{d_{\text{grain}}} \frac{d d_{\text{grain}}}{dt} = \frac{J v_{\text{atom}}}{d_{\text{grain}}} = A_{\text{NH}} D_{\text{v}} \frac{c_{\text{v0}}}{d_{\text{grain}}^2} \frac{\sigma v_{\text{atom}}}{k_{\text{B}} T} \tag{5.6}$$

where Eq. (5.3) has been inserted for J. The expression for d_{eff} in Eq. (5.4) has also been used where $A_{\text{NH}} = 10$. The vacancy diffusion coefficient D_{v} is related to the self-diffusion coefficient D_{latt}

$$D_{\text{latt}} = D_{\text{v}} c_{\text{v0}} \tag{5.7}$$

If this expression is applied the final expression for the Nabarro-Herring creep rate is obtained.

$$\dot{\varepsilon}_{\text{NH}} = A_{\text{NH}} \frac{D_{\text{latt}}}{d_{\text{grain}}^2} \frac{\sigma v_{\text{atom}}}{k_{\text{B}} T} \tag{5.8}$$

The result in Eq. (5.8) is identical to the original expression derived by Herring for quadratic grains [1]. However, it is more common to use the expression for spherical grains and then $A_{\text{NH}} = 14$ instead of 10 [1, 23]. Greenwood has presented expressions for Nabarro-Herring creep for more general grain structures [24].

It is possible to extend the equation to Coble creep by introducing an effective diffusion coefficient D_{eff} that takes both lattice diffusion and grain boundary diffusion into account

$$D_{\text{eff}} = D_{\text{latt}} \left(1 + \frac{\pi \delta_{\text{GB}}}{d_{\text{grain}}} \frac{D_{\text{GB}}}{D_{\text{latt}}} \right) = D_{\text{latt}} \left(1 + \frac{\pi}{d_{\text{grain}}} \frac{\delta D_{\text{GB}}}{D_{\text{latt}}} \right) \tag{5.9}$$

where δ_{GB} is the grain boundary width. In this book the grain boundary diffusion coefficient is represented by δD_{GB} that includes the grain boundary width and has the unit m^3/s. This is the quantity that is most often measured. But Eq. (5.9) is also expressed in terms of the grain boundary diffusion coefficient D_{GB} that does not

include δ_{GB} and has the unit m^2/s. The factor π in front of δD_{GB} can take different values in different sources but π is the most common choice. If D_{latt} is replaced by D_{eff} in Eq. (5.8), Coble creep is covered by the second term in the brackets

$$\dot{\varepsilon}_{diffcreep} = A_{NH} \frac{\sigma v_{atom}}{k_B T d_{grain}^2} D_{latt} \left(1 + \frac{\pi}{d_{grain}} \frac{\delta D_{GB}}{D_{latt}} \right) \tag{5.10}$$

5.3 Grain Boundary Creep

As will be seen in Sects. 5.6 and 5.8, the classical model for Coble creep can overestimate the observed creep rates by at least an order of magnitude. This means that diffusional creep must be blocked by one or more processes. Such processes have been proposed. A survey of earlier work is provided by Arzt et al. [25]. The diffusion process in the grain boundary can be affected. However, it is difficult to see how such processes can provide mechanisms that are sufficient large to explain the mentioned observations. In a number of papers including [25], it assumed that dislocation activities are needed to make grain boundaries involved in diffusional creep and provide the necessary sources and sinks of vacancies. This gives a way to explain the large blocking effects. Another mechanism that does not seem to have been raised in the literature, is that the dislocations in the grain boundaries can give a direct contribution to the creep rate without involving diffusional creep. In this section, a model is presented for this contribution. In the derivation, due to the lack of access, specific properties for grain boundary dislocations will not be used. Instead, parameters for bulk dislocations will be applied.

The first step is to formulate a model for development of the dislocation density during creep in the grain boundaries equivalent to Eq. (2.17). In the same way as for deformation in the bulk, the starting point is the Orowan Eq. (2.6). It has a different form for GB dislocations [26]

$$\dot{\varepsilon} = \frac{b_n \rho v_{disl}}{m_T d_{grain}} \tag{5.11}$$

where b_n is the component of the Burgers vector perpendicular to the GB, ρ the dislocation density and v_{disl} the velocity of the dislocations. Equation (5.11) is integrated and derivated with respect to the strain to give

$$\frac{d\rho}{d\varepsilon} = \frac{m_T d_{grain}}{b_n L_s} \tag{5.12}$$

L_s is the spurt distance, cf. Eq. (2.5) and it is assumed that it can be expressed in the subgrain diameter d_{sub}. In the same way as for bulk deformation

$$L_s = n_{sub} d_{sub} \tag{5.13}$$

where the constant n_{sub} is close to 3 [27, 28]. The subgrain size can be related to the dislocation stress

$$d_{sub} = \frac{K_{sub} G b}{\sigma_{disl}} \tag{5.14}$$

K_{sub} is a constant typically in the range 10–20. The expression for the Taylor Eq. (2.20) has to be modified [25]

$$\sigma_{disl} = \alpha m_T G b \rho = \sigma - \sigma_i \tag{5.15}$$

The dislocation stress σ_{disl} is now linear in the density. σ_i is the back stress from solid solution and particle hardening. By combining Eqs. (5.11)–(5.15) it is found that the change in the dislocation density contributing to the work hardening is given by

$$\frac{d\rho}{d\varepsilon} = \frac{m_T d_{grain}}{b c_L} \rho \qquad \text{(work hardening)} \tag{5.16}$$

where

$$c_L = \frac{n_{sub} K_{sub}}{m_T \alpha} \tag{5.17}$$

In comparison to the bulk Eq. (2.9), the difference is that the work hardening contribution is linear in the dislocation density. Since the dislocation stress σ_{disl} is linear in the dislocation density, the strain dependence of σ_{disl} is also linear.

$$\frac{d\sigma_{disl}}{d\varepsilon} = \frac{m_T d_{grain}}{c_L b_n} \sigma_{disl} \qquad \text{(work hardening)} \tag{5.18}$$

For the elastic properties and the Burgers vector for example in Eq. (5.15), grain boundary values should be applied. However, for metals the values of the elastic properties are of the order of 93% of the bulk values [29]. Considering the uncertainties involved in modeling grain boundary properties, these replacements have not been made.

For the static recovery, the starting point is Eq. (2.16).

$$\frac{dR}{dt} = \frac{M_B \tau_L}{R} \tag{5.19}$$

where R is the spacing between dislocations and τ_L the dislocation line tension. The boundary climb mobility is given by

$$M_B = \frac{bD_{GB}}{k_B T} \tag{5.20}$$

Notice the difference between the two grain boundary diffusion coefficients

$$\delta D_{GB} = \delta_{GB} D_{GB} \tag{5.21}$$

δD_{GB} and D_{GB} have the units m^3/s and m^2/s, respectively. δ_{GB} is the grain boundary width that is usually taken as 5×10^{-10} m. The dislocation spacing R in the boundary is

$$R = 1/\rho \tag{5.22}$$

Inserting Eq. (5.22) into (5.19) gives

$$\frac{d\rho}{dt} = -\tau_L M_B \rho^3 \qquad \text{(static recovery)} \tag{5.23}$$

There are two differences between Eq. (5.23) and the bulk version, Eq. (2.13). First, the factor of 2 is missing and the dislocation density appears to the third order. By summing the contributions from Eqs. (5.16) and (5.23), an expression for the strain dependence of the dislocation density is obtained

$$\frac{d\rho}{d\varepsilon} = \frac{m_T d_{grain}}{bc_L}\rho - \tau_L M_B \rho^3 / \dot{\varepsilon}_B \tag{5.24}$$

The time derivative in Eq. (5.23) has been changed to a strain derivative by dividing by the strain rate. $\dot{\varepsilon}_B$ is the local creep rate in the grain boundary. During stationary condition the strain derivative of the dislocation density vanishes and the creep rate can be found directly. The overall grain boundary creep rate $\dot{\varepsilon}_{GB}$ is given by

$$\dot{\varepsilon}_{GB} = \frac{\delta_{GB}}{d_{grain}}\dot{\varepsilon}_B = \frac{\delta_{GB} b c_L \tau_L M_B \rho^2}{d_{grain}^2 m_T} \tag{5.25}$$

With the modified Taylor, Eqs. (5.15) and (5.25) can be expressed in terms of stress

$$\dot{\varepsilon}_{GB} = \frac{\delta_{GB} b c_L \tau_L M_B (\sigma - \sigma_i)^2}{d_{grain}^2 m_T (\alpha m_T G b)^2} \tag{5.26}$$

The grain boundary creep rate is inversely proportional to the square of the grain size and has a stress exponent of about 2 at low stresses. At higher stresses the role of pipe diffusion, strain induced vacancies, etc. should be taken into account in the same way as for creep in the bulk. Equation (5.26) has the same temperature, stress

and grain size dependence as the creep rate during superplastic deformation due to GBS, Eq. (9.20), but the equations are not identical.

Equation (5.26) can give quite a high strain rate. The grain boundary diffusion coefficient is much larger than the bulk diffusion coefficient and that is only compensated to some extent by the ratio δ_{GB}/d_{grain}. It is important to take into account the role of cross-slip. If the grain boundaries are fully straight, cross-slip has to take place at the triple points. However, the boundaries are often curved, and then cross-slip is continuous. With cross-slip an extra activation energy has to be introduced, Eq. (2.47)

$$g_{\text{cross-slip}} = \exp\left(-\frac{E_{cs}}{R_G T}\right) \tag{5.27}$$

Equation (5.26) is multiplied by Eq. (5.27). The problem is that the value of the activation energy for cross-slip is uncertain. As summarized in Sect. 2.6.3, ab initio values for the activation energy vary from 50 to 270 kJ/mol. The values for alloys appear to be larger than for pure metals. The role of cross-slip remains an open issue.

5.4 Constrained Grain Boundary Creep

Creep in the grain boundaries without plastic deformation in the neighboring grain interiors is not possible. Perhaps, the most obvious effect is for superplasticity. In this case the main deformation takes place by GB sliding. However, extensive deformation cannot occur in a material without the grain interiors being affected. In other words, creep in the grain boundaries must always be accompanied by creep in the whole grains as well. This phenomenon will be referred to as *constrained grain boundary creep*. The term is taken from growth of creep cavities that inside a material growth cannot be faster than the creep deformation, see Sect. 10.5.2.

Grain boundary creep according to Eq. (5.26) can give quite a high creep rate, in many cases higher than bulk dislocation creep, but such a phenomenon has not been reported in the literature. It is assumed that the grain boundary creep rate $\dot{\varepsilon}_{GB}$ cannot exceed the creep rate in the bulk $\dot{\varepsilon}_{bulk}$ significantly. The bulk creep mechanism is practically always dislocation creep but could in principle also be Nabarro-Herring creep. If the grain boundary creep rate $\dot{\varepsilon}_{GB}$ is estimated to be higher than the bulk creep rate, the creep rates must be matched approximately

$$\dot{\varepsilon}_{GB}(\sigma_{red}) \approx \dot{\varepsilon}_{bulk}(\sigma) \tag{5.28}$$

Thus, the stress controlling the grain boundary creep rate must be reduced to ensure that the creep rates match.

In Sects. 5.6 and 5.8.1 it is shown that the Coble creep model rates can exceed the observations by more than an order of magnitude. Several mechanisms have been proposed that could retard diffusional creep. These are in general based on the

assumption that the creep rate is controlled by GB dislocations [25]. For Nabarro-Herring creep, they can account for that GBs are not perfect sources and sinks for vacancies. For Coble creep the GB dislocations assure that atoms and vacancies can leave the GBs to avoid that they are getting saturated. Many mechanisms are available that can reduce the mobility of GB dislocations. Further details are given in the mentioned sections.

If the estimated Coble creep rate is still higher than the bulk creep rate, constrained GB creep is active. This means that Eq. (5.28) must be satisfied for Coble creep as well

$$\dot{\varepsilon}_{\text{Coble}}(\sigma_{\text{red}}) \approx \dot{\varepsilon}_{\text{bulk}}(\sigma) \tag{5.29}$$

Thus, if the Coble creep rate is nominally higher than the bulk creep rate, matching of the two creep rates must take place and the stress driving Coble creep is reduced. Exceptions to this principle can be found for hypothetical grain structures. A grain structure consisting of identical rectangular prisms where there is a homogeneous padding of atoms on the planes perpendicular to the loading directions is an example where bulk deformation may not take place. Such cases have of course no practical relevance.

When the bulk creep rate is controlled by dislocation creep, it shows a higher creep rate in the primary stage and this allows Coble creep to have a higher creep rate initially as well. This means that Coble creep can have a primary stage. The main conclusion of this section is that any creep deformation mechanism that is entirely concentrated to the GBs cannot be significantly faster than the bulk creep rate.

5.5 Primary Creep at Low Stresses

One major concern when making creep tests at low stresses is whether stationary conditions have been reached. Most creep models refer to the stationary creep rate when identifying creep mechanisms. If the creep test has not been carried out long enough the wrong conclusions can be drawn. At low stresses, the interesting question is often if diffusional or dislocation creep is observed. The stress exponent for diffusional creep is always assumed to be 1 according to the models for Nabarro-Herring and Coble creep. A possible exception exists for nanocrystalline alloys. It has been proposed that Coble creep can appear also at higher stresses and with a stress exponent larger than unity [30]. This possibility will not be considered here. If stationary creep has been reached, the stress exponent is 3 or more for dislocation creep. The known exception is superplasticity where the stress exponent can be 2. This is discussed in Sect. 9.4. Then it is straightforward to distinguish between diffusional and dislocation creep. However, if dislocation creep is in the primary stage, the stress exponent can be lower and the identification can be difficult.

In recent years basic models for primary creep have been developed. They are described in Chap. 4. With the help of these models a better understanding of the

creep behavior during non-stationary conditions can be established. Low stresses are often associated with low strains. The appropriate model is given in Eqs. (4.13) and (4.14). The model is called *stress adaptation*. In the same way as for the other models for primary creep in Chap. 4, the starting point is the creep rate in the stationary stage and the rate in the primary stage is related to that in the stationary stage. The only change is that an effective stress is introduced that is higher than the stationary stress, which can represent the higher creep rate in the primary stage. In the stress adaption model the effective stress is given by [31]

$$\sigma_{\text{primSA}} = \sigma_{\text{y}}(T, \dot{\varepsilon}) + \frac{\sigma - \sigma_{\text{y}}(T, \dot{\varepsilon})}{1 - e^{-\Omega\varepsilon/2}} \tag{5.30}$$

The quantity σ_{y} is the yield strength that depends on temperature and the strain rate $\dot{\varepsilon}$, Ω is related to the dynamic recovery constant, and σ the applied stress in the creep test. One requirement on the effective stress is that it tends to the applied stress at large strains. This is obviously the case in Eq. (5.30). The second part of the model is the rate for stationary creep, Eq. (4.3)

$$\dot{\varepsilon} = h(\sigma - \sigma_{\text{i}}) \quad \text{with} \quad h(\sigma) = \frac{2\tau_{\text{L}} b c_{\text{L}} M(T, \sigma)}{m_{\text{T}}} \frac{\sigma^3}{(\alpha m_{\text{T}} G b)^3} \tag{5.31}$$

where m_{T} is the Taylor factor, b burgers vector, G the shear modulus, c_{L} and α dimensionless constants, τ_{L} the dislocation line tension and M the dislocation climb mobility. σ_{i} is an internal stress that includes contributions from solid solution hardening and particle hardening. If the effective stress in Eq. (5.30) is inserted into (5.31), an expression for the creep rate is obtained that is valid for primary and stationary creep

$$\frac{d\varepsilon}{dt} = h\left(\sigma_{\text{y}}(T, \dot{\varepsilon}) + \frac{\sigma - \sigma_{\text{y}}(T, \dot{\varepsilon})}{1 - e^{-\Omega\varepsilon/2}} - \sigma_{\text{i}}, T\right) \tag{5.32}$$

Equation (5.32) is complicated but not impossible to integrate, since σ_{y} depends on the strain rate. This means that the equation has to be solved by iteration in each integration step. In addition, the primary stress in Eq. (5.30) is singular at small strains. However, it was demonstrated in Sect. 4.4.2 that these difficulties can be avoided. Equation (5.32) can be reformulated and the most suitable form is given in Eq. (4.25)

$$\dot{\varepsilon} = h\left(\frac{\sigma(\sigma_{\text{y}}(T) + K(T))}{\sigma_{\text{y}}(T) + K(T)(1 - \text{e}^{-\Omega\varepsilon/2})} - \sigma_{\text{i}}, T\right) \tag{5.33}$$

where $K(T)$ is given by

$$K(T) = \frac{\alpha G m_{\text{T}}^2}{\omega c_{\text{L}}} = \sigma_{\text{sat}}(T) - \sigma_{\text{y}}(T) \tag{5.34}$$

The saturation stress (maximum stress) σ_{sat} during plastic deformation at constant strain rate is the sum of $\sigma_y(T)$ and $K(T)$. In Eq. (5.33), the strain rate dependence of $\sigma_y(T)$ and $K(T)$ has been eliminated. These quantities are assumed to be influenced by the strain rate in the same way. This means that their values can in principle be selected at any strain rate.

Up to the creep range, the temperature dependence of σ_y and K are at least approximately known. The temperature dependence of the yield strength is proportional to that of the shear modulus, Eq. (3.15). The temperature dependence of the dynamic recovery constant ω is inversely proportional to that of the square of the shear modulus. However, in the creep range the increase in ω can be much faster with temperature. This is illustrated in Fig. 3.13. The role of Ω is that it describes how large the strain must be before the stationary or semi-stationary stage is reached. If the primary data are close to stationary conditions, the value of Ω can be assumed to be equal that of ω. However, if this is not the case, Ω is given by another expression, Eq. (4.33)

$$\Omega \approx \frac{3}{\varepsilon_{stat}} = \frac{3\alpha G m_T^2}{2c_L(\sigma - \sigma_i)} \tag{5.35}$$

To understand the behavior of Eq. (5.33) a simplified version is presented in Sect. 4.4.2. The strain dependence follows the ϕ model with a ϕ value of $n_N/(n_N + 1)$. Some requirements must be fulfilled. In particular, the following criterion must be satisfied, Eq. (4.30)

$$\frac{\sigma_y}{K} < \frac{\Omega\varepsilon}{2} \tag{5.36}$$

5.6 Creep at Low Stresses in an Austenitic Stainless Steel

In this section, creep of the austenitic stainless 17Cr12Ni2Mo steel 316H will be analyzed at low stresses. The creep data is taken from a paper of Kloc et al. [20] and the analysis from [32]. Very low stresses could be reached with the help of a helicoid spring specimen technique. Some of the experimental results are shown in Fig. 5.1.

The creep strain rate versus stress is given in Fig. 5.1. Two distinct regions of stress dependence are evident. At low stresses the stress exponent is about 1. At higher stresses, the stress exponent is 7, i.e. in the range for power-law creep. With a stress exponent of 1, it was initially thought that diffusional creep was observed. However, the presence of primary creep, see Fig. 5.1b suggests that dislocation creep is the controlling mechanism also at low stresses. In [20] similar creep tests were also performed for the 9Cr1Mo (P91) steel at 650 °C demonstrating a stress exponent of 1 at low stresses and a stress exponent of 12 at high stresses. For P91 stress change experiments were performed resulting in a stress exponent of 4.5 verifying dislocation

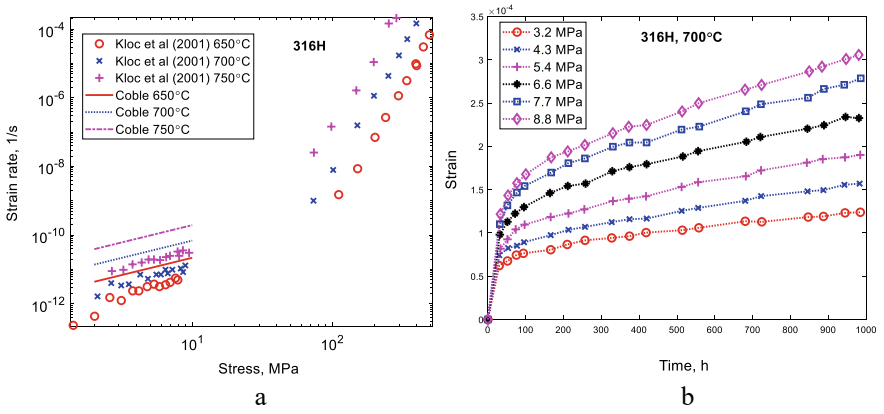

Fig. 5.1 Creep data for the austenitic stainless 17Cr12Ni2Mo steel 316H; **a** strain rate versus stress at 650–750 °C (exp.) and Coble creep model; **b** creep strain versus time at 700 °C for six stresses (creep data from [20]). Redrawn from [32] with permission of Elsevier

creep [21]. It can be expected that similar results would have been obtained for 316H if stress change experiments had been carried out. The creep rates at low stresses were assessed after testing for 1000 h. The natural interpretation of these results is that 1000 h is not long enough to reach stationary conditions. The consequences of this will be analyzed below.

In Fig. 5.1, predictions with the classical Coble model, Eq. (5.10) are included. It can be seen that the Coble model over predicts the observations by about one order of magnitude. The grain boundary diffusion coefficient from Smith and Gibbs has been used [33]. Their measurements are in the same temperature range as the creep data. However, the results are sensitive to the choice of diffusion coefficient. If the value from Mizouchi et al. [34] is chosen instead, the Coble predictions would be three orders of magnitude above the observations. Nabarro-Herring creep is not marked in the Figure but it gives values about an order of magnitude below the experimental data. Several papers in the literature address the problem that the diffusional models can overestimate the creep rate. A summary of early work is given by [25]. In these papers it is in general assumed that the required vacancies during diffusional creep are generated by the motion of GB dislocations. In some papers, a related concept of disconnections is considered, but the equations and effects are not very different from those of GB dislocations [35] and no distinctions between these concepts will be made here.

The main idea in these papers is that for Nabarro-Herring creep, GB dislocations are needed to emit and absorb vacancies at the GBs, since the GBs cannot be assumed to be perfect sources and sinks for vacancies. If the motion of GB dislocations is slowed down, it will impair the access of vacancies and reduce the creep rate. For Coble creep, the GB must be able to emit and absorb atoms and vacancies to avoid being over-saturated. This role of GB dislocations makes it easy to explain

deviations from the classical models. Mo in 316H gives a large solid solution hardening effect that reduces the creep rate dramatically. The influence of Mo has not yet been predicted but it can be assumed that it is of the same order as that of W, which raises the activation energy by about 50 kJ/mol [36]. This might seem like a high value but if the creep activation energy is assessed from the NIMS data [37], a value of 487 kJ/mol is obtained which should be compared with the activation energy for self-diffusion of 293 kJ/mol for 316H. Thus, the activation energy for creep is almost 200 kJ/mol higher than that for self-diffusion. The largest contribution to this increase comes from Mo. Therefore, a value of 50 kJ/mol for Mo that gives an Arrhenius factor of 0.002 at 700 °C is likely to underestimate its effect. The solid solution hardening effect can be assumed to be about the same for GB and bulk dislocations. As a consequence solid solution hardening alone can explain the deviation from the classical expression for Coble creep.

Particles can also influence the motion of dislocations in the grain boundaries. Arzt et al. suggest that a threshold stress σ_{th} is formed of about [25]

$$\sigma_{th} \approx 0.1\sigma_O \tag{5.37}$$

where σ_O is Orowan stress, Eq. (7.3). If typical values for $M_{23}C_6$ carbides are assumed with a volume fraction of 0.005 and particle radius of 0.1 mm, a σth value of 1.6 MPa is obtained. Such a threshold stress would certainly influence the prediction, but would not have a dramatic effect on the results. However, for other austenitic stainless steels the Orowan stress could be much higher. This could block diffusional creep completely if Eq. (5.37) describes the situation correctly and climb across particles is ignored. There are further constraints on grain boundary dislocations. But they are primarily of interest for pure metals. These constraints will be discussed in connection with creep of copper at low stresses in Sect. 5.8.

If the Coble creep rate taking these effects into account would still be higher than the dislocation creep rate, constrained GB creep would be active and adjust this situation, see Sect. 5.4.

From now on in this section, it will be assumed that the creep data in Fig. 5.1 are controlled by dislocation creep. Since primary creep data are available at 700 °C, the analysis will be concentrated to that temperature. First a model is needed for stationary creep. Strain induced vacancies are taken into account according to Eq. (2.37)

$$\frac{\Delta c}{c_0} = 0.5\frac{\sqrt{2}K_{sub}^2\dot{\varepsilon}b^2}{D_{self}}\frac{G}{\sigma} \tag{5.38}$$

K_{sub} provides a relation between the subgrain size and the stress, Eq. (8.4). The strain rate in Eq. (5.31) is used in Eq. (5.38). Austenitic stainless have typically a low stacking fault energy which is important to take into account with the help of Eq. (3.30). These assumptions are the same as in a model for pure Ni, Sect. 2.8 [38], which is expected to have similar properties. The effect of dislocation dipoles have been taken into account. It increases the climb mobility by a factor f_{dip}

$$f_{\text{dip}} = 1 + 2\rho d_{\text{dip}}^2 \tag{5.39}$$

where d_{dip} is the distance between the dislocations in a dipole which is set to 1×10^{-7} m. In Sect. 2.8, pipe-diffusion is taken into account instead, which gives an almost identical effect. This effect is of special importance at high stresses. This expression can be derived in the same way as Eq. (2.13). The constant term in Eq. (5.39) raises the stress exponent at higher stresses by 2. The solid solution hardening due to Mo is taken into account by adding 50 kJ/mol to the activation energy following the discussion above. In the model for the non-stationary behavior, Eq. (5.32), the value for $\sigma_y/K(T) = 0.02$ has been selected to satisfy the criterion (5.36). The Ω value in the exponent in Eq. (5.32) has been determined with the help of Eq. (5.35). Quite a high value of $\Omega = 800$ is obtained.

Predictions of the creep strain during primary creep with the help of Eq. (5.33) are given in Fig. 5.2.

As can be seen that a reasonable representation of the experimental data is obtained. The strain rate versus time is shown in Fig. 5.3a.

Fully straight lines are found in the double logarithmic diagram in Fig. 5.3a indicating that the phi-model is satisfied, see Sect. 3.2. The slope of the strain rate versus time curves is 0.8. The stress exponent is 1. The corresponding strain rate versus strain curves are presented in Fig. 5.3b. Approximately straight lines are obtained. However, the slope is considerably higher than for the time dependence varying from 2 to 4.5. The stress exponent is close to 7 so it is the same as for stationary creep.

Results for strain rates as a function of stress are given in Fig. 5.4.

The stationary model has a stress exponent of 7 at high stresses. At low stresses the non-stationary primary creep models gives a stress exponent of 1 in agreement

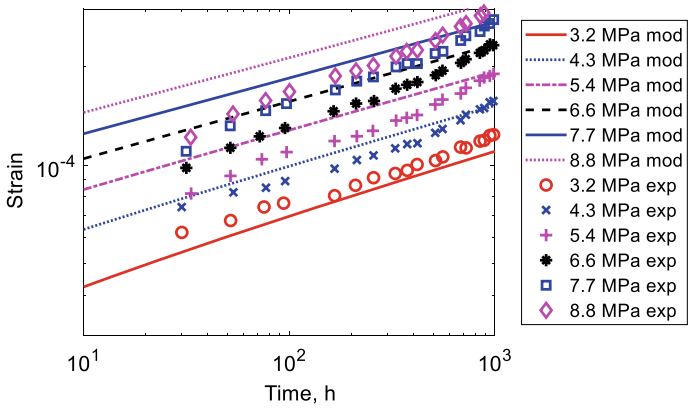

Fig. 5.2 Creep strain versus time at 700 °C for the austenitic stainless 17Cr12Ni2Mo steel 316H at low stresses during primary creep. Non-stationary model rates according to Eq. (5.33) compared to experimental data from [20]. Redrawn from [32] with permission of Elsevier

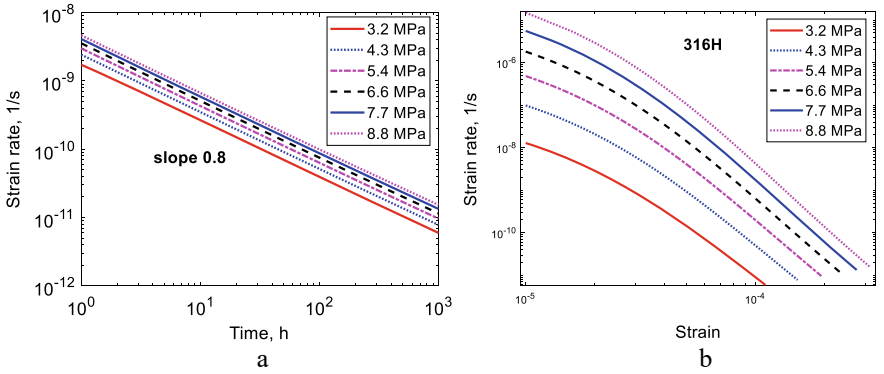

Fig. 5.3 Strain rate at 700 °C for the austenitic stainless 17Cr12Ni2Mo steel 316H at low stresses during primary creep. Non-stationary model rates according to Eq. (5.33); **a** strain rate versus time; **b** strain rate versus strain. **a** is redrawn from [32] with permission of Elsevier

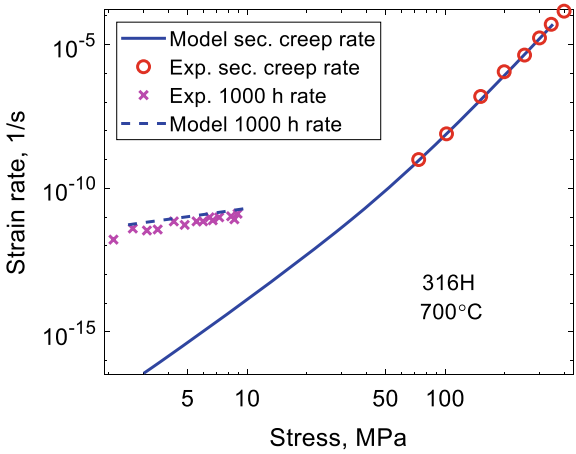

Fig. 5.4 Strain rate versus stress at 700 °C for the austenitic stainless 17Cr12Ni2Mo steel 316H with creep data from [20]. The full model line represents stationary creep rates and the dashed line non-stationary rates according to Eq. (5.33). Redrawn from [32] with permission of Elsevier

with observations. In Fig. 5.5 the time dependence of the strain rate versus stress curves is illustrated.

The strain rate decreases with increasing time in the primary stage. But even the longest time gives strain rates that are orders of magnitude above the stationary values, Fig. 5.4. At low stresses the activation energy in the model is 60 kJ/mol which is considerably less than the experimental value which is 140 kJ/mol. This value is almost the same as for grain boundary diffusion, which is 150 kJ/mol [34]. This is the expected value if Coble creep would have been the operating mechanism. The activation energy for stationary creep in the model is 340 kJ/mol, which is about 50 kJ/mol above the value for self-diffusion. The observed value is 420 kJ/mol. As discussed above that are good reasons to select a higher value than 50 kJ/mol for solid solution hardening, but due to lack of data this has not been done.

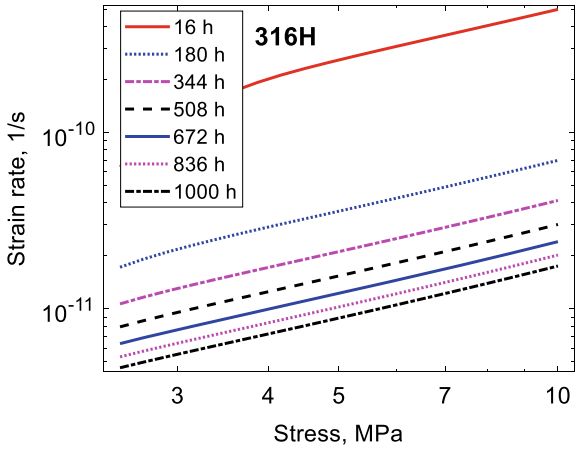

Fig. 5.5 Time dependence of the strain rate versus stress at 700 °C for the austenitic stainless 17Cr12Ni2Mo steel 316H at low stresses. Non-stationary model rates according to Eq. (5.33)

In summary, primary creep curves and their stress dependence of the creep rate can be described quite well with the model assuming dislocation creep. Thus, the model can explain the observations in a satisfactory way. It is clearly demonstrated that the stress exponent can be much lower during primary creep than during stationary creep. The activation energy is also lower during primary than during stationary creep although the model exaggerates the effect.

5.7 Creep in Aluminium at Very Low Stresses (Harper-Dorn Creep)

Creep at very low stresses and at very high temperatures in aluminum has received considerable interest in the scientific literature. The reason is that Harper and Dorn [14] looking for diffusional creep, in fact observed a stress exponent of 1 as expected but a creep rate that was about two orders of magnitude higher than the predicted one for diffusional creep. They drew the conclusion that they had observed dislocation creep with a stress exponent of 1. In two more recent papers available data have been summarized and analyzed [15, 19]. Kumar et al. [19] made also new tests for high purity aluminum to reduce the effect of non-stationary conditions. They could give a satisfactory explanation to most of the existing data. They found a creep exponent of 3 clearly indicating dislocation creep. The Harper and Dorn data also give this stress exponent when a threshold stress that they introduced was removed. Any indication of a threshold stress has not been found in more recent data.

In this section both stationary and non-stationary modeling will be presented taken from [32]. It has always been assumed that the controlling mechanism is dislocation creep. For stationary creep, the same model for aluminum as in Chap. 2 has been used, Eq. (5.31). The classical value for the self-diffusion coefficient with an activation energy of 142 kJ/mol has been applied. In the non-stationary model, Eq. (5.33), the

choice $\Omega = 40$ is taken directly from the formulae in Chap. 3. To satisfy the criterion (5.36) a value of $\sigma_y/K = 0.01$ has been chosen.

The results for the stress dependence of strain rate are given in Fig. 5.6.

The stationary creep model with a stress exponent of 3 can describe the bulk of creep of data. The only data that deviate significantly from the stationary curve are those of Barrett et al. [16]. They used testing times of 300–1000 h. In the other investigations longer testing times were utilized, which makes the results lying closer to the stationary values. It is evident that the modest deviations from the stationary curve can be well represented by the non-stationary model. How the results are approaching stationary conditions is illustrated in Fig. 5.7.

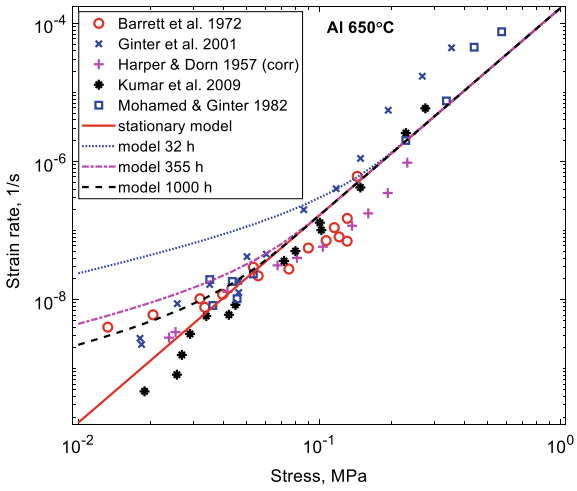

Fig. 5.6 Strain rate versus stress at 650 °C for pure aluminum. The full model line represents stationary creep rates and the dashed line non-stationary rates at three times according to Eq. (5.33). The five sources of the experimental data can be found in [19]. Redrawn from [32] with permission of Elsevier

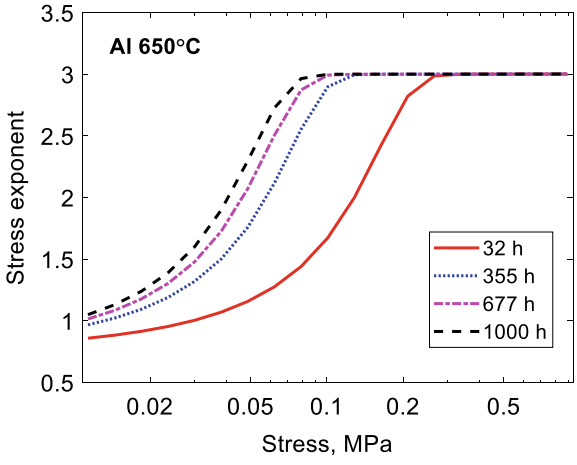

Fig. 5.7 Stress exponent versus stress at 650 °C for pure aluminum during non-stationary conditions at four times according to Eq. (5.33). Redrawn from [32] with permission of Elsevier

It can be seen from Fig. 5.7 that the values are close to stationary conditions. For stresses larger than 0.3, stationary creep has been reached even for the shortest time and the stress exponent is 3. Only for stresses below 0.03 MPa, stress exponents below 1.5 are found. The stress exponent clearly increases with increasing observation time.

Creep strain versus time curves are shown in Fig. 5.8.

The linear behaviour except at the highest stress is consistent with the phi-model. The variation of the strain rate with time and strain is demonstrated in Fig. 5.9.

The approximate straight lines again show that the phi-model is obeyed. The exception is the higher stresses where stationary conditions are reached at longer times or larger strains. This is the same behavior that is observed in Fig. 5.7.

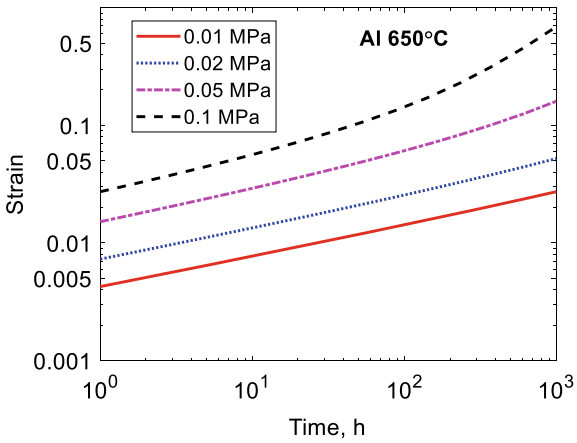

Fig. 5.8 Creep strain versus time at 650 °C for pure aluminum at different stresses according to Eq. (5.33)

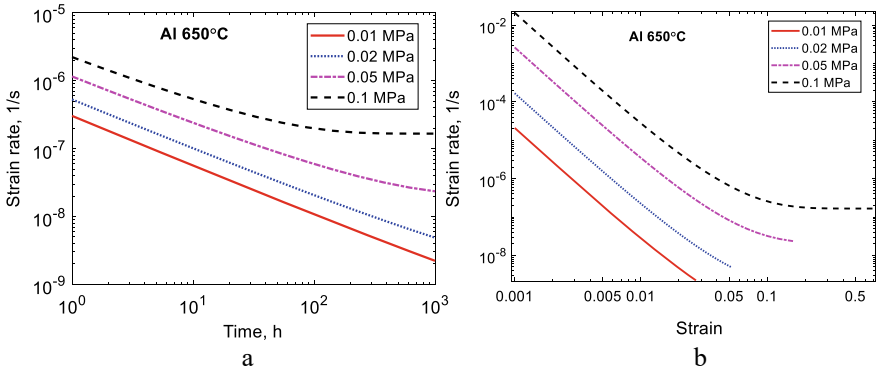

Fig. 5.9 Creep strain versus time **a** and versus strain **b** at 650 °C for pure aluminum at four stresses according to Eq. (5.33). **a** is redrawn from [32] with permission of Elsevier

These results above suggest that the high temperature creep of aluminum can be fully explained quantitatively based on ordinary dislocation creep. There is no need to refer to any special Harper-Dorn creep.

From Fig. 5.6 it can be seen that the basic creep model in Eq. (5.31) can describe the stationary creep rate quite accurately at least down to 0.02 MPa at 650 °C. The same model can represent creep data at 27 °C up to 50 MPa [39]. If the stress is raised from 0.02 to 50 MPa at 27 °C, the creep rate is increased by 21 orders of magnitude, see Table 5.1. The corresponding increase at 650 °C is 13 orders of magnitude. In the same way if the temperature is raised from 27 to 650 °C at 0.02 MPa, the creep rate is enhanced 17 orders of magnitude. At 50 MPa the increase is 9 orders of magnitude. Thus, Eq. (5.31) can cope with very large variation in the strain rate over a range of conditions. This is clearly strong justification for the validity of the creep model.

More recently, annealing experiments have been performed for aluminum single crystals by Smith et al. [40]. Even after long annealing times the dislocation density never fell below 1×10^9 1/m^2. With the help of the Orowan equation for the deformation, they suggest that this would give a stress exponent of 1, recovering Harper-Dorn creep. A constant dislocation density would imply that recovery of dislocations would be blocked. But if recovery is blocked, creep is not possible. Without recovery there would be a continuous increase in the dislocation density until the deformation stops as observed for many alloys at ambient temperatures. In addition, several other studies (some of which are summarized in [40]) have observed that the dislocation density varies with stress and that the dislocation density can be much below 1×10^9 1/m^2, see for example [19]. Furthermore, creep of aluminum can quantitatively be described from ambient temperatures, Sect. 2.7 to close to the melting temperature, see above, with the help of the creep-recovery theory. The observations in [40] cannot be explained at present.

Table 5.1 Creep rate ratios of aluminum

Temperature, °C	Stress, MPa	Creep rate ratio, stress	Creep rate ratio, temperature
27	0.02 → 50	2×10^{21}	
650	0.02 → 50	6×10^{13}	
27–>650	0.02		1×10^{17}
27–>650	50		4×10^9

5.8 Creep in Copper at Low Stresses

5.8.1 Creep of Cu-OFP at 600 °C

Creep tests of copper at very low stresses at 600 °C were performed at the author's laboratory many years ago but the results have only been published recently [41]. The material used was oxygen free copper alloyed with 54 wt. ppm P, Cu-OFP. The material had good purity. All other elements than Cu and P had a total amount of 30 wt. ppm. The batch had the designation 500. The detailed composition of the batch can be found in [42]. The grain size of the material was 100 μm. Three tests were carried out at 1, 1.5 and 2 MPa. The testing times were between 12000 and 17000 h. The conditions were selected to be well inside the stress range for diffusional creep. Results for the stress dependence of the strain rate are shown in Fig. 5.10.

The experimental data give a stress exponent of 3. A comparison to the model for stationary creep for Cu-OFP, Eq. (5.31) is given. It is evident that the model gives strain rate values that are quite close but with a slightly higher stress exponent of 4. For pure Cu without P the creep rate according to the stationary model is almost an order of magnitude higher and the stress exponent is 3.

In the primary creep model, Eq. (5.33), Ω has been selected according Eq. (5.35). For σ_y and K the room temperature values in [42] have been used. These values for σ_y and K satisfy the criterion (5.36). In Fig. 5.11, the strain rate versus time is illustrated for the test at 1.5 MPa.

Distinct primary creep is observed. Both the experiments and the predictions follow the phi-model. Thus, there are three ways that demonstrate that dislocation creep is involved; (i) a stress exponent of 3; (ii) the results are in agreement with the predictions for stationary dislocation creep; (iii) well-developed primary creep is present.

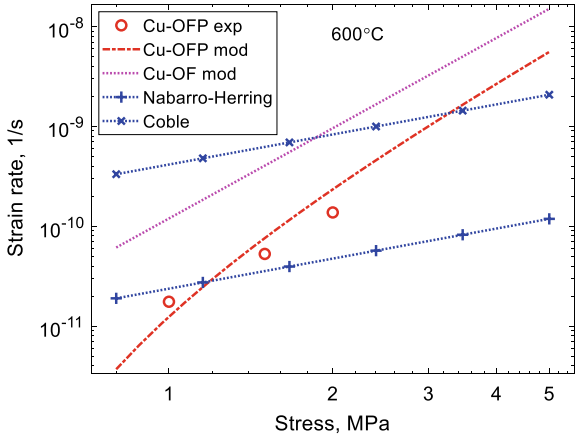

Fig. 5.10 Creep rate versus stress at 600 °C for Cu-OFP. Model values for stationary creep for Cu-OFP and for pure Cu without P (Cu-OF). Model results for diffusional creep are also included

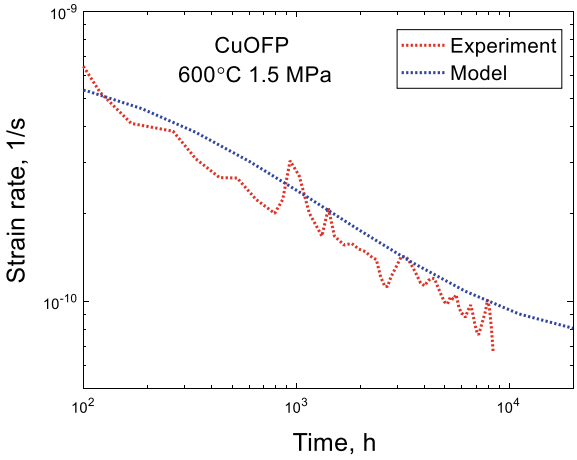

Fig. 5.11 Creep rate versus time at 600 °C and 1.5 MPa for Cu-OFP. Model values according to (5.33)

The basic stationary creep can describe creep rate values down to 1 MPa at 600 °C, Fig. 5.10. The model can also represent creep data at 75 °C up to 180 MPa, Fig. 6.6. This involves a large variation in the creep rate. Raising the stress from 1 to 180 MPa increases the creep rate by 21 orders of magnitude according to Eq. (5.31), Table 5.2. The corresponding increase at 600 °C is 13 orders of magnitude. There is also an increase due to change in temperature, which is 15 order of magnitude at 1 MPa and 9 orders of magnitude at 180 MPa.

These wide ranges of creep rate are of the same order as those for aluminum, Table 5.1. Which of the ratios in Tables 5.1 or 5.2 that is chosen is not important. The high ratios demonstrate that the basic creep model can cope with a wide range of conditions. Since the model was originally developed for creep close to ambient temperature at high stresses [31], the applicability at high temperatures and low stresses can be seen as a possibility to extrapolate over many order of magnitude in creep rate. It is clearly a strong justification for the validity of the basic creep model.

In Fig. 5.10, the classical models for diffusional creep are compared with the observations. It is evident that the model for Coble creep significantly overestimates the creep rate and that applies to Nabarro-Herring creep as well but to a less extent. Consequently, there must be one or more mechanisms that strongly block the diffusional processes. Such a diffusion mechanism is not easy to identify. P is known to raise the diffusion coefficients in both the bulk and in the grain boundaries [43], so

Table 5.2 Creep rate ratios of copper

Temperature, °C	Stress, MPa	Creep rate ratio, stress	Creep rate ratio, temperature
75	$1 \rightarrow 180$	4×10^{21}	
600	$1 \rightarrow 180$	2×10^{13}	
$75 \rightarrow 600$	1		6×10^{15}
$75 \rightarrow 600$	180		2×10^{9}

that effect works in the wrong way. Zhevnenko shows that surface active elements like P reduces the diffusional creep rate, but fairly large amounts of alloying elements are needed to give a significant effect [44]. Solid solution hardening due to P gives a back stress of 0.4 MPa at 600 °C [45]. This is the main reason why the stationary curve for Cu-OFP in Fig. 5.10 is lower than that for pure Cu. If dislocations control the amount of vacancies that escapes the grain boundaries, the solid solution hardening would be expected to be the same in the bulk and the grain boundaries. This effect is represented by the difference in the stationary creep rate between Cu with and without P. Thus, this would explain a part of the blocking of diffusional creep. P is fully in solid solution so there is no effect of particles. It has been suggested that if the curvature of the dislocation is too small, the grain boundary dislocations become immobile. This gives a back stress of [25, 46]

$$\sigma_{\text{curv}} = \frac{\tau_{\text{L}}}{bd_{\text{grain}}} \tag{5.40}$$

where τ_{L} is the dislocation line tension. For the case in Fig. 5.10, σ_{curv} is equal to 0.05 MPa, which is negligible. The remaining discrepancy for Coble creep is possibly due to constrained grain boundary creep, Sect. 5.4.

5.8.2 *Creep of Copper at 820 °C*

In one of the first attempts to measure diffusional creep, Burton and Greenwood studied pure copper at 820 °C [22]. Some of their results for a grain size of 35 μm are shown in Fig. 5.12.

Below 5 MPa their data gave a stress exponent close to 1. Above 5 MPa, the stress exponent is 5. The values for the classical Coble and Nabarro-Herring models

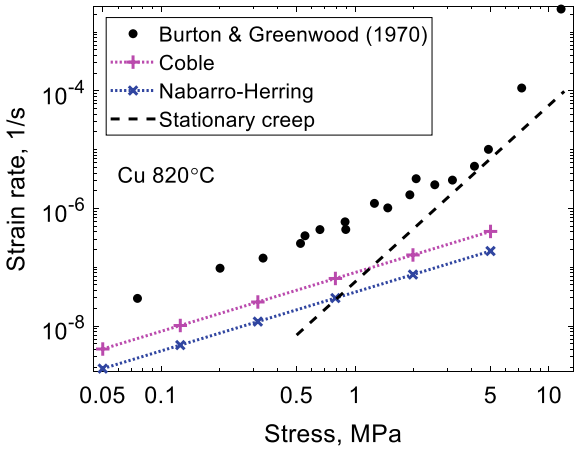

Fig. 5.12 Creep rate versus stress at 820 °C for Cu. Experimental data from [22]. Coble and Nabarro-Herring creep according to Eq. (5.10), stationary creep model according to (5.31). Redrawn from [41] with permission of Elsevier

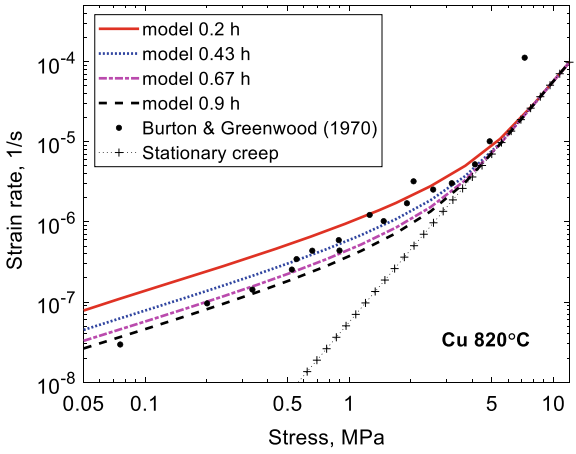

Fig. 5.13 Creep rate versus stress at 820 °C for Cu. Experimental data from [22]. Stationary and non-stationary creep models according to (5.31) and (5.33). Redrawn from [41] with permission of Elsevier

are quite close to the experimental data at low stresses. Burton and Greenwood suggested that the low stress behavior was controlled by Nabarro-Herring creep but with the diffusion coefficients that are available today, the Coble creep values are even closer. With a stress exponent of 5 at stresses above 5 MPa, dislocation creep must be controlling. It is interesting to note that the stationary creep model in Eq. (5.31) matches the position of the change in stress exponent quite well, but the stress exponent in the stationary model is 3.

It will now be analyzed whether non-stationary conditions could have been of importance in this study [41]. Detailed analysis shows that transition to the semi-stationary stage occurs later than given by Eq. (5.35) so the Ω value has been reduced by a factor of 2 to satisfy these findings in the non-stationary model (5.33). For σ_y/K a value of 0.01 has been chosen to ensure that the criterion (5.36) is fulfilled. In [22] very short testing times were used of about 0.4 h. The results for stress dependence of the creep rate are given in Fig. 5.13.

Results for testing times between 0.2 and 0.9 h are shown. The non-stationary values fall in the same range as the experimental data. The variation of the stress exponent is presented in Fig. 5.14.

Below 1 MPa, the stress exponent is close to unity. From 1 to 5 MPa the stress exponent increases to the stationary value of 3. The strain variation with time is reproduced in Fig. 5.15a.

The creep curves are consistent with the observation in [22], see [41]. For example, a strain of 0.002 is reached after 0.5 h for a stress of 1 MPa. In Fig. 5.15b the time dependence of the strain rate is given. It is evident that stationary conditions are reached at the two highest stresses at "longer" times.

It is clear that the data in Fig. 5.12 can be explained either with diffusional creep or with non-stationary dislocation creep. One argument against diffusional creep is the short testing times that would give non-stationary effects. Another argument is that the purity of the investigated alloy is modest with a total impurity content of 167 wt. ppm. This should be compared with the copper in Sect. 5.8.1, where

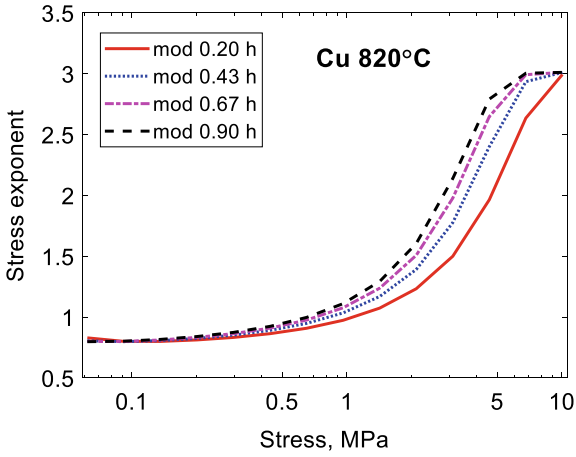

Fig. 5.14 Stress exponent versus stress at 820 °C in Cu at four testing times. Non-stationary creep models according to Eq. (5.33). Redrawn from [41] with permission of Elsevier

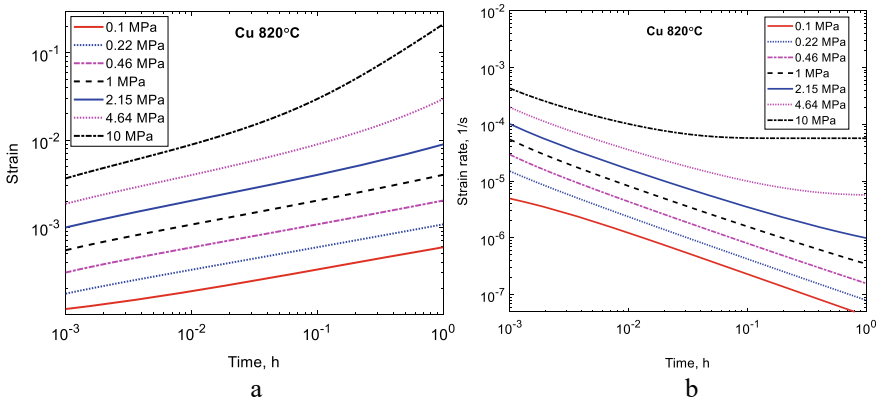

Fig. 5.15 Strain **a** and strain rate **b** versus time at 820 °C in Cu at seven stresses. Non-stationary creep model according to (5.33)

the impurity content was 30 wt. ppm and the P content 54 wt. ppm. Why would diffusional creep be blocked by element additions in the latter but not in the former case? The paper [22] has been criticized in the literature, for example, for being performed in a temperature range where the microstructure is not stable [4, 12]. This might not be important due to the short testing times. However, there are arguments in [22] in favor of diffusional creep. For example, the correct grain size dependence if Nabarro-Herring creep is controlling (which however is not the case if Coble creep is controlling). It is not possible to decide which creep mechanisms that is the correct one and it is not the aim of this book to try to make that decision. Instead, the main message is that dislocation creep often occurs in parallel and in competition with diffusional creep.

5.8.3 Creep of Copper at 480 °C

McKnee et al. have made creep tests of copper at low stresses [9]. Most tests were performed at 480 ºC probably for the same material used by Burton and Greenwood but with a grain size of 55 μm. These results are compared with the non-stationary model, Eq. (5.33). The parameter values are taken directly from the basic model ($\sigma_y = 0.01$ MPa, $K(T) = 69$ MPa, $\Omega = 32$). The results in [9] are compared to the model in Fig. 5.16.

Below 3 MPa the results by McKnee et al. give a stress exponent of 1 and above 3 MPa a stress exponent of 2. They attribute this change of stress exponent to a transition from diffusional creep to dislocation creep. A comparison to stationary creep is provided in Fig. 5.17.

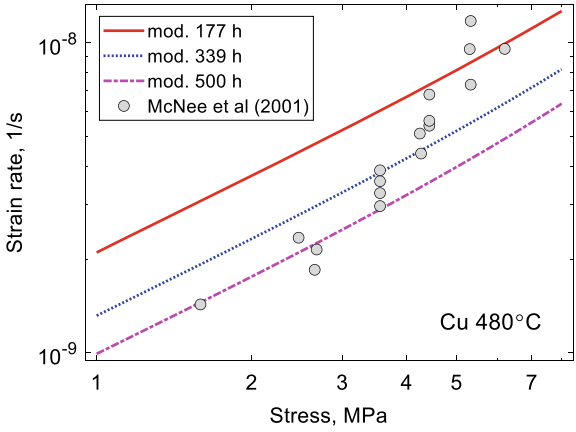

Fig. 5.16 Creep rate versus stress at 480 °C for Cu. Experimental data from [9]. Non-stationary creep model according to Eq. (5.33)

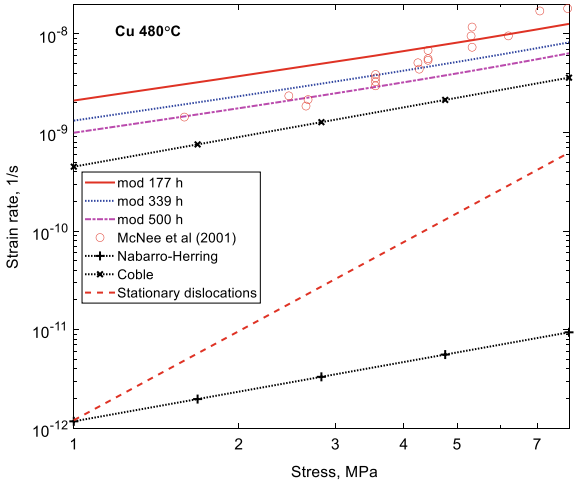

Fig. 5.17 Creep rate versus stress at 480 °C for Cu. Experimental data from [9]. Stationary and non-stationary creep models according to Eqs. (5.31) and (5.33). Classical diffusional creep models are given, Eq. (5.10)

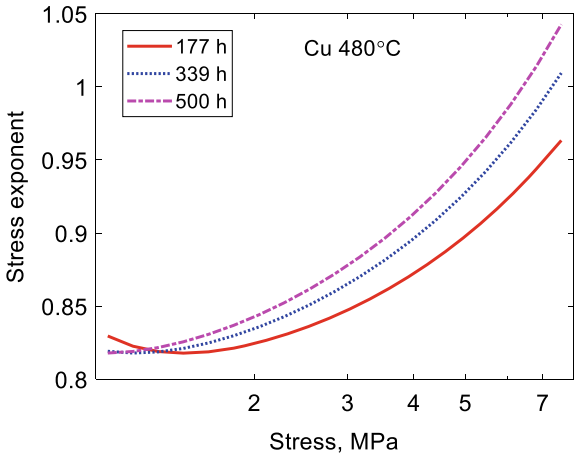

Fig. 5.18 Stress exponent for the creep rate versus stress at 480 °C for Cu for three testing times. Non-stationary creep model according to Eq. (5.33)

Results for stationary creep according to Eq. (5.31) are 1.5 orders of magnitude or more below the results in [9]. Considering the precision of the prediction of stationary creep in Fig. 5.10, the results in [9] must represent non-stationary creep. The non-stationary model, Eq. (5.33), generates values that are in agreement with the observations in [9] considering the length of testing times that were used in that investigation. The stress exponent in the non-stationary model is illustrated in Fig. 5.18.

The stress exponent in the range of data of [9] is about 1. There is a slight increase with stress but it is not enough to explain the observed increase to 2. The stationary creep values are simply too far below the observation to give such an increase. The Coble results in Fig. 5.17 are close to both the values in [9] and the non-stationary results. The activation energy predicted from the non-stationary model, Eq. (5.33) is shown in Fig. 5.19.

In the model, lattice diffusion with an activation energy of 198 kJ/mol from [47] is used. In spite of this, the non-stationary model gives a value of about 70 kJ/mol at 480 °C. Via step change tests, McKnee et al. found a creep activation energy of 99 ± 5 kJ/mol. Both these values are close to the accepted value for grain boundary diffusion of 84.5 kJ/mol [48] which is the relevant value for Coble creep. It can be seen that the mechanical data in [9] can be explained at least partially with the help of non-stationary dislocation creep.

5.9 Summary

- One issue when performing creep tests at low stresses is to ensure that stationary conditions have been reached. At normal stresses when tests run to failure the minimum creep rate usually gives a good estimate of the stationary rate. However, creep tests at low stresses when the stress exponent is close to unity practically

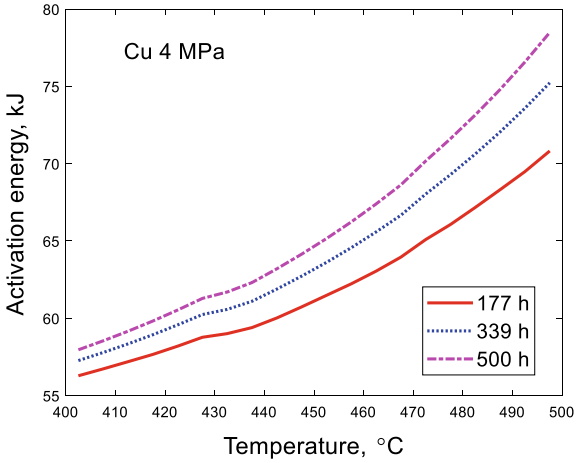

Fig. 5.19 Activation energy for the creep rate versus temperature for Cu at three testing times. Non-stationary creep model according to Eq. (5.33)

never are taken to failure. Often this is simply not possible because the estimated rupture time could be 10 years or more.

- Stationary creep rates have traditionally been the basis of identifying operating mechanisms, for example for distinguishing between diffusional creep, power-law dislocation creep and power-law break-down. For a long time only empirical dislocation creep models were available but this identification could still be made as long as stationary conditions could be ascertained. However, at low stresses it must in general be assumed that a stationary state has not been reached during the testing. It is then essential to use non-stationary models.
- In recent years basic dislocation creep models that can cope also with the primary stage have been formulated. These models are at least partially predictable and that is essential to analyze the data. During the primary stage the creep rate drops quickly. Where in the primary stage the test is stopped must be determined.
- Traditionally it has been assumed that a stress exponent close to 1 should imply that diffusional creep is active. The classical models for diffusional creep are simple and well established. They give well-defined stress, temperature and grain size dependence. In spite of this it has been difficult to obtain agreement with the models in many cases. In several classical studies for pure metals, the diffusional models overestimate the creep rate by two orders of magnitude. Since quite accurate diffusion coefficients are available, the deviations cannot be accounted for by lack of precision. Two alternatives then remain. Either the observations are non-stationary dislocation creep or non-stationary diffusional creep.
- Experimental results for an austenitic stainless at 700 °C gave a stress exponent of 1, but the presence of primary creep and a stress exponent of 4.5 in related stress change tests clearly demonstrated that dislocation creep was the operating mechanism. The same results were found for Cu at 600 °C since the observed stress exponent was 3 and distinct primary creep was observed. In spite of these quite clear verifications that dislocation creep was the controlling mechanism,

the classical Coble creep model predicted creep rates one order of magnitude higher than the observed ones. Consequently, Coble creep must be blocked by one or more mechanisms. If Coble creep is controlled solely by diffusion in the grain boundaries, this is virtually impossible to account for. Several authors have proposed that the motion of vacancies is controlled by grain boundary dislocations. If this assumption is correct, and the amount of solid solution hardening is the same for GB and bulk dislocations, the observations are at least partially possible to explain although very large blocking effects would be required since the mobility of the grain boundary dislocations is very high. The more likely explanation is due to constrained grain boundary creep. see next bullet [41].

- Any creep mechanism that is located in the grain boundaries is proposed to be accompanied by bulk deformation. Such mechanisms are superplasticity due to grain boundary sliding, grain boundary dislocation creep and Coble creep. Thus, the bulk creep rate must be at least of the same magnitude as the creep in the grain boundaries to accommodate local strain changes. This is referred to as *constrained grain boundary creep.* This has important implications. The Coble creep rate can never exceed the bulk creep rate by a significant margin. In addition, since the Coble creep rate must be adapted to the bulk rate, it will show primary creep.
- A primary creep model has been used to describe dislocation creep with low creep exponents. The model has been applied successfully to an austenitic stainless steel, to pure Al and to pure Cu. It is shown that dislocation creep can be active in stress and temperature ranges that traditionally have been attributed only to diffusional creep. The low stress exponents observed is a result of stationary conditions not being reached. It is demonstrated that if non-stationary conditions are assessed the apparent activation energy can be much lower than the lattice diffusion activation energy used in the model.
- Creep at very high temperature and low stresses for pure Al has in the past been considered as a special case with the designation Harper-Dorn after the researchers that first proposed it. For the first time a basic model has been used to describe data from a number of investigations for this type of creep. The model successfully shows that the bulk of data can be represented by a stationary model giving a stress exponent of 3 in agreement with observations. The data that deviate from this behavior can be handled with the non-stationary model. In agreement with results in the literature, there is no longer any need to consider this phenomenon as something special, since the dislocation creep model can describe these results in a similar way as for other alloys.
- It has been demonstrated that the basic models for primary and secondary creep can accurately describe experimental data at high temperatures and low stresses. For secondary creep the model parameters are identical to the ones used at lower temperature. Thus, for aluminum the application of the basic creep model has been verified from 50 MPa at room temperature to 0.02 MPa at 650 °C. For copper the corresponding range is from 180 MPa at 75 °C to at least 1 MPa at 600 °C. For both the stress and temperature ranges, they represent a variation of in the creep rate over many orders of magnitude. For copper primary creep is accurately represented in the same range also without any change of parameter

values. These facts clearly show that the basic creep model can handle a wide range of experimental conditions. Primary creep of aluminum has not been investigated at ambient temperatures.

References

1. C. Herring, Diffusional viscosity of a polycrystalline solid. J. Appl. Phys. **21**, 437–445 (1950)
2. R.L. Coble, A model for boundary diffusion controlled creep in polycrystalline materials. J. Appl. Phys. **34**, 1679–1682 (1963)
3. M.E. Kassner, *Fundamentals of Creep in Metals and Alloys* (Butterworth-Heinemann, 2015)
4. O.A. Ruano, J. Wadsworth, J. Wolfenstine, O.D. Sherby, Evidence for Nabarro-Herring creep in metals: fiction or reality? Mater. Sci. Eng. A **165**, 133–141 (1993)
5. T. Sritharan, H. Jones, The creep of Beta-Cobalt at low stresses. Acta Metall. **27**, 1293–1300 (1979)
6. D.J. Towle, H. Jones, The creep of alpha-iron at low stresses. Acta Metall. **24**, 399–407 (1976)
7. T.G. Langdon, A method of distinguishing between diffusion creep and Harper-Dorn creep at low stress levels. Scripta Mater. **35**, 733–737 (1996)
8. R.L. Squires, R.T. Weiner, M. Phillips, Grain-boundary denuded zones in a magnesium-12 wt % zirconium alloy. J. Nucl. Mater. **8**, 77–80 (1963)
9. K.R. McNee, G.W. Greenwood, H. Jones, Microstructural evidence for diffusional creep in copper using atomic force microscopy. Scripta Mater. **44**, 351–357 (2001)
10. K.R. McNee, G.W. Greenwood, H. Jones, Observation and interpretation of some microstructural features of low stress creep. Scripta Mater. **47**, 619–623 (2002)
11. K.R. McNee, G.W. Greenwood, H. Jones, The effect of stress orientation on the formation of precipitate free zones during low stress creep. Scripta Mater. **46**, 437–439 (2002)
12. O.A. Ruano, O.D. Sherby, J. Wadsworth, J. Wolfenstine, Rebuttal to "In defense of diffusional creep." Mater. Sci. Eng. A **211**, 66–71 (1996)
13. J. Wadsworth, O.A. Ruano, O.D. Sherby, Denuded zones, diffusional creep, and grain boundary sliding. Metall. Mater. Trans. A **33**, 219–229 (2002)
14. J. Harper, J.E. Dorn, Viscous creep of aluminum near its melting temperature. Acta Metall. **5**, 654–665 (1957)
15. M.E. Kassner, P. Kumar, W. Blum, Harper-Dorn creep. Int. J. Plast **23**, 980–1000 (2007)
16. C.R. Barrett, E.C. Muehleisen, W.D. Nix, High temperature-low stress creep of Al and Al+0.5%Fe. Mater. Sci. Eng. **10**, 33–42 (1972)
17. F.A. Mohamed, T.J. Ginter, On the nature and origin of Harper-Dorn creep. Acta Metall. **30**, 1869–1881 (1982)
18. W. Blum, P. Eisenlohr, F. Breutinger, Understanding creep—A review. Metall. Mater. Trans. A **33**, 291–303 (2002)
19. P. Kumar, M.E. Kassner, W. Blum, P. Eisenlohr, T.G. Langdon, New observations on high-temperature creep at very low stresses. Mater. Sci. Eng. A **510–511**, 20–24 (2009)
20. L. Kloc, V. Sklenička, J. Ventruba, Comparison of low stress creep properties of ferritic and austenitic creep resistant steels. Mater. Sci. Eng. A **319–321**, 774–778 (2001)
21. L. Kloc, V. Sklenička, Confirmation of low stress creep regime in 9% chromium steel by stress change creep experiments. Mater. Sci. Eng. A **387–389**, 633–638 (2004)
22. B. Burton, G.W. Greenwood, The contribution of grain-boundary diffusion to creep at low stresses. Metal Sci. J. **4**, 215–218 (1970)
23. M.F. Ashby, R.A. Verrall, Diffusion-accommodated flow and superplasticity. Acta Metall. **21**, 149–163 (1973)
24. G.W. Greenwood, A formulation for anisotropy in diffusional creep, Proc. Roy. Soc. A **A436**, 187–196 (1992)

25. E. Arzt, M.F. Ashby, R.A. Verrall, Interface controlled diffusional creep. Acta Metall. **31**, 1977–1989 (1983)
26. M.F. Ashby, On interface-reaction control of Nabarro-Herring creep and sintering. Scr. Metall. **3**, 837–842 (1969)
27. D. Francke, W. Pantleon, P. Klimanek, Modelling the occurrence of disorientations in dislocation structures. Comp. Mater. Sci. **5**, 111–125 (1996)
28. P. Ambrosi, C. Schwink, Slip line length of copper single crystals oriented along [100] and [111]. Scr. Metall. **12**, 303–308 (1978)
29. L.C. Lim, On the elastic properties of grain boundary dislocations. Acta Metall. **35**, 163–169 (1987)
30. A.H. Chokshi, Unusual stress and grain size dependence for creep in nanocrystalline materials. Scripta Mater. **61**, 96–99 (2009)
31. R. Sandstrom, Basic model for primary and secondary creep in copper. Acta Mater. **60**, 314–322 (2012)
32. R. Sandström, Creep at low stresses in aluminium (Harper-Dorn) and in an austenitic stainless steel with a stress exponent of 1. Mater. Today Commun. **36**, 106556 (2023)
33. A.F. Smith, G.B. Gibbs, The volume and grain-boundary diffusion of iron in 20 Cr/25 Ni/Nb stainless steel. Metal Sci. J. **2**, 47–50 (1968)
34. M. Mizouchi, Y. Yamazaki, Y. Iijima, K. Arioka, Low temperature grain boundary diffusion of chromium in SUS316 and 316L stainless steels. Mater. Trans. **45**, 2945–2950 (2004)
35. F. Delannay, Contribution of the nucleation and recovery of disconnections to shear viscosity in diffusional creep. Materialia **20** (2021)
36. P.A. Korzhavyi, R. Sandström, First-principles evaluation of the effect of alloying elements on the lattice parameter of a 23Cr25NiWCuCo austenitic stainless steel to model solid solution hardening contribution to the creep strength. Mater. Sci. Eng. A **626**, 213–219 (2015)
37. Data Sheet on the Elevated-Temperature Properties of 18Cr–8Ni–Mo Stainless Steel Tubes for Boiler and Heat Exchangers (SUS 316H TB), National Research Institute for Metals Tokyo, Japan, Report No. 6B (2000)
38. R. Sandström, J. Zhang, Modeling the creep of nickel. J. Eng. Mater. Technol. **143**(4), 041011–1 (2021)
39. S. Spigarelli, R. Sandström, Basic creep modelling of aluminium. Mater. Sci. Eng. A **711**, 343–349 (2018)
40. K.K. Smith, M.E. Kassner, P. Kumar, Long-term annealing of high purity aluminum single crystals: new insights into Harper-Dorn creep. Mater. Sci. Eng. A **705**, 1–5 (2017)
41. R. Sandström, Primary creep at low stresses in copper. Mater. Sci. Eng.: A **873**, 144950 (2023)
42. R. Sandstrom, Extrapolation of creep strain data for pure copper. J. Test. Eval. **27**, 31–35 (1999)
43. R. Sandström, R. Wu, J. Hagström, Grain boundary sliding in copper and its relation to cavity formation during creep. Mater. Sci. Eng. A **651**, 259–268 (2016)
44. S.N. Zhevnenko, Effect of surface-active metallic impurities on diffusion creep of polycrystalline copper. Mater. Lett. **282** (2021)
45. R. Sandstrom, H.C.M. Andersson, The effect of phosphorus on creep in copper. J. Nucl. Mater. **372**, 66–75 (2008)
46. B. Burton, Grain boundary dislocation geometry during diffusional creep. Mater. Sci. Technol. (United Kingdom) **2**, 1202–1204 (1986)
47. G. Neumann, V. Tölle, C. Tuijn, Monovacancies and divacancies in copper Reanalysis of experimental data. Phys. B **271**, 21–27 (1999)
48. T. Surholt, C. Herzig, Grain boundary self-diffusion in Cu polycrystals of different purity. Acta Mater. **45**, 3817–3823 (1997)

Chapter 6
Solid Solution Hardening

Abstract The size and modulus misfit between solute and parent atoms gives rise to strengthening, solid solution hardening (SSH). With the development of Argon's expression for the interaction energies for solute atoms and dislocations for size and modulus misfit, both effects can now be modeled without the introduction of adjustable or arbitrary parameters. These expressions are used to derive models for SSH during creep. Although the constants for the modulus misfit can be an order larger than those for size misfit, the latter effect is still dominating. The interaction energy gives a direct contribution to the activation energy for creep. The solutes form Cottrell atmospheres around the dislocations. For slowly diffusion elements, these atmospheres give rise to a drag force that slows down the motion of the dislocations. Fast diffusing elements have to break away from the dislocations to enable their motion. This creates a break stress that is the source of SSH in this case.

6.1 General

Elements in solid solution are used in many alloy systems to increase the strength and that is referred to as solid solution hardening (SSH). When the size of the solute atoms is different from that of the parent metal atoms, it makes it more difficult for the dislocations to propagate and that raises the strength. SSH is in fact one of the major ways to increase the strength of creep resistant alloys.

The size misfit is not the only way that solute atoms can affect the strength. If the shear modulus of the solutes is different from that of the parent metal, it is also of importance for SSH. This will be analyzed in the present chapter. This effect is less easy to understand intuitively than that of the size misfit. The most direct way to recognize the significance of this effect is to consider that the expression for interaction energy between a solute and a dislocation is proportional to the shear modulus. Any change in the value of shear modulus would affect the size of the interaction energy. There are a number of other mechanisms that can influence SSH. Examples are the presence of stacking faults, short range order of solutes (solutes are not fully randomly distributed), and the solutes from more or less complex defects.

R. Sandström, *Basic Modeling and Theory of Creep of Metallic Materials*, Springer Series in Materials Science 339,
https://doi.org/10.1007/978-3-031-49507-6_6

These cases will not be covered here. When the solutes agglomerate in particles, it is considered outside SSH and will be discussed in Chap. 7 on precipitation hardening.

SSH at ambient temperatures and at lower temperatures have been covered extensively in the literature. There are excellent reviews on SSH on this topic. The texts by Haasen [1], Suzuki et al. [2] and Argon [3] can be mentioned. At elevated temperatures and particularly for creep the number of publications is much more limited. Primarily solid solution hardened aluminum alloys have been studied. We will cover this literature below.

At low temperatures, SSH is assessed as the force that the solutes give on the dislocations. This is in principle the force acting on the dislocation at 0 K. In several papers, semi-empirical temperature dependencies have been introduced (summarized in [1, 3]) to find values at ambient temperatures. In some of the models for binary alloys, SSH is proportional to $c^{1/2}$ in some models, and to $c^{2/3}$ in others, where c is the concentration of the solute. In engineering applications where more than one alloying element is involved, SSH is often linear in c [4, 5]. At elevated temperatures, it is the interaction energy between the solutes and the dislocations that is of interest. This interaction energy has the consequence that the solutes gather around the dislocations and form so-called Cottrell atmospheres. The Cottrell atmospheres slow down the motion of the climbing dislocation and thereby strengthening the alloy. The mechanisms for SSH are different at ambient and high temperatures. We will focus on the creep case at high temperatures.

In many alloy systems, SSH is of high significance for raising the creep strength. Thus, SSH is extensively used in creep resistant austenitic stainless steels, superalloys (both Co and Ni based) and titanium alloys. Many experiments on the role of Mg in Al–Mg have been published. They have in general been analyzed according to Weertman's original proposals [6, 7]. This is referred to as the classical picture, which is presented in Sect. 6.2. Basic models for the influence of lattice and shear modulus misfit on SSH are given in Sect. 6.3. In Sect. 6.4, the role of the drag stress is discussed. The mechanisms for slow and fast diffusion elements are different. The first case is covered in Sect. 6.3 and the latter case in Sect. 6.5.

6.2 The Classical Picture

6.2.1 Observations

In the analysis of the influence of solid solution hardening on creep much focus has been devoted to Al–Mg alloys. The reason is that there is a change in the stress exponent for the secondary creep rate with stress above 300 °C. As was discussed in Chap. 2, change in the stress exponent has often been associated with a change in creep mechanism. The effect of magnesium on the creep rate is illustrated in Fig. 6.1.

With increasing Mg content, the creep rate rapidly decreases. The creep exponent of pure aluminum is $n = 5$, as marked with the number 5 on the curve. At least for

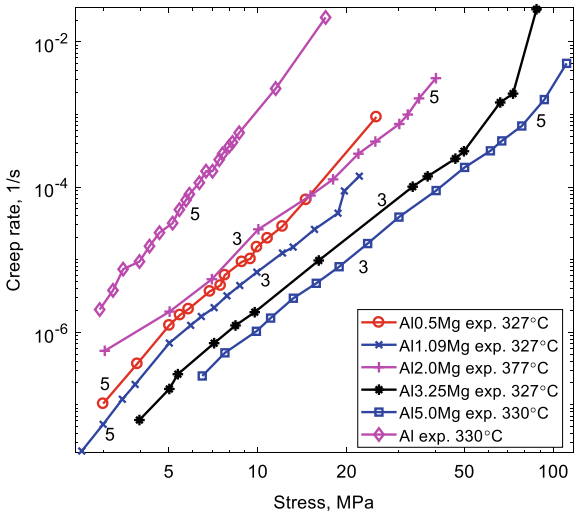

Fig. 6.1 Observed creep rate versus applied stress for Al–Mg alloys between 300 and 400 °C. Mg content from 0.5 to 5%. Values for pure aluminum are shown for comparison [8]. Data for Al–Mg alloys from [9–11]. The approximate values for the creep exponent are marked

some of the Al–Mg alloys, the creep exponent at low stresses is 5 but it is reduced to 3 at slightly higher stresses. At still higher stresses the creep exponent increases again first in some cases to 5 and then to still higher values.

Al–Mg alloys are rarely used above 150 °C. All the interest in the Al–Mg alloys is thus mechanistic. For Al–Mg alloys the classic assumption is that the various creep exponents are due to different creep mechanisms. Two papers of Weertman from 1957 suggested that $n = 3$ and $n = 5$ correspond to dislocation glide and climb, respectively [6, 7].

The unusual transition from $n = 5$ and $n = 3$ is attributed to a sudden introduction of viscous glide of dislocations where solute atmospheres (Cottrell atmospheres) are dragged along with the dislocations. In general, dislocation climb is slower than glide, and is therefore expected to control the creep rate. However, the drag was assumed to slow down the gliding dislocations sufficiently to make them control the creep process. At high stresses, the gliding dislocations could break away from the solute atmospheres. This would make the gliding dislocations move faster and climb would become controlling. Hence, a transition from $n = 3$ and $n = 5$ is expected. Friedel has given a model for such a break away [12].

The distinction between glide and climb controlled alloys is considered so important that they are described as Class I and Class II alloys, respectively. In Class I alloys the dislocations interact with the solutes forming atmospheres around the dislocations. Since the solutes follow the dislocation through diffusion which is a slow process and slower than the glide velocity, the dislocations are slowed down and creep can be controlled by glide. The dislocations are dragged by the solutes and hence the designation solute drag.

When no solute atmospheres are formed, glide will take place without any effect of solutes, and the glide velocity will be high. Creep will be climb controlled in the same way as for pure metals. Such materials are referred to as Class II materials. Most

alloys for example stainless steels and superalloys are of Class II type. In addition to Al–Mg some Fe–Mo alloys are of Class I type. Another distinction that is often mentioned is that Class II form substructure during creep whereas Class I do not. However, this is not general since Fe–Mo alloys also form substructure [13].

6.2.2 Issues with the Classical Picture

There are a number of problems with the classical pictures

- We saw in Chap. 2 that in many cases there is a continuous increase in the creep exponent with stress if a sufficiently large interval of stresses is considered. This applies to aluminum as well [14]. The change in creep exponent is therefore not necessarily associated with a change in creep mechanism.
- Even Weertman who was the first to suggest a difference in creep exponent between glide and climb, made the statement that practically all creep laws based on creep recovery give $n = 3$, which is referred to as the natural mode [8]. Although this statement is not correct, it illustrates that it is not directly possible to use the creep exponent to distinguish between glide and climb.
- The Class I alloy Fe–1.8Mo shows the same type of behavior as Al–Mg [15]. However, creep exponent in the assumed glide region is $n = 4$, not $n = 3$.
- The influence of solid solution on glide and climb is now well understood, see below. As demonstrated in Chap. 2, glide is always faster than climb. Solutes are now believed to influence climb and glide in the same way. Consequently, the transition from $n = 5$ to $n = 3$ cannot be explained by the presence of solutes.
- If the dislocations move fast enough, they will break away from their Cottrell atmospheres. The required stress for the breakaway was first derived by Friedel [12]. A numerical more precise solution has then been given by Hirth and Lothe [16], Eqs. 18–131.

$$\sigma_{max} = \frac{m_T c_0 \beta^2}{\Omega_a b^2 k_B T} \tag{6.1}$$

where m_T is the Taylor factor, c_0 the concentration of the solute in at.%, Ω_a is atomic volume, β is the solute strengthening parameter (defined below), b is Burgers' vector and k_B T has its usual meaning. The values of c_0 and β are given in Sect. 6.4. For the alloys in Fig. 6.1, the following values are obtained from Eq. (6.1): 55, 120, 226, 359 and 640 MPa. They are all outside the range of the experimental data and cannot explain the observed change in stress exponent.

One can conclude that many of the classical assumptions about creep of Al–Mg alloys are questionable. There are clear distinctions between pure aluminum and Al–Mg alloys with respect to creep. The origin of these differences is less clear than what has been assumed in the past. An alternative way of explaining the observations will be presented below.

6.3 Modeling of Solid Solution Hardening. Slowly Diffusing Elements

For slowly diffusing solutes, the solutes form Cottrell atmosphere that follow the dislocations as described above. This creates a back stress on the dislocations that slows down their motion. This is referred to as solute drag. Slowly diffusing elements are often major alloying elements that are in solid solution.

Fast diffusing elements like the interstitial elements C and N in steel also raise the creep strength but the mechanism is different. These elements can lock the dislocations and they have to break away to contribute to the straining. The critical quantity is the break stress which is needed to make the dislocations move. The break stress is derived in Sect. 6.5.

6.3.1 Lattice and Modulus Misfit

If the atomic radius of solutes that are present in the lattice is different from that in the matrix, it creates an interaction between the solutes and the dislocations. This is referred to as lattice misfit. It generates a friction stress that influences the motion of the dislocations and thereby increases the strength of the alloy. A difference in the modulus also influences the forces on the dislocations.

The lattice misfit can be expressed in terms of the difference in atomic volume between the solute and the host matrix. The atomic volumes can be obtained from the lattice parameters a_i as $\Omega_i = a_i^3/4$ (for fcc). These volumes are linearly expanded (as a function of concentration) around the host composition. The linear misfit δ_i is given by:

$$\delta_i = \frac{1}{3\Omega}\frac{\partial \Omega}{\partial c_i} \approx \frac{1}{3\Omega}\frac{\Omega_i - \Omega_0}{c_i} \tag{6.2}$$

where Ω_0 is the atomic volume of the matrix, Ω_i the atomic volume of the solute of element i and c_i the concentration of the solute. It can also be related to the change in the lattice parameter,

$$\delta_i = \frac{1}{a}\frac{\partial a}{\partial c_i} \approx \frac{1}{a}\frac{a_i - a}{c_i} \tag{6.3}$$

where a_i and a are the lattice parameters of the solute and the matrix, respectively. The linear misfit is a third of the volume misfit as shown in Eq. (6.2). The modulus misfit μ_i can be expressed as

$$\mu_i = \frac{1}{G}\frac{\partial G}{\partial c_i} \approx \frac{1}{G}\frac{G_i - G}{c_i} \tag{6.4}$$

where G_i and G are the shear modulus in the solute and the matrix, respectively.

Values for experimental lattice spacings and misfit parameters can be found in Pearson's handbook [17] and in King's paper [18]. The interaction of solutes with stacking faults (Suzuki effect) can also contribute to the creep strength. However, models for these interactions are currently unavailable. For example, for aluminum King gives the following values for the linear misfit $\delta_{Cu} = -0.13$, $\delta_{Mg} = 0.12$, and $\delta_{Mn} = -0.19$. Experimental modulus misfit values are less readily available in the literature, and in general modulus misfits have to be computed with ab initio methods.

6.3.2 Solute Atmospheres

The dislocation-solute interaction can be estimated from elasticity theory by assuming the solute to be a dilation center. Due to the interaction, solute agglomerates around the dislocation. The concentration around a dislocation can be expressed as [16]

$$c_i = c_i^0 \exp\left(-\frac{U_i(\mathbf{r})}{k_B T}\right) \tag{6.5}$$

where c_i^0 is the mean concentration of the solute i, c_i the local concentration of the solute and $U_i(\mathbf{r})$ at position $\mathbf{r}$ from the dislocation. The interaction energies take the values [3]

$$U_i^{e\delta} = \frac{1}{\pi}\frac{(1+\nu_\mathrm{P})}{(1-\nu_\mathrm{P})} G\Omega\delta_i \frac{by}{r^2} \tag{6.6}$$

$$U_i^{s\delta} = \frac{1}{2\pi^2}\frac{(1+\nu_\mathrm{P})B}{(1-2\nu_\mathrm{P})} G\Omega\delta_i \frac{b^2}{r^2} \tag{6.7}$$

$$U_i^{e\mu} = \frac{1}{8\pi^2}\frac{1}{(1-\nu_\mathrm{P})^2} G\Omega\mu_i \frac{b^2 z^2}{r^4} \tag{6.8}$$

$$U_i^{s\mu} = \frac{1}{8\pi^2} G\Omega\mu_i \frac{b^2}{r^2} \tag{6.9}$$

where G is the shear modulus, and ν_P is the Poisson's ratio of the material. The indices for U_i refer to edge (e) and screw (s) dislocations and size (δ) and modulus (μ) misfit. r is the overall distance from the dislocation core, y the distance above the dislocation, and z the distance in the plane. The expressions (6.6)–(6.9) are illustrated in Fig. 6.2. The value of y is set to correspond to the distance to the second plane of atoms, in fcc $y = \sqrt{3/2}b$. The first atom plane cuts the dislocation core and gives a weaker interaction.

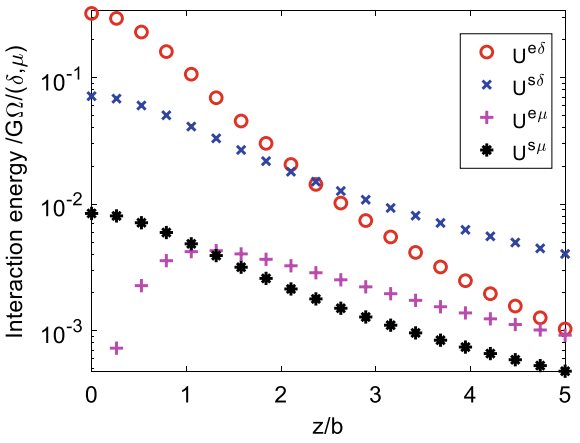

Fig. 6.2 The interaction energies in Eqs. (6.6)–(6.9) versus the distance z/b from the dislocation core. The interaction energies are normalized with respect to $G\Omega$ and the misfit parameters δ_i or μ_i

In Fig. 6.2, the interaction energies are normalized with respect to $G\Omega$ and the misfit parameters δ_i or μ_i. In this way the result is material independent. In spite of the fact that μ_i is often 10 times larger than δ_i, it is evident from Fig. 6.2 that the lattice misfit for edge dislocations, Eq. (6.6), gives the largest interaction energy

$$U_i^{\max} = \frac{1}{\pi}\frac{(1+\nu_P)}{(1-\nu_P)} G\Omega_0 \delta_i \tag{6.10}$$

The dislocations that are slowed down mostly by the interaction with the solutes will also control the magnitude of SSH. Consequently, it is the interaction energy in Eq. (6.10) that is the important quantity.

Due to the interaction energy, it is energetically favorably for the solutes to be located close to the dislocations. Therefore, atmospheres of solutes are created around the dislocations. If the dislocations are not moving (they are static), the concentration of solute atoms c_i^{stat} is given by Eq. (6.5). The concentration of solutes around a moving dislocation can be derived from the following diffusion equations [16], Eqs. 18–10

$$D_i^{\text{sol}} \frac{\partial^2 c_i}{\partial y^2} + \frac{D_i^{\text{sol}}}{k_B T}\frac{\partial}{\partial y} c_i \frac{\partial U_i(y,z)}{\partial y} + v\frac{\partial c_i}{\partial y} = 0 \tag{6.11}$$

This is just Fick's second law taking into account the dislocation-solute interaction in the second and the moving frame with a velocity v in the third term. D_i^{sol} is the diffusion coefficient for the solute i in the matrix. The Cartesian coordinates represent the position of the solute relative to an edge dislocation that is climbing in the y-direction. Equation (6.11) can be integrated directly.

$$D_i^{\text{sol}} \frac{\partial c_i}{\partial y} + \frac{D_i^{\text{sol}}}{k_B T} c_i \frac{\partial U_i(y,z)}{\partial y} + v(c_i - c_0) = 0 \tag{6.12}$$

By solving Eq. (6.12), the concentration c_i^{dyn} of solutes around a dislocation moving in the y-direction can be obtained [16, 19]

$$c_i^{\mathrm{dyn}} = \frac{vc_i^0}{D_i^{\mathrm{sol}}}\left(e^{-\frac{U_i(y,z)}{kT}-\frac{vy}{D_i^{\mathrm{sol}}}}\right)\int_{-\infty}^{y} e^{\frac{U_i(y',z)}{kT}+\frac{vy'}{D_i^{\mathrm{sol}}}}dy' \tag{6.13}$$

The quantities β and r_i are introduced that will be used below

$$\beta_i = bU_i^{\max} \quad r_i = \frac{\beta_i}{k_\mathrm{B}T} \tag{6.14}$$

β_i is the maximum force of the dislocation from individual solutes, and r_i the radius of the Cottrell atmosphere or cloud of solutes around the dislocations. The velocity of a climbing dislocation v is given by

$$v_{\mathrm{climb}} = M_{\mathrm{climb}}b\sigma \tag{6.15}$$

M_{climb} is the climb mobility and σ the applied stress. M_{climb} can be expressed in terms of the coefficient of self-diffusion $\mathrm{D_{self}}$, Eq. (2.34), and the activation energy for the solutes Q_{sol}.

$$M_{\mathrm{climb}} = \frac{D_{\mathrm{self}}b}{kT}e^{\frac{\sigma b^3}{k_\mathrm{B}T}}\exp(-\frac{Q_{\mathrm{sol}}}{kT}) \tag{6.16}$$

The size of Q_{sol} is taken as $U_i^{\max}$, Eq. (6.10), for the element that has the largest solid solution hardening effect on the creep strength. At lower temperatures, the climb enhancement factor g_{climb}, Eq. (2.37) should be taken into account. For gliding dislocations, the velocity is given by Eqs. (2.39) and (2.42)

$$v_{\mathrm{glide}} = M_{\mathrm{glide}}b\sigma = M_{\mathrm{climb}}g_{\mathrm{glide}}b\sigma = M_{\mathrm{climb}}\frac{1}{b\sqrt{\rho}}b\sigma \tag{6.17}$$

again ignoring the climb enhancement factor. ρ is the dislocation density. Since g_{glide} is much larger than unity, the glide velocity is always higher than the climb velocity. The distribution of solutes around dislocations is illustrated in Fig. 6.3.

For a climbing dislocation there is agglomeration of solutes on one side and depletion on the other side. For a gliding dislocation the static distribution is symmetric in the direction of the motion. The concentration in the static model is slightly higher than according to the dynamic model for climbing dislocations, Fig. 6.3a. For glide the dynamic concentration is much lower than the static one, Fig. 6.3b. The reason is the much higher glide velocity in comparison to the climb velocity.

By integrating over the profiles, the agglomeration of solutes can be determined. For the case corresponding to Fig. 6.3a, the agglomeration is 25 and 27 for the static and dynamic distribution, respectively. For the gliding dislocation, the agglomeration

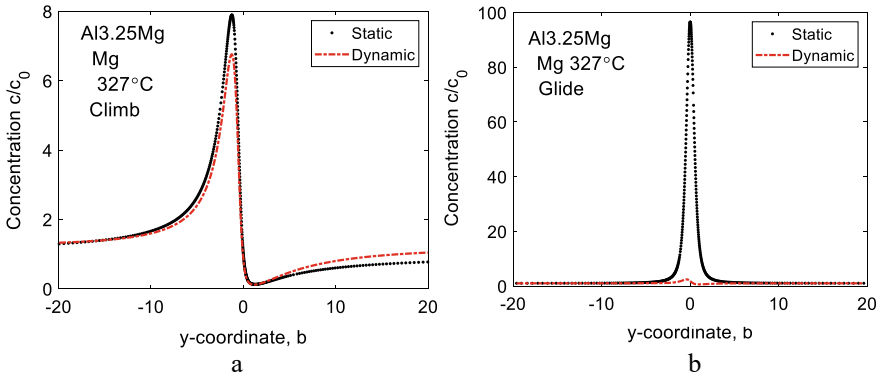

Fig. 6.3 Agglomeration of Mg solutes in Al3.25 Mg at 327 °C around a dislocation that is climbing **a** or gliding **b** in the positive y-direction. Results are given for a static distribution, Eq. (6.5) and a dynamic distribution, Eq. (6.13). The coordinates are those in these equations

is 128 and 1.2 for the static and dynamic distribution, respectively. The agglomeration factor can be interpreted in two ways. If all the additional atoms are placed at the dislocation core over a distance of a Burgers vector, the concentration there of the solute would be enhanced by the agglomeration factor. Alternatively, it can be taken as the distance in terms of Burgers vectors over which the concentration is more than twice the average solute concentration.

6.4 Drag Stress

For slowly moving dislocations, the solutes exert a drag stress on the dislocations that is the source of SSH. The drag stress can be derived numerically from Eq. (6.13) [16].

$$\sigma_i^{\text{drag}} = \frac{k_B T v_{\text{climb}}}{b^2 D_i} \int c_i^{\text{dyn}} \, dz \tag{6.18}$$

Alternatively the drag stress can be expressed as

$$\sigma_i^{\text{drag}} = -\int c_i^{\text{dyn}} \frac{\partial U(y,z)}{\partial z} \, dz \tag{6.19}$$

It is important that the dynamic solution is used in Eqs. (6.18) and (6.19). The static solution in Eq. (6.5) cannot be utilized because it does not give the correct behavior at large z. The need to use the dynamic expression makes the full solution fairly complex. An approximate solution was derived in [16]. The approximate solution

illustrates important features of SSH and will be summarized below. A common form of the drag stress σ_i^{drag} for element i is

$$\sigma_i^{\text{drag}} = \frac{v_{\text{climb}} c_{i0} \beta_i^2}{b D_i k_B T} I(z_0) \tag{6.20}$$

where

$$I(z_0) = \int_1^{z_0} \frac{2\sqrt{2\pi}}{3z^{2.5}} e^z \, dz \tag{6.21}$$

v_{climb} is the dislocation climb speed, cf. Equation (6.15), c_{i0} is the concentration of solute i, and D_i the diffusion constant for solute i. $I(z_0)$ is an integral of $z_0 = b/r_0 k_B T$ where r_0 is the dislocation core radius. $I(z_0)$ often has values of about 3. β_i is the force in Eq. (6.14).

If the radius of the static cloud r_i is less than the burgers' vector b or if D_i/v_{climb} is larger than the average distance between the dislocations R_{disl}, Eq. (6.20) is replaced by

$$\sigma_i^{\text{drag}} = \frac{v_{\text{climb}} c_{i0} \beta_i^2}{b D_i k_B T} \log\left(\frac{D_i}{v_{\text{climb}} b}\right) \quad r_i < b \text{ or } D_i > v_{\text{climb}} R_{\text{disl}} \tag{6.22}$$

Finally, if $r_i > R_{\text{disl}}$ the expression for σ_i^{drag} takes the form

$$\sigma_i^{\text{drag}} = \frac{v_{\text{climb}} c_{i0} \beta_i^2}{b D_i k_B T} \log\left(\frac{D_i}{v_{\text{climb}} r_i}\right) \quad D_i > v_{\text{climb}} R_{\text{disl}} \tag{6.23}$$

The four alternative expressions are not very different. Only the final (logarithmic) factor varies. The situation is another if the dislocation speed v_{disl} is high and the motion of the solute cloud is no longer diffusion controlled.

$$\sigma_i^{\text{drag}} = \frac{\pi D_i c_{i0} \beta_i^2}{k_B T b^2 v_{\text{climb}}} \quad v_{disl} > 4 D_i k_B T / \beta_i \tag{6.24}$$

or

$$\sigma_i^{\text{drag}} = \pi c_{i0} \beta_i \quad r_i > \sqrt{D_i \beta_i / v_{\text{disl}} k_B T} \tag{6.25}$$

The dependence of v_{disl}/D_i is inverted in Eq. (6.24) and absent in Eq. (6.25).

In the computation of the secondary creep, the drag stress is added to the internal stress σ_i in Eq. (2.29). An application of the drag stress is illustrated in Fig. 6.4. The contribution from Q_{sol} in Eq. (6.15) to the creep activation energy is also taken into account. This increases the activation energy by $U_i^{\max}$. i is the element Mg in this case. In Fig. 6.4, Eq. (6.20) for the drag stress was used.

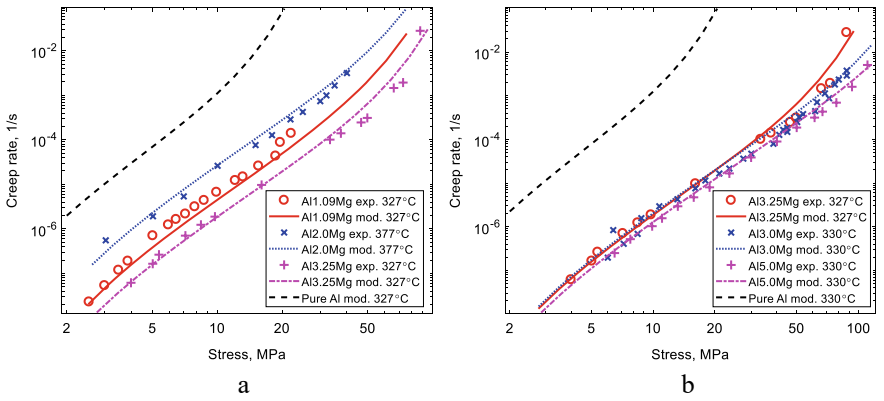

Fig. 6.4 Secondary creep rate versus stress for Al–Mg alloys at around 330 °C. The stress contribution to the internal stress is from Eq. (6.20) and the increase in activation energy from Eq. (6.16). The model results are compared to experimental data [9–11]; **a** Alloys Al0.9 Mg, Al2.0 Mg, Al3.25 Mg; **b** Alloys Al3.25 Mg, Al3.0 Mg, Al5.0 Mg. **a** Redrawn from [20] with permission of intechopen

Three stages of stress dependence can be found in Fig. 6.4. At low stresses there is a slight increase in the stress exponent n_N due to the presence of the Peierls stress. Its value is the same as for pure aluminum used in Fig. 2.9. For stresses in the middle range a power-law behavior is observed. At higher stresses the stress exponent increases and a tendency to power-law break down is found.

The modeling in Fig. 6.4 is based on climb and it is assumed that climb is the controlling mechanism. It has been suggested many times in the literature that glide should be controlling for Al–Mg in part of the studied stress range, see Sect. 6.2. The background is that the stress exponent in the middle stress range is about three and that is what Weertman suggested for glide control in his original paper on the topic. However, it is evident from the analysis in Chap. 2 that climb control often gives the same stress exponent at modest stress levels. According to the classical picture, see Sect. 6.2, two changes in models and mechanisms have to be assumed to represent the stress dependence in Fig. 6.4. The absence of substructure in Al–Mg has been taken as one reason for not considering climb as the controlling mechanism. But that could also be a consequence of the presence of the alloying element. Increasing amounts of alloying elements tend to reduce the stacking fault energy and give a more planar dislocation structure [3]. It is demonstrated in Fig. 6.4 that the present model can describe the experimental data. In the same way as for other comparison with experiments in this book no adjustable parameters are involved. In summary, a single climb based model can accurately reproduce the creep data for Al–Mg. There is no need to assume that glide is controlling in part of the stress range which avoids a number of the difficulties discussed in Sect. 6.2.

6.5 Modeling of Solid Solution Hardening. Fast Diffusing Elements

Fast diffusing elements can have a dramatic effect on the creep rate and the rupture strength. Addition of 50 ppm phosphorus to pure copper reduces the creep rate and increases the creep rupture strength. Phosphorus reduces the experimentally observed creep rate by about a factor of 100 at 75 °C. This will be illustrated below. At the same time the creep strength at 10000 h rupture time is raised from about 140 to 170 MPa at the same temperature [21]. Another example is nitrogen in solid solution in austenitic stainless steel. An addition of 0.1% N can reduce the creep rate by an order of magnitude and increase the rupture strength at 650 °C for a rupture time of 10000 h by about 40 MPa [22].

These pronounced effects of small additions of alloying elements cannot be explained by solute drag. To get a significant contribution from solute drag to SSH, fairly large amounts of alloying elements are needed. We will concentrate on the influence of P on Cu. There are two reasons for that. The influence of P on creep in copper has been analyzed in detail [19]. In addition the low amount of P is clearly in solid solution so there are no particles present that can disturb the analysis. In [19] it has been demonstrated that the solute drag stress is at most 1 MPa. If the accurate expression in Eq. (6.18) is evaluated numerically, the solute drag value is even several orders of magnitude below 1 MPa. It can be concluded that solute drag cannot explain the influence of P on creep in Cu.

In [19] a model is presented that can explain the effect of P on creep quantitatively. It is assumed that the P atoms are agglomerated at the dislocations in the same way as for elements in solute drag and that the distribution of P atoms can be described by Eq. (6.5) for the static distribution and by Eq. (6.13) for the dynamic distribution. These distributions are illustrated in Fig. 6.5.

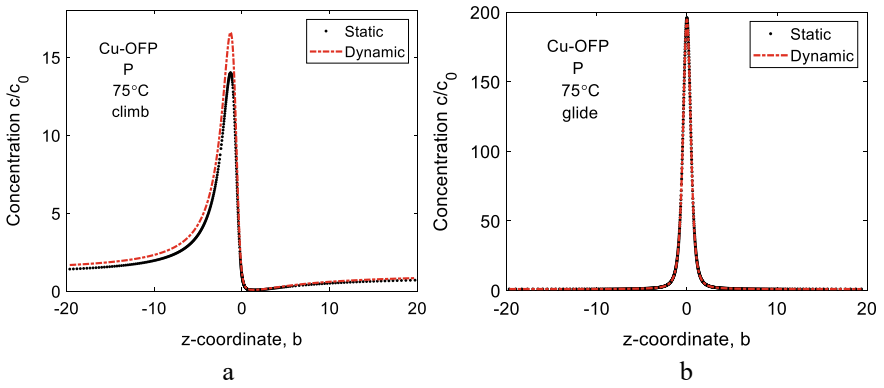

Fig. 6.5 Agglomeration of P solutes in oxygen free copper with 50 ppm P (Cu-OFP) at 75 °C around a dislocation that is climbing **a** or gliding **b** in the positive z-direction. Results are given for a static distribution, Eq. (6.5) or a dynamic distribution, Eq. (6.13). After [19]

The general behavior of these profiles is the same as for Al–Mg in Fig. 6.3. However, there are differences. The diffusion rate for P is so fast that even in the glide case, the dynamic distribution is virtually identical to the static one. In the climb case the agglomeration is even higher in the dynamic distribution than in the static one.

The main difference to the solute drag model is that the P atoms are assumed to lock the dislocations [19]. For the dislocations to move they must break away from the P atmospheres. But since the P atoms are rapidly moving, they will immediately catch up with the dislocations and lock them again. So there is a continuously repeating break away and locking process. When dislocations are more permanently breaking away from solute locking, serrated yielding is often observed. However, since the breakaway—locking is taking place continuously for P in Cu no serrated yielding is observed.

The stress needed to move a dislocation σ_{break} can be determined from an energy balance [19]. According to Peach-Koehler's formula the force F on a dislocation length segment $2L$ is $F = \sigma_{\text{break}} 2Lb$. If the dislocation is moved by one burgers' vector, the consumed energy is $Fb/2$. This energy corresponds to the maximum binding energy $U_i^{\max}$

$$\sigma_{\text{break}} L b^2 = U_i^{\max} \tag{6.26}$$

The average distance L between solute pinning points on a dislocation is

$$L = \frac{b}{\int c_i^{\text{dyn}} dz} \tag{6.27}$$

Combining Eqs. (6.26) and (6.27) gives an expression for σ_{break}

$$\sigma_{\text{break}} = \frac{U_i^{\max}}{b^3} \int c_i^{\text{dyn}} \, dz \tag{6.28}$$

The index i refers in this case to the element P.

To find the influence of σ_{break} on the creep rate, σ_{break} is added to the internal stress in Eq. (2.29). The creep rate versus stress for oxygen free copper with (Cu-OFP) and without P (Cu-OF) is shown in Fig. 6.6.

As stated above, the presence of 50 ppm P reduces the creep rate by two orders of magnitude and this can be fully accounted for by the model for the break stress in Eq. (6.28).

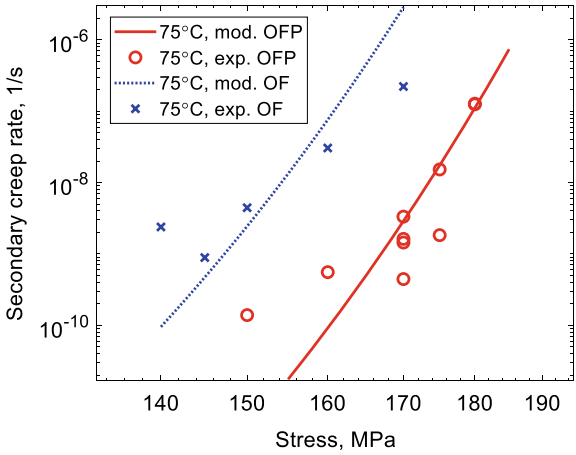

Fig. 6.6 Secondary creep rate versus stress for oxygen free copper with 50 ppm P (Cu-OFP) and without P (Cu-OF) at 75 °C. Modeling values are derived with the help of Eq. (2.28) where σ_{break} is chosen according to Eq. (6.28) has been added to σ_i in Eq. (2.29) for Cu-OFP. The model values are compared to experimental data. Redrawn from [20] with permission of intechopen

6.6 Summary

- Solid solution hardening (SSH) is a result of the misfit between solutes and the matrix with respect to lattice parameters and elastic moduli. This makes it more difficult for the dislocation to move in the lattice which results in a hardening effect. The interaction energies between dislocations and solutes are proportional to the misfit in the lattice parameters and in the elastic moduli. In spite of the fact that the misfit parameters are larger for the elastic moduli than for the lattice parameters, the former give lower interaction energies and can in general be neglected.
- The interaction energies between dislocations and solutes give a direct contribution to the activation energy for creep. This is the main reason why alloys typically have higher activation energy for creep than that for self-diffusion.
- Slowly diffusion solute elements give rise to a drag stress. This drag stress is proportional to the interaction energies squared and inversely proportional to the diffusion coefficient of the solutes.
- Since the diffusion coefficient appears in the denominator in the expression for solute drag, the effect is small or negligible for fast diffusion elements like interstitial elements. Instead the dislocations must break away from the fast diffusing elements to be able to move.
- To verify the models it is suitable to study systems with only one main solute that contributes to the creep strength and without particles present. For slowly diffusion solutes the system Al–Mg alloys at around 300 °C has been chosen. The model can accurately describe the complex dependence on the creep stress and the Mg content. In the past it was necessary to involve several changes in the creep mechanisms which is no longer the case.
- For fast diffusion elements, P in copper has been considered. The addition of 50 ppm P raises the creep strength significantly and that is possible to model quite well.

References

1. R.W. Cahn, P. Haasen, *Physical Metallurgy* (North-Holland, Amsterdam, 1996)
2. T. Suzuki, S. Takeuchi, H. Yoshinaga, *Dislocation Dynamics and Plasticity* (Springer-Verlag, Berlin [etc.], 1991)
3. A. Argon, *Strengthening Mechanisms in Crystal Plasticity* (Oxford University Press, Oxford, 2008)
4. J. Zander, R. Sandstrom, L. Vitos, Modelling mechanical properties for non-hardenable aluminium alloys. Comp. Mater. Sci. **41**, 86–95 (2007)
5. H. Sieurin, J. Zander, R. Sandstrom, Modelling solid solution hardening in stainless steels. Mater. Sci. Eng. A-Struct. **415**, 66–71 (2006)
6. J. Weertman, Steady-state creep of crystals. J. Appl. Phys. **28**, 1185–1189 (1957)
7. J. Weertman, Steady-state creep through dislocation climb. J. Appl. Phys. **28**, 362–364 (1957)
8. S. Straub, W. Blum, Does the "natural" third power law of steady state creep hold for pure aluminium? Scr. Metall. Mater. **24**, 1837–1842 (1990)
9. H. Sato, K. Maruyama, H. Oikawa, Effects of the third element on creep behavior of Al–Mg and αFe–Be solid solution alloys. Mater. Sci. Eng. A **234–236**, 1067–1070 (1997)
10. H. Oikawa, K. Honda, S. Ito, Experimental study on the stress range of class I behaviour in the creep of Al–Mg alloys. Mater. Sci. Eng. **64**, 237–245 (1984)
11. Z. Horita, T.G. Langdon, High temperature creep of Al–Mg alloys, in *Strength of Metals and Alloys (ICSMA 7)* (Pergamon, 1985), pp. 797–802
12. J. Friedel, *Dislocations* (Addison-Wesley, Reading (MA), USA, 1964)
13. H. Oikawa, M. Saeki, S. Karashima, Steady-state creep of Fe-4.1 at% Mo alloy at high temperatures. Trans. Jpn. Inst. Metals 21, 309–318 (1980)
14. B. Wilshire, Observations, theories, and predictions of high-temperature creep behavior. Metall. Mater. Trans. A **33**, 241–248 (2002)
15. H. Oikawa, D. Mizukoshi, S. Karashima, Creep mechanism in Fe-1.8 at. Pct Mo alloy at high temperatures. Metall. Trans. A 9, 1281–1285 (1978)
16. J.P. Hirth, J. Lothe, *Theory of Dislocations* (Krieger, Malabar, Florida, 1982)
17. W.B. Pearson, *A Handbook of Lattice Spacings and Structures of Metals and Alloys*, vol. 2 (Pergamon Press, Oxford, 1967)
18. H.W. King, Quantitative size-factors for metallic solid solutions. J. Mater. Sci. **1**, 79–90 (1966)
19. R. Sandstrom, H.C.M. Andersson, The effect of phosphorus on creep in copper. J. Nucl. Mater. **372**, 66–75 (2008)
20. R. Sandström, Fundamental models for the creep of metals, in *Creep* (inTech, 2017)
21. R. Sandstrom, H.C.M. Andersson, Creep in phosphorus alloyed copper during power-law breakdown. J. Nucl. Mater. **372**, 76–88 (2008)
22. M.D. Mathew, K. Laha, V. Ganesan, Improving creep strength of 316L stainless steel by alloying with nitrogen. Mater. Sci. Eng. A **535**, 76–83 (2012)

Chapter 7
Precipitation Hardening

Abstract Models for precipitation hardening (PH) at room temperature have been available for a long time. In spite of the importance of PH, it took a long time to establish models for elevated temperatures. In fact, empirically the room temperature models have also been used at higher temperatures. This gives the wrong temperature dependence and overestimates PH. It was for a long time thought that it was an energy barrier for climb across particles that was the controlling mechanism, but it was gradually appearing that this effect was so small that it could be neglected. Instead it is time it takes for dislocations to climb across particles that is the critical factor. Small particles are readily passed and do not contribute to the strengthening. Particles larger than a critical size have to be passed by the Orowan mechanism, because there is not time enough for dislocations to climb across these particles. This mechanism was finally verified for Cu–Co alloys.

7.1 General

The precipitation of phases in the form of particles is probably the most effective way of increasing the creep strength in alloys. Precipitation hardening is utilized in many types of steels and Ni-base alloys. Because of its technical significance there are a large number of publications on precipitation hardening in these alloy systems. The role of carbides and nitrides in Cr–Mo steels and γ' in Ni-base alloys has been extensively studied. It is well established that the presence of fine precipitates in these systems is essential to get good creep strength.

The understanding of precipitation hardening (PH) at ambient temperatures has been well established for a long time. However, in spite of its technical importance, this has not been the case for the role of precipitation hardening during creep. Only recently, a satisfactory description has been formulated. In fact, many scientists have tried to use models developed for applications at ambient temperatures for PH at elevated temperatures. This does not work well because methods at ambient temperatures are essentially temperature independent. The temperature dependence they involve is often only that of the shear modulus and that is weak. However, the

R. Sandström, *Basic Modeling and Theory of Creep of Metallic Materials*, Springer Series in Materials Science 339,
https://doi.org/10.1007/978-3-031-49507-6_7

creep rate and strength typically decrease exponentially with increasing temperature (see Chap. 2) and this is strongly at variance with models for applications at ambient temperatures.

It was early on recognized that climb must play an important role for describing PH. It was thought that there is a significant energy barrier for dislocations to climb across particles. More and more accurate models for the energy barrier were developed. However, at the same time the predicted size of the energy barrier decreased when new models were presented. Eventually the magnitude became so small that they were no longer near to explain the large size of PH observed in commercial alloys. This development will briefly be summarized in Sect. 7.2.

It was evident that an entirely new principle was needed to understand PH. The solution was to assume that it is the time for a dislocation to climb across a particle rather than the size of the energy barrier that is the controlling factor [1]. A critical particle size is introduced. If a particle is large enough, there will not be sufficient time to get across it and the particle will block the motion of the dislocation. This gives a contribution to the creep strength. On the other hand if the particles are small they will readily be climbed across and they will not contribute to the creep strength. With this model is has been possible to describe PH of 9 and 12Cr steels, austenitic stainless steels and Cu–Co alloys [2–4]. The model development will be presented in Sect. 7.3. The application to Cu–Co alloys is covered in Sect. 7.4.

7.2 Previous Models for the Influence of Particles on the Creep Strength

7.2.1 Threshold Stress

At about half the absolute melting point T_m, many particle free materials have a stress exponent n_N for the creep rate in the interval 4–7. Particle strengthened alloys typically have a higher stress exponent. This can be rationalized if the creep rate $\dot{\varepsilon}$ is expressed as

$$\dot{\varepsilon} = A_n(\sigma - \sigma_i)^{n_i} \tag{7.1}$$

σ is the applied stress, σ_i the internal stress from the particles, and A_n and n_i constants. With this formulation, the stress exponent n_i is smaller than n_N. As can be seen from the analysis in Chap. 2, an equation of the type in Eq. (7.1) can be derived from basic principles so the equation has a good basis. In a number of papers, σ_i, A_n and n_i have been used as adjustable parameters to make Eq. (7.1) fit the experiments and to have n_i to fall in the range 4–7. A special procedure called the Lagneborg-Bergman plot was developed for this purpose [5].

Assuming that σ_i is constant which was frequently done, it implies that σ_i is a threshold stress and below this stress no creep will take place. For oxide dispersion

strengthened alloys (ODS) such a threshold stress has been observed [6, 7], but there are also ODS where a threshold is not found. However, for most particle strengthened materials for example the common CrMo steels, no threshold stress has been recorded. By analyzing Eq. (7.1), it is found that the stress exponent n_N decreases with increasing stress. This behavior is observed for a few ODS alloys [7], but not for most particle strengthened alloys, which is a drawback of the model.

The reasons for the failure of the assumption with a constant threshold stress are now well understood. It is now possible to derive σ_i directly. In fact, it is shown later in this chapter that σ_i is not a constant. It depends on both temperature and stress and there is no indication that it will tend to a limiting value at low stresses.

7.2.2 Orowan Model

Dislocations can pass particles by cutting through them, by flowing around them or climbing across them. At ambient temperatures only the first two are usually considered. Particle cutting will not be analyzed in the present text because as we will see later in this chapter, it is unlikely that it is of importance in creep exposed materials except in special cases. For a summary of mechanisms for particle cutting, see [8].

The Orowan model for dislocation looping of particles will briefly be described here because it is needed in Sect. 7.3. When the stress increases for a dislocation attached to particles, the dislocation will eventually almost meet itself around the particles. The maximum force F that the dislocation can take is $2\tau_L \approx 2Gb^2/2$ where τ_L is the dislocation line tension. The external force F on a dislocation segment of length λ is (Peach-Koehler formula)

$$F = \sigma\lambda b/m_T \tag{7.2}$$

where σ is the external stress and m_T is the Taylor factor. By equating the two forces the critical stress is obtained. This is the stress for Orowan looping σ_O

$$\sigma_O = \frac{m_T C_O G b}{\lambda} \tag{7.3}$$

Many refinements of this expression are available in the literature. However, they can approximately be taken into account by adding a factor $C_O = 0.8$ [9]. The precision in the prediction of PH does not justify that a more elaborate formulation is needed. λ is usually assumed to be taken as the nearest neighbor distance for randomly distributed spherical particles of radius r and a volume fraction of f_V. This distance is usually referred to as the planar lattice square spacing λ_s

$$\lambda_s = r(2\pi/3f_V)^{1/2} \tag{7.4}$$

As can be seen from Eqs. (7.3) and (7.4), the Orowan strength increases with decreasing particle radius and increasing volume fraction of particles.

As pointed out above, the Orowan strength has been used many times to estimate the influence of particles on the creep strength. This overestimates the strength contribution since Eq. (7.3) is only weakly temperature dependent through the shear modulus G, which decreases approximately linearly with temperature.

7.2.3 The Role of the Energy Barrier

Many attempts were made in the past to generalize the Orowan model by taking climb into account. For a review, see [7, 10]. Initial attempts to determine the size of the energy barrier and the associated value for σ_i were made by Brown and Ham [9] and by Lagneborg [11]. They found a value for internal stress σ_i of about half the Orowan stress, which was in agreement with observations for some materials. However, they assumed the presence of local dislocations that were attached to the particles and that the dislocations remained in the glide planes between the particles. This introduces sharp bends on the dislocations that are easily relaxed. Further modeling therefore concentrated to general dislocations that are only attached to a single point on the particles and have more general degrees of freedom. The assumption about climb of general dislocations rather than of local dislocations is clearly more realistic. However, with this approach the values for σ_i turned out to be quite small and tended to decrease with each investigation [6, 7, 12]. The best estimate for the minimum climb stress σ_{clmin} is [6, 7]

$$\frac{\sigma_{clmin}}{\sigma_O} = \frac{\alpha_{cl}}{\alpha_{cl} + 2C_O} \tag{7.5}$$

where

$$\alpha_{cl} = \frac{2\bar{r}}{3\lambda_s} = \sqrt{\frac{2f_V}{3\pi}} \tag{7.6}$$

α_{cl} is called the climb resistance. This gives a value of 0.02–0.06 for σ_{clmin} of the Orowan stress for common particle volume fractions of $f_V = 1$ to 5%.

The predicted energy barriers are so low that they are of little practical value to describe the significant PH in engineering alloys. One possibility is that there is an attractive interaction between the dislocations and the particles. Such an interaction has been observed for ODS [13, 14] but not in general for other PH systems. This behavior has also been modeled [15, 16]. The dilemma with this model is that the interaction strength is considered as an adjustable parameter and this means that the model is not predictive. The nature of the interaction cannot therefore be ascertained.

Clearly, the energy barriers against climb cannot be used as a basis for explaining PH. Instead another approach will be presented in Sect. 7.3 that is based on the time it takes for a dislocation to climb across a particle.

7.3 Precipitation Hardening Based on Time Control

It is evident from the summary in Sect. 7.2.3 that an energy barrier against climb cannot be the controlling factor for the role of precipitates during creep. For this reason, an alternative approach is considered. The following assumptions are involved [1, 2, 4]

- Precipitation hardening is considered but not oxide dispersion strengthening (ODS). This means that the attractive interaction that sometimes appears for ODS alloys is not taken into account.
- The controlling mechanism is assumed to be the time it takes for a dislocation to climb across a particle, not an energy barrier. It is this time that decides whether a particle will be climbed or not.
- The critical particles radius r_{crit} is taken for the largest particle where there is sufficient time for the dislocation to climb across.
- For particles smaller than r_{crit} they will freely be climbed across and will not contribute to the creep strength.
- Particle shearing is not taken into account since small particles will be passed by climb anyway.
- Particles larger than r_{crit} have to be passed by Orowan bowing and this determines their contribution to the creep strength.

These principles for PH have for example been used for austenitic stainless steel [3, 17–19]. The total creep strength has been possible to predict in a precise way.

For climb to be of importance, the climb time t_{climb} must be as long as the glide time t_{glide} between particles. This criterion can be used to find the critical particle radius

$$t_{\text{climb}} = t_{\text{glide}} \tag{7.7}$$

The critical radius r_{crit} is equal to the climb time multiplied by the climb velocity v_{climb}

$$t_{\text{climb}} = \frac{r_{\text{crit}}}{v_{\text{climb}}} \tag{7.8}$$

The climb velocity can be derived from the climb mobility, Eq. (2.29)

$$v_{\text{climb}} = M_{\text{climb}}(T, \sigma) b \sigma \tag{7.9}$$

where σ is the applied stress. The glide time t_{glide} is controlled by the average distance between particles λ_s

$$t_{\text{glide}} = \frac{\lambda_s}{v_{\text{glide}}} \tag{7.10}$$

The Orowan equation for the creep rate gives the glide velocity

$$\dot{\varepsilon} = v_{\text{glide}} \frac{b\rho}{m_T} \tag{7.11}$$

where ρ is the dislocation density. From Eqs. (7.7) to (7.11) an expression for the critical radius can be derived.

$$r_{\text{crit}} = M_{\text{climb}}(T, \sigma) b^2 \sigma \lambda_F \frac{\rho}{\dot{\varepsilon}_{\text{sec}} m_T} \tag{7.12}$$

The secondary creep rate $\dot{\varepsilon}_{\text{sec}}$ is given by Eq. (2.30). In Eq. (7.12) the Friedel spacing between the particles λ_F has been introduced. It is thought that it is the best way of representing the average distance between the pinning points along the dislocations and it is a better alternative than the planar lattice square spacing λ_s [7, 8]. λ_F can be related to the force acting on a climbing segment

$$\left(\frac{\lambda_s}{\lambda_F}\right)^2 = \frac{F}{2\tau_L} = \frac{\sigma_{\text{clmin}} b \lambda_F}{2 m_T \tau_L} = \frac{\sigma_{\text{clmin}}}{\sigma_O} \frac{\lambda_F}{\lambda_s} \tag{7.13}$$

In deriving Eq. (7.13), Eqs. (7.2) and (7.3) have been used. By applying also Eq. (7.5), we find that

$$\left(\frac{\lambda_s}{\lambda_F}\right)^3 = \frac{\alpha_{cl}}{\alpha_{cl} + 2C_O} \tag{7.14}$$

With the help of Eqs. (7.4), (7.6) and (7.14), the Friedel spacing can be derived.

To determine the contribution from the particles to the strength, their size distribution must be known. Particles of significance in creep resistant materials often follow an exponential size distribution [2, 18]. Then the number of particles per unit area N_A can be expressed as

$$N_A = N_{A0} e^{-k(r - r_0)} \tag{7.15}$$

where $N_{A0} = 1/\lambda_s^2$, and r is the particle radius. r_0 takes into account that there are often no accurate observations at small particle sizes; r_0 is taken as 1 μm for scanning microscopy. k is related to the average particle size $\bar{r}$ as $k = 1/(\bar{r} - r_0)$. As pointed out above only particles larger than r_{crit} contribute to the creep strength. Thus the average spacing between these particles λ_{crit} is an important quantity

$$\lambda_{\text{crit}} = \sqrt{N_{A0}} e^{-k(r_{\text{crit}} - r_0)/2} \tag{7.16}$$

The contribution to the creep strength can then be expressed as

$$\sigma_{\text{part}} = \frac{C_O G b m_T}{\lambda_{\text{crit}}} = \sigma_O e^{-k(r_{\text{crit}} - r_0)/2} \tag{7.17}$$

This contribution is added to σ_i in Eq. (2.30). The critical radius depends on temperature and stress and consequently, so does σ_{part}.

7.4 Application of the Precipitation Hardening Model

7.4.1 Analyzed Materials

The model in Sect. 7.3 was first published in 2000 and was successfully applied both to Cr–Mo steels [2] and to austenitic stainless steels [1, 3, 17]. In these applications, PH is not the dominating contribution to the creep strength. Therefore they could not be considered as full verification of the PH model. In this section results on creep in Cu–Co alloys published by Wilshire and coworkers will be analyzed [20, 21]. This system has the advantage that the particles have a large influence on the creep rate. In addition, several ageing conditions with different particle size distributions were studied, so the influence of the particles can safely be ascertained. A valuable feature is that the effect of solid solution hardening in these studies is negligible small as will be shown and will not interfere with the analysis.

The analyzed alloys and conditions are summarized in Table 7.1.

Three alloys were included in the study with 0.88, 2.48 and 4.04 wt.% Co. In their main condition the alloys were fully aged at 600 and 700 °C generating a stable particle structure. These temperatures were sufficiently high that no particle

Table 7.1 Investigated Cu–Co alloys

Co, wt.%	Heat treatment temperature, °C	Heat treatment type	Particle volume fraction	Co in solid solution, wt.%	Particle radius, nm	Particle spacing, nm	Orowan stress, MPa
0.88	600	Underaged	0.00567	0.33	1.2	41	593
0.88	600	Aged	0.00567	0.33	4.2	98	250
0.88	600	Overaged	0.00567	0.33	17.2	405	60
2.48	600	Aged	0.0222	0.33	7.6	90	272
4.04	700*	Aged	0.0344	0.33*	22.6	215	113

* Stabilized at 600 °C after heat treatment at 700 °C

Reprinted from [4] with permission of Springer

coarsening took place during the creep testing at 439 °C. In addition, underaged and overaged conditions were covered for the 0.88 wt.% alloy.

The volume fraction of particles for the different alloys and the amount of Co were calculated with the thermodynamic software Thermo-Calc, see Table 7.1. The particle sizes were measured with transmission electron microscopy [20, 21]. Using the expression for the square lattice spacing, Eq. (7.4), the particle spacing was determined. With the help of Eq. (7.3) the Orowan strength for the alloys was computed, see Table 7.1. The Orowan strength significantly exceeds the creep strength of the alloys as will be seen.

The amount of solid solution hardening of the alloys was evaluated with the help of Eq. (6.22). Some of the Co is in solid solution, Table 7.1. The computed solute drag stress was in the interval from 0.15 to 0.25 MPa, which is negligible in the context.

7.4.2 Pure Copper

To demonstrate the validity of PH model, it is essential to verify that strength contribution from the dislocations can be described with the model in Chap. 2. This is tested for pure copper. Some creep data for pure copper can be found in [20, 21]. In addition creep data have been taken from [22] where tests were performed at 400–500 °C that are close to the test temperature for the Cu–Co alloys. The creep rate versus applied stress is shown in Fig. 7.1.

From Fig. 7.1 it can be seen that the predicted temperature dependence is larger than the observed one. The reason is that the activation energy for creep is lower than the activation energy of self-diffusion which is used in the prediction. That the

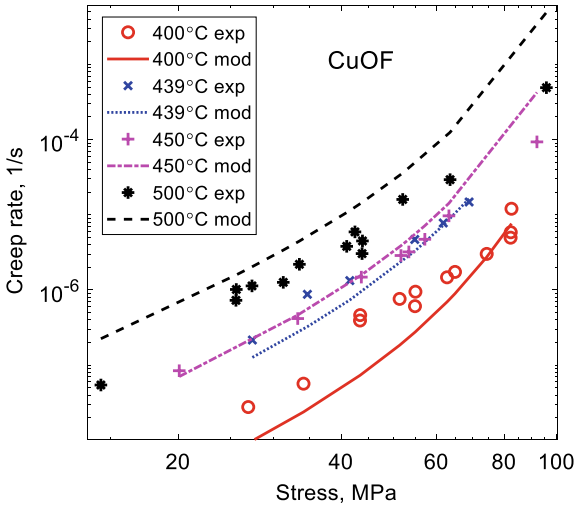

Fig. 7.1 Modeling of stationary creep rate (Eq. (2.29)) for Cu-OF at different test temperatures compared with experimental data [20–22]. Redrawn from [4] with permission of Springer

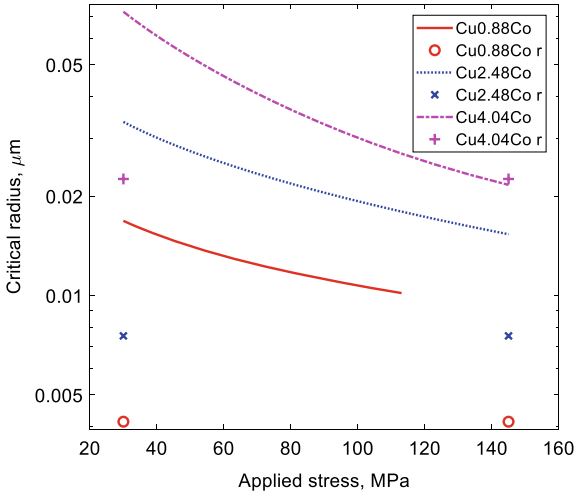

Fig. 7.2 Critical radius, Eq. (7.12) versus applied stress for three Cu–Co alloys. The average particle radiir are included for comparison, Table 7.1

activation energy for creep is lower than that for self-diffusion is unusual. This has been discussed by Raj and Langdon [22]. The stress exponent, i.e. the slope of the curves in Fig. 7.1 is in acceptable agreement with the observations. The model and experimental values at 439 and 450 °C are in close agreement.

7.4.3 Cu–Co Alloys

Only particles larger than the critical size contribute to the creep strength. Such particles have to be passed by Orowan bowing. The critical particles radius is given by Eq. (7.12). The critical particle radii for the three Cu–Co alloys is illustrated in Fig. 7.2.

In Fig. 7.2 in addition to the critical radii, the average particle sizes are shown. Both the typical radii and the critical radii increase with the Co content. At low stresses the critical radii are about a factor of four larger than the average particle radii. At larger stresses the difference is smaller. For the two lower Co contents it is a factor of two. For the highest Co content, there is no longer any difference anymore. This means that all particles contribute to the creep strength.

When the volume fraction and the average radius are known, the size distribution can be estimated with the help of Eq. (7.15). The result is illustrated in Fig. 7.3.

Exponential size distributions imply that the number of particles per unit area can decrease quite rapidly with increasing radius. The Co content has a large impact on the slope of the size distributions. The critical radii are marked in Fig. 7.3 for different applied stresses. As is evident from Fig. 7.2, the largest critical radii correspond to the lowest stresses.

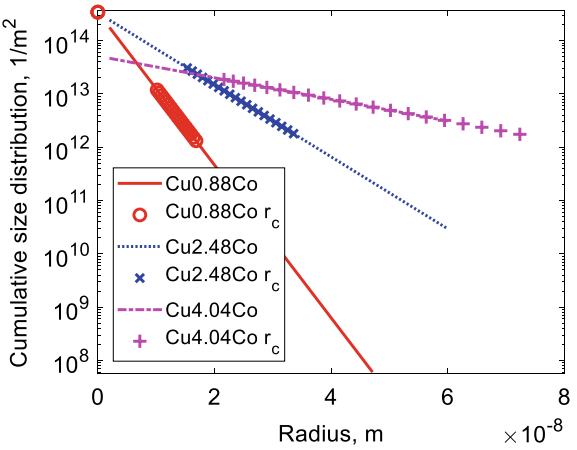

Fig. 7.3 Particle size distributions, Eq. (7.15) for the three Cu–Co alloys in aged condition with critical radii marked, Eq. (7.12)

The influence of particles on the creep strength is via the critical Orowan strength in Eq. (7.17). This strength is added to internal stress in Eq. (2.29). The critical Orowan strength is shown in Fig. 7.4.

The critical strength increases with the applied stress. It might be thought that if the Co content is raised it would automatically enhance PH. From Fig. 7.4 it is clear that this is not the case. In fact, the alloy with 2.48 wt.% Co gives the highest strength. The predicted creep rate as a function of applied stress is shown in Fig. 7.5.

The Co particles reduce the creep rate by about two orders of magnitude in relation to that of pure copper. It is evident that the model can reproduce this behavior quite well. The ranking of the three Cu–Co alloys is also in accordance with experiments. The stress dependence is handled in an acceptable way.

If Figs. 7.4 and 7.5 are compared, the difference in critical Orowan stress is directly related to the observed relations between the creep rates as proposed by the model.

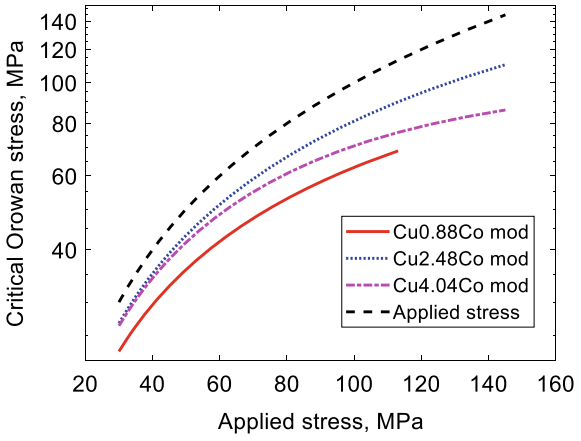

Fig. 7.4 Critical Orowan stress, Eq. (7.17) versus applied stress for three Cu–Co alloys. For comparison, a 1:1 line for the applied stress is included in the diagram. Redrawn from [4] with permission of Springer

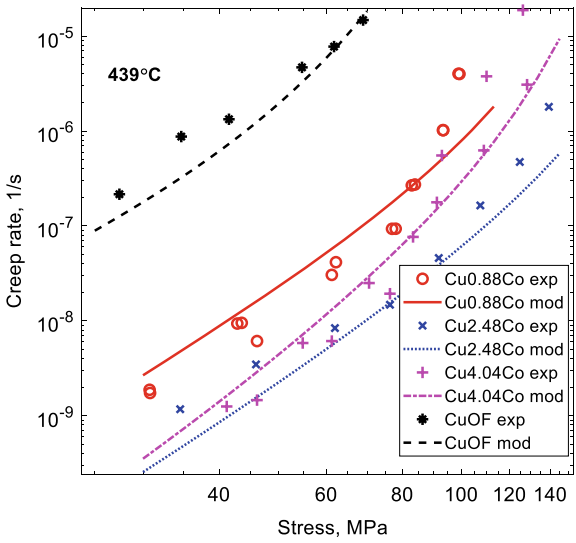

Fig. 7.5 Modeling of stationary creep rate for three Cu–Co alloys and pure copper compared with experimental data from [20]. Redrawn from [4] with permission of Springer

If the values for the Orowan strength at room temperature (Table 7.1) would be used to rank the creep strength it would suggest that Cu0.88Co and Cu2.48Co would have about the same creep strength and would be significantly better than Cu4.04Co. This is clearly not consistent with the model or with the experimental results. Another way of demonstrating that creep strength is not close related to the Orowan strength is illustrated in Fig. 7.6.

It can be seen that the ratio between the critical Orowan strength and room temperature Orowan strength varies with applied stress and alloy composition.

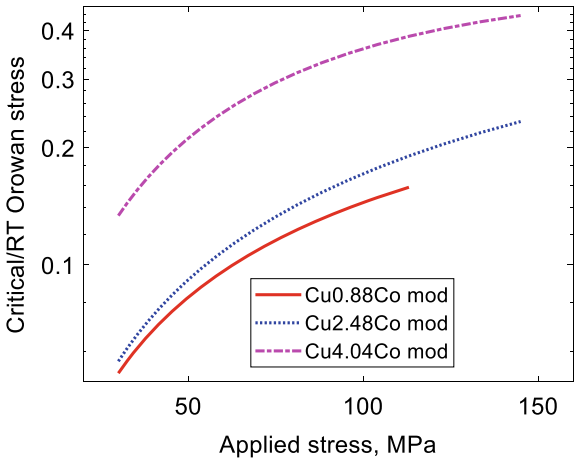

Fig. 7.6 Critical Orowan stress, Eq. (7.17), divided by the room temperature Orowan stress, Eq. (7.3) versus applied stress for three Cu–Co alloys. Redrawn from [4] with permission of Springer

In [20] there is also a comparison between underaged, aged and overaged conditions for the Cu0.88Co alloy. The computed size distributions for these conditions are shown in Fig. 7.7.

There is obviously a large difference between these conditions which makes it an interesting additional test of the model. Furthermore the size distributions are different from those in Fig. 7.3. The strain rate versus stress curves are presented in Fig. 7.8.

As can be seen in the Figure, the model can describe the experimental data fairly well. The difference between the conditions can be accounted for, and the stress dependence is well reproduced.

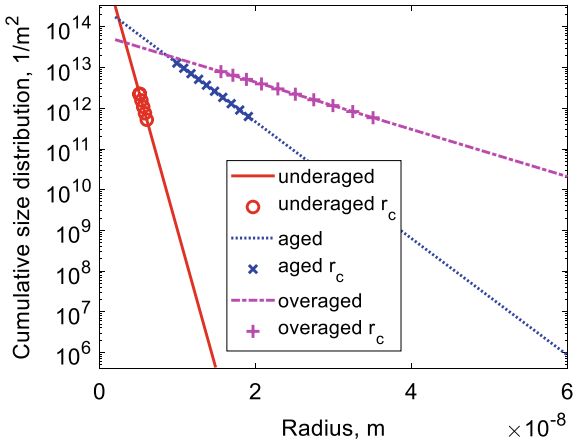

Fig. 7.7 Size distributions, Eq. (7.15) for Cu0.88Co particles in aged, underaged and overaged conditions with critical radii marked, Eq. (7.12). Redrawn from [4] with permission of Springer

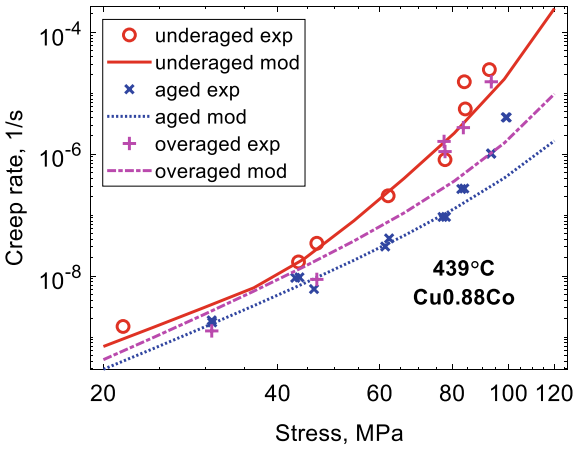

Fig. 7.8 Modeling of stationary creep rate, Eq. (2.29) with the internal stress taken from Eq. (7.17) for Cu0.88Co in underaged, aged and overaged conditions compared with experimental data from [20]. Redrawn from [4] with permission of Springer

7.5 Summary

- Empirical models for the influence of particles on the creep strength have often simply used the Orowan model. This has the consequence that the strong temperature dependence is almost completely neglected and hardening effect is exaggerated.
- Traditional systematic models for precipitation hardening during creep have been based on energy barriers. However, assessment of the size of the energy barriers has shown that it is negligibly small. Instead the modeling in this chapter is starting from the assumption that the time it takes for a particle to be climbed is the factor that controls if the particle contributes to the creep strength or not.
- A critical particle size is introduced. Particles that are smaller than the critical size do not contribute to the creep strength. Particles larger than the critical size must pass particles by Orowan bowing and they contribute to the creep strength.
- To find the critical particle size, the particle size distribution must be known. Exponential size distributions have been assumed. Such distributions have been found a number of times for creep resistant steels.
- A critical test has been performed for Cu–Co alloys. This is a suitable system since the amount of solid solution hardening is quite small. The model can account for the reduction in creep rate due to the presence of Co particles in Cu.
- Observed effects of Co content, heat treatment condition and stress dependence on the creep rate can be satisfactorily reproduced.
- The predicted increase in the creep strength is significantly smaller than the Orowan strength (except at high stress and high alloy content). The ratio between the predicted increase in strength and the Orowan strength varies with applied stress, Co-content and ageing condition.

References

1. J. Eliasson, A. Gustafson, R. Sandstrom, Kinetic modelling of the influence of particles on creep strength. Key Eng. Mater. **171–1**, 277–284 (2000)
2. H. Magnusson, R. Sandstrom, The role of dislocation climb across particles at creep conditions in 9–12 pct Cr steels. Metall. Mater. Trans. A **38A**, 2428–2434 (2007)
3. S. Vujic, R. Sandstrom, C. Sommitsch, Precipitation evolution and creep strength modelling of 25Cr20NiNbN austenitic steel. Mater. High Temp. **32**, 607–618 (2015)
4. F. Sui, R. Sandström, Creep strength contribution due to precipitation hardening in copper–cobalt alloys. J. Mater. Sci. **54**, 1819–1830 (2019)
5. R. Lagneborg, B. Bergman, The stress/creep rate behaviour of precipitation-hardened alloys. Metal Sci. **10**, 20–28 (1976)
6. E. Arzt, M.F. Ashby, Threshold stresses in materials containing dispersed particles. Scr. Metall. **16**, 1285–1290 (1982)
7. W. Blum, B. Reppich, Creep of particle-strengthend alloys, in *Creep Behaviour of Crystalline Solids*. ed. by B. Wilshire, R.W. Evans (Pineridge Press, Swansea U.K., 1985), p.83
8. J.W. Martin, *Precipitation Hardening*, 2nd edn. (Butterworth-Heinemann, Oxford, England, Woburn, Massachusetts, 1998)

9. L.M. Brown, R.K. Ham, *Strengthening Methods in Crystals*, in, Appl. Sci. Publ.. Ltd., (1971), p. 9
10. M. Heilmaier, B. Reppich, Particle threshold stresses in high temperatures yielding and creep: a critical review, in *Creep Behavior of Advanced Materials for the 21st Century, The Minerals, Metals and Materials Society* (1998), pp. 267–281
11. R. Lagneborg, Bypassing of dislocations past particles by a climb mechanism. Scr. Metall. **7**, 605–613 (1973)
12. R.S.W. Shewfelt, L.M. Brown, High-temperature strength of dispersion-hardened single crystals II. Theory Philos. Mag. **35**, 945–962 (1977)
13. V.C. Nardone, J.K. Tien, Pinning of dislocations on the departure side of strengthening dispersoids. Scr. Metall. **17**, 467–470 (1983)
14. J.H. Schröder, E. Arzt, Weak beam studies of dislocation/dispersoid interaction in an ods superalloy. Scr. Metall. **19**, 1129–1134 (1985)
15. E. Arzt, J. Rösler, The kinetics of dislocation climb over hard particles—II. Effects of an attractive particle-dislocation interaction. Acta Metall. **36**, 1053–1060 (1988)
16. J. Rösler, E. Arzt, The kinetics of dislocation climb over hard particles—I. Climb without attractive particle-dislocation interaction. Acta Metall. **36**, 1043–1051 (1988)
17. R. Sandström, Fundamental models for creep properties of steels and copper. Trans. Indian Inst. Met. **69**, 197–202 (2016)
18. R. Sandström, M. Farooq, J. Zurek, Basic creep models for 25Cr20NiNbN austenitic stainless steels. Mater. Res. Innov. **17**, 355–359 (2013)
19. J. He, R. Sandström, Basic modelling of creep rupture in austenitic stainless steels. Theoret. Appl. Fract. Mech. **89**, 139–146 (2017)
20. P.L. Threadgill, B. Wilshire, Effect of particle size and spacing on creep of two-phase copper—Cobalt alloys. Metal Sci. **8**, 117–124 (1974)
21. J.D. Parker, B. Wilshire, The effect of a dispersion of cobalt particles on high-temperature creep of copper. Metal Sci. **9**, 248–252 (1975)
22. S.V. Raj, T.G. Langdon, Creep behavior of copper at intermediate temperatures-I. Mechanical characteristics, Acta Metall. **37**, 843–852 (1989)

Chapter 8
Cells and Subgrains. The Role of Cold Work

Abstract In almost all metals and alloys, dislocations are concentrated to narrow regions after plastic deformation that divide the material into cells or subgrains. The cell walls consist of tangles whereas the subgrains are surrounded by thin regular networks of dislocations. The cells are transferred to subgrains with increasing temperature. Although these substructures have been analyzed for many years, basic models of their development have only appeared recently. Models for substructures are presented for plastic deformation at constant stress and at constant strain rate. During straining the dislocations can move in opposite directions creating a polarized structure, where the possibility for recovery of dislocations is reduced. This can be expressed in term of a back stress. Its presence explains why creep curves at near ambient temperatures could have an appearance that is similar to that at elevated temperatures. It is also the basis for the effect of cold work on creep. The models can quantitatively describe why the creep rate can be reduced by up to six orders of magnitude for Cu after cold work.

8.1 General

Tangles of dislocations are formed in virtually all alloys during plastic deformation. With increasing strain the tangles form boundaries that divide the materials into micrometer sized cells or subgrains, Fig. 8.1. With increasing temperature and strain the boundaries become better developed and thinner. At high temperatures the boundaries consist of regular networks of dislocations, and are then referred to as subboundaries or subgrain boundaries. At lower temperatures the boundaries are made up of loose tangles that are called cell boundaries. Expressed in another way subgrains are formed in the creep range and cells in the work hardening range [1], although there is no sharp transition. For a definition of the work hardening and the creep range, see Sect. 3.4. Both cells and subgrains are referred to as substructure. In most materials the substructure is well developed already at modest strains. This means that the substructure can be observed in tensile and creep tests. However in

R. Sandström, *Basic Modeling and Theory of Creep of Metallic Materials*, Springer Series in Materials Science 339,
https://doi.org/10.1007/978-3-031-49507-6_8

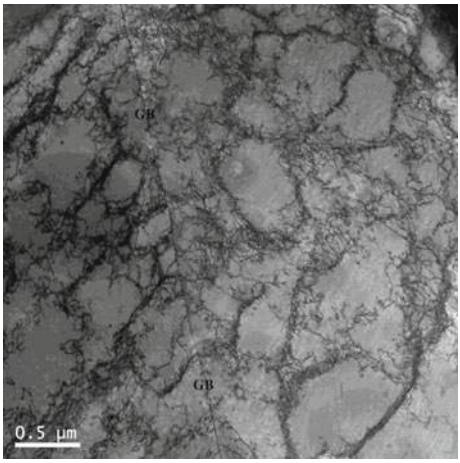

Fig. 8.1 Cell structure in Cu-OFP after 24% cold working [3]

some alloys, for example Al–Mg alloys, the development of substructure is delayed to higher strains [2].

There are excellent reviews on substructure formation in the literature [2, 4, 5]. Many results are similar for cells and subgrains so there is no need in general to make a clear distinction between them. For example, both the cell and subgrain sizes are related to the applied stress in the same way. One question that appeared early on was if the substructure contributed to the creep strength [5, 6]. In a number of investigations it has been shown that strength contribution from the dislocations in the subgrain interiors could account for the full creep strength in single phase alloys, see for example Orlova's paper [7]. However, with the event of Mughrabi's composite model where the subboundaries are considered as hard zones, it is clear that there are long range stresses from the subboundaries [8]. In the composite model, the strength is taken as a weighted average of the "hard" boundaries and the "soft" subgrain interiors. In a single phase alloy, the subgrain size is fully controlled by the applied stress and there is no way of varying the strength contribution from the subgrains [5]. However, the presence of particles can stabilize the subgrain size. In this way a major contribution to the creep strength from subgrains stabilized by $M_{23}C_6$ carbides is obtained in modern creep resistant 9–12% Cr steels [9].

There are many investigations on the formation of substructure but few of them are quantitative. Notable exceptions are work by Blum and Straub and coworkers who measured the development of the subgrain size during creep in martensitic steels [10–12]. These results could be combined with a basic model for the influence of particles on subgrain growth [13] to understand the long term behavior of 9–12% Cr steels [9].

Dislocations with burgers vectors $\mathbf{b}$ and $-\mathbf{b}$ in a slip system are moving in opposite directions in an applied stress field inside a cell. Dislocations with $\mathbf{b}$ and $-\mathbf{b}$ end up at opposite sides of the cells. If a cell boundary is considered, dislocations with $\mathbf{b}$ are found on one side of the boundary and those with $-\mathbf{b}$ on the other side. This means

that the cell boundaries become polarized. It has also the consequence that there is a boundary between the dislocations with **b** and $-\mathbf{b}$ and recovery of them cannot take place. These dislocations are also referred to as unbalanced because in the region with **b** dislocations there are no $-\mathbf{b}$ dislocations. This should be contrasted with balanced dislocations where dislocations with opposite burgers vectors are present. Models for the formation of substructure is presented in Sect. 8.2.

When unbalanced dislocations are present static recovery is slowed down since dislocation with opposite burgers vectors cannot meet and annihilate. The unbalanced dislocations are of importance for several properties. Modeling tertiary creep of copper has demonstrated that the recovery rate of the substructure gives a main contribution to the increasing strain rate [14]. This is likely to be the case for other ductile alloys as well. This will be further discussed in Sect. 12.4. Cold work can reduce the creep rate by many orders of magnitude. Taking balanced and unbalanced dislocations in the subgrain walls into account has made it possible to explain this quantitatively for copper [15]. The role of cold work is discussed in Sect. 8.3.

Most creep tests are performed at constant load. For example, when the creep rate is plotted versus stress, usually the engineering stress, i.e. the nominal stress is used, not the true stress. At high temperatures when the creep exponent is about 5 this is not so critical, but at lower temperatures in the power-law break down regime where the creep exponent can be 30–50, the difference between using the engineering and the true stress is huge, which can easily be demonstrated. It turned out for copper that the engineering stress is still the relevant quantity. It took many years to explain this feature, but by considering the role of the substructure it was possible, Sect. 8.4 [16].

8.2 Modeling of Subgrain Formation

8.2.1 The Stress from Dislocations

In previous chapters, the Taylor equation has been applied to describe the contribution to the strength from the dislocations, Eq. (2.28)

$$\sigma_{\text{disl}} = \alpha m_{\text{T}} G b \sqrt{\rho} \tag{8.1}$$

where α is constant, m_{T} the Taylor factor, G the shear modulus and b burgers vector. In the presence of substructure the relation has to be modified because the α value is different for dislocations in the cell boundary. This can be illustrated by an expression for α given by Kuhlmann-Wilsdorf [17]

$$\alpha_{\text{KW}} = \frac{(1 - \nu_{\text{P}}/2)}{6\pi(1 - \nu_{\text{P}})} \log \frac{R_{\text{CO}}}{b} \tag{8.2}$$

ν_P is Poisson's ratio and R_{CO} a cut-off ratio that is taken as the spacing between dislocations. This spacing is of the order of 10^{-7} m and 10^{-8} m in the cell interior and the cell boundaries respectively. This gives that α is close to a factor of 2 larger for dislocations in the cell interior than for dislocations in the cell boundaries. For this reason Eq. (8.1) is replaced by the following expression

$$\sigma_{\text{disl}} = \alpha m_T G b \sqrt{\rho_{\text{int}}} + \frac{1}{2} \alpha m_T G b \sqrt{\rho_{\text{bound}}} \tag{8.3}$$

where ρ_{int} is the dislocation density in the cell interior and ρ_{bound} the dislocation density in the cell boundaries. The value for α_{KW} will not be used in the present book, since there is an expression that is adapted to elevated temperatures, Eq. (3.17). As discussed in Sect. 8.1, there are many different results in the literature for the influence of boundary dislocations on the strength. Rather than trying to select between the various experimental results, a direct derivation has been chosen.

There is a well-established relation between the cell or subgrain size d_{sub} and the stress

$$d_{\text{sub}} = \frac{K_{\text{sub}} G b}{\sigma_{\text{disl}}} \tag{8.4}$$

K_{sub} is a dimensionless constant that typically takes values in the interval 10 to 20. The first ones to propose an equation of this form were Staker and Holt [18]. It is assumed that it is the dislocation stress that is used in Eq. (8.4) [17]. Eq. (8.4) was already given in Sect. 2.4. It has been suggested that Eq. (8.4) is general and does not only apply to stationary conditions [19]. There are two well-known derivations of Eq. (8.4) in the literature. In the first one a spinodal decomposition of a set of parallel screw dislocations was considered [20]. In the second one the energy of a substructure was assumed to be the sum of the dislocation line energy and the dislocation cell stresses. By minimizing the sum of these two contributions, Eq. (8.4) was obtained [17].

The distance between dislocations in the cell walls which is referred to as the dislocation separation can be estimated in the following way. For the sake of argument, the cell walls are assumed to consist of one layer of μ sets of dislocations and cells arranged as packed cubes. The density of boundary dislocations is then given by

$$\rho_{\text{bnd}} = \frac{3\mu d_{\text{sub}}^2}{d_{\text{sub}}^3 l_{\text{sep}}} \tag{8.5}$$

where l_{sep} is the dislocation separation. Each corner in the arrangements of the cube substructure is associated with three cube sides and that is the reason for the factor 3 in Eq. (8.5). The density is taken as the average over the volume of each cell d_{sub}^3. Equation (8.5) will be used below to obtain an estimate for the dislocation separation.

8.2.2 Formation of Subgrains During Creep

In most materials well-formed subgrains are present in the secondary stage. This means that the subgrains are created during primary creep. There are exceptions. In Al-Mg alloys at around 300 °C, subgrains are not formed until a strain of about 1 [2]. In addition, in some stainless steels a homogeneous dislocation structure appears under certain conditions. For 17Cr12Ni2Mo subgrains appeared at 704 °C but not at 593 °C [21]. For 17Cr12Ni2MoN no subgrains were present at higher N content [22]. A possible qualitative explanation to these observations is that the stacking fault energy γ_{SFE} plays a role and that the subgrain formation increases with the value of γ_{SFE}. For 17Cr12Ni2Mo there is a dramatic increase in γ_{SFE} with temperature [23], which could explain the observations in [21]. The results of the influence of N on γ_{SFE} in the literature are far from unanimous but a recent analysis of existing data [24] suggests that N reduces γ_{SFE} and this could be a reason for the findings in [22]. For Al–Mg, the value of γ_{SFE} is considerably lower than for Al, but if this is of importance for the substructure formation is uncertain.

The normal case where subgrains are present in the secondary stage will now be considered. The changes of the substructure have been quantitatively studied for an Al5Zn alloy at a temperature of 250 °C and an applied stress of 16 MPa. The study was performed by Blum and co-workers. The original papers are not readily available anymore, but fortunately the results are reproduced in other sources [2, 25]. In Sect. 4.3, a model for primary creep is presented. The creep rate is given by Eqs. (4.3) and (4.9)

$$\dot{\varepsilon} = h(2(\sigma - \sigma_{\mathrm{i}}) - \sigma_{\mathrm{disl}}) \tag{8.6}$$

where

$$h(\sigma) = 2\tau_{\mathrm{L}} M(T,\sigma) \frac{\sigma^3}{(\alpha m_{\mathrm{T}} G b)^3} \Big/ \left(\frac{m_{\mathrm{T}}}{b c_L} - \omega \frac{\sigma}{\alpha m_{\mathrm{T}} G b} \right) \tag{8.7}$$

In Eq. (8.6), there is an effective stress that controls the creep rate in the primary stage

$$\sigma_{\mathrm{eff}} = 2(\sigma - \sigma_{\mathrm{i}}) - \sigma_{\mathrm{disl}} \tag{8.8}$$

As can be seen from Eq. (4.10), there is a contribution from solid solution hardening. For Al5Zn, this contribution comes from the Zn content. The linear misfit for Zn in Al is −0.02. The drag stress from the Zn content is given by (Eq. (6.20))

$$\sigma_i^{\mathrm{drag}} = \frac{v_{\mathrm{climb}} c_{i0} \beta^2}{b D_i k_{\mathrm{B}} T} I(z_0) \tag{8.9}$$

The resulting value of σ_i is 4.6 MPa. For $h(\sigma)$ values for Al are used, see Sect. 2.7. The creep strain and the strain rate are illustrated Fig. 8.2.

The creep rate versus strain follows the ϕ-model, Sect. 4.2, although the slope is not quite the same in the experiments and the model.

Since the effective stress controls the primary creep rate, it is natural to assume that it also governs the subgrain size. By applying Eq. (8.8) in Eq. (8.4) a simple model is obtained. The findings are shown in Fig. 8.3a.

The variation of the dislocation density with strain can also be derived with the help of Eq. (4.5). The result is given in Fig. 8.3b. Once the dislocation density is known, the dislocation separation in the subgrain boundaries can be obtained with the help of Eq. (8.5). It is assumed that most of the dislocations are located in the boundaries. The result is demonstrated in Fig. 8.4.

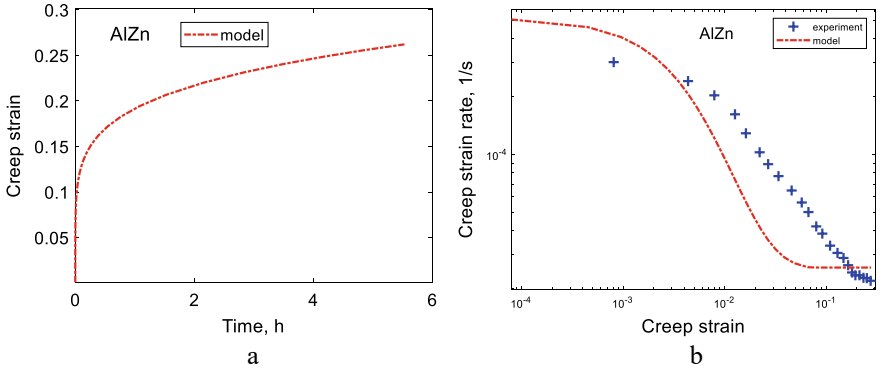

Fig. 8.2 Creep strain versus time **a** and creep rate versus strain **b** for Al5Zn at 250 °C and 16 MPa. Experimental data from [2, 25]. Redrawn from [26] with permission of MDPI

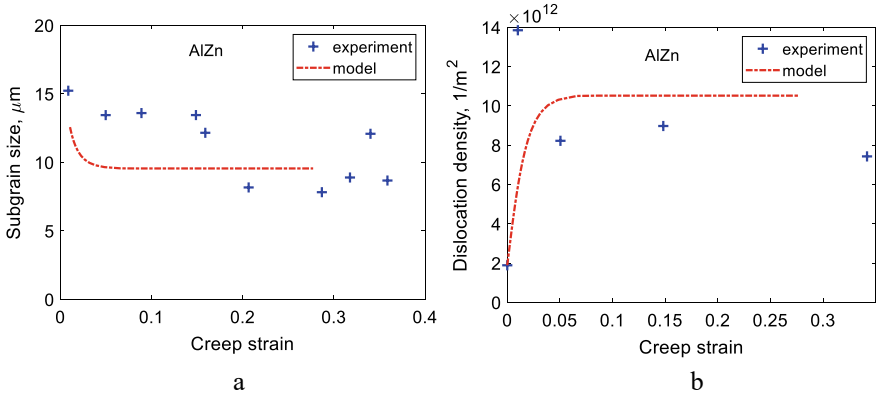

Fig. 8.3 Subgrain size **a** and dislocation density **b** versus strain for Al5Zn at 250 °C and 16 MPa. Experimental data from [2, 25]. Redrawn from [26] with permission of MDPI

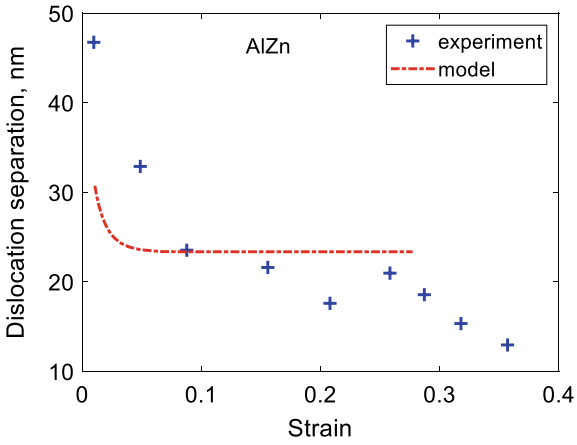

Fig. 8.4 Dislocation separation in the subgrain boundaries versus strain for Al5Zn at 250 °C and 16 MPa. Experimental data from [2, 25]. Redrawn from [26] with permission of MDPI

It is clear that the model presented here can predict the general behavior of the subgrain formation in Figs. 8.3 and 8.4 although the details are not fully accurate.

8.2.3 Cell Formation at Constant Strain Rate

Dislocation cells are formed in virtually all alloys during tensile and compression testing at ambient temperatures. A brief survey is given by Koneva et al. [27]. In the same way as during creep, the cell diameter decreases with increasing strain. They summarize findings that the cell diameter is proportional to the inverse of the square root of the dislocation density.

$$d_{\text{sub}} = K_{\text{rho}} \rho^{-1/2} \tag{8.10}$$

This is consistent with Eq. (8.4). This is seen by combining Eqs. (8.3) and (8.4) with (8.10)

$$K_{\text{rho}} = \frac{K_{\text{sub}} \mu_{\text{sub}}}{\alpha m_{\text{T}}} \tag{8.11}$$

where $\mu_{\text{sub}} = 1$ and 2 for dislocation densities in the subgrain interior and walls respectively. A value of $K_{\text{rho}} = 15$ was found for Cu which is in reasonable agreement with $K_{\text{sub}} = 10$, since $\alpha \approx 0.19$ and $m_{\text{T}} \approx 3.1$. The location of dislocation in cell interiors or boundaries was not specified. Their results for K_{rho} for Cu–Al (2–5) and for Cu–Mn (2–5) illustrate that K_{rho} can be significantly smaller for alloys in comparison to pure metals. In [27] early investigations for K_{rho} are also referenced but these results are difficult to match to K_{sub} values.

Subgrain boundaries have essentially zero width in particular at high temperatures. Cell walls on the other hand have a significant width w_{cell}. This means that Eq. (8.5) must be replaced by

$$\rho_{\text{bnd}} = \frac{3\mu w_{\text{cell}}}{d_{\text{sub}} l_{\text{sep}}^2} \tag{8.12}$$

In Eq. (8.12), the separation distance between dislocations is assumed to be the same in the boundary plane and perpendicular to the plane. In the boundary several types of dislocations must be taken into account [15]. This will be explained in detail in Sect. 8.2.3, where the equations for the dislocation densities will be given. Using these equations the developments of dislocation densities and the corresponding dislocation stress, Eq. (8.3), can be computed. Once the dislocation stress is known, the cell size can be obtained with the help of Eq. (8.4). The variation of the cell size as a function of strain is illustrated in Fig. 8.5. The cell diameter decreases with increasing strain and tends towards a stationary value at larger strains.

In addition to the overall dislocation density in the boundary ρ_{bnd}, there is a formation of dislocation locks that are believed to create the stability of the boundary. The density of the locks is designated ρ_{lock}. Following [15] the cell wall width is related to the lock density

$$w_{\text{cell}} = \frac{1}{l_{\text{sep}} \rho_{\text{lock}}} \tag{8.13}$$

If Eqs. (8.12) and (8.13) are combined, expressions for the dislocation separation and wall width in terms of the dislocation densities are obtained

$$l_{\text{sep}} = \left(\frac{3\mu}{d_{\text{sub}} \rho_{\text{bnd}} \rho_{\text{lock}}} \right)^{1/3} \tag{8.14}$$

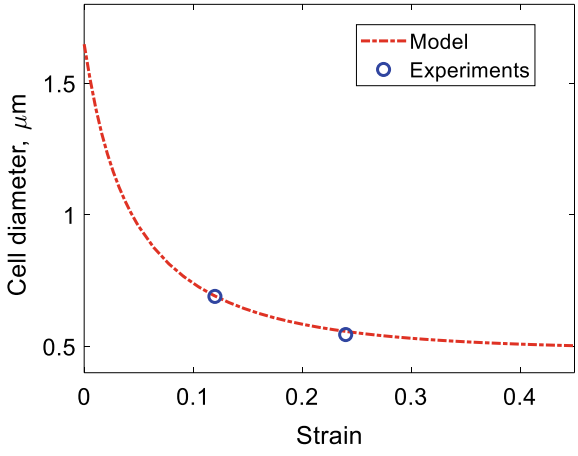

Fig. 8.5 Cell diameters as a function of strain for Cu-OFP at 75 °C and 1×10^{-5} 1/s [15]. Experimental data from [3]. Redrawn from [15] with permission of Elsevier

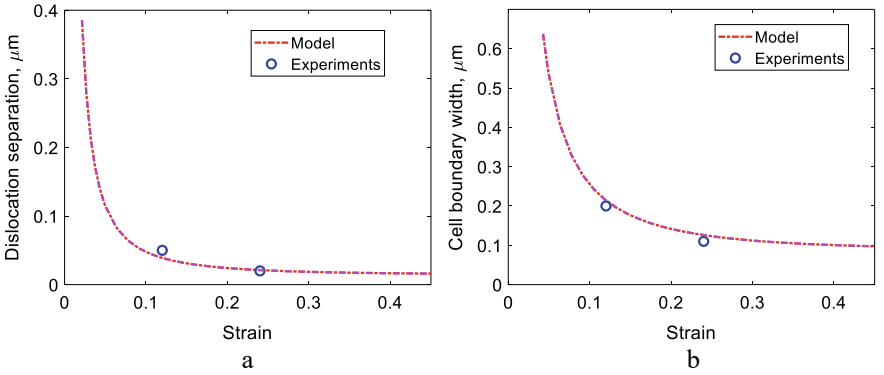

Fig. 8.6 **a** Dislocation separation in the cell boundaries and **b** cell boundary width as a function of strain for Cu-OFP at 75 °C and 1×10^{-5} 1/s [15]. Redrawn from [15] with permission of Elsevier

$$w_{\text{cell}} = \left(\frac{d_{\text{sub}} \rho_{\text{bnd}}}{3\mu\rho_{\text{lock}}^2} \right)^{1/3} \tag{8.15}$$

Equations (8.14) and (8.15) are compared to experimental data in Fig. 8.6.

In the same way as for the cell size, the dislocation separation and cell boundary width decrease with strain. The variation of the dislocation separation and cell boundary width with strain is more rapid than for the cell size. These results are not consistent with those of Koneva et al., who suggest a constant ratio between the cell boundary width and the cell diameter.

In a test series for 18Cr8Ni austenitic stainless at 865 °C, the formation of subgrains as a function of strain at constant strain rate is studied in [2]. In the same way as for Al5Zn and Cu-OFP above, it is demonstrated that the subgrain size and dislocation separation in subgrain walls decrease and tend to stationary values with increasing strain. The dislocation density rapidly increases with strain and also levels off to a stationary value. Since the variation of the stress with strain can be predicted, it was thought that the results should be possible to model. Unfortunately, the published stress strain curve is not consistent with the creep models.

8.3 Influence of Cold Work on the Creep Rate

The influence of cold deformation on the creep rate and creep rupture is a classical problem. During primary creep of annealed material, the dislocation density is normally raised from a low value to a stationary one when the secondary stage is reached. This is a direct outcome of the creep recovery theory and it is well described by the basic dislocation equation used in this book, Eq. (4.5). On the other hand for a cold deformed material, the initial dislocation density is high.

If Eq. (4.5) is applied, the dislocation density would be reduced during primary creep and the same stationary dislocation density as for an annealed material would be found and no effect of the cold deformation would remain. This is in direct at variance with observations for example for fcc alloys. For a number of austenitic stainless steels the creep strength can be increased significantly [28–31]. A review is given in [32]. If the temperature is too high or the strain is too large the effect of cold work disappears. The reason is that the dislocation structure is not sufficiently stable under such conditions and recrystallization may appear.

In this section the influence of cold work on the creep of Cu-OFP will be analyzed. Results for creep rupture data are shown in Fig. 8.7.

Values for 0, 12 and 24% cold work are compared. It is evident that the cold work has a dramatic effect on the rupture time. For 12% cold work the rupture time is increased by more than three orders of magnitude. For 24% cold work the rupture time is raised by six orders of magnitude. This effect is only observed if the cold work is performed in tension. If the cold work is in compression only quite a small increase in the rupture time is found. The creep testing was carried out in tension. Thus if the deformation direction is reversed between the cold work and creep testing only a limited effect is observed.

With increasing cold deformation, the creep ductility is practically always reduced. This is clearly found for Cu-OFP, Fig. 8.8.

For Cu-OFP without cold work the rupture elongation is typically quite high, above 40%. For 12% cold deformation in tension the rupture elongation is still high, 30% and above. For 24% cold deformation, the rupture elongation is a little bit above 10%. It is interesting to note that the creep ductility of Cu-OFP deformed in compression is low in spite of the small increase in the rupture time.

It has now been found that the role of the substructure must be taken into account to understand the influence of cold working [15]. This has also been suggested in the past but without any basic analysis that could predict the magnitude of the effect [4, 33]. As described in Sects. 8.1 and 8.2 a cell structure is formed in practically all alloys

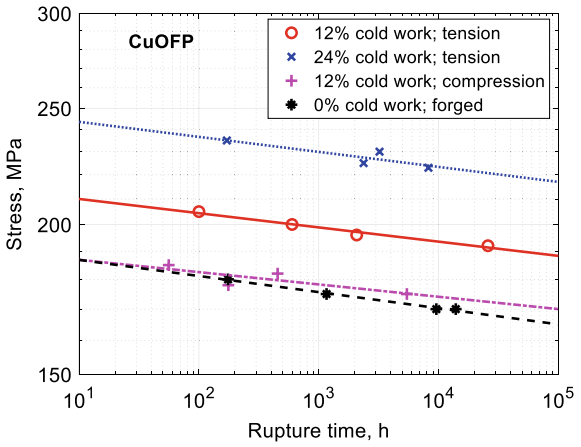

Fig. 8.7 Stress versus rupture time for 12 and 24% cold deformed Cu-OFP at 75 °C. For comparison data for material without cold deformation is included. The lines are fitted to the experimental data to illustrate the influence of rupture time. Experimental data from [3]. Redrawn from [15] with permission of Elsevier

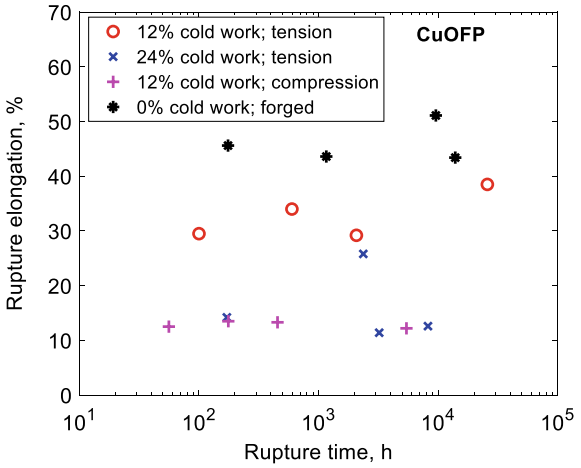

Fig. 8.8 Rupture elongation versus rupture time for 12 and 24% cold deformed Cu-OFP at 75 °C. For comparison data for material without cold deformation is included. Experimental data from [3]. Redrawn from [26] with permission of MDPI

during deformation at ambient temperatures. A large fraction of the dislocations moves to the cell boundaries and in this way they create the cell structure. During the deformation all dislocations do not behave in the same way. Dislocations with opposite burgers vectors move in opposite directions in a given stress field. This can be seen from the Peach-Koehler formula for the force **F** on a dislocation with direction ξ and burgers vector **b**

$$\mathbf{F} = (\mathbf{b}\sigma) \times \boldsymbol{\xi} \tag{8.16}$$

If the direction of the burgers vector is changed to the opposite one ($-\mathbf{b}$), this is the same as changing the sign of the burgers vector. For this reason, burgers vectors of opposite directions will also be referred to as burgers vectors of opposite signs. From Eq. (8.16), it can be seen that if the direction of the burgers vector is changed to the opposite one, the sign and the direction of the force is also changed. Dislocations of opposite signs on the same glide plane move to different ends of the cell. With opposite signs at different ends of the cell, the dislocations are said to be polarized. Not all dislocations are polarized. It is assumed that the outer layers of the boundaries are polarized.

The polarization of dislocations has a pronounced effect on the recovery. Since dislocations with opposite burgers vectors cannot be found amongst polarized dislocations, static recovery is not possible. Polarized dislocations are referred to as unbalanced since dislocations with opposite burgers vector are not present. For unpolarized dislocations, dislocations with opposite burgers vectors can be found and they are therefore referred to as balanced.

In the model for the development of the cell structure, the following dislocation densities in the cell boundaries are taken into account: balanced dislocation density ρ_{bnd}, the unbalanced dislocation density ρ_{bnde}, and the density of the locks ρ_{lock} [15]. Most of the dislocations are in the boundaries, and the content in the cell interiors is

neglected. The equation for the balanced dislocation density ρ_{bnd} is almost identical to Eq. (2.17)

$$\frac{d\rho_{\text{bnd}}}{d\varepsilon} = k_{\text{bnd}} \frac{m\rho_{\text{bnd}}^{1/2}}{bc_L} - \omega\rho_{\text{bnd}} - 2\tau_{\text{L}} M\rho_{\text{bnd}}^2/\dot{\varepsilon} \tag{8.17}$$

Work hardening, dynamic recovery and static recovery are considered. The only difference is the introduction of the factor k_{bnd}. It takes into account since Eq. (8.3) is modified in comparison to the ordinary version of the Taylor equation. For the unbalanced content ρ_{bnde}, the equation corresponding to (8.17) is

$$\frac{d\rho_{\text{bnde}}}{d\varepsilon} = k_{\text{bnde}} \frac{m(\rho_{\text{bnd}}^{1/2} + \rho_{\text{bnde}}^{1/2})}{bc_L} - \omega\rho_{\text{bnde}} \tag{8.18}$$

There are two significant differences between (8.17) and (8.18). There is no static recovery term in Eq. (8.18). Unbalanced dislocations cannot annihilate by combining with dislocations of opposite signs, since such dislocations are not present. The other difference is that both balanced and unbalanced contribute to the generation of the unbalanced content since both types move across the cell interiors.

The traditional view is that dynamic recovery is due to dislocations coming sufficiently close that they can combine with dislocations of opposite sign and annihilate [34]. This assumption tends to overestimate the recovery rate, see Sect. 2.3.2. In addition, the mechanisms for dynamic and static recovery would be similar although their temperature and time dependencies are quite different. Argon has instead suggested that the dynamic recovery is due to the interaction between dislocations generated during work hardening and the cell boundaries [35]. It is known experimentally that spurting dislocations are moving a distance of about three cell diameters [36] and consequently they will pass through more than one cell boundary. During this passage boundary dislocations will be removed. When the dislocations hit the boundaries low energy configurations will be formed and this is part of the dynamic recovery process. Some of these low energy configurations are locks that are dominated by Cottrell-Lomer locks. They are created when partial dislocations cross. The formation of locks are assumed to be controlled by the following equation

$$\frac{d\rho_{\text{lock}}}{d\varepsilon} = k_{\text{lock}}\omega(\rho_{\text{bnd}} + \rho_{\text{bnde}}) - \omega\rho_{\text{lock}} - 2\tau_{\text{L}} M\rho_{\text{lock}}^2/\dot{\varepsilon} \tag{8.19}$$

This equation describes how both balanced and unbalanced dislocations contribute to the formation of locks. Dynamic recovery influences the number of locks since spurting dislocations passing through the boundaries remove locks. The locks can also be eliminated by static recovery since this process reduces the energy even for complex dislocation configurations.

In Sect. 3.3, experimental stress strain curves for Cu-OFP were accurately reproduced using Eq. (2.17) assuming a homogenous distribution of dislocations. If now

the dislocations are considered to be located in the cell boundaries and Eqs. (8.17)–(8.19) are used, the stress should be computed with the help of Eq. (8.3) with ρ_{bound} equal to the sum of ρ_{bnd}, ρ_{bnde} and ρ_{lock}. The results for the stress strain curves should be the same. With $k_{bnd} = \sqrt{2}$ and $k_{bnde} = \sqrt{2}$ this is the case. The value of k_{lock} should be considerably smaller than the value for k_{bnd}. A value of $k_{lock} = 0.1$ has been assumed. With Eq. (8.14), this gives a value for the separation distance of the dislocations in the cell walls of about 20 nm that is in accordance with experiments for several materials, see Sect. 8.2. The selection of k_{lock} also affects the values k_{bnd} and k_{bnde}. Values $k_{bnd} = 1.7$, $k_{bnde} = 0.2$ and $k_{lock} = 0.1$ reproduce the stress strain curves [15].

The results for the influence of cold work in Fig. 8.7 will now be analyzed. 12% and 24% cold deformation at ambient temperature gives stresses of 154 and 191 MPa, respectively. Assuming the dislocations are located in cell boundaries in agreement with observations [3], and using the modified Taylor Eq. (8.3), this gives total densities of dislocations in the cell walls of 8.7×10^{14} and 1.5×10^{15} $1/m^2$. The development of the dislocation densities according to in Eqs. (8.17)–(8.19) is shown in Fig. 8.9. In this case the balanced dislocations dominate the total content. It should be emphasized that the stresses from the cold work are much higher than even the dramatic increase in creep strength demonstrated in Fig. 8.7. Extensive recovery is taken place but not to such an extent that the stationary state for annealed material is reached.

The key to understanding the influence of cold work is the unbalanced dislocation density ρ_{bnde} that is not exposed to static recovery. It is assumed to give rise to a back stress that reduces the creep rate

$$\sigma_{back} = \frac{m\alpha Gb}{2}\sqrt{\rho_{bnde}} \tag{8.20}$$

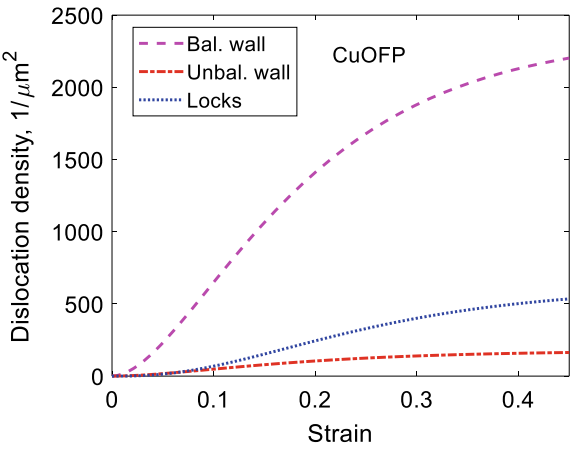

Fig. 8.9 Densities of balanced, unbalanced and lock dislocations in the cell boundaries as a function of strain for Cu-OFP. Redrawn from [15] with permission of Elsevier

If the secondary creep rate for undeformed material is $\dot{\varepsilon}_{\text{sec}}(\sigma)$, the corresponding value for cold worked material is

$$\dot{\varepsilon}_{\text{sec CW}}(\sigma) = \dot{\varepsilon}_{\text{sec}}(\sigma - \sigma_{\text{back}}) \tag{8.21}$$

where σ is the applied creep stress. It might be thought that the back stress could be measured in a stress drop test by reducing the applied stress until the creep rate vanishes. However, this is not possible. The stress drop is in general based on the assumption that the dislocation structure is essentially unchanged after the reduction in stress. With dislocation dynamics it has been demonstrated that the dislocation structure is adapted to the new stress level within milliseconds [37]. This applies both to the dislocations in the cell interior and in the cell walls. On the other hand it takes a longer time before the cell size corresponds to the new stress level. Thus the dislocation structure after a stress drop neither represents the old stress level nor the new one. Back stresses can be quite useful in modeling, but to measure them would require quite a sophisticated analysis to interpret the results.

The stress dependence of the secondary creep rate according to Eq. (4.3) is given by

$$h(\sigma) = 2\tau_{\text{L}} M(T,\sigma)\frac{\sigma^3}{(\alpha m_{\text{T}} Gb)^3} \Big/ \left(\frac{m_{\text{T}}}{bc_L} - \omega\frac{\sigma}{\alpha m_{\text{T}} Gb}\right) \tag{8.22}$$

which is inserted into Eq. (8.21)

$$\dot{\varepsilon}_{\text{sec CW}}(\sigma) = h(\sigma - \sigma_{\text{back}}) \tag{8.23}$$

To handle primary creep, Eqs. (4.6) and (4.7) are applied

$$\sigma_{\text{prim}} = \sigma_{\text{disl sec}} - \sigma_{\text{disl}} \tag{8.24}$$

$$\dot{\varepsilon} = h(\sigma + \sigma_{\text{disl sec}} - \sigma_{\text{disl}} - \sigma_{\text{back}}) \tag{8.25}$$

σ_{disl} is the stress created by the dislocations. In the secondary stage this stress takes the value σ_{dislsec}. Thus, in the secondary stage, Eq. (8.25) is identical to Eq. (8.21).

The use of Eq. (8.25) with no cold work present has been illustrated for Cu-OFP in Fig. 4.10. It was demonstrated that the primary creep could be well reproduced and that both the experimental and the model results followed the ϕ-model.

Two examples of creep-strain curves for 12% cold-work Cu-OFP are shown in Fig. 8.10.

Both the experimental and model curves show distinct primary and secondary stages. The model exaggerates somewhat the size of the primary stage and reaches the secondary stage too soon. The model accurately reproduces the creep rate in the secondary stage in spite of the fact that the creep rate is three orders of magnitude lower than without cold work. This would not be possible unless the recovery rate

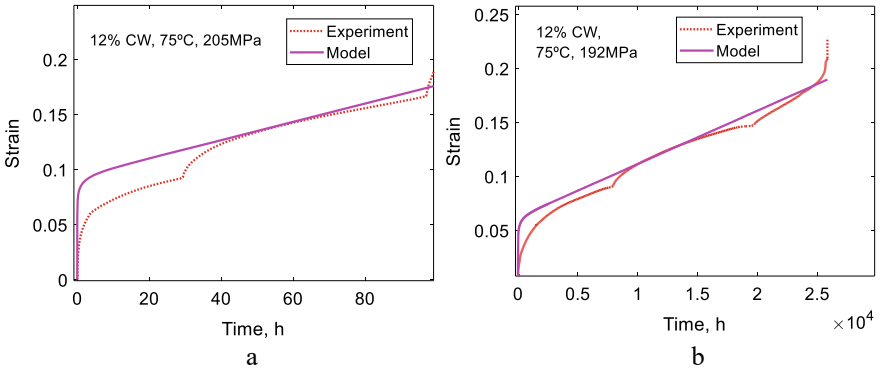

Fig. 8.10 Creep strain versus time for 12% cold worked Cu-OFP at 75 °C, **a** 205 MPa and **b** 192 MPa. Model results from integration of Eq. (8.25). Redrawn from [15] with permission of Elsevier

of the unbalanced dislocations would be much lower than for the other types of dislocations. The amount of tertiary creep is very limited in the experimental data and the tertiary stage appears late in the test. It is probably caused by necking [14]. Since necking is not taken into account in the creep model, it is then natural that tertiary creep is absent in the model curves.

For one of the cases in Fig. 8.10, the creep rate as a function of time is given in Fig. 8.11.

In the same way as in Fig. 4.10b the experiment and the model obeys the ϕ-model at least approximately. The drop in strain rate with increasing time is however much more dramatic in Fig. 8.11 in comparison to Fig. 4.10b.

Creep strain curves for 24% cold deformed Cu-OFP are illustrated in Fig. 8.12.

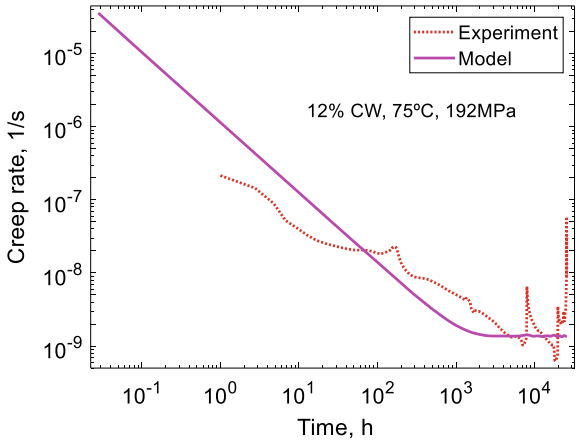

Fig. 8.11 Creep strain rate versus time for 12% cold-work Cu-OFP at 75 °C and 192 MPa. Model results from Eq. (8.25). Redrawn from [15] with permission of Elsevier

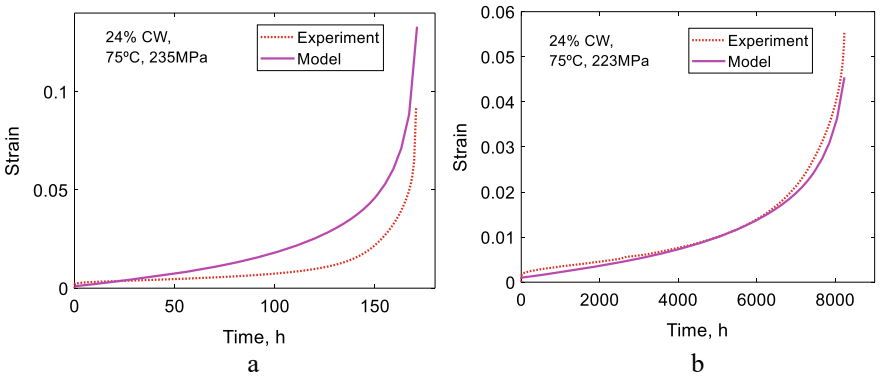

Fig. 8.12 Creep strain versus time for 24% cold-work Cu-OFP at 75 °C, **a** 235 MPa and **b** 223 MPa. Model results from integration of Eq. (8.25). Redrawn from [15] with permission of Elsevier

It is immediately evident that that creep strain curves for 24% cold deformed material are very different from those of 12% cold deformed. In Fig. 8.12, primary and secondary creep is only present to a limited extent and tertiary creep is totally dominating. It is striking that the model can reproduce the creep strain curves also in this case. The cell sizes are smaller, the boundaries are narrower and the dislocations in the walls are closer for 24% cold deformed materials in comparison to 12% cold deformed, see Figs. 8.5 and 8.6. It is believed that the continuously increasing creep rate is due to enhanced recovery [14]. Tertiary creep will be further discussed in Chap. 12.

It can be concluded that by taking the back stress from the unbalanced dislocations into account, Eq. (8.12), the main features for cold deformed Cu-OFP can be well described. Thus, the reduction of the creep rate by three and six orders of magnitude for 12 and 24% can be modeled. The whole creep curves can be reproduced in a reasonable way. In the argument above the model was analyzed for primary and secondary creep. It will be seen in Chap. 12 on tertiary creep that Eq. (8.25) is also valid for tertiary creep. This is also clearly demonstrated in Fig. 8.12.

In the analysis above it has been assumed that the substructure is stabilized by the presence of unbalanced dislocation. An alternative way is to use particles to stabilize the substructure. This is extensively utilized for modern 9%Cr steels [38]. For the influence of cold work on the creep rate of austenitic stainless steels it has been suggested that particles can lock the substructure and prevent that the effect of cold work is lost [28, 29]. However, no detailed analysis of the role of the particles has been performed.

8.4 Formation of a Dislocation Back Stress

Cu-OFP close to ambient temperatures show creep curves that have the same appearance as at much higher temperatures with distinct primary, secondary and tertiary creep. One example is given in Fig. 8.13.

The cusp on the experimental curve is due to the necessity to reload the creep machine. Thus, the creep curves have many characteristics in common with typical creep curves at higher temperatures at about half the melting point. However, there is one aspect that is different. It is in general assumed that the true creep rate is constant in the secondary stage. This is frequently a starting point in stress analysis with finite element programs. To check if that is the case for the creep curve in Fig. 8.13, it is assumed for simplicity that the creep rate can be described with a Norton equation

$$\frac{d\varepsilon}{dt} = A_0(\sigma_0 e^{\varepsilon})^{n_N} \tag{8.26}$$

where A_0 is a constant and σ_0 is the nominal applied stress. The stress exponent n_N is about 70 for the case in Fig. 8.13. The factor e^{ε} takes into account the increase in the true stress when the specimen cross section is reduced during straining. A_0 is chosen so the Norton expression crosses the experimental at 600 h, which is about half the rupture time. Equation (8.26) is now integrated starting with $\varepsilon_0 = 0.17$ to simulate the influence of primary creep. The result is included in Fig. 8.13. It is obvious that Eq. (8.26) cannot represent the creep curve in Fig. 8.13. This conclusion is in no way affected by the choice of parameter values in Eq. (8.26).

The creep exponent $\exp(n_N\ \varepsilon)$ in Eq. (8.26) has a dramatic effect on the strain rate giving a creep curve with rapidly increasing slope that is fully inconsistent with observations. The effect is in fact quite large. For example, for $\varepsilon = 0.1$, $\exp(n_N\ \varepsilon)$ is equal to 1100. This enormous increase has never been observed in creep curves and

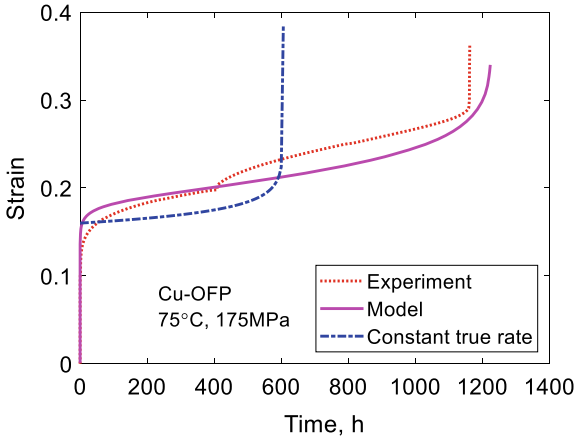

Fig. 8.13 Creep strain versus time for Cu-OFP at 75 °C and 175 MPa. Forged material. The model curve is derived with Eq. (8.25). Redrawn from [16] with permission of Elsevier

one can conclude that the simple assumption of a constant true strain is strongly at variance with observations.

Instead there must be a back stress that prevents the rapid increase in the strain rate. The back stress must be built up in the dislocation structure

$$\sigma_{\text{back}} = \sigma_{\text{disl}} - \sigma_0 \tag{8.27}$$

σ_{disl} is given by Eq. (8.3). σ_0 is again the nominal applied stress. It is related to the true applied stress σ as

$$\sigma = \sigma_0 \exp(\varepsilon) \tag{8.28}$$

The stress σ_{creep} that drives the creep deformation is given by

$$\sigma_{\text{creep}} = \sigma - \sigma_{\text{back}} = \sigma + \sigma_0 - \sigma_{\text{disl}} \tag{8.29}$$

In the second equality, Eq. (8.27) has been applied. Thus by applying Eq. (4.6), the creep rate is given by

$$\dot{\varepsilon} = h(\sigma + \sigma_0 - \sigma_{\text{disl}}) \tag{8.30}$$

It is interesting to compare this equation with the simplified version in Eq. (4.9). In Eq. (4.9), the applied stress is the nominal one but at the same time the full impact of substructure on σ_{disl} is not included. For primary and secondary creep these differences are not very important. However, Eq. (4.9) cannot describe tertiary creep contrary to Eq. (8.30), which will be explained now.

The development of the balanced and unbalanced dislocation densities ρ_{bnd} and ρ_{bnde} for the case in Fig. 8.13 is illustrated in Fig. 8.14. Equations (8.17) and (8.18) are used. The small contribution from ρ_{lock} is neglected in this case. Since the relation between ρ_{bnd} and ρ_{bnde} is not known, the relation between k_{bnd} and k_{bnde} cannot be determined. It is assumed that $k_{\text{bnd}} = k_{\text{bnde}}$ with a value of $\sqrt{2}$ that reproduces the results of Sect. 4.3.

As can be seen from Fig. 8.14a, the balanced dislocation density reaches an approximately constant value in the secondary stage whereas the unbalanced content increases continuously even during the secondary stage. The implication for the dislocation stresses is shown in Fig. 8.14b. The total stress from the balanced and the unbalanced dislocation stresses are marked as 'all'. This total dislocation stress matches the true applied stress σ in the secondary stage. This is the reason why the creep rate does not increase in an uncontrolled way. This balance is possible due to the increase in the unbalanced stress. The difference between the starting value of the applied stress of 150 MPa and the test stress of 175 MPa is the value of the yield strength. With increasing strain the total dislocation stress cannot match the true applied stress anymore. Then the tertiary stage is reached and the creep rate increases.

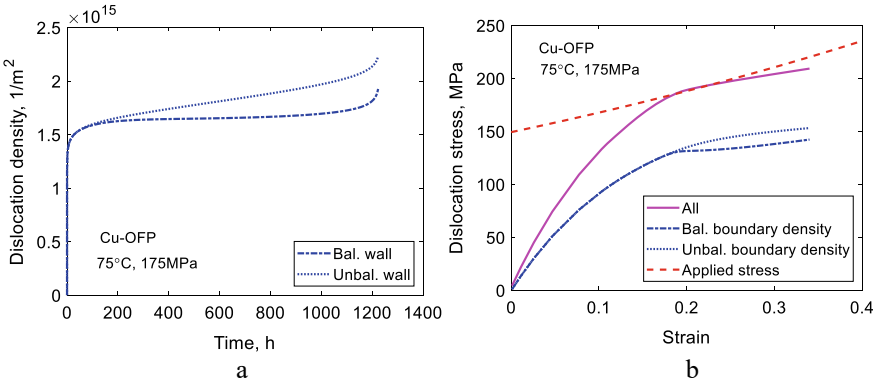

Fig. 8.14 Model results for the same case as in Fig. 8.13 (Cu-OFP at 75 °C and 175 MPa). **a** Dislocation densities versus time; **b** dislocation stresses versus strain. Redrawn from [16] with permission of Elsevier

It can be seen from Fig. 8.13 that tertiary creep is reasonably well represented. This can also be demonstrated by plotting the strain rate as a function of time, Fig. 8.15.

Although the cusps in the experimental data do not make a detailed comparison possible, it is evident that the overall picture reproduces both the primary and tertiary stages in a good way.

It can be concluded that the presence of back stress from the unbalanced dislocations, prevents the creep rate from increasing in an uncontrolled way that would be suggested if a constant true strain rate in the secondary would be assumed. In addition, the introduction of this back stress makes it possible to model tertiary creep.

Also stress strain curves seem to be affected by the back stress. One example is illustrated in Fig. 8.16. A stress strain curve for 15% cold worked Cu-OFP is shown. A model curve using Eqs. (8.3), (8.17) and (8.18) is also included in Fig. 8.16a.

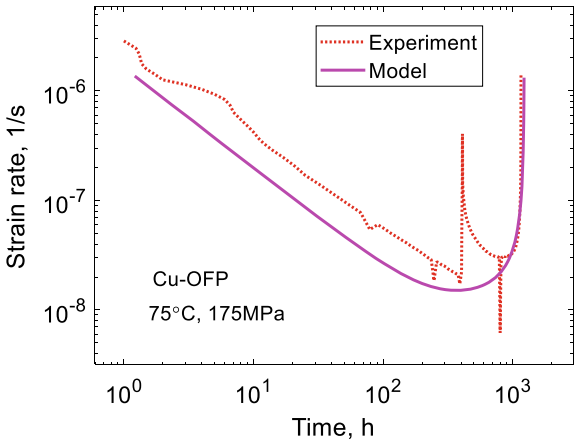

Fig. 8.15 Creep rate versus time for the curve in Fig. 8.13 (Cu-OFP, 75 °C and 175 MPa). Forged material. Redrawn from [16] with permission of Elsevier

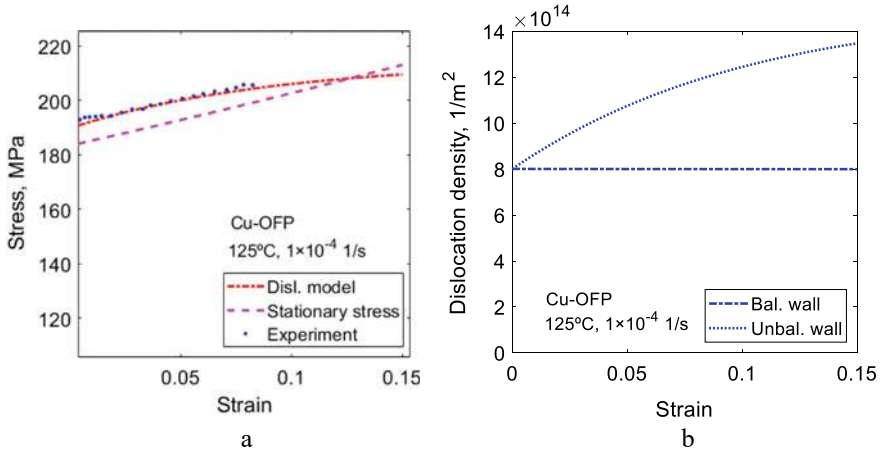

Fig. 8.16 Stress strain curve for 15% cold worked Cu-OFP at 125 °C and 1×10^{-4} 1/s; **a** the experimental curve is compared to modeling results with Eqs. (8.3), (8.17) and (8.18) for balanced and unbalanced boundary dislocations; **b** balanced and unbalanced boundary (wall) dislocation density. Experiments from [39]. Redrawn from [16] with permission of Elsevier

It is assumed that the stress strain relations are controlled by the same equations as the creep curves in the same way as in other parts of this book. This means that the stress level at higher strains should correspond to the stationary stress in a creep test. This stress is given by

$$\sigma_{\text{stat}} = \sigma_{\text{stat0}} e^{\varepsilon} \tag{8.31}$$

where σ_{stat0} and σ_{stat} are the nominal and the true stationary stress that give the same strain rate as in the stress strain curve (1×10^{-4} 1/s at 125 °C). The stationary stress is not identical to the stress strain curve but it is very close to supporting the assumed principle.

The strain dependence of the dislocation densities is given in Fig. 8.16b. The balanced and unbalanced dislocation densities are assumed to be the same at zero strain. Using these assumptions, the values of k_{bnd} and k_{bnde} can be determined, see [16] for details. It can be seen from Fig. 8.16b that the unbalanced dislocation density increases with strain and compensates for the increase in the true stationary stress.

It has been seen above that both creep curves and stress strain curves are strongly affected by the back stress from the unbalanced dislocation content. In particular for creep, it was demonstrated above that the effect is huge and cannot be ignored. This is especially important to take into account in stress analysis with finite element methods (FEM). There are two straight forward alternative ways to handle the problem. The first way is to take the back stress into account explicitly. This requires however the development of special software. The other alternative is to replace the true stress σ with $\sigma \exp(-\varepsilon)$. This alternative represents no practical problem but there is a

psychological barrier because it is not in accordance with what people have been trained to do. However, ignoring it will give rise to large errors.

The dramatic effect of the back stress has only been verified for copper at lower temperatures. There are no reasons to believe that it should not applicable to other materials as well because there is nothing in the derivation that is specific for copper. The open question is to what temperature the effect survives. At a sufficiently high temperature the back stress from the unbalanced dislocations cannot be expected to be stable anymore. This section is mainly taken from [16] where further detail can be found.

8.5 Summary

- Dislocation cells are formed in virtually all alloys during plastic deformation at ambient or near ambient temperatures. Typically the cells and the surrounding cell walls are well developed after a plastic strain of about 0.3. At elevated temperatures subgrains are formed instead at least for alloys where the stacking fault energy is not too low. The subboundaries consist of thin networks of dislocations. The presence of cells or subgrains is referred to as substructure.
- Although the presence of the substructure has been discussed in many contexts in the literature, the development of substructure has only been modeled recently. Models for subgrain formation during creep and creation of cells during plastic deformation are presented in the chapter. The models can describe the limited amount of data that are available.
- During plastic deformation dislocations with opposite burgers vectors move in opposite directions in cells with the results that some parts of the cell walls have only one type of dislocations. This is referred to as unbalanced dislocations.
- The unbalanced dislocations are not exposed to static recovery since they cannot meet a dislocation of opposite sign. As a consequence the dislocation density and creep strength can continue to grow. This is believed to be the main mechanism behind the sometimes dramatic increase of the creep strength after cold work.
- The presence of unbalanced dislocations can also explain why creep curves at near ambient temperatures have a similar appearance as at much higher temperatures. The unbalanced dislocations form a massive back stress that counteracts the rapidly increasing true applied stress with increasing strain.

References

1. D.J. Michel, J. Moteff, A.J. Lovell, Substructure of type 316 stainless steel deformed in slow tension at temperatures between 21° and 816 °C. Acta Metall. **21**, 1269–1277 (1973)
2. M.E. Kassner, M.T. Pérez-Prado, Five-power-law creep in single phase metals and alloys. Prog. Mater Sci. **45**, 1–102 (2000)

3. R. Wu, N. Pettersson, Å. Martinsson, R. Sandström, Cell structure in cold worked and creep deformed phosphorus alloyed copper. Mater. Charact **90**, 21–30 (2014)
4. L. Bendersky, A. Rosen, A.K. Mukherjee, Creep and dislocation substructure. Int. Metals Rev. **30**, 1–15 (1985)
5. O.D. Sherby, R.H. Klundt, A.K. Miller, Flow stress, subgrain size, and subgrain stability at elevated temperature. Metall. Trans. A **8**, 843–850 (1977)
6. M.E. Kassner, A.K. Miller, O.D. Sherby, Separate roles of subgrains and forest dislocations in the isotropic hardening of type 304 stainless steel. Metall. Trans. A **13**, 1977–1986 (1982)
7. A. Orlová, Constitutive description of creep in polygonized substructures. Mater. Sci. Eng. A **194**, L5–L9 (1995)
8. H. Mughrabi, Dislocation wall and cell structures and long-range internal stresses in deformed metal crystals. Acta Metall. **31**, 1367–1379 (1983)
9. H. Magnusson, R. Sandstrom, The role of dislocation climb across particles at creep conditions in 9–12 pct Cr steels. Metall. Mater. Trans. A **38A**, 2428–2434 (2007)
10. S. Straub, W. Blum, D. Röttger, P. Polcik, D. Eifler, A. Borbély, T. Ungár, Microstructural stability of the martensitic steel X20CrMoV12-1 after 130000 h of service at 530 °C. Steel Res. **68**, 368–373 (1997)
11. P. Polcik, T. Sailer, W. Blum, S. Straub, J. Buršík, A. Orlová, On the microstructural development of the tempered martensitic Cr-steel P 91 during long-term creep—A comparison of data. Mater. Sci. Eng. A **260**, 252–259 (1999)
12. W. Blum, S. Straub, P. Polcik, K.H. Mayer, Quantitative investigation of microstructural evolution of two melts of the martensitic rotor steel X12CrMoWVNbN10-1-1 during long-term creep. VGB PowerTech **80**, 59–66 (2000)
13. R. Sandstrom, Subgrain growth occurring by boundary migration. Acta Metall. Mater. **25**, 905–911 (1977)
14. F. Sui, R. Sandström, Basic modelling of tertiary creep of copper. J. Mater. Sci. **53**, 6850–6863 (2018)
15. R. Sandström, The role of cell structure during creep of cold worked copper. Mater. Sci. Eng. A **674**, 318–327 (2016)
16. R. Sandström, Formation of a dislocation back stress during creep of copper at low temperatures. Mater. Sci. Eng. A **700**, 622–630 (2017)
17. D. Kuhlmann-Wilsdorf, Theory of plastic deformation: properties of low energy dislocation structures. Mater. Sci. Eng. A **113**, 1–41 (1989)
18. M.R. Staker, D.L. Holt, The dislocation cell size and dislocation density in copper deformed at temperatures between 25 and 700 °C. Acta Metall. **20**, 569–579 (1972)
19. U.F. Kocks, H. Mecking, Physics and phenomenology of strain hardening: the FCC case. Prog. Mater. Sci. **48**, 171–273 (2003)
20. D.L. Holt, Dislocation cell formation in metals. J. Appl. Phys. **41**, 3197–3201 (1970)
21. K.D. Challenger, J. Moteff, Quantitative characterization of the substructure of AISI 316 stainless steel resulting from creeP. Metall Trans **4**, 749–755 (1973)
22. V. Ganesan, M.D. Mathew, P. Parameswaran, K. Laha, Effect of nitrogen on evolution of dislocation substructure in 316LN SS during creep. Procedia Eng. **55**, 36–40 (2013)
23. D. Molnár, X. Sun, S. Lu, W. Li, G. Engberg, L. Vitos, Effect of temperature on the stacking fault energy and deformation behaviour in 316L austenitic stainless steel. Mater. Sci. Eng. A **759**, 490–497 (2019)
24. G. Meric de Bellefon, J.C. van Duysen, K. Sridharan, Composition-dependence of stacking fault energy in austenitic stainless steels through linear regression with random intercepts. J. Nucl. Mater. **492**, 227–230 (2017)
25. J.-S. Zhang, 2—Evolution of dislocation substructures during creep, in *High Temperature Deformation and Fracture of Materials* (Woodhead Publishing, 2010), pp. 14–27
26. R. Sandström, Formation of cells and subgrains and its influence on properties. Metals **12** (2022)
27. N.A. Koneva, V.A. Starenchenko, D.V. Lychagin, L.I. Trishkina, N.A. Popova, E.V. Kozlov, Formation of dislocation cell substructure in face-centred cubic metallic solid solutions. Mater. Sci. Eng. A **483–484**, 179–183 (2008)

28. V.D. Vijayanand, M. Nandagopal, P. Parameswaran, K. Laha, M.D. Mathew, Effect of prior cold work on creep rupture and tensile properties of 14Cr–15Ni–Ti stainless steel. Procedia Eng. **55**, 78–81 (2013)
29. G. Pilloni, E. Quadrini, S. Spigarelli, Interpretation of the role of forest dislocations and precipitates in high-temperature creep in a Nb-stabilised austenitic stainless steel. Mater. Sci. Eng. A **279**, 52–60 (2000)
30. J.L. Adelus, V. Guttmann, V.D. Scott, Effect of prior cold working on the creep of 314 alloy steel. Mater. Sci. Eng. **44**, 195–204 (1980)
31. T. Furuta, S. Kawasaki, R. Nagasaki, The effect of cold working on creep rupture properties for helium-injected austenitic stainless steel. J. Nucl. Mater. **47**, 65–71 (1973)
32. F. Müller, A. Scholz, C. Berger, R.-U. Husemann, Influence of cold working in creep and creep rupture behaviour of materials for super-heater tubes of modern high-end boilers and for built-in sheets in gas turbines, in *2nd International ECCC Conference. Creep & Fracture in High Temperature Components–Design & Life Assessment Issues*, ed. by S.R.H. I A Shibli (2009)
33. K.D. Challenger, J. Moteff, A correlation between strain hardening parameters and dislocation substructure in austenitic stainless steels. Scr. Metall. **6**, 155–160 (1972)
34. F. Roters, D. Raabe, G. Gottstein, Work hardening in heterogeneous alloys—A microstructural approach based on three internal state variables. Acta Mater. **48**, 4181–4189 (2000)
35. A. Argon, *Strengthening Mechanisms in Crystal Plasticity* (Oxford University Press, Oxford, 2008)
36. P. Ambrosi, C. Schwink, Slip line length of copper single crystals oriented along [100] and [111]. Scr. Metall. **12**, 303–308 (1978)
37. A.H. Delandar, R. Sandström, P. Korzhavyi, The role of glide during creep of copper at low temperatures. Metals **8** (2018)
38. H. Magnusson, R. Sandstrom, Creep strain modeling of 9–12 pct Cr steels based on microstructure evolution. Metall. Mater. Trans. A **38A**, 2033–2039 (2007)
39. R. Sandström, J. Hallgren, The role of creep in stress strain curves for copper. J. Nucl. Mater. **422**, 51–57 (2012)

Chapter 9
Grain Boundary Sliding

Abstract During plastic deformation at elevated temperatures, grains move relative to each other which is referred to as grain boundary sliding (GBS). The amount of GBS is proportional to the creep strain with a proportionality constant that is known from finite element analyses, and found to agree with experiments for Cu. The most import effect of GBS is that it gives rise to the initiation of creep cavities, Chap. 10. GBS is also the main mechanism for superplasticity. A basic model for superplasticity is presented.

9.1 General

During creep neighboring grains are displaced along the grain boundaries (GB) relative to each other when they are exposed to shear stresses. This is referred to as *grain boundary sliding* (GBS). GBS can easily be observed by metallography by introducing scribe lines or a micro grid before the test. The principle is illustrated in Fig. 9.1. Using scribe lines on a polished and etched surface, the shear offset under application of stress can be observed and measured where the lines cross the grain boundary (GB).

The appearance of GBS in a micrograph is shown in Fig. 9.2.

The displacement of the scribe line in Fig. 9.2 was about 5 μm, which is the amount of GBS. For a flat GB, the sliding itself experiences little resistance but significant stresses appear at the triple points in the grain boundary corners, which have to be relaxed by creep deformation. Sometimes the stresses are large enough to initiate micro-cracks at the triple points. This is illustrated in Fig. 9.3.

GBS can also result in grains moving perpendicular to the surface. This has the consequence that the specimen surface appears wavy. This has often been observed for pure Al, see for example [2]. However, using the GB offset technique illustrated in Fig. 9.1, the GBS events are only found locally at a limited number of GBs [1, 3]. Unfortunately, only a limited number of studies where a systematic measurement of the GB offsets has been performed are available.

R. Sandström, *Basic Modeling and Theory of Creep of Metallic Materials*, Springer Series in Materials Science 339,
https://doi.org/10.1007/978-3-031-49507-6_9

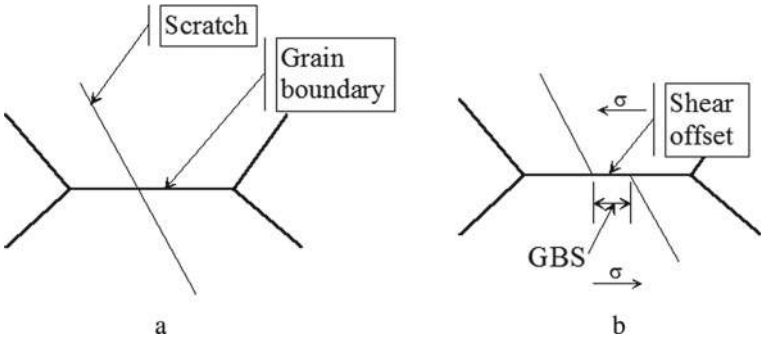

Fig. 9.1 Schematic illustration of observation and measurement of GBS; **a** before test; **b** after test

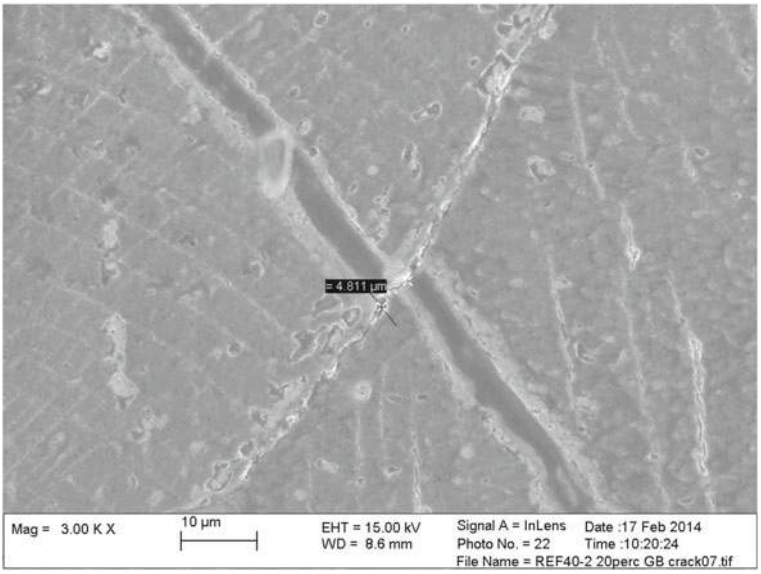

Fig. 9.2 SEM observations of GBS in Cu-OFP after 507 h in a creep test at 125ºC, 47 MPa. The strain was 20.8%. The grain boundary goes from northeast to southwest. The scribe line is almost perpendicular to the grain boundary. Reprinted from [1] with permission of Elsevier

What is causing GBS is not understood in detail. From TEM observations on Al, Kokawa et al. have suggested that it is only random grain boundaries that slide. Lattice dislocations move into the GBs and introduce the sliding. Ordered GBs (coincidence sites) contain extrinsic GB dislocations but they do not contribute to the sliding [4].

One sometimes distinguishes between two types of GBS: Rachinger sliding and Lifshitz sliding that occur during dislocation creep and diffusion creep, respectively [5]. Unfortunately, it has turned out to be difficult to distinguish between dislocation creep and diffusion creep experimentally even if the principles are straightforward.

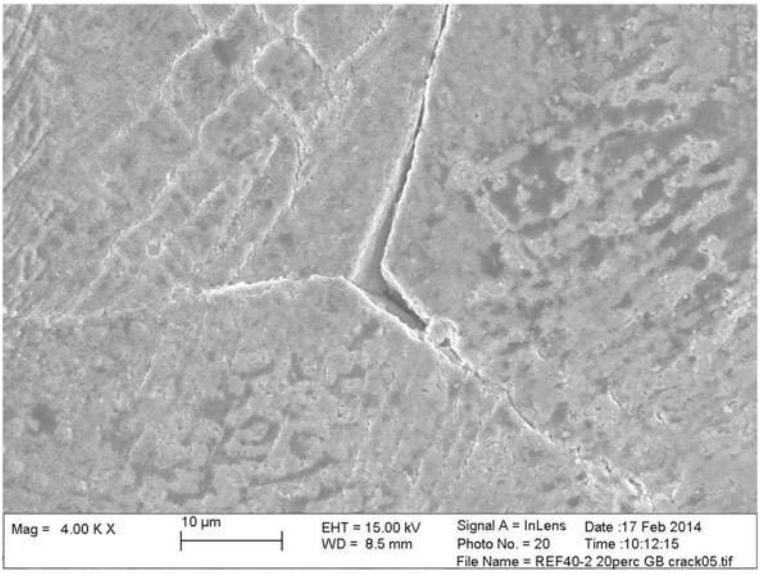

Fig. 9.3 SEM observation of a micro-crack at a triple point after GBS. The same specimen as in Fig. 9.2 [1]

There are numerous scientific papers discussing this issue. The simple principle that will be followed in this book is that it is Rachinger sliding when we discuss dislocation creep and Lifshitz sliding when diffusion creep is analyzed but without being explicit about the type of sliding.

GBS gives a contribution to the overall creep strain. In general, this contribution is expected to be limited. The model analysis in Sect. 9.3 suggests that the contribution is about 15% if all the grain boundaries are active in GBS. However, since only a limited number of GBs give GBS offsets, the effective contribution is likely to be much smaller. However, there is one main exception, superplasticity. The main mechanism for superplastic deformation is believed to be GBS of a fine grained structure, where more or less all grain boundaries participate. This means that the deformation takes place by the sliding of grains against each other without the grains being elongated. In this way large elongation values can be obtained during superplasticity. Empirical modeling of superplasticity will be discussed in Sect. 9.2. In Sect. 9.3, a basic model for grain boundary sliding is presented. This result is used in Sect. 9.4 to find a basic model for superplasticity. Another case where GBS plays a major role is for nano-crystalline materials. The reason is the same as for superplastic materials. The GBs constitute a large fraction of the nano-crystalline structures, and GBS is an important deformation mechanism [6]. However, it has turned out that the behavior is complex and the topic will not be dealt with here.

During creep, the formation and growth of cavities generate creep damage and often initiate failure. In the past, it was believed that creep cavities were nucleated due to the presence of large local stresses. However, detailed analysis demonstrated

that this would require very high stresses and in addition these high stresses would relax very quickly during creep. Nowadays, most scientists are convinced that GBS is the main mechanism for forming cavities. For example, it can quantitatively explain the strain dependence of the number of creep cavities and why creep cavities can be formed at low creep stresses. Initiation and growth of cavities will be discussed in Chap. 10. The required model for GBS will be presented in Sect. 9.3.

9.2 Empirical Modeling of GBS During Superplasticity

Discussion of various aspects of GBS can be found in many papers. However, the number of direct measurements of GBS is limited. Results for copper will be presented in Sect. 9.3 together with basic modeling. The only area where numerous measurements can be found is for superplasticity, where stress strain curves and creep rates have been determined. In general, it is assumed that superplasticity is controlled by GBS.

Superplasticity is a mechanism where elongations of several hundred percent can be achieved. This makes it possible to produce deeper drawings and more complex shapes than in ordinary sheet pressing. There are a number of requirements on the alloy to enable superplasticity [7]. The grain size must be fine, less than 10 μm and equiaxed. The pressing must be performed at temperatures above half the absolute melting point ($>T_m/2$). The strain rate should lie in the interval 1×10^{-5} to 1×10^{-1} 1/s. The lower limit is to ensure that pressings can be carried out in a reasonable time. The upper limit is to prevent damage formation such as the development of cavities. Finally the strain rate sensitive m_r

$$m_r = \frac{\partial \ln \sigma}{\partial \ln \dot{\varepsilon}}$$

should be about 0.5. Under stationary condition, m_r is the inverse of the stress exponent n_N

$$m_r = 1/n_N \tag{9.1}$$

The choice of temperature is critical. If the temperature is too low, climb will be slow and the pressing would require a long time. A too high temperature will initiate grain growth that will destroy the superplastic properties. Often a two-phase structure is used to prevent grain growth. An alternative is to have a fine distribution of particles that acts as grain refiner. Both these alternatives are associated with the risk that abnormal grain growth is initiated implying that some very large grains are created, which is totally unacceptable [8].

Superplastic formed parts are nowadays used in many applications [9]. High strength alloys are typically difficult to form with conventional techniques because of

limited ductility. Then superplastic forming can be quite helpful. In particular, applications in aero planes, trains and cars are common. Special high strength aluminum alloys probably cover most of the market. However, there are many components produced in Mg, Ti and Ni base alloys as well. The total number of commonly used alloys for superplastic forming is not very large. Barnes lists 13 alloys [9].

After superplastic deformation, the grain shape is still equiaxed. The only imaginable mechanism that can accomplish this is GBS. Detailed measurements of the amount of GBS during superplasticity confirm that GBS can account for almost all of the strain [10]. Creep deformation inside the grains must also take place to accommodate local strains. First, bulk dislocations moving towards the GBs are the basis of GBS. Secondly, the grains must constantly adapt their shape during the deformation and this takes place by intragranular creep.

A number of authors have used empirical relations to describe the strain rate during superplasticity as a function of temperature, stress and grain size, see for example [11, 12]. The most common form is

$$\dot{\varepsilon} = A\frac{bD_{\mathrm{GB}}}{Gk_{\mathrm{B}}T}\left(\frac{b}{d_{\mathrm{g}}}\right)^2\sigma^2 \tag{9.2}$$

where $\dot{\varepsilon}$ is the strain rate, σ the applied stress, b burgers vector, G the shear modulus, d_{g} the grain size, D_{GB} the grain boundary diffusion coefficient and A a dimensionless factor. For GBS it is natural to assume that it is grain boundary diffusion that supplies the vacancies although the contribution from the lattice dislocation is also of importance. Eq. (9.2) gives a stress exponent of 2 and exponent of -2 for the grain size. It is not possible to intuitively understand the values of these exponents. However, it will be explained in Sect. 9.4 that detailed modeling actually gives these exponents.

Data for a superplastic Zn22%Al alloy is illustrated in Fig. 9.4.

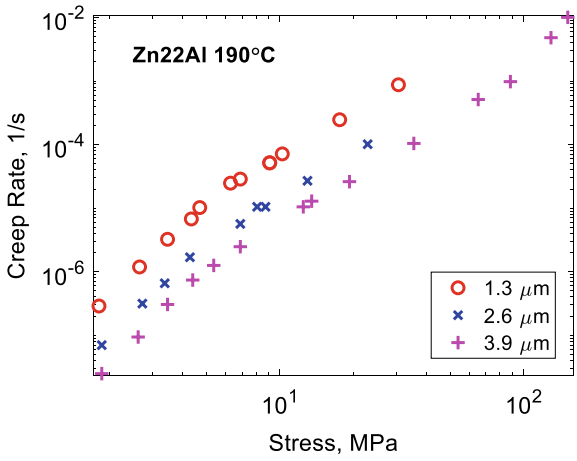

Fig. 9.4 Creep rate versus stress for at Zn22%Al alloy at 190 °C at the three grain sizes 1.3, 2.6. and 3.9 μm. Data from [13]. The grain sizes in [13] have been transferred to linear intercept values

In Fig. 9.4, there are two different levels of the stress exponent. At low stresses, the stress exponent is 4, at higher stresses 2. It is the high stress range where the superplastic behavior appears. The lower stress range is nowadays assumed to be due to the presence of impurities [5]. This range will be discussed further in Sect. 9.4. In the superplastic range the grain size dependence has an exponent of about −2 again in accordance with Eq. (9.2). A comparison of the data with modeling will be presented in Sect. 9.4.

9.3 Grain Boundary Sliding in Copper

Crossman and Ashby [14] formulated a model for the contribution from GBS to the overall creep strain. The basic steps in this model will be followed. The inverse relation namely the amount of GBS generated by an amount of creep strain is equally interesting. The relative displacement u_{GB} of neighboring grains is controlled by viscous flow. If the GB is exposed to a shear stress, the displacement rate can then be expressed as

$$\frac{du_{\mathrm{GB}}}{dt} = \frac{\delta_{\mathrm{GB}}}{\eta_{GB}}\tau \tag{9.3}$$

where δ is the width of the grain boundaries (taken as 2 b, where b is burgers' vector; a common assumption) and τ is the shear stress acting on the grain boundary. η_{GB} is the viscosity of a flat grain boundary

$$\eta_{\mathrm{GB}} = \frac{k_{\mathrm{B}}T}{8bD_{\mathrm{GB}}} \tag{9.4}$$

k_{B} is Boltzmann's constant, T the absolute temperature and D_{GB} the grain boundary diffusion coefficient. If ledges with the height h_{L} are present, the viscosity in Eq. (9.4) for a flat GB is increased by a factor of $(h_{\mathrm{L}}/b)^2$ [15]

$$\eta_{\mathrm{GB}} = \frac{k_{\mathrm{B}}Th_{\mathrm{L}}^2}{8b^3D_{\mathrm{GB}}} \tag{9.5}$$

Presence of a distribution of particles also increases the viscosity [15]

$$\eta_{\mathrm{GB}} = \frac{k_{\mathrm{B}}Tf_Ad_{\mathrm{part}}^2}{8b^3D_{\mathrm{GB}}} \tag{9.6}$$

where f_A and d_{part} are the area fraction and diameter of particles in the boundary. Equations (9.5)–(9.7) thus represent three different types of GBs. A finite element analysis was performed for hexagonal grains with sliding boundaries and grains following power-law creep [14]. The sliding of the boundaries is so fast that in

general they can be considered as flaws. The overall creep rate could be described by introducing a stress enhancement factor f_c

$$\dot{\varepsilon} = \dot{\varepsilon}_0 \left(f_c \frac{\sigma}{\sigma_0} \right)^n \tag{9.7}$$

σ is the applied stress and n is the creep exponent. $\dot{\varepsilon}_0$ and σ_0 are constants. Crossman and Ashby [14] gave a value of $f_c = 1.1$. Ghahremani refined the analysis and found a value of $f_c = 1.16$–1.3 [16]. Also Hsia et al. [17] repeated the analysis and got $f_c = 1.17$ for the same geometry. In [14, 16] also the contribution to the overall displacement rate was assessed

$$\phi = \frac{\dot{U}_{\mathrm{GBS}}}{\dot{U}_{\mathrm{All}}} \tag{9.8}$$

$\dot{U}_{\mathrm{All}}$ is the total displacement rate, which must be precisely defined in relation to the grain structure. The ϕ values found were from 0.15 ($n_N = 1$) to 0.33 ($n_N = \infty$) depending on the creep exponent [16]. Both $\dot{U}_{\mathrm{All}}$ and $\dot{U}_{\mathrm{GBS}}$ are proportional to the creep rate $\dot{\varepsilon}$. The finite element analysis [14] shows that the overall displacement rate can be expressed as

$$\dot{U}_{All} = \frac{3 d_g \dot{\varepsilon}}{2\xi} \tag{9.9}$$

where d_g is the linear intercept grain size and ξ is a factor that gives the relation to the side length a_{hex} of the hexagonal grains [1].

$$\xi = d_g / a_{\mathrm{hex}} = \pi/4 \tan(\pi/6) = 1.36 \tag{9.10}$$

It was early on recognized that the displacement due to GBS is proportional to the creep strain [18]

$$u_{\mathrm{GBS}} = C_s \varepsilon \tag{9.11}$$

From Eqs. (9.8), (9.9), and (9.11), the constant C_s can be expressed as

$$C_s = \dot{U}_{\mathrm{GBS}} / \dot{\varepsilon} = \frac{3\phi}{2\xi} d_g \tag{9.12}$$

The model results above will now be compared with experiments for oxygen free copper with P (Cu-OFP) and without P (Cu-OF). Observed values from three investigations are shown in Fig. 9.5.

The values in Fig. 9.5 represent three types of tests: creep at constant load [19], creep at constant loading rate [1] and slow strain rate tests at constant strain rate [20]. Pettersson's values increase faster with strain in particular in comparison to the

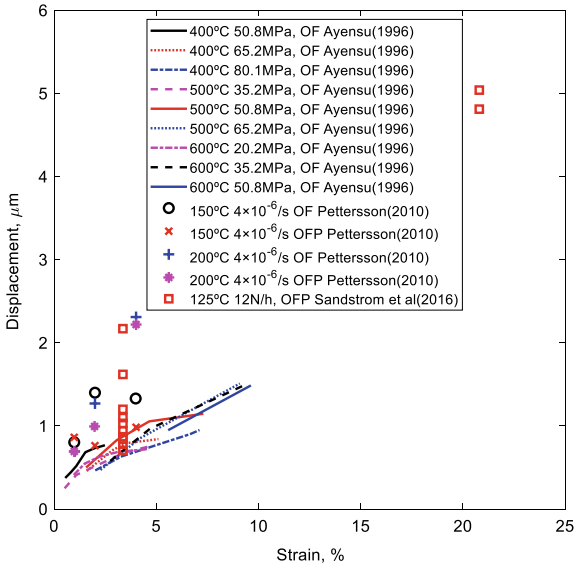

Fig. 9.5 Observed displacements at grain boundaries as a function of strain in Cu-OF and Cu-OFP. Data from [1, 19, 20]. Redrawn from [1] with permission of Elsevier

data from [19]. Considering that a wide range of temperatures and strain rates are covered, it is not surprising that the values differ. But they are clearly of the same order.

In Fig. 9.6, the displacement in Fig. 9.5 are divided by the strain to obtain the values for the constant C_s in Eq. (9.11).

The constant C_s depends on the strain. C_s is higher at lower strains in all three studies. There is a tendency that the rate of decrease is slower at higher strains. This

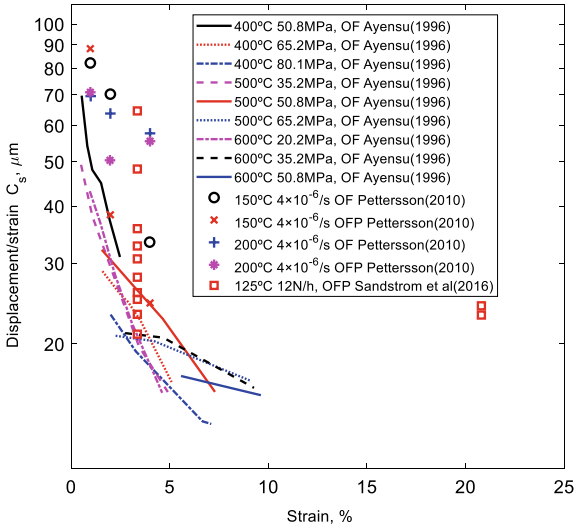

Fig. 9.6 Observed displacements at grain boundaries as a function of strain in Cu-OF and Cu-OFP divided by the creep strain giving the constant C_s, Eq. (9.11). Data from [1, 19, 20]. Redrawn from [1] with permission of Elsevier

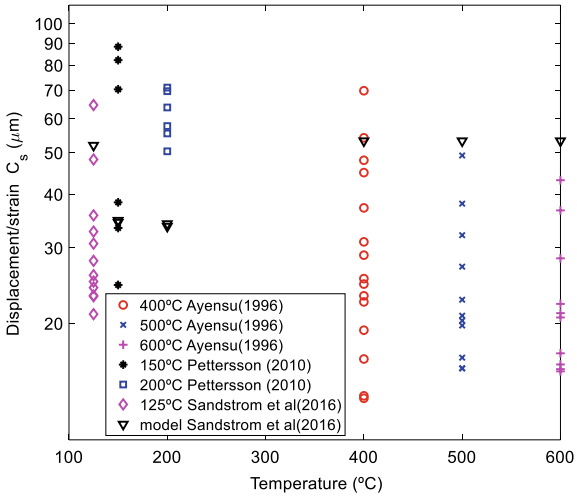

Fig. 9.7 Comparison of modeled and observed values for the constant C_s, Eq. (9.11). Modeled values according to Eq. (9.12). Data from [1, 19, 20]. Redrawn from [1] with permission of Elsevier

decrease in slope has also been found for austenitic stainless steels, although the absolute value of C_s is smaller [21]. A complicating factor is that at large strains new grains are frequently formed [22].

The observed values for C_s are compared to the model in Eq. (9.12) in Fig. 9.7. Since the model does not take the strain dependence into account, experimental values for all strains are included in the Figure. The model values are at the lower end of the slow strain rate data, but at the upper end for the other data. One complication is that both large and fine grains were present in the copper in [1]. Since the model values are proportional to the grain size, the use of an average grain size does not take this variation into account. Results on stainless steels demonstrate that the effect is weaker than the model suggests. If this is the case also for copper, the C_s values would be underestimated in [20] where grain size is smaller and overestimated in [19] where the grain size is larger. This is consistent with the results in Fig. 9.7.

Although there is considerable variation, a general approximate value of 50 μm for C_s seems reasonable, taking into account that it covers a range of temperatures, strain rates and three testing techniques. No significant difference between Cu-OF and Cu-OFP has been observed.

9.4 Superplasticity

As was explained in Sect. 9.2, studies of superplasticity show that the strain rate during this process can be described by an empirical equation given in Eq. (9.2). According to this equation, the strain rate is proportional to the grain boundary diffusion coefficient D_{GB}, it has a stress exponent of 2 and the exponent for the

grain size dependence is −2. The controlling mechanism is well established. Intuitively this is obvious because an equiaxed grain structure remains equiaxed even after larger strain, and this would be difficult to reconcile unless GBS is the controlling mechanism. The fact that GBS is highly active has also been demonstrated in metallographic studies [10].

In spite of the fact that the mechanisms are well established and the process is well described, no basic model of the creep strain rate during superplasticity has been found in the literature. An attempt will be made here is to formulate such a model.

Grain boundaries (GBs) are normally considered as good sources and sinks for dislocations. For superplastic alloys that are fine grained, the recovery of dislocations at the grain boundaries must be taken into account. This is referred to as *GB annihilation recovery*. The rate for this mechanism can be represented as

$$\frac{d\rho}{dt} = -\frac{2\rho v_{\mathrm{cl}}}{d_{\mathrm{g}}} = -\frac{2\rho}{d_{\mathrm{g}}} M_{\mathrm{cl}}^{\mathrm{GB}} b\sigma \tag{9.13}$$

where ρ is the dislocation density, v_{cl} the climb velocity and $M_{\mathrm{cl}}^{\mathrm{GB}}$ the climb mobility. A dislocation has to travel a distance of half the grain size to reach a GB and to be annihilated. Since GBS is the controlling mechanism, the dislocations are active close to the GB. Consequently, the climb mobility $M_{\mathrm{cl}}^{\mathrm{GB}}$ involves GB diffusion. The effective contribution from GB to the diffusion coefficient can be expressed as

$$D_{\mathrm{GBeff}} = \frac{\pi \delta_{\mathrm{GB}}}{d_{\mathrm{g}}} D_{\mathrm{GB}} = \frac{\pi \delta_{\mathrm{GB}}}{d_{\mathrm{g}}} D_{\mathrm{GB0}} e^{-\frac{Q_{\mathrm{GB}}}{R_{\mathrm{G}} T}} \tag{9.14}$$

where δ_{GB} is the width of the grain boundary (taken as 2 b), D_{GB} is the GB diffusion coefficient, D_{GB0} the pre-exponential factor of D_{GB} and Q_{GB} the activation energy for grain boundary diffusion. To find $M_{\mathrm{cl}}^{\mathrm{GB}}$ Eq. (9.14) for the effective grain boundary diffusion coefficient should replace the lattice diffusion coefficient in the expression for the climb mobility in Eq. (2.34)

$$M_{\mathrm{cl}}^{\mathrm{GB}} = \frac{\pi \delta_{\mathrm{GB}}}{d_{\mathrm{g}}} \frac{D_{\mathrm{GB}} b}{k_{\mathrm{B}} T} e^{\frac{\sigma b^3}{k_{\mathrm{B}} T}} \tag{9.15}$$

The contribution to the recovery in Eq. (9.14), can now be added to the total expression for time derivative in Eq. (2.17)

$$\frac{d\rho}{dt} = \frac{m_{\mathrm{T}}}{bc_L} \rho^{1/2} \dot{\varepsilon} - \omega \rho \dot{\varepsilon} - 2\tau_{\mathrm{L}} M_{\mathrm{cl}} \rho^2 - \frac{2\rho}{d_{\mathrm{g}}} M_{\mathrm{cl}}^{\mathrm{GB}} b\sigma \tag{9.16}$$

In Eq. (9.16), a time derivative instead of the strain derivative in Eq. (2.15) is used. This is achieved by multiplying the equation by the strain rate. There are three recovery terms (with minus sign) on the right hand side of Eq. (9.16): dynamic, static and GB annihilation recovery. The role of the dynamic recovery is small and that term is dropped in Eq. (9.16).

Considering stationary conditions where the time derivative disappears, an expression for the stationary creep rate can be obtained from Eq. (9.16)

$$\dot{\varepsilon}_{\text{sec}} = (2\tau_{\text{L}} M_{\text{cl}} \rho^{3/2} + \frac{2\rho^{1/2}}{d_{\text{g}}} M_{\text{cl}}^{\text{GB}} b\sigma)/(\frac{m_{\text{T}}}{bc_L}) \tag{9.17}$$

To transfer Eq. (9.17) to stresses, the Taylor Eq. (2.29) is used

$$\alpha m_{\text{T}} G b \rho^{1/2} = \sigma - \sigma_i \tag{9.18}$$

where α is the deformation hardening constant and σ_{i} the internal stress from other contributions such as precipitation hardening. Inserting Eqs. (9.15) and (9.18) into (9.17) gives

$$\dot{\varepsilon}_{\text{sec}} = \left(2\tau_{\text{L}} M_{\text{cl}} \left(\frac{(\sigma - \sigma_i)}{\alpha m_{\text{T}} G b}\right)^3 + \frac{2(\sigma - \sigma_i)^2}{(\alpha m_{\text{T}} G b)} \frac{\pi \delta_{\text{GB}}}{d_{\text{g}}^2} \frac{D_{\text{GB}} b^2}{k_{\text{B}} T} e^{\frac{\sigma b^3}{k_{\text{B}} T}}\right) / \left(\frac{m_{\text{T}}}{bc_L}\right) \tag{9.19}$$

Equation (9.19) includes contributions from both creep in the bulk and GBS. To analyze the contribution from GBS, it is given separately

$$\dot{\varepsilon}_{\text{sec}}^{\text{GBS}} = \frac{2bc_{\text{L}}}{\alpha m_{\text{T}}^2} \frac{(\sigma - \sigma_i)^2}{G} \frac{\pi \delta_{\text{GB}}}{d_{\text{g}}^2} \frac{D_{\text{GB}} b}{k_{\text{B}} T} \tag{9.20}$$

Equation (9.20) gives a stress exponent of 2 and exponent of −2 for the grain size dependence. The creep rate in this equation is proportional to the grain boundary diffusion coefficient. These features are the same as in the empirical Eq. (9.2). Equation (9.20) is compared to experimental data for the eutectoid alloy Zn22%Al in Fig. 9.8.

The creep rate is shown as a function of stress for five grain sizes at 230 °C. In the model a grain boundary diffusion coefficient for Zn is used [23]. The experimental curves have two slopes. The slope at the lower range of stresses is believed to be due to the presence of impurities [5]. This could be handled in the model by introducing a small internal stress in the same way as was done for aluminum for the Peierls stress, see Sect. 2.7. However, since the magnitude of the internal stress would not be known, it would be meaningless to take it into account. The part with the higher slope at low stresses is ignored. In the GBS range for larger stresses, both the stress and grain size dependencies are well represented by the model.

In Fig. 9.9 the corresponding data for Zn22Al are presented at 190 °C. There is a difference between Figs. 9.8 and 9.9. In the latter Figure, there is a third stress range at higher stress where the slope of the curves increases. This is believed to be due to ordinary lattice diffusion controlled creep that is starting to contribute. In this case, Eq. (9.19) is used in the model where both GBS and creep by lattice dislocations are taken into account. The lattice diffusion coefficient for Zn is used [24].

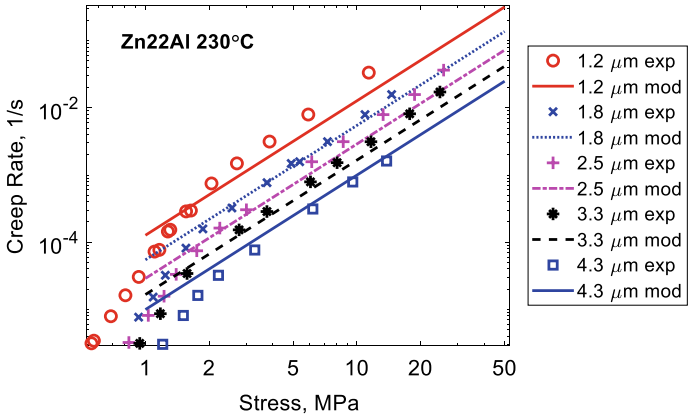

Fig. 9.8 Creep rate during superplasticity in Zn22Al for the five grain sizes 1.2, 1.8, 2.5, 3.3 and 4.3 μm at 230 °C. Model according to Eq. (9.20). Data from [13]

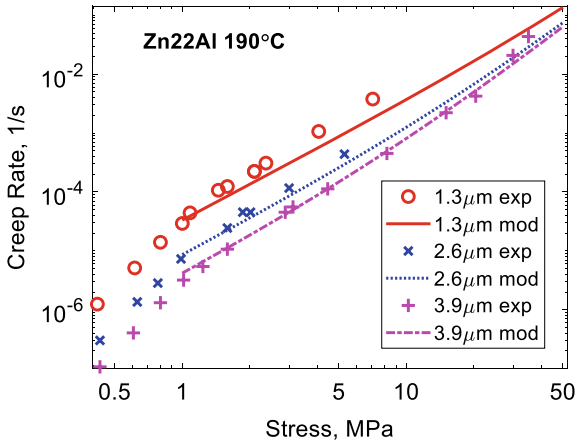

Fig. 9.9 Creep rate during superplasticity in Zn22Al for the three grain sizes 1.3, 2.6 and 3.9 μm at 190 °C. Model according to Eq. (9.19). Experimental data from [13]

Again both the stress and grain size dependence can be represented by the model. From Figs. 9.8 and 9.9, it is apparent that the experimental stress exponent is slightly larger than 2 and the absolute value of the exponent for the grain size dependence is somewhat larger than 2. This was already observed in the original work [13]. It has also been found for other superplastic alloys [11].

To illustrate the temperature dependence of the GBS rate, results at 130 °C are illustrated in Fig. 9.10.

It can be seen that the model yields values that are higher than the experimental values. This suggests that the grain boundary diffusion coefficient is slightly overestimated in the model. However, the stress dependence is well described.

It has been shown in Figs. 9.9 and 9.10 that there is a transition from GBS to lattice creep at high stresses. Langdon has suggested that this corresponds to a situation

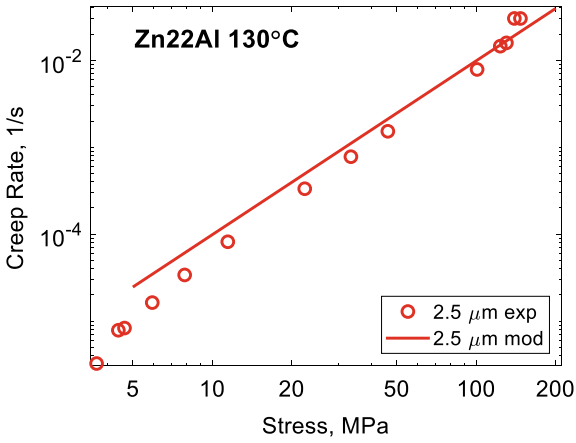

Fig. 9.10 Creep rate during superplasticity in Zn22Al for the grain size 2.5 μm at 130 °C. Model according to Eq. (9.19). Experimental data from [13]

where the grain size goes from being smaller than the subgrain size to being bigger. If the grain size is smaller than the nominal subgrain size according to Eq. (9.21), no subgrains are present. The subgrain size d_{sub} can be directly related to the dislocation stress, Eq. (2.18)

$$d_{\text{sub}} = \frac{K_{\text{sub}} G b}{\sigma_{\text{disl}}} \tag{9.21}$$

K_{sub} is a non-dimensional constant that typically takes values between 10 and 20. Since no value has been found for Zn, the value 18 for Al has been used. The idea that the subgrain size is of importance for GBS is natural. In alloys with normal grain sizes, dislocations can move 1–3 subgrain diameters. If the grain size is smaller than the subgrain size, the dislocations are clearly influenced. In particular, the recovery is affected. Annihilation at GBs becomes of importance. In addition, the recovery at the subgrains disappears which is equivalent to ordinary static recovery in the bulk.

In Fig. 9.11 the subgrain size is shown as a function of stress. The range of grain sizes from [13] is also presented. The grain size is equal to the subgrain size for stresses between 50 and 200 MPa. This is in good qualitative agreement with the transitions in Figs. 9.9 and 9.10. The equivalence of the grain size and the subgrain size cannot be considered as a general principle since the exact position of the transition depends for example on the ratio between the diffusion coefficients for grain boundary and lattice diffusion. So the precise position must be analyzed for each specific experimental case.

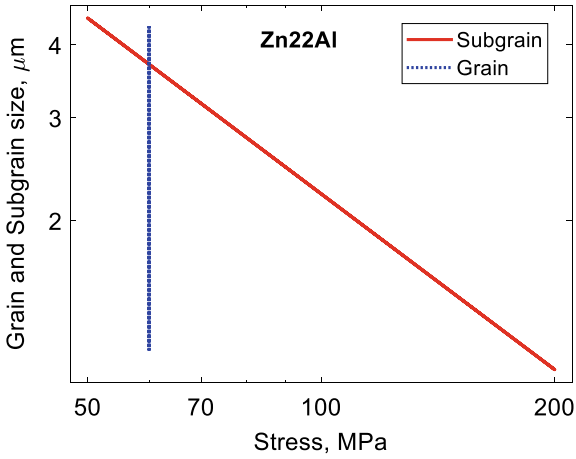

Fig. 9.11 Subgrain size for Zn22Al versus stress. The range of grain size from [13] is included for reference

9.5 Summary

- Grain boundary sliding (GBS) is believed to constitute the main mechanism for nucleation of creep cavities and to some extent growth of cavities, see Chap. 10. GBS is therefore of considerable scientific and technical significance.
- According to finite element simulations, the amount of GBS is directly proportional to the overall creep strain with a constant C_s that is known.
- Detailed measurements of GBS have been performed for copper with three techniques; creep at constant load, creep at constant loading rate, and slow strain rate tests at constant strain rate over a range of temperatures and strain rates. In spite of the varying testing conditions, the measured values for C_s are in close agreement with the theoretical value of 50 μm.
- A basic model for superplasticity is presented. It can successfully describe published data for Al22Zn. The form of the basic model is not very different from an earlier presented empirical model, but in the basic derivation of the model, parameter values could be fixed.

References

1. R. Sandström, R. Wu, J. Hagström, Grain boundary sliding in copper and its relation to cavity formation during creep. Mater. Sci. Eng. A **651**, 259–268 (2016)
2. V.E. Panin, N.S. Surikova, T.F. Elsukova, I.V. Vlasov, D.V. Borisyuk, Grain boundary sliding and rotational mechanisms of intragranular deformation at different creep stages of high-purity aluminum polycrystals at various temperatures and stresses. Mater. Sci. Eng. A **733**, 276–284 (2018)
3. J.D. Parker, B. Wilshire, A surface measurement study of grain-boundary sliding during creep of a two-phase, copper-cobalt alloy. Mater. Sci. Eng. **29**, 219–225 (1977)

4. H. Kokawa, T. Watanabe, S. Karashima, Sliding behaviour and dislocation structures in aluminium grain boundaries. Philos. Mag. A **44**, 1239–1254 (1981)
5. T.G. Langdon, Grain boundary sliding revisited: developments in sliding over four decades. J. Mater. Sci. **41**, 597–609 (2006)
6. M.A. Meyers, A. Mishra, D.J. Benson, Mechanical properties of nanocrystalline materials. Prog. Mater Sci. **51**, 427–556 (2006)
7. M. Kawasaki, T.G. Langdon, Review: achieving superplasticity in metals processed by high-pressure torsion. J. Mater. Sci. **49**, 6487–6496 (2014)
8. L. Bhatta, A. Pesin, A.P. Zhilyaev, P. Tandon, C. Kong, H. Yu, Recent development of superplasticity in aluminum alloys: a review. Metals **10** (2020)
9. A.J. Barnes, Superplastic forming 40 years and still growing. J. Mater. Eng. Perform. **16**, 440–454 (2007)
10. T.G. Langdon, An evaluation of the strain contributed by grain boundary sliding in superplasticity. Mater. Sci. Eng. A **174**, 225–230 (1994)
11. O.A. Ruano, O.D. Sherby, Low stress creep of fine-grained materials at intermediate temperatures: diffusional creep or grain boundary sliding? Mater. Sci. Eng. **56**, 167–175 (1982)
12. T.G. Langdon, A unified approach to grain boundary sliding in creep and superplasticity. Acta Metall. Mater. **42**, 2437–2443 (1994)
13. F.A. Mohamed, T.G. Langdon, Creep at low stress levels in the superplastic Zn-22% Al eutectoid. Acta Metall. **23**, 117–124 (1975)
14. F.W. Crossman, M.F. Ashby, The non-uniform flow of polycrystals by grain-boundary sliding accommodated by power-law creep. Acta Metall. **23**, 425–440 (1975)
15. R. Raj, M.F. Ashby, On grain boundary sliding and diffusional creep. Metall. Trans. **2**, 1113–1127 (1971)
16. F. Ghahremani, Effect of grain boundary sliding on steady creep of polycrystals. Int. J. Solids Struct. **16**, 847–862 (1980)
17. K.J. Hsia, D.M. Parks, A.S. Argon, Effects of grain boundary sliding on creep-constrained boundary cavitation and creep deformation. Mech. Mater. **11**, 43–62 (1991)
18. D. McLean, M.H. Farmer, The relation during creep between grain-boundary sliding, sub-crystal size, and extension. J. Inst. Metals **85**, 41–50 (1957)
19. A. Ayensu, T.G. Langdon, The inter-relationship between grain boundary sliding and cavitation during creep of polycrystalline copper. Metall. Mater. Trans. A **27**, 901–907 (1996)
20. K. Pettersson, A study of grain boundary sliding in copper with and without an addition of phosphorus. J. Nucl. Mater. **405**, 131–137 (2010)
21. S. Kishimoto, N. Shinya, H. Tanaka, Grain boundary sliding and surface cracking during creep of 321 stainless steel. Zairyo/J. Soc. Mater. Sci. Jpn. **37**, 289–294 (1988)
22. Q.S. Mei, K. Tsuchiya, H. Gao, Different stages in the continuous microstructural evolution of copper deformed to ultrahigh plastic strains. Scripta Mater. **67**, 1003–1006 (2012)
23. E.S. Wajda, Grain boundary self-diffusion in zinc. Acta Metall. **2**, 184–187 (1954)
24. G.A. Shirn, E.S. Wajda, H.B. Huntington, Self-diffusion in zinc. Acta Metall. **1**, 513–518 (1953)

Chapter 10
Cavitation

Abstract Cavitation is of great technical importance. Nucleated cavities grow and link to form cracks that can cause rupture. During creep, cavities are initiated in the grain boundaries. The nucleation takes place at particles or at subboundary—grain boundary junctions. The main mechanism is believed to be grain boundary sliding (GBS), Chap. 9. According to the double ledge model, cavities are formed when the particles or subboundaries meet other subboundaries. With this assumption quantitative models for cavity nucleation can be derived. They show that the nucleated number of cavities is proportional to the creep strain in good accordance with observations. Cavities can grow by diffusion or by straining. It is important to take into account that cavities cannot grow faster than the surrounding creeping matrix, which is referred to as constrained growth. Otherwise the growth rate can be significantly overestimated. Models both for diffusion and strain controlled growth have been available for a long time. A recently developed model for strain controlled growth is presented based on GBS. It has the advantage that is associated with a well-defined initiation size of cavities and that constrained growth is automatically taken into account, features that some previous strain controlled models miss.

10.1 General

During creep micrometer sized holes are formed in alloys. These holes are called cavities. The presence of cavities is technologically important because the cavities have a strong influence on the final rupture, in particular at low stresses. Quantitative studies of cavitation have mainly been performed in three groups of alloys that will be referred to as Group I, Group II and Group III. Group I consists of fcc alloys: copper, austenitic stainless steels and nickel-base alloys. Group II includes creep resistant low alloy steels typically with a ferritic-bainitic microstructure. Also the classical 12%Cr steel (X20) is included in this group because it shows the same type of behavior. Group III represents the advanced martensitic 9% Cr creep resistant steel. The reason why it is important to distinguish between these groups is that the cavitation occurs in different ways. In Group I, the cavities appear mainly in the

R. Sandström, *Basic Modeling and Theory of Creep of Metallic Materials*, Springer Series in Materials Science 339,
https://doi.org/10.1007/978-3-031-49507-6_10

grain boundaries, and in Group II the cavities are found in the prior austenite grain boundaries. The main location of cavities in Group III is the lath boundaries in the martensite. For a review on earlier work on cavitation during creep, see [1] and for more recent work [2].

Models for the formation and growth of cavities have primarily been developed for Group I and II alloys. The analysis in this chapter will concentrate on these types. Much less is known about the martensitic steels in Group III in spite of their extensive use in modern fossil fired power plants. Information about Group III steels will be summarized in Sect. 10.3.

The cavitation in Group I and II can be discussed in the same way, just recalling that when grain boundaries are discussed they are the genuine grain boundaries in Group I but the prior austenite grain boundaries in Group II.

During creep deformation there is some sliding along grain boundaries. Thus, there is a movement between neighboring grains that is called *grain boundary sliding (GBS)*, Chap. 9. The distance that neighboring grains move with respect to each other is referred to as the amount of GBS. According to finite element work, the amount of GBS is proportional to the creep strain. This is further discussed in Chap. 9.

GBS is believed to be essential for cavity formation. If particles are present in the grain boundaries cavities can be created when the boundaries slide. Modeling of initiation of creep cavitation was first made with the help of classical nucleation theory (CNT) [3]. This approach is however associated with several disadvantages. It suggests that cavitation would essentially appear at high stresses, which is in contrast to observations for engineering steels where cavitation is primarily observed at low stresses. CNT tends to give results that appear as a step function in stress and temperature again at variance with observations. With CNT it is very difficult to make quantitative predictions since results are sensitive to the exact values of the chosen parameters. There are many experiments that give that the number of cavities is proportional to the creep strain [4, 5] which is difficult to model with CNT.

With the help of dislocation pile-ups, large stresses can be introduced that could initiate creep cavities [6]. Very large stresses in the GPa range are needed to form cavities in this way. Very long pile-ups are required that are rarely observed in the presence of creep cavities. High stresses can also be generated with the help of a shear crack. Riedel used that approach to model cavity formation with the help of CNT [7]. However, both these types of models have the same problems with the stress dependence as for CNT models in general.

It has been even more challenging to understand how cavities can be created in essentially particle free materials like pure copper. It has been demonstrated that the substructure can act as hard zones in the same way as particles. Lim has shown that subboundaries interacting with a sliding grain boundary can form cavities and that the process is thermodynamically feasible [8]. It is therefore natural to assume that the cavity formation around particles that is experimentally well documented is associated with the interaction with the substructure.

Taking into account the role of GBS and the substructure it can directly be explained why the number of nucleated cavities is proportional to the creep strain for many materials. The proportionality to the strain was first demonstrated by Dyson

[4] and later surveyed in [5]. Although this empirical rule has been known for many years, a basic model was only derived recently based on the so called double ledge principle. In this way the value of the proportionality constant could be derived. This is shown in Sect. 10.4.

Already during the 1950ties, Hull and Rimmer derived a model for growth of cavities based on diffusion control. However, it was found that their model typically exaggerated the growth rate. Dyson realized that the cavities could not grow faster than what the creep rate allows [9]. This is referred to as constrained growth. Although good models for this effect were derived, they still tended to give a too large growth rate. In fact, in models for creep damage development, strain dependent growth is often used in spite of the availability of basic diffusion controlled growth models [10]. A revised constrained cavity growth model has recently been presented, which gives significantly reduced growth rates and solves some of the previous issues. This is analyzed in Sect. 10.5.

After the design life of fossil fired power plants and other high temperature units has expired, almost invariably the plant owners want to extend the service time. Then it is essential to demonstrate that continued operation is safe. The main life controlling factors are related to material properties, not least to creep. Many material properties degrade during service. The determination of the degree of property degradation is referred to as *residual life analysis*, which is a major research area today. Concerning creep properties, the study of cavitation has and is playing a major role in this respect. Neubauer found that the structure of the cavitation changed in components during service [11]. It could be followed by taking replicas on components, which were studied in the laboratory. First a limited number of single cavities appeared in the grain boundaries (category I). Then single cavities were observed in larger numbers (category II). Cavities gradually linked to micro-cracks (shorter than a grain diameter) (category III). Finally macro-cracks appeared (larger than the grain diameter) (category IV). These categories and their interpretation can be found in many versions. Their value is that it typically takes a number of years from category I to II and from II to III. Only for category IV, immediate action in the form of repair or replacement of the component is essential. In this way a system of early warning of serious creep damage was established. It has been extensively used. It has avoided many fatal accidents and saved many lives. Fatal accidents are fortunately rare nowadays.

The use of replication to follow the development of creep damage is the most used traditional method in residual life analysis and also the most successful one. A review of non-destructive methods for residual life analysis can be found in [12]. Welded joints are particularly prone to creep damage, and in particular the fine grained part of the heat affected zone. The Neubauer scheme seems to work well for Group I and Group II materials. However, for the modern martensitic steels in Group III, single cavities in large extent only appear close to rupture and to find cavities that have linked to microcracks is unusual. Early warning of serious creep damage is difficult to get. This will be further discussed in Sect. 10.3.

10.2 Empirical Cavity Nucleation and Growth Models

As mentioned above, the number of cavities formed during creep n_{cav} was early on observed to be approximately proportional to the creep strain ε

$$n_{cav} = B_s \varepsilon \tag{10.1}$$

B_s is a constant. This relation was found to be valid for Group I materials 347 (austenitic stainless steel) and Nimonic 80A (nickel base alloy) and for low alloy steels in Group II 1Cr0.5Mo, 0.5Cr0.5Mo0.25 V, 1Cr1Mo0.25 V and 2.25Cr1Mo as well as 12CrMoV steels [4, 5]. Notice that there is no constant term in Eq. (10.1). The observations show that the formation of cavities starts already at small strains.

Hull and Rimmer formulated a basic expression for diffusion controlled growth of cavities [13]. The equation expresses that the time derivate of the cavity volume is proportional to the grain boundary diffusion coefficient and the applied stress. As pointed out above the resulting growth rate often greatly exceeded the observed values. The situation was much improved when constrained growth was taken into account to ensure that cavity growth rate was not faster than the creep rate. A number of authors derived models for the reduced stress during constrained growth. For example, Rice derived such a model [14].

Cavitation models are extensively used in continuum damage mechanics (CDM) to assess the (remaining) creep life of components. Three of the common approaches in CDM that are supposed to be based on physical constitutive equations are given in [15–17]. A review of the models can be found in [10]. In all three papers an empirical combination of cavity nucleation and growth is used.

$$\dot{\omega}_{cav} = C \dot{\varepsilon}_e \left(\frac{\sigma_1}{\sigma_e} \right)^{\nu} \tag{10.2}$$

where $\dot{\omega}_{cav}$ is the creep damage due to the cavities, $\dot{\varepsilon}_e$ the effective creep rate, σ_1 the maximum principal stress, σ_e the effective stress, and C and ν are constants. Equation (10.2) was originally proposed by Cane [18]. There is no indication in the papers [15–17] why the empirical Eq. (10.2) was chosen and not the basic constrained growth models that were available at the time. There are cases where the growth rate is proportional to the creep strain but that cannot be considered to be a general solution. This will be further discussed in Sect. 10.5.

10.3 Cavitation in 9% Cr Steels

Cavitation has been studied quantitatively to a less extent for modern 9Cr steels (P91, P92) in Group III in comparison to materials in Group I and II. This is surprising considering that they are common materials in pipes and tubes in modern fossil fired

power plants. Much of the data has been collected from ruptured specimens with welds or failed welded components. For a survey, see [19].

In 9Cr steels cavities are primarily formed at lath boundaries, but also at prior austenite grain boundaries. The cavities appear as single units even close to fracture. This should be contrasted to the Group I and II materials where even at fairly low fraction of the rupture life the cavities are arranged in rows at the grain boundaries ("pearls on string"). At higher life fraction the cavities link and form microcracks and then macrocracks. These three later stages are absent in Group III materials. In addition the cavities in Group III materials are observed only very close to the fine grained zone in the HAZ, where the failure takes place (type IV cracking). All these facts make is more difficult to locate the cavitation.

Siefert and Parker [19] made an attempt to estimate the number of cavities n_{cav} as a function of the life fraction t/t_R

$$\frac{n_{cav}}{n_{cavR}} = \left(1 - \frac{t}{t_R}\right)^{\mu_{cav}} \tag{10.3}$$

where n_{cavR} is the number of cavities close to rupture that is estimated to be about 800 cavities per mm^2. μ_{cav} is a constant. For materials with a low creep ductility $\mu_{cav} = 0.5$. Although the majority of casts of P91 has a high ductility, there is a significant fraction where the reduction of area at rupture is less than 20%. μ_{cav} is reduced with increasing ductility, which means that the cavitation appears later in life. This has to be taken into account in residual life time analysis.

It has been found that it is often more difficult to observe cavities metallographically for Group III than for the other Groups. This applies both to replication and direct observation in the lab (Charman, personal communication 2021). It is recommended to use laser microscopy to safely observe the cavities.

In Sects. 10.4 and 10.5 basic models for cavity nucleation and growth are introduced. These models are based on the assumption that the cavities are located at the grain boundaries. Since this is not always the case for Group III materials, the models are not automatically satisfied. Since suitable data for the strain and time dependence of cavitation of 9Cr steels cannot be located, it is not possible to be more specific about the applicability of the models for the Group III materials.

10.4 Basic Model for Cavity Nucleation

10.4.1 Thermodynamic Considerations

In the past a number of mechanisms have been proposed for the formation of creep cavities. One idea is that atomic bonds are ruptured. However, this requires very high stresses and even if such stresses would be initiated they would quickly relax in a creeping material [6]. Another suggestion is that the accumulation of vacancies

can be handled with classical nucleation theory [3]. This gives a very strong stress dependence suggesting that cavities would almost exclusively appear at high stresses [20]. This is at variance with observations since most cavities are formed at low stresses. High stresses can appear at grain boundary ledges, triple points and particles. A common assumption is that cavities are formed by decohesion at particles. High stresses are required in most models. A threshold must be exceeded and an incubation time is required [3, 21]. Contrary to these suggestions, observations demonstrate that cavity nucleation is strain controlled rather than by stress and cavitation is particularly frequent at low stresses as pointed out above. Statements in the literature have also concluded that earlier theories are not successful [22, 23]. These papers also give excellent reviews of earlier work.

New ideas for nucleation mechanisms came from the studies on copper. It is well established that extensive cavitation can take place in copper during creep [24]. It is noticeable that the number of particles is typically so low that they cannot contribute significantly to the cavitation. A model by Lim gave a possible explanation [25]. He assumed that a sliding grain boundary can form cavities where subboundaries reach the boundary. Grain boundary dislocations formed pile ups that exerted sufficient stress on the grain boundary–subboundary intersection that a cavity could be nucleated. He made a thermodynamic analysis of the situation and showed that an energy gain was obtained when a cavity was formed. In his model, the high stress is a result of a stationary creep process and avoids the problem with stress relaxation. The change in free energy during the formation of a cavity can be expressed as

$$\Delta G = -r^3 F_v \sigma_{appl} + r^2 F_s \gamma_s - r^2 F_{GB} \gamma_{GB} - (\Delta G_1 + \Delta G_2 + \Delta G_3) \qquad (10.4)$$

γ_s and γ_{GB} are the surface and grain boundary energies per unit area and

$$F_v = 2\pi/3(2 - 3\cos\alpha + \cos^3\alpha)$$

$$F_s = 4\pi(1 - \cos\alpha)$$

$$F_{GB} = \pi \sin^2\alpha$$

where α is half the tip angle of the cavity. The first term in Eq. (10.4) is the work done by the applied stress. The second and third terms represent the modification in the surface and grain boundary energies when a cavity is formed. The fourth term is the decrease in the strain energy. ΔG_1 is the change in the line energy of the grain boundary dislocations (GBD). ΔG_2 is the interaction energy between the remaining and the consumed GBD. The strain energy ΔG_3 is the reduction of the strain energy of GBDs outside the cavity. Details of the application of Lim's fairly complex model can be found in [26, 27].

Cavitation in copper and austenitic stainless steels has been analyzed with Lim's model. If ΔG in Eq. (10.4) is negative, cavitation can take place. When the applied stress σ_{appl} is raised ΔG becomes more negative and cavitation is more likely. On the

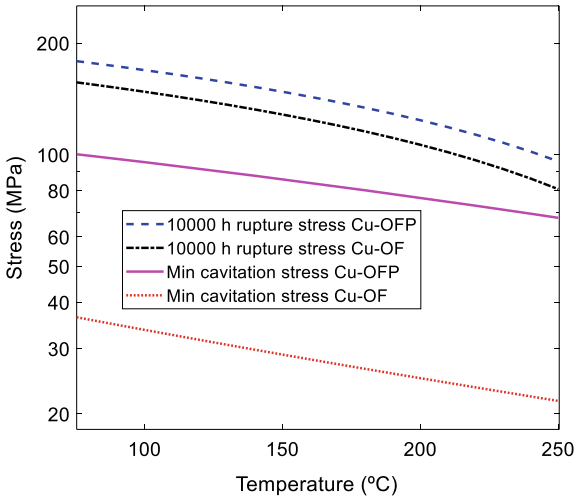

Fig. 10.1 Minimum stress to form cavities at cell boundaries versus temperature for oxygen free pure Cu-OF and phosphorus alloyed copper Cu-OFP. For comparison the stress that gives creep rupture after one year (10000 h) is included. From [28]. Reproduced with the permission of Elsevier

other hand if σ_{appl} is reduced cavitation does not readily occur. This is precisely as expected. When σ_{appl} is below a minimum value ΔG becomes positive and cavitation is no longer possible. This minimum cavitation stress for Cu is shown as a function of temperature in Fig. 10.1. The main temperature dependence is due to the last term in Eq. (10.4).

A comparison is made in Fig. 10.1 to the creep rupture strength for copper for 10000 h. The rupture strength are higher than the minimum cavitation stresses. Since the rupture strength is used in design (with a safety factor), this demonstrates that cavitation at the intersections between subboundaries and grain boundaries is a thermodynamically feasible process.

It is well documented that oxygen free copper Cu-OF can have a much lower creep ductility than the same alloy with 50 wt. ppm P, Cu-OFP [29]. It has therefore been decided to use Cu-OFP but not Cu-OF in copper canisters for disposal of spent nuclear fuel [30]. The origin of the low creep ductility of Cu-OF is the extensive formation of creep cavities [30]. It is evident from Fig. 10.1 that the minimum cavitation stress is much lower for Cu-OF than for Cu-OFP, which explains the difference in creep ductility between the materials, Sect. 13.3.1.

It can also be demonstrated that the minimum cavitation stress is well below the rupture strength for common austenitic stainless steels 304H (18Cr10Ni), 316H (17Cr12Ni2Mo), 321H (18Cr12NiTi), 347H (18Cr12NiNb) [31]. This is illustrated for 347H in Fig. 10.2. The ratio between the rupture strength and the minimum cavitation stress is reduced with increasing temperature, which would suggest that the amount of cavitation would be reduced with increasing temperature contrary to observations. It is likely that Lim's model does not fully give the correct temperature dependence.

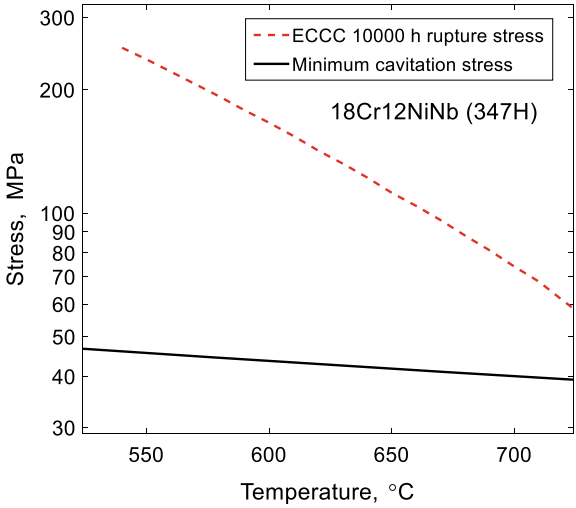

Fig. 10.2 Minimum cavitation stress versus temperature for TP347H austenitic stainless steel. 10000 h rupture data from ECCC for 347H are shown for comparison. Redrawn from [2] with permission of intechopen

10.4.2 Strain Dependence

Most researchers today assume that the nucleation of cavities is due to grain boundary sliding (GBS). There are several reasons for this. In many materials cavities are formed around particles in the grain boundaries. It has often been found experimentally that the number of cavities is proportional to the creep strain, Eq. (10.1). In addition, the amount of GBS is also proportional to the creep strain, Eq. (9.11)

$$u_{\mathrm{GBS}} = C_{\mathrm{s}}\varepsilon \tag{10.5}$$

The constant C_{s} is given by, Eq. (9.12)

$$C_{\mathrm{s}} = \dot{u}_{\mathrm{GBS}}/\dot{\varepsilon} = \frac{3\phi}{2\xi} d_{\mathrm{g}} \tag{10.6}$$

where d_{g} is the grain size, ϕ and ξ are constants.

To explain the experimental observations that the nucleation rate is proportional to the creep strain rate, Eq. (10.1), Sandström and Wu proposed the so called *double ledge model* [30]. Following the ideas in Lim's model [25], nucleation is assumed to take place when a subboundary on one side of a sliding grain boundary meets another subboundary on the opposite side. The position where a subboundary meets a grain boundary is referred to as a subgrain corner. The nucleation rate then takes the form

$$\frac{dn_{\mathrm{cav}}}{dt} = \frac{\dot{u}_{\mathrm{GBS}}}{d_{\mathrm{sub}}} \frac{1}{d_{\mathrm{sub}}^2} \tag{10.7}$$

where d_{sub} is the subgrain diameter. d_{sub} is inversely proportional to the dislocation stress that is in general close to the applied stress, Eq. (8.4). Equation (10.7) gives the nucleation rate per unit grain boundary area. It must also be added to Eq. (10.7) that at most one nucleus is formed in each subgrain. Equation (10.7) describes the situation for a particle free material. If particles are present, nucleation is assumed to occur when a subboundary hits a particle on a sliding grain boundary. Considering the nucleation at both particles and subgrain corners, the nucleation rate can be expressed as [31]

$$\frac{dn_{cav}}{dt} = \frac{0.9C_s}{d_{sub}}\left(\frac{g_{sub}}{d_{sub}^2} + \frac{g_{part}}{\lambda^2}\right)\dot{\varepsilon} = B_s\dot{\varepsilon} \tag{10.8}$$

where λ is the interparticle spacing in the grain boundary. In Eq. (10.8), factors g_{sub} and g_{part} are introduced for the fraction of subgrain corners and particles where cavity nucleation takes place. The values of g_{sub} and g_{part} will be discussed below. 0.9 is a factor that takes into account the averaging of different orientation. The derivation is comparatively lengthy. For this reason the derivation is not presented here [31].

10.4.3 Comparison to Experiments for Copper

Das et al. have recently presented measurements on nucleation of creep cavities in copper using small angle neutron scattering (SANS) [32]. Their results will be compared with the model in Sect. 10.4.2. They give values for the spacing λ_{cav} between cavities in the grain boundaries. The spacing can be transferred to the number of cavities n_{cav} per unit grain boundary area as

$$n_{cav} = 1/\lambda_{cav}^2 \tag{10.9}$$

The results for n_{cav} as a function of stress is shown in Fig. 10.3.

In Fig. 10.3 the model values are about a factor of 4 below the experimental ones but show the same stress dependence. The ratio between the tests at the two times is about the same. There is also another way to determine the cavity density in [32] from their volume fraction f_V and the cavity radii R_{cav}

$$n_{cav} = \frac{f_V}{\pi R_{cav}^2} \tag{10.10}$$

The values from Eq. (10.10) fall below the model values contrary to the values according to Eq. (10.9). Since it is more difficult to measure the volume fraction and the cavity radius than the cavity spacing, the values from Eq. (10.10) are more uncertain and are not shown in Fig. 10.3.

Das el al. evaluated the parameter B_s in Eq. (10.8), i.e. the ratio between the nucleation rate and the creep rate or expressed in another way the ratio between the

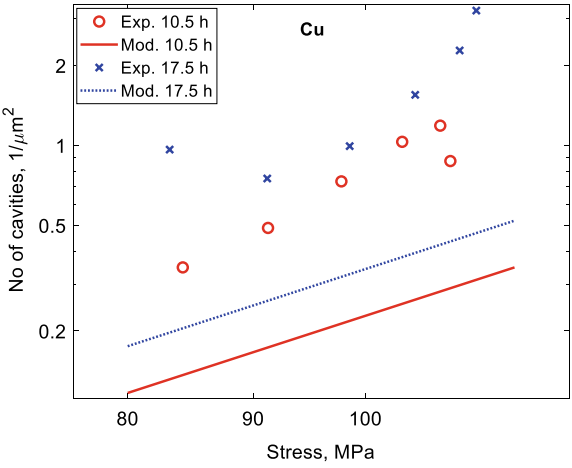

Fig. 10.3 Modeling and experimental number of cavities per unit grain boundary area as a function of stress for two testing times. Model values from Eq. (10.8) and experiments from [32]

cavity density and the creep strain. The experimental and the model values are given in Fig. 10.4. Unfortunately data are not available for exactly the testing time as in Fig. 10.3.

The model values are a factor of 2 above the experimental data this time. The stress dependence is about the same in the model and the experiments. It should be noticed that with the same model in the Figures, model values are above the experimental ones in Fig. 10.4 contrary to those in Fig. 10.3. This indicates an uncertainty in the experimental data and the consistency between models and observations is acceptable considering this effect. It is valuable that the fairly dramatic stress dependence in the model (σ^3) is reproduced in the observations.

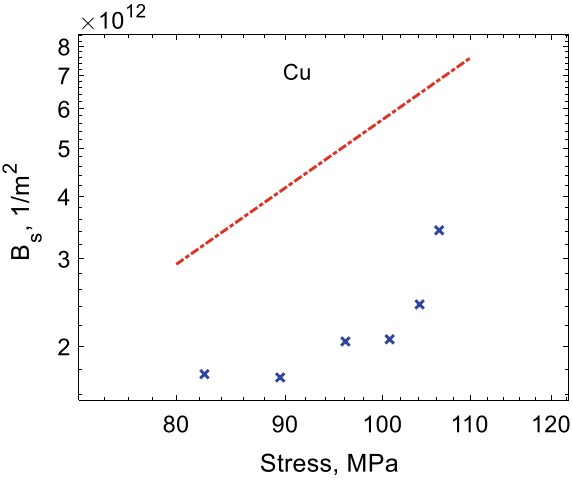

Fig. 10.4 Modeling and experimental values for the ratio B_s between the number of cavities per unit grain boundary area and the creep strain as a function of stress for a testing time of 17.5 h. Model values (line) from Eq. (10.8) and experiments (points) from [32]

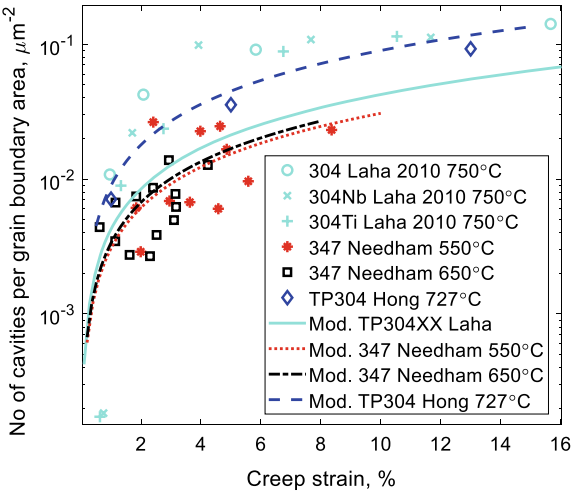

Fig. 10.5 Modeling and experimental number of cavities per unit grain boundary area as a function of creep strain for austenitic stainless steel collected from literature. Redrawn from [31] with permission of Springer

10.4.4 Comparison to Experiment for Austenitic Stainless Steels

A comparison of the model in Eq. (10.8) to experimental data for austenitic stainless is given in Fig. 10.5. Data for TP347 (17Cr12NiNb), TP304 (18Cr10Ni) and TP321 (17Cr10NiTi) are presented. Nucleation at both subgrain corners and particles are taken into account. Considering the scatter in the data, the observations give good support to the model. In Fig. 10.5, the factors g_{sub} and g_{part} are taken as unity. Thus every subgrain corner and particle is assumed to contribute to the nucleation. This cannot always be assumed to be the case but systematic studies have not been found.

10.5 Models for Cavity Growth

10.5.1 Unconstrained Cavity Growth Model

Once the cavities have been nucleated they can start to grow if they exceed a critical size. Growth of creep cavities are in general assumed to be controlled by diffusion. There can also be contributions from straining. Strain controlled growth is considered in Sect. 10.5.3. A diffusion controlled growth model was first proposed by Hull and Rimmer [13]. Beere and Speight simplified this formulation [33] and this is the version that is used nowadays

$$\frac{dR_{\text{cav}}}{dt} = 2D_0K_{\text{f}}(\sigma - \sigma_0)\frac{1}{R_{\text{cav}}^2} \tag{10.11}$$

R_{cav} is the cavity radius in the grain boundary plane, dR_{cav}/dt its growth rate, σ the applied stress, σ_0 the sintering stress $2\gamma_s \sin(\alpha)/R_{cav}$, where γ_s is the surface energy of the cavity per unit area and α the cavity tip angle. The presence of the sintering stress σ_0 ensures that only cavities that are larger than a critical size grow. δ the grain boundary width, D_{GB} the grain boundary self-diffusion coefficient, Ω the atomic volume are combined into a grain boundary diffusion parameter D_0, $D_0 = \delta D_{GB}\Omega/k_B T$. k_B is the Boltzmann's constant and T the absolute temperature. The factor K_f was introduced in [34]. It takes into account the role of the size of the cavity in relation to that of the surrounding area that can deliver vacancies for the growth of the cavity. It is a function of the cavitated grain boundary area fraction $f_a = (2R/\lambda_{cav})^2$

$$K_f = -1/\left[2\log f_a + (1 - f_a)(3 - f_a)\right] \tag{10.12}$$

λ_{cav} is the spacing between cavities in the grain boundary. It can be determined from number of cavities per unit grain boundary area n_{cav}, cf. Eq. (10.9)

$$\lambda_{cav} = 1/\sqrt{n_{cav}} \tag{10.13}$$

n_{cav} is derived with the nucleation relation, Eq. (10.8).

The cavities cannot grow unless the stress is larger than the sintering stress σ_0. This means that the cavity radius must have reached a certain size for growth to take place, which is referred to as the nucleation radius R_{nucl}. From the expression for the sintering stress, R_{nucl} can be found

$$R_{nucl} = \frac{2\gamma_s \sin(\alpha)}{\sigma} \tag{10.14}$$

Das et al. give data for the cavity radius for short creep testing times measured with small angle neutron scattering (SANS) [32]. The cavity radii should be close to R_{nucl}. A comparison between their data and Eq. (10.14) is illustrated in Fig. 10.6.

In Fig. 10.6, a cavity tip angle of 55° has been assumed. A precise value of the tip angle is not known but in the literature values of 50–70° are often used. It can be seen that the nucleation radius is well represented by Eq. (10.14). The mechanisms for the initial growth of creep cavities are not well established. But it is likely that it takes place by GBS, see Sect. 10.5.4. Since the cavities are initiated by GBS, it is reasonable that the first growth also occurs by this mechanism.

10.5.2 Constrained Cavity Growth

It was early on found that the expression for diffusion growth in Eq. (10.11) often exceeded observed values. Dyson noticed that the predicted growth rate many times was larger than the creep strain rate which he considered to be unphysical [9]. He

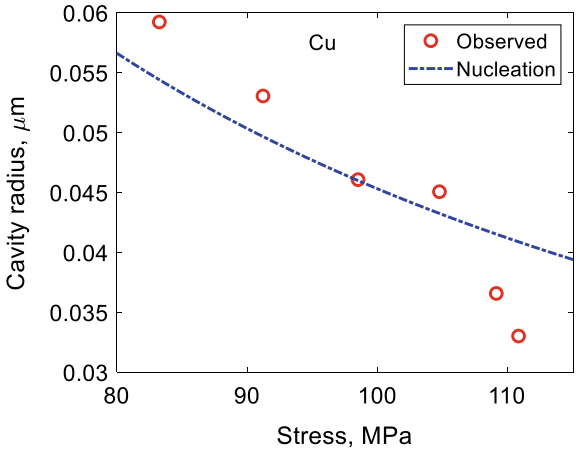

Fig. 10.6 Modeling and experimental values for the cavity nucleation radius as a function of stress for the testing time 17.5 h for Cu. Model values from Eq. (10.14) and experiments from [32]

suggested that the growth rate should always be less than the creep rate that is referred to as *constrained growth*. Here the expression for constrained growth derived by Rice will be used [14]

$$\frac{dR_{\text{cav}}}{dt} = 2D_0K_{\text{f}}(\sigma_{\text{red}} - \sigma_0)\frac{1}{R_{\text{cav}}^2} \tag{10.15}$$

The only difference between Eqs. (10.11) and (10.15) is that the applied stress is replaced by a reduced stress σ_{red}

$$\sigma_{\text{red}} = \sigma_0 + \frac{1}{\frac{1}{\sigma} + \frac{32D_0K_{\text{f}}}{\lambda_{\text{cav}}^2 d_{\text{g}}\beta\dot{\varepsilon}(\sigma)}} \tag{10.16}$$

where β is a material constant (β = 1.8 for homogeneous materials), and d_{g} the grain diameter. Equation (10.15) satisfies the criterion formulated by Dyson.

In Rice's paper an assumption was made about linear viscoplastic opening of a crack. In a reanalysis, He and Sandström did not make the assumption about linearity [35]. A grain structure with a pillar of height h and width corresponding to the grain size d_{g} was set up. The creep deformation in this pillar in the loading direction z can be expressed as

$$\frac{dz}{dt} = 4\pi D_0K_{\text{f}}(\sigma_{\text{red}} - \sigma_0)n_{\text{cav}} + h\dot{\varepsilon}(\sigma_{\text{red}}) = h\dot{\varepsilon}(\sigma) \tag{10.17}$$

$\dot{\varepsilon}(\sigma_{\text{red}})$ and $\dot{\varepsilon}(\sigma)$ are the creep rates at the reduced and applied stress, respectively. In the first expression for $\frac{dz}{dt}$ the first term is the volume growth rate of a cavity multiplied by the number of cavities per unit grain boundary area. The second term is the creep displacement of the pillar at the reduced stress. The second expression for $\frac{dz}{dt}$ is the displacement of the surrounding material at the applied stress. According

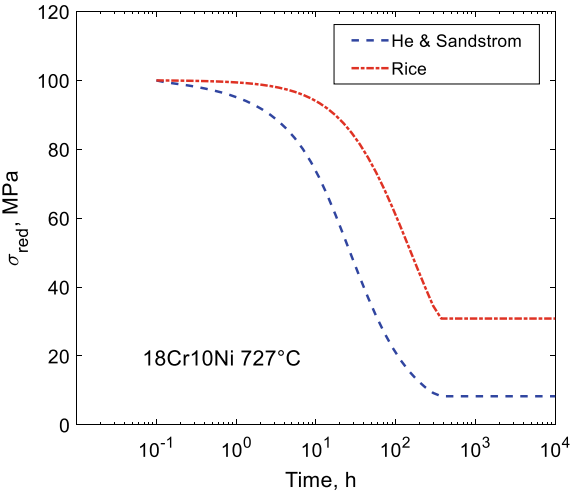

Fig. 10.7 Reduced stresses according to Eq. (10.16) (dash-dotted) and (10.18) (dashed) versus time for the austenitic stainless steel 18Cr10 Ni (TP304) at 727 °C and 100 MPa. Redrawn from [36] with permission of Elsevier

to Eq. (10.17), the cavity growth rate plus the creep rate around the cavity matches the average creep rate. This is a stronger criterion than the original requirement on constraint. The height of the pillar h was determined with finite element analysis. The finding was that the pillar height was related to the cavity radius $h \approx 2R_{\text{cav}}$ [35]. With this result, Eq. (10.17) takes the form

$$2\pi D_0 K_{\text{f}}(\sigma_{\text{red}} - \sigma_0)/L^2 R_{\text{cav}} + \dot{\varepsilon}(\sigma_{\text{red}}) = \dot{\varepsilon}(\sigma) \tag{10.18}$$

To find σ_{red}, the equation has to be solved by iteration. This new value for σ_{red} is lower than what the expression (10.16) gives. An illustration of this is presented in Fig. 10.7. In particular, the difference is significant at longer times.

These reduced stresses are quite important when describing experimental data. A comparison to experimental data for common austenitic stainless steel is shown in Fig. 10.8. Data for 18Cr10Ni steel with and without Nb or Ti are illustrated. This new model for constrained growth clearly gives an improved description of data.

10.5.3 Strain Controlled Cavity Growth

A contribution from plastic deformation to cavity growth can also be obtained. The most well established model is due to Cocks and Ashby [37]. They analyze how the area fraction f_{h} of cavities in a grain boundary perpendicular to the loading direction increases with strain. They derived the following time derivatives for f_{h} and the axial strain ε_{a} in the loading direction

$$\frac{df_{\text{h}}}{dt} = \frac{\dot{\varepsilon}_{\text{ss}}}{\alpha_h}\left\{\frac{1}{(1-f_{\text{h}})^{n_{\text{N}}}} - (1-f_{\text{h}})\right\} \tag{10.19}$$

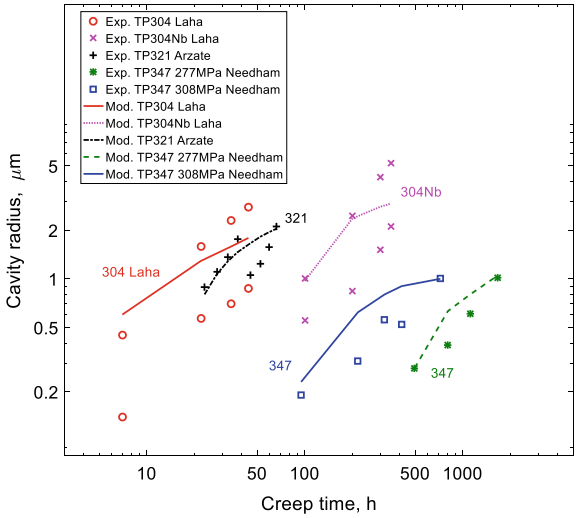

Fig. 10.8 Cavity radius as a function of creep time for 18Cr10Ni without or with Nb (347) or Ti (321) austenitic stainless steels. The creep tests were performed at temperatures in the interval of 650–812 °C. Redrawn from [36] with permission of Elsevier

$$\frac{d\varepsilon_a}{dt} = \dot{\varepsilon}_{ss}\left\{1 + \frac{2R_h}{\alpha_h d_g}\left(\frac{1}{(1-f_h)^{n_N}} - (1-f_h)\right)\right\} \tag{10.20}$$

where the stationary creep is given by

$$\dot{\varepsilon}_{ss} = \dot{\varepsilon}_0\left(\frac{\sigma_e}{\sigma_0}\right)^{n_N} \tag{10.21}$$

and

$$\alpha_h = 1/\sinh\left\{\frac{(n_N - 1/2)}{(n_N + 1/2)}\frac{\sigma_h}{\sigma_e}\right\} \tag{10.22}$$

R_h is the initial cavity radius, d_g the grain size, σ_e the effective stress and σ_h the hydrostatic stress. $\dot{\varepsilon}_0$, σ_0, and n_N are constants describing the creep rate. By integrating Eqs. (10.19) and (10.20) the cavitated area fraction can be obtained. An example is shown in Fig. 10.9. An initial cavitated area fraction of 0.001 is assumed.

The increase in cavitated area fraction is much larger if a larger initial value is assumed, which does not seem to be realistic. If the plastic growth is combined with diffusion growth, significant contributions can be obtained. The problem with the model is that it is not consistent with the principle of constrained growth. The strain rate around the cavities can become many times larger than the average creep rate and that should not be the situation during constrained growth. This effect is however small for low cavitated area fractions, so the results in Fig. 10.9 are still valid.

Describing the growth rate due to plastic deformation can be handled with a model that has been developed by Danavas and Solomon [38]

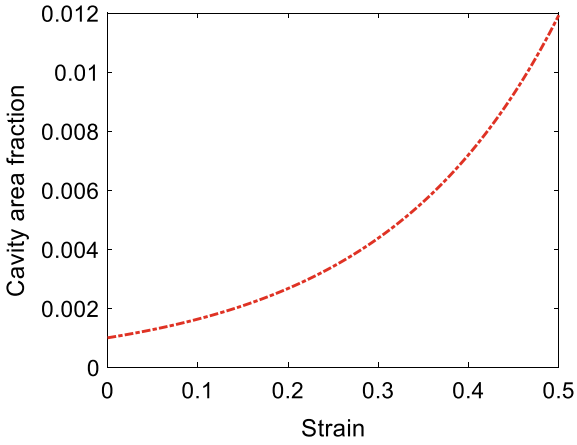

Fig. 10.9 Cavitated area fraction in grain boundary as a function of strain according to Eqs. (10.19) and (10.20). Creep exponent $n_N = 7$

$$\frac{dR_{cav}}{dt} = \frac{\sin^2(\alpha_{tip})}{\alpha_{tip} - \sin(\alpha_{tip})\cos(\alpha_{tip})} \exp\left(\frac{3\sigma_H}{2\sigma_e} - \frac{1}{2}\right) \frac{R_{cav}}{3} \dot{\varepsilon}(\sigma_{red}) \tag{10.23}$$

where α_{tip} is the tip angle of the cavity. An important modification has been made in Eq. (10.23) in comparison to the original model in [38]. The creep rate is computed for the reduced stress, not for the applied stress to make it consistent with Eq. (10.18). The expression gives a modest increase in the cavity size except if multiaxial stress states are taken into account. In Eq. (10.23) this is considered with the help of an expression from Rice and Tracey [39]. There are several alternative ways that have been proposed for the influence of multiaxial stress state derived from cavity growth during ductile fracture. The role of multiaxial stress cannot be considered to be fully settled.

10.5.4 Growth Due to Grain Boundary Sliding

It is well established that cavities are often elongated in the plane of the grain boundary. As has been analyzed in detail above, it is natural to assume that cavities are nucleated due to grain boundary sliding (GBS). Once the cavities have been nucleated for example around particles, the cavities will be exposed to shearing due to the continuing GBS. It is possible that some cavities expand at the same rate as the GBS. From Eq. (10.5) this will give a cavity size of

$$R_{cav} = C_s \varepsilon \tag{10.24}$$

where C_s is again given by Eq. (10.6), This expression is compared with data for a 12CrMo steel and a TP347 (17Cr12NiNb) austenitic stainless steel in Fig. 10.10.

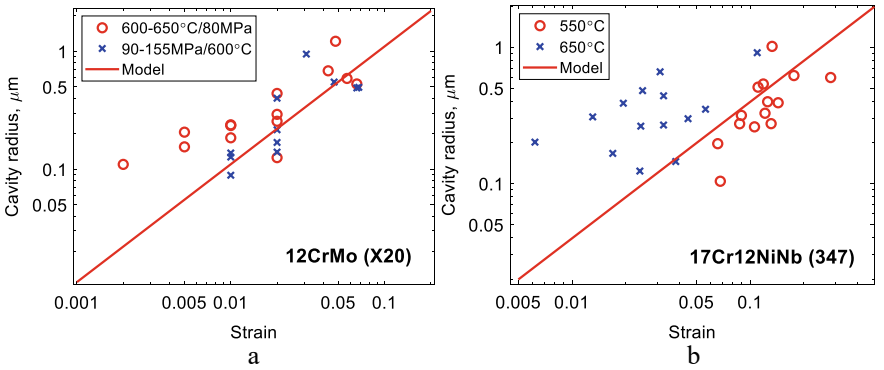

Fig. 10.10 Cavity radius versus strain. Model according Eq. (10.24); **a** 12CrMo steel (X20). Data from [40]; **b** TP347 (17Cr12NiNb). Data from [41]. **b** Redrawn from [42] with permission of Taylor & Francis

The results give a reasonable description of the cavity growth data for the two steels. The amount of data to make comparisons to the model is limited. Since the constant C_s is proportional to the grain size, the model predicts large cavity radii when the grain size is large, which might not be realistic.

10.6 Summary

- Nucleation of creep cavities is assumed to take place at particles and subboundary junctions in the grain boundaries by grain boundary sliding (GBS). This assumption makes it possible to quantitatively explain the observed strain dependence of the number of cavities. In the past attempts have been made to use classical nucleation theory, but it gives essentially a step function in stress that is in direct variance with observations.
- Diffusion controlled growth of cavities can satisfactorily describe observations for austenitic stainless steels if recent modeling for constrained growth is taken into account. Constrained growth ensures that the cavities are not expanding faster than the creep rate of the matrix.
- Several expressions for strain controlled growth exist that are derived from basic physical principles. However, these expressions are difficult to verify experimentally since the starting cavity size has a significant effect on the result and there is no well-defined way of choosing the size. In addition, some expressions do not fulfil the requirements on constrained growth which can give overestimated growth rates. A recent model based on GBS avoids these difficulties. The model reproduces the limited experimental data that are available.

References

1. M.E. Kassner, T.A. Hayes, Creep cavitation in metals. Int. J. Plast. **19**, 1715–1748 (2003)
2. R. Sandström, J. He, Survey of creep cavitation in fcc metals, in *Study of Grain Boundary Character* (inTech, 2017), pp. 19–42
3. R. Raj, M.F. Ashby, Intergranular fracture at elevated temperature. Acta Metall. **23**, 653–666 (1975)
4. B.F. Dyson, Continuous cavity nucleation and creep fracture. Scr. Metall. **17**, 31–37 (1983)
5. R. Wu, R. Sandstrom, Strain dependence of creep cavity nucleation in low alloy and 12%Cr steels. Mater. Sci. Technol. Ser. **12**, 405–415 (1996)
6. M.H. Yoo, H. Trinkaus, Crack and cavity nucleation at interfaces during creep. Metall. Trans. A Phys. Metall. Mater. Sci. **14 A**, 547–561 (1982)
7. H. Riedel, Cavity nucleation at particles on sliding grain boundaries. A shear crack model for grain boundary sliding in creeping polycrystals. Acta Metall. **32**, 313–321 (1984)
8. L.C. Lim, H.H. Lu, Effect of substructure on intergranular cavitation at high temperature. Scripta Metall. Mater. **31**, 723–728 (1994)
9. B.F. Dyson, Constraints on diffusional cavity growth rates. Metal Sci. **10**, 349–353 (1976)
10. Q. Meng, Z. Wang, Creep damage models and their applications for crack growth analysis in pipes: a review. Eng. Fract. Mech. **205**, 547–576 (2019)
11. B. Neubauer, F. Arens-Fischer, Determination of residual life of power station components subject to creep stress. VGB-Kraftwerkstechnik **63**, 637–645 (1983)
12. G. Sposito, C. Ward, P. Cawley, P.B. Nagy, C. Scruby, A review of non-destructive techniques for the detection of creep damage in power plant steels. NDT E Int. **43**, 555–567 (2010)
13. D. Hull, D.E. Rimmer, The growth of grain-boundary voids under stress. Philos. Mag. **4**, 673–687 (1959)
14. J.R. Rice, Constraints on the diffusive cavitation of isolated grain boundary facets in creeping polycrystals. Acta Metall. **29**, 675–681 (1981)
15. A.M. Othman, B.F. Dyson, D.R. Hayhurst, J. Lin, Continuum damage mechanics modelling of circumferentially notched tension bars undergoing tertiary creep with physically-based constitutive equations. Acta Metall. Mater. **42**, 597–611 (1994)
16. Z.L. Kowalewski, D.R. Hayhurst, B.F. Dyson, Mechanisms-based creep constitutive equations for an aluminium alloy. J. Strain Anal. Eng. Des. **29**, 309–316 (1994)
17. I.J. Perrin, D.R. Hayhurst, Creep constitutive equations for a 0.5Cr–0.5Mo–0.25V ferritic steel in the temperature range 600–675 °C. J. Strain Anal. Eng. Des. **31**, 299–314 (1996)
18. B.J. Cane, Creep fracture of dispersion strengthened low alloy ferritic steels. Acta Metall. **29**, 1581–1591 (1981)
19. J.A. Siefert, J.D. Parker, Evaluation of the creep cavitation behavior in Grade 91 steels. Int. J. Pres. Ves. Pip. **138**, 31–44 (2016)
20. E. Smith, J.T. Barnby, Crack nucleation in crystalline solids. Metal Sci. J. **1**, 56–64 (1967)
21. R. Raj, Nucleation of cavities at second phase particles in grain boundaries. Acta Metall. **26**, 995–1006 (1978)
22. H. Riedel, Life prediction methods for constrained grain boundary cavitation. Int. J. Pres. Ves. Pip. **39**, 119–134 (1989)
23. X.G. Jiang, J.C. Earthman, F.A. Mohamed, Cavitation and cavity-induced fracture during superplastic deformation. J. Mater. Sci. **29**, 5499–5514 (1994)
24. T.G. Langdon, The role of grain boundaries in high temperature deformation. Mater. Sci. Eng. A **166**, 67–79 (1993)
25. L.C. Lim, Cavity nucleation at high temperatures involving pile-ups of grain boundary dislocations. Acta Metall. **35**, 1663–1673 (1987)
26. J. He, R. Sandström, Modelling grain boundary sliding during creep of austenitic stainless steels. J. Mater. Sci. **51**, 2926–2934 (2016)
27. R. Wu, J. Hagstrom, R. Sandstrom, Grain boundary sliding in phosphorus alloyed oxygen-free copper under creep, Swedish Nuclear Waste Management Company Report R-15-14 (2015)

28. R. Sandström, R. Wu, J. Hagström, Grain boundary sliding in copper and its relation to cavity formation during creep. Mater. Sci. Eng. A **651**, 259–268 (2016)
29. P.J. Henderson, R. Sandstrom, Low temperature creep ductility of OFHC copper. Mater. Sci. Eng. A **246**, 143–150 (1998)
30. R. Sandström, R. Wu, Influence of phosphorus on the creep ductility of copper. J. Nucl. Mater. **441**, 364–371 (2013)
31. J. He, R. Sandström, Formation of creep cavities in austenitic stainless steels. J. Mater. Sci. **51**, 6674–6685 (2016)
32. Y. Das, A. Fernandez-Caballero, E. Elmukashfi, H. Jazaeri, A. Forsey, M.T. Hutchings, R. Schweins, P.J. Bouchard, Stress driven creep deformation and cavitation damage in pure copper. Mater. Sci. Eng.: A **833** (2021)
33. M.V. Speight, W. Beere, Vacancy potential and void growth on grain boundaries. Metal Sci. J. **9**, 190–191 (1975)
34. W. Beere, M.V. Speight, Creep cavitation by vacancy diffusion in plastically deforming solid. Metal Sci. **21**, 172–176 (1978)
35. J. He, R. Sandström, Growth of creep cavities in austenitic stainless steels, in *8th European Stainless Steel & Duplex Stainless Steel Conference, ASMET* (2015), pp. 561–570
36. J. He, R. Sandström, Creep cavity growth models for austenitic stainless steels. Mater. Sci. Eng. A **674**, 328–334 (2016)
37. A.C.F. Cocks, M.F. Ashby, Intergranular fracture during power-law creep under multiaxial stresses. Metal Sci. **14**, 395–402 (1980)
38. K. Davanas, A.A. Solomon, Theory of intergranular creep cavity nucleation, growth and interaction. Acta Metall. Mater. **38**, 1905–1916 (1990)
39. J.R. Rice, D.M. Tracey, On the ductile enlargement of voids in triaxial stress fields*. J. Mech. Phys. Solids **17**, 201–217 (1969)
40. R. Wu, R. Sandstrom, Creep cavity nucleation and growth in 12Cr–Mo–V Steel. Mater. Sci. Technol. Ser. **11**, 579–588 (1995)
41. N.G. Needham, T. Gladman, Nucleation and growth of creep cavities in a type 347 steel. Metal Sci. **14**, 64–72 (1980)
42. R. Sandström, J.-J. He, Prediction of creep ductility for austenitic stainless steels and copper. Mater. High Temp. **39**(6), 427–435 (2022)

Chapter 11
The Role of Cavitation in Creep-Fatigue Interaction

Abstract There are many empirical models for the development of creep and fatigue damage. The perhaps most well-known ones are Robison's and Miner's damage summation rules. They are based on the mechanical behavior during monotonous and cyclic loading. To improve the accuracy of the damage assessment, it is important to analyze the changes in the microstructure as well, not least the cavitation. To describe cyclic loading, special empirical models have often been used in the past, some with numerous adjustable parameters. Recently, a model for cyclic loading has been formulated that is based on the corresponding expressions for monotonous loading. The main change is that the value of the dynamic recovery constant is increased. In this way, cyclic hysteresis loops can be reproduced without adjustable parameters. Cavitation is believed to be of the same technical importance during cyclic as during static loading. In spite of this, the number of studies of cavitation during cyclic loading is quite limited. One set of data exists for a 1Cr0.5Mo steel. The static cavitation models have been transferred to cyclic conditions. It is demonstrated that these models can describe the cavitation both during low cycle fatigue (LCF) and combined creep and LCF.

11.1 General

High temperature plants are often exposed to a combination of creep and fatigue. A common feature is thermal fatigue where components are exposed to straining during start-ups and shut-downs. During operation primary stresses (direct loading) as well as secondary stresses (self-equilibrium stresses) appear that give rise to creep damage. Although some types of plants like steam and gas turbines are particularly exposed to cyclic loading, both creep and fatigue are of importance in many plants. In recent years significant contributions from solar and wind power have been added to the electric supply. Since the amount of power of these renewable sources depends on the weather, additional basic power is needed. This has implied that many fossil fired power plants have been put into standby and are operated intermittently. This

R. Sandström, *Basic Modeling and Theory of Creep of Metallic Materials*, Springer Series in Materials Science 339,
https://doi.org/10.1007/978-3-031-49507-6_11

means that number of start-ups and shut-downs are increased and thereby the amount of cyclic loading.

Different types of damage appear depending on the relative amounts of creep and fatigue. If there is limited creep due to short loading times at high temperatures, the life time is controlled by fatigue [1]. Pure fatigue is dominated by transgranular crack initiation, Fig. 11.1a. On the other hand if there is modest amount of fatigue, the damage will be dominated by creep. Creep gives rise to cavitation in the grain boundaries, Fig. 11.1b. If fatigue and creep take place sequentially, the main cracks changes from transgranular to intergranular, Fig. 11.1c. If creep and fatigue loading occur simultaneously, the creep damage in the grain boundaries provides easy paths for the fatigue cracks, Fig. 11.1d.

Creep-fatigue interactions have traditionally been studied with low cycle fatigue (LCF) at a temperature close to the maximum operation temperature [3]. To observe any influence of creep, it is essential to include hold times in the load cycles [1]. However, it has turned out that LCF typically gives a lower amount of damage than is found in components. For simulating the role of straining during start-ups and shut-downs, thermal mechanical fatigue (TMF) is often used where both the loading and temperature are varied during the cycle. It is important that the minimum temperature in the cycle is low, since a significant part of the damage is generated at low temperatures [4]. LCF and TMF are commonly performed under strain control. A number of tests are carried out with a sequence of different maximum strains in the cycles. Hold times are introduced at the maximum and/or minimum strains. During

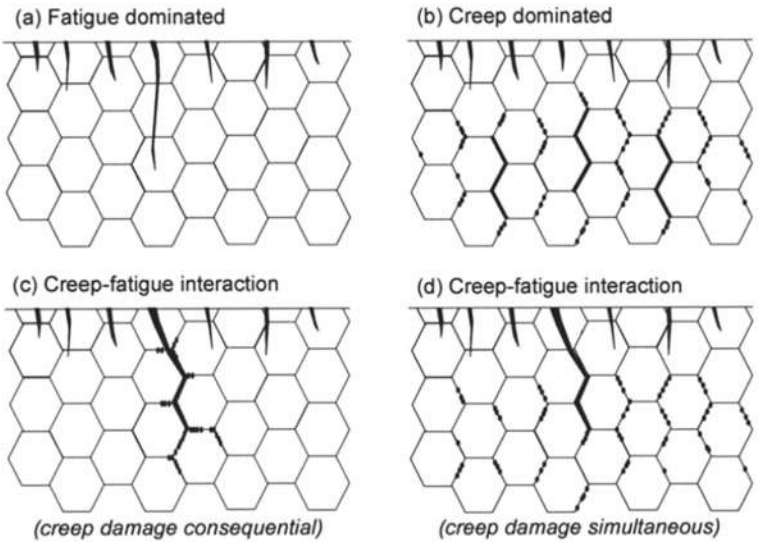

Fig. 11.1 Appearance of creep-fatigue damage mechanisms; **a** fatigue controlled; **b** creep controlled; **c** creep-fatigue interaction (sequential); **d** creep-fatigue interaction (simultaneous). Reprinted from [2] with permission of Taylor & Francis

the hold times the strain level is fixed during which the stress is relaxing due to creep. An alternative is to have hold times at a fixed stress. Since the absolute value of the average stress is larger during the hold times in this case, it gives rise to more creep damage than for a hold time at constant strain. The amount of creep damage can be increased by raising the length of the hold time or by lowering the strain rate in the cycle.

It is well-known that formation of creep cavities plays an important role during creep-fatigue interaction. This is illustrated in Fig. 11.1. In spite of the importance of creep cavities during creep-fatigue, only limited efforts to generate basic modeling of the phenomenon have been taken [5]. Instead, reference has to be made to brittle creep rupture during static conditions. It can be assumed that many of the mechanisms are similar for cyclic and static loading. The main mechanism for creep damage is believed to be initiation and growth of creep cavities in the grain boundaries. When the cavitated area fraction in the grain boundaries has reached a certain level, cracks are formed and rupture is close in common specimens [6]. In larger specimens and components the crack propagation stage is also of major importance [7].

Grain boundary sliding (GBS) is commonly assumed to give rise to cavity formation. This is a natural assumption. Considering for example particles in the grain boundaries. GBS will generate extensive shearing around the particles that can easily initiate cavities. However, cavities can also be formed in grain boundaries where very few particles are present such as in pure copper. Lim provided a model for this situation by taking into account the presence of substructure [8]. Cavities can form at the intersection between grain boundaries and the substructure. He showed that this process is thermodynamically feasible and there is an energy gain when cavities are formed. Quantitative models for cavity nucleation could now be formulated.

It has been shown experimentally and with the help of finite element methods (FEM) that the amount GBS is proportional to the creep strain [8, 9]. The FEM modeling also gives the proportionality constant, so it can be used for quantitative predictions. Using these findings and the assumption that cavities can nucleate at particles and subgrain-grain boundary junctions, the double ledge model was formulated [10]. This model gives that the number of cavities is proportional to the creep strain and the results are in quantitative agreement with observations [11]. It is assumed that these principles can be taken over for cyclic loading, Sect. 11.4.

Models for diffusion controlled growth of creep cavities have been available for many years. Unfortunately, these models typically predict much higher growth rates than the observed ones. It was however realized that cavities inside a material (not on the surface) cannot grow faster than the creep rate of the surrounding material. This is referred to as constrained growth in contrast to the unconstrained models [12]. Models for constrained growth were quickly developed and gave a better agreement with observations, see for example [13]. The models still tended to overestimate the growth rate. For this reason, the models were reanalyzed and with the help of FEM studies. A new and improved model could be established that is in better agreement with experiments [14].

Strain controlled growth of creep cavities can also take place in addition to diffusion growth. There are number of models based on plastic straining in the literature.

Unfortunately, most of these models do not consider constrained growth contrary to the situation for diffusion growth, which means that the predicted grow rate can give quite large cavity growth during creep. Recently, a model that takes the criterion for constraint growth into account has been presented which is of importance during creep [5]. During cyclic deformation, constrained cavity growth is not expected to be significant due to the often small creep strain in the cycles. This will be discussed in Sect. 11.4.2.

For creep failure it is important to distinguish between ductile and brittle rupture. Ductile rupture has been shown to occur after ductility exhaustion or after plastic instability has taken place (in specimens necking) [15]. Brittle rupture in many engineering materials takes place after the cavitated area fraction in the grain boundaries has reached a certain level. To predict creep rupture, the development of the microstructure must be possible to model including the dislocation structure, particle structure and the fraction of elements in solid solution. In this way the dislocation strengthening, particle hardening and solid solution hardening can be computed. In addition, quantitative models for cavity nucleation and growth must be available. Such models have been established and the creep rupture behavior has successfully been predicted for austenitic stainless steels without the use of adjustable parameters, see for example [16].

For monotonous loading these principles are well established. However, data and parameter values cannot be applied to cyclic loading directly and basic models for this case are only available to a limited extent. For example, the value of the dynamic recovery constant is much larger during cyclic than during static loading [5]. This will be analyzed in Sect. 11.3. Models for cavitation during low cycle fatigue will be presented in Sect. 11.4 and compared to experimental data for 1Cr0.5Mo steel.

11.2 Empirical Principles for Development of Creep-Fatigue Damage

11.2.1 Fatigue and Creep Damage

Basic models for describing creep rupture are available. Several models have been given in this book. However, for cyclic loading basic models do not seem to have been developed. However, many empirical models can be found. A model that is applicable to many materials is the Coffin-Manson equation

$$N_{\text{init}} = C_{\text{CM}}(\Delta\varepsilon_{\text{pl}})^{-\beta_{\text{CM}}} \tag{11.1}$$

where N_{init} is the number of cycle to crack initiation and $\Delta\varepsilon_{\text{pl}}$ the plastic strain range in the load cycle. C_{CM} and β_{CM} are constants that are fitted to the observations. Equations of type in (11.1) can sometimes also be used for the elastic and total strain range. The use of Eq. (11.1) is illustrated in Fig. 11.2.

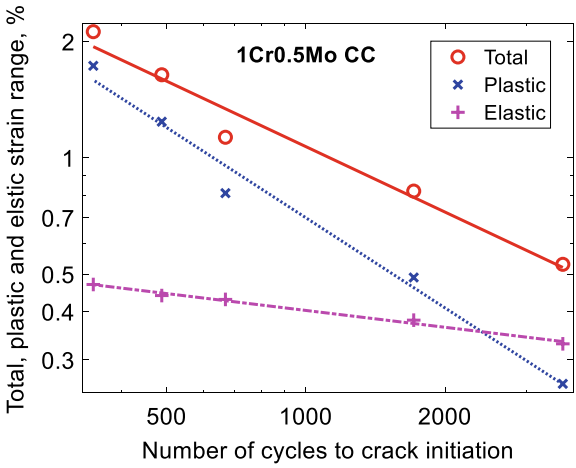

Fig. 11.2 Relation between the number of cycles to crack initiation and the total, plastic and elastic strain ranges for 1Cr0.5Mo during continuous cycling (CC). Experimental data from [17]. Redrawn from [18] with permission of Taylor & Francis

The influence of pre-creep before LCF and/or hold time during the LCF is illustrated in Fig. 11.3. With increasing amount of creep, the elastic strain range at a given number of cycles to crack initiation is significantly reduced. However, the effect of creep on the plastic strain range relation is not very pronounced.

The total fatigue damage D_F is often determined with the help of Miner's law. It is based on linear summation of the damage over individual cycles

$$D_F = \sum_i \frac{n_i}{N_{init}(\Delta\varepsilon_{pl}(i))} \tag{11.2}$$

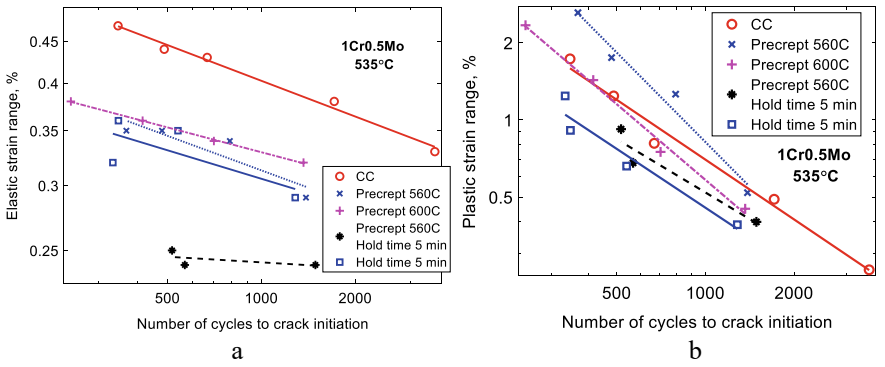

Fig. 11.3 Influence of 5% pre-creep strain and/or 5 min hold time on the number of cycles to crack initiation as a function of strain range for 1Cr0.5Mo. Experimental data from [17]; **a** elastic strain range; **b** plastic strain range

where n_i is the number of cycles when the plastic strain range is $\Delta\varepsilon_{pl}(i)$ giving a number of cycles to crack initiation of $N_{init}(\Delta\varepsilon_{pl}(i))$. When the damage reaches unity, failure is assumed to take place.

There are many expressions for the creep damage D_C. The classical principle is based on linear time fractions (Robinson rule)

$$D_C = \int_0^t \frac{dt_1}{t_R(T(t_1), \sigma(t_1))} \tag{11.3}$$

where $t_R(T, \sigma)$ is the rupture time at temperature T and stress σ as a function of time t. An alternative way is to base the damage on ductility exhaustion

$$D_C = \int_0^t \frac{\frac{d\varepsilon}{dt}(T(t_1), \sigma(t_1))dt_1}{\varepsilon_R(T(t_1), \sigma(t_1))} \tag{11.4}$$

where the accumulated creep strain is compared to the rupture ductility. A simple assumption of how to combine D_F and D_C would be to just add them. This means that rupture is predicted to occur when

$$D_F + D_C = 1 \tag{11.5}$$

However, detailed experiments have shown that such a relation is not conservative enough. In fact, bilinear equations have been demonstrated to agree with observations and have also been standardized by ASME

$$\begin{aligned} D_F &= 1 - \frac{1-\alpha_{FC}}{\alpha_{FC}} D_C \quad D_F \geq D_C \\ D_C &= 1 - \frac{1-\alpha_{FC}}{\alpha_{FC}} D_F \quad D_C \geq D_F \end{aligned} \tag{11.6}$$

The constant α_{FC} has been found to be material dependent. Holdsworth [7] gives the following values: for the austenitic stainless steels 18Cr10Ni and 17Cr12Ni2Mo, $\alpha_{FC} = 0.33$, for 20Cr30NiTi, $\alpha_{FC} = 0.11$, for 9Cr1Mo (P91), $\alpha_{FC} = 0.25$ and for 2.25Cr1Mo, $\alpha_{FC} = 0.11$. The bilinear relation in Eq. (11.6) is illustrated in Fig. 11.4. For comparison Eq. (11.5) would give a straight line between (0, 1) and (1, 0). Equation (11.6) is thus considerably more conservative than Eq. (11.5).

For plain specimens of parent metal, Eq. (11.6) is very well supported. However, already by considering multi-axial stresses, the prediction of the rupture time in Eq. (11.3) becomes an issue. Hayhurst [19] proposed that the rupture stress σ_R under multi-axial conditions could be represented by

$$\sigma_R = \gamma_1\sigma_1 + \gamma_2\sigma_h + \gamma_3\sigma_e \tag{11.7}$$

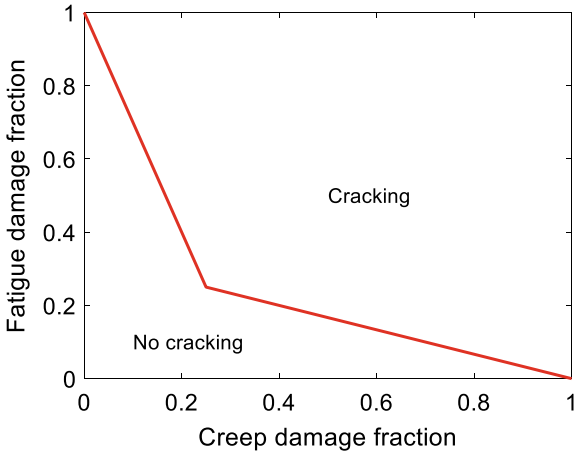

Fig. 11.4 Bilinear criterion for failure with combined fatigue and creep damage according to Eq. (11.6) with $\alpha_{FC} = 0.25$. Below the criterion line no cracking should take place

where σ_1 is the maximum principal stress, σ_h the average of the principal stresses and σ_e the effective stress. γ_1, γ_2 and γ_3 are constants that are fitted to creep rupture data under multi-axial conditions. It has been shown that Eq. (11.7) can be used to describe experimental data in a number of cases. However, it turns out that different authors give different values for γ_1, γ_2 and γ_3. Since the results of Eq. (11.7) are very sensitive to the values of these constants, it is difficult to use Eq. (11.7) to estimate the rupture stress. The issues with Eq. (11.7) have been discussed by Wen et al. [20]. This is one of the reasons why the ductility exhaustion expression for creep damage Eq. (11.4) is preferred by many authors to the estimate of the damage by integration over the rupture time, Eq. (11.3) [2]. The influence of multiaxiality on the creep rate can be described directly with the Odqvist equation [21]

$$\dot{\varepsilon}_{ij} = \frac{3}{2}\frac{s_{ij}}{\sigma_e} h(\sigma_e) \tag{11.8}$$

The stress dependence of the creep rate $h(\sigma)$ in the secondary stage can be found in Eq. (5.31). The stress deviator s_{ij} and the effective stress σ_e are given by

$$s_{ij} = \sigma_{ij} - \sigma_h \delta_{ij} \tag{11.9}$$

$$\sigma_e = \sqrt{\left((\sigma_1 - \sigma_2)^2 + (\sigma_2 - \sigma_3)^2 + (\sigma_3 - \sigma_1)^2\right)/2} \tag{11.10}$$

where σ_{ij} is the stress tensor, δ_{ij} the Kronecker delta, σ_1, σ_2 and σ_3 the principal stresses, and σ_h the hydrostatic stress (the average of the principal stresses). i and j runs over the coordinate directions 1, 2 and 3. By considering uniaxial conditions ($\sigma_1 = \sigma$, $\sigma_2 = \sigma_3 = 0$), it can easily be shown that the expected creep rates $\dot{\varepsilon}_{11} = \dot{\varepsilon}_u$, $\dot{\varepsilon}_{22} = -\dot{\varepsilon}_u/2$, $\dot{\varepsilon}_{33} = -\dot{\varepsilon}_u/2$ are reproduced, where $\dot{\varepsilon}_u$ is the uniaxial creep rate.

For the creep ductility, the influence of multiaxiality has been characterized quite well and there is a fair agreement between several models and experiments at least for notched bars. This is analyzed in Sect. 13.4.4. For example, the model by Wen and Tu seems to represent many sets of experimental data [22].

In the paper by Wen et al. [20] it is quite well documented that ductility exhaustion, Eq. (11.4) gives a considerably safer prediction than that based on the life fraction rule, Eq. (11.3). Even for ductility exhaustion, they demonstrate that the predicted damage typically deviates a factor of three up or down.

These results confirm many earlier results that it is not safe to base damage estimates solely on mechanical properties. It is also important to predict the microstructure development in terms of particle coarsening, subgrain growth, cavitation, etc. and compare the findings with observations. If it can be done with continuum damage mechanics that is fine, but it is strongly recommended to use basic models of the type formulated in this book.

A third way to estimate the damage is to compute the cavitated area fraction A_{cav} in the grain boundaries (Eq. (13.8))

$$A_{\text{cav}} = \int_0^t \frac{dn_{\text{cav}}}{dt'}(t')\pi R_{\text{cav}}^2(t,t')dt' \tag{11.11}$$

where n_{cav} is the number of creep cavities per unit grain boundary area and R_{cav} their radius. The amount of damage is then

$$D_{\text{C}} = A_{\text{cav}}/A_{\text{cavcrit}} \tag{11.12}$$

A_{cavcrit} is the amount of cavitation when cracks are initiated. If it is possible to record the cavitation, it is usually the safest way to assess the amount of damage. The modeling of n_{cav} and R_{cav} during cyclic loading is handled in Sect. 11.4.

11.2.2 Loops During Cyclic Loading

During cyclic loading the stress versus strain curves form loops that are called hysteresis loops. Perhaps the most common way of describing a hysteresis loop is with the Ramberg-Osgood equation

$$\varepsilon_{\text{a}} = \frac{\sigma_{\text{a}}}{E} + \left(\frac{\sigma_{\text{a}}}{K_{\text{lp}}}\right)^{\gamma_{\text{lp}}} \tag{11.13}$$

where ε_{a} is the strain, σ_{a} is stress, and E the elastic modulus. K_{lp} and γ_{lp} are adjustable parameters that are fitted to the experimental data. There are more complex approaches based on the assumption that the loops are due to the build-up of residual

stresses. The first such approach was due to Masing but models based on the superposition of a distribution of yield strengths have also been proposed [23].

The creep damage in a stress strain loop is primarily due to the stress relaxation during a hold time and thereby the amount of creep strain. To describe the stress relaxation during a hold time, the Feltham equation is often used for this purpose

$$\sigma_{\text{rel}} = \sigma_{\text{st}}(1 - \sigma_0 B_{\text{rel}} \log(1 + b_{\text{rel}} t)) \tag{11.14}$$

where σ_{st} is the start stress, σ_{rel} is the stress after relaxation and t the relaxation time. B_{rel}, b_{rel} and σ_0 are adjustable parameters. References to the original papers can be found in [24] where also some applications of the equations are given.

11.3 Deformation During Cyclic Loading

11.3.1 Basic Model for Hysteresis Loops

Empirical models for representing hysteresis loops are readily available. A few examples were mentioned in Sect. 11.2.2. Adjustable parameters in these models are fitted to the experimental data. Often a reasonable fit to the data can easily be obtained. There are however drawbacks with the empirical approaches. Typically a good fit can be found with many mathematical expressions and then it is difficult to know which one represents the correct mechanism. It is practically always desirable to extrapolate the results to new condition but if the operating mechanisms are not safely identified, generalization of the results becomes quite uncertain unless a large set of experimental data is available. Phrased in another way, empirical models are not predictable.

For creep under non-cyclic conditions, basic models have been presented in several chapters in the book and also in publications, for a survey, see [25]. The models are formulated from basic physical principles and have been shown to reproduce experimental data for copper, aluminum and austenitic stainless steels in a satisfactory way without using adjustable parameters. Such models are referred to as basic in this book. Only limited attempts have been made to perform the corresponding derivation for cyclic deformation, which involves elastic, plastic and creep deformation. The procedure described in [5] will be followed. The Voce equation can describe the plastic flow curve for a number of materials. This equation is given in Eq. (3.14) and can also be found in [26].

$$\sigma = \sigma_y + (\sigma_{\text{max flow}} - \sigma_y)(1 - e^{-\omega \varepsilon_{\text{pl}}/2}) \tag{11.15}$$

where σ is the applied stress, ε_{pl} the plastic strain, σ_y the yield strength, $\sigma_{\text{max flow}}$ the maximum flow stress, and ω the dynamic recovery constant. The deviation from linear behavior of the work hardening is controlled by ω. The plastic strain rate can

be obtained from Eq. (11.15)

$$\frac{d\varepsilon_{\mathrm{pl}}}{dt} = \frac{2}{\omega(\sigma_{\max\,\mathrm{flow}} - \sigma)}\frac{d\sigma}{dt} \tag{11.16}$$

The creep rate in the secondary stage $\dot{\varepsilon}_{\mathrm{sec}}$ is given in Eq. (4.3). The original derivation can be found in [27]

$$h(\sigma) = \frac{2bc_{\mathrm{L}}}{m_{\mathrm{T}}}\frac{D_{\mathrm{self0}}b\tau_L}{k_{\mathrm{B}}T}\left(\frac{\sigma}{\alpha Gb}\right)^3 e^{\frac{\sigma b^3}{k_{\mathrm{B}}T}} e^{-\frac{Q_{\mathrm{self}}}{R_{\mathrm{G}}T}\left[1-\left(\frac{\sigma}{\sigma_{\mathrm{imax}}}\right)^2\right]} e^{-\frac{Q_{\mathrm{sol}}}{RT}} \tag{11.17}$$

$$\frac{d\varepsilon_{\mathrm{sec}}}{dt} = h(\sigma - \sigma_{\mathrm{i}}) \tag{11.18}$$

where T is the absolute temperature, σ the applied stress, D_{s0} the pre-exponential coefficient for self-diffusion, Q_{self} the activation energy for self-diffusion, k_{B} Boltzmann's constant, R_{G} the gas constant, m_{T} the Taylor factor, b Burger's vector, τ_{L} the dislocation line tension, σ_{imax} the maximum flow stress, and c_{L} a work hardening constant. Solid solution hardening gives an additional contribution Q_{sol} to the activation energy. σ_{i} is an internal stress that includes contributions from solid solution hardening and particle hardening. The stress exponent is about 3 at low stresses, but increases rapidly with increasing stress. According to Eq. (4.6), the primary creep rate is given by

$$\frac{d\varepsilon_{\mathrm{prim}}}{dt} = h(\sigma + \sigma_{\mathrm{disl\,sec}} - \sigma_{\mathrm{disl}} - \sigma_{\mathrm{i}}) \tag{11.19}$$

In comparison to (11.18) an extra stress has been introduced

$$\sigma_{\mathrm{prim}} = \sigma_{\mathrm{disl\,sec}} - \sigma_{\mathrm{disl}} \tag{11.20}$$

For this model for primary creep that was described in Sect. 4.3, primary creep is fully accounted for just by introducing the extra stress in Eq. (11.20). It is the difference between the dislocation stress in the secondary stage $\sigma_{\mathrm{disl\,sec}}$ and that in the primary stage σ_{disl}. Since the dislocation density in the primary stage is normally much lower than that in the secondary stage, consequently $\sigma_{\mathrm{disl\,sec}}$ is much higher than σ_{disl}. The result is that the creep rate is much higher in the primary stage than in the secondary stage as it should. This is also directly evident from Eq. (11.19).

In a hysteresis loop, the stress is not stationary but varies all the time. It goes through the cycle so the creep process is restarted in every half cycle. This means that primary creep is involved. But in fact, Eq. (11.18) is still valid [28]. This can be seen from Eqs. (11.20) and (11.21). In these equations, $\sigma + \sigma_{\mathrm{prim}}$ correspond to the stress during cyclic loading. The result is simply

$$\frac{d\varepsilon_{\mathrm{prim}}}{dt} = h(\sigma - \mathrm{sgn}(\dot{\varepsilon}_{\mathrm{tot}})\sigma_{\mathrm{i}}) \tag{11.21}$$

This equation is obviously identical to Eq. (11.18) apart from the different sign in front of σ_i in the compression and the tension going part of the cycle.

The total strain rate $\dot{\varepsilon}_{tot}$ has contributions from the elastic $\dot{\varepsilon}_{el}$, plastic $\dot{\varepsilon}_{pl}$, and creep strain rate $\dot{\varepsilon}_{prim}$. The sum of the elastic, plastic, and creep strain rate is equal to the external strain rate

$$\frac{d\varepsilon_{el}}{dt} + \frac{d\varepsilon_{pl}}{dt} + \frac{d\varepsilon_{prim}}{dt} = \frac{d\varepsilon_{tot}}{dt} \tag{11.22}$$

where the elastic strain rate $\dot{\varepsilon}_{el}$ is

$$\frac{d\varepsilon_{el}}{dt} = \frac{d\sigma}{dt}\frac{1}{E} \tag{11.23}$$

and E is the elastic modulus. By combining Eqs. (11.16), (11.21), (11.22) and (11.23), the stress rate that gives the hysteresis loops is found

$$\frac{d\sigma}{dt} = \frac{1}{1/E + 2/\left[\omega(\sigma_{\max\,flow} - \mathrm{sgn}(\dot{\varepsilon}_{tot})\sigma)\right]}\left[\frac{d\varepsilon_{tot}}{dt} - h(\sigma - \mathrm{sgn}(\dot{\varepsilon}_{tot})\sigma_i)\right] \tag{11.24}$$

The sign function sgn in Eq. (11.21) is necessary to make the equation valid for both the tension and compression going parts of the loop.

When applying Eq. (11.24) for hysteresis loops, the starting point is that the properties used in monotonous loading should be taken over to as large extent as possible. Creep properties can be found for many materials. However, tensile properties at elevated temperatures are often more difficult to locate. The temperature dependence of the maximum flow stress below the creep range is approximately related to that of the elastic modulus (unpublished results)

$$\sigma_{\max\,flow}(T) = \sigma_{\max\,flow}(\mathrm{RT})\left[\frac{E(T)}{E(\mathrm{RT})}\right]^2 \tag{11.25}$$

where T and RT represent the value at temperature and room temperature, respectively. The dynamic recovery constant ω has also a related temperature dependence. But there is also another effect. ω describes how fast dislocations of opposite burgers' vectors on the same slip plane annihilate when they meet. But during cyclic deformation dislocations meet much more frequently that raises the value of ω. Each half cycle in the hysteresis loop can in this respect be considered equivalent to the strain to uniform elongation in the monotonous case. The resulting equation for ω is then

$$\omega(T) = \omega(\mathrm{RT})\frac{\varepsilon_u}{\varepsilon_r}\left[\frac{E(\mathrm{RT})}{E(T)}\right]^2 \tag{11.26}$$

where ε_u is the uniform elongation during monotonous loading and ε_r the strain range during cycling. Observe that the influence of the temperature dependence of the elastic modulus is opposite for $\sigma_{max\ flow}$ and ω.

11.3.2 Application of the Cycling Model

A model for the hysteresis loop is given in Eq. (11.24) based on the same principles as for stationary deformation. Elastic, plastic and creep deformation are considered. It involves parameter values for monotonous loading except for the dynamic recovery constant ω which has to be raised due to the frequent encounter of dislocations during cyclic deformation according to Eq. (11.26).

Equation (11.24) is applied in Fig. 11.5 to the 21Cr11Ni austenitic stainless steel 253 MA, that has rare earth metal additions to improve the oxidation resistance and can therefore be used up to 1000 °C. A loop for continuous cycling is illustrated.

An acceptable description of the loop is obtained. Data for the studied material can be found in [29].

The high value of ω is quite important. If the monotonous value for ω is used ($\omega = 15$ at room temperature) without taking the loop factor $\varepsilon_u/\varepsilon_r$ into account, the observed type of loop cannot be reproduced. This is shown in Fig. 11.6. Obviously, a reasonably formed looped cannot be formed.

In Sect. 11.4 on cavitation, the steel 1Cr0.5Mo will be studied. Since creep rate data for the steel have not been found, the model values have been compared to rupture data assuming that the Monkman-Grant relationship is valid. The rupture data is shown in Fig. 11.7.

An Arrhenius expression is fitted to the data

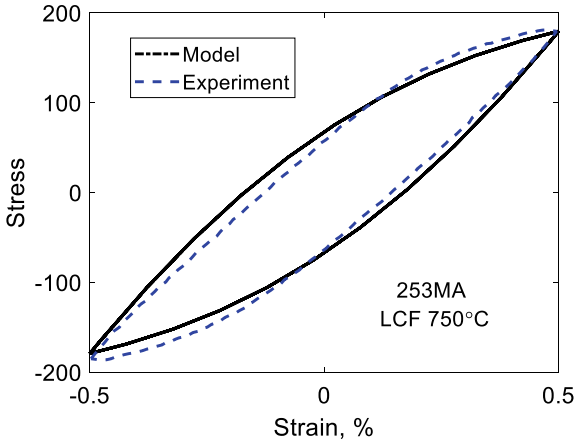

Fig. 11.5 Hysteresis loop for low cycle fatigue (LCF) of the austenitic stainless steel 253 MA at 750 °C. Experimental data are compared with the model in Eq. (11.24). Redrawn from [18] with permission of Taylor & Francis

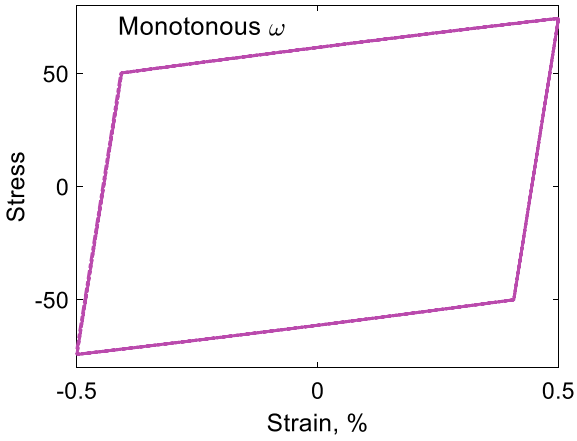

Fig. 11.6 Simulated hysteresis loop for low cycle fatigue (LCF) with the same parameter values except that a low ω (=15 at room temperature) value characteristic of monotonous deformation is used

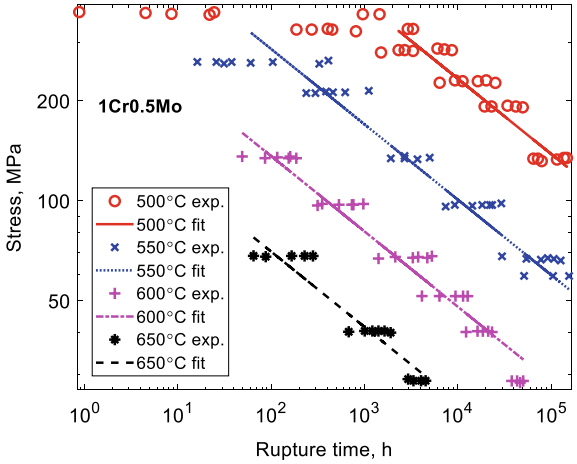

Fig. 11.7 Creep rupture data for 1Cr0.5Mo steel [30] fitted to an Arrhenius expression. Redrawn from [18] with permission of Taylor & Francis

$$\frac{1}{t_R} = C_R \exp\left(-\frac{Q_R}{k_B T}\right)\sigma^{n_N} \tag{11.27}$$

The data for stresses above 300 MPa are ignored since they are not of importance for the hysteresis loops. The values of the constants are $Q_R = 391$ kJ/mol, $n_N = 4.4$ and $C_R = 1.0 \times 10^{12}$ with the rupture time t_R in hours. Equation (11.27) is transferred to strain rate with the help of the modified Monkman-Grant relation.

$$\dot{\varepsilon} = \frac{\varepsilon_R}{t_R} \tag{11.28}$$

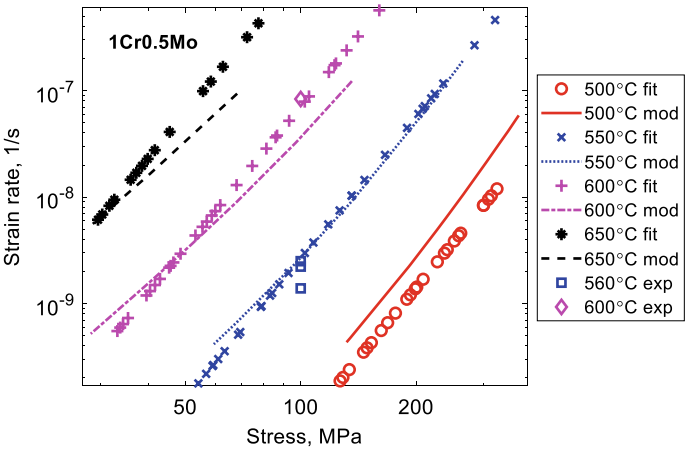

Fig. 11.8 Creep rate model values for 1Cr0.5Mo steel according to Eqs. (11.17) and (11.18) compared creep rupture data [30] fitted to an Arrhenius expression as well as to experimental creep rate values from [17]

The rupture ductility ε_R is taken as 0.1. The strain rate according to the model in Eqs. (11.17) and (11.18) is compared to that in Eq. (11.28) in Fig. 11.8. A few experimental data points for the creep rate from [17] are also included.

A precise agreement in Fig. 11.8 is not to be expected because the Monkman-Grant equation is only an approximate relation. In addition, the activation energy for the rupture is quite high, 390 kJ/mol. This should be compared to the activation energy for self-diffusion for ferrite that is 240 kJ/mol. For the creep rate this value is raised by the contribution from solid solution hardening that has been taken as 50 kJ/mol. The difference in activation energy between creep rupture and rate is still quite significant. The modelled strain rate are anyway of the right order around 550 °C, where the results are used for modeling hysteresis loops.

Four modeled loops for 1Cr0.5Mo steels are compared to experimental data in Figs. 11.9 and 11.10.

In Fig. 11.9, two loops cycled at 535 °C with and without pre-creep are compared. Pre-creep reduces the stress range probably due to softening of the microstructure during the creep process. In Fig. 11.10, the influence of a hold time is illustrated that decreases the stress range further. Pre-creep reduces the stress range also in this case. It is evident that the model in Eq. (11.24) can at least approximately describe the influence of pre-creep and hold time on the hysteresis loops.

To illustrate the applicability of the model in Eq. (11.24) quite a different case where creep has the main influence on the hysteresis loops is considered. This should be contrasted to Figs. 11.9 and 11.10 where the dominant influence on the loops is from cycling. Loops have been computed for alloy PM2000, which is a ferritic oxide dispersion strengthened (ODS) alloy with the approximate composition 20Cr5Al0.4Ti0.5Y2O3 [31]. Loops are presented in Fig. 11.11 at 1200 °C for two different strain rates. The dominance of creep is demonstrated by the flat upper

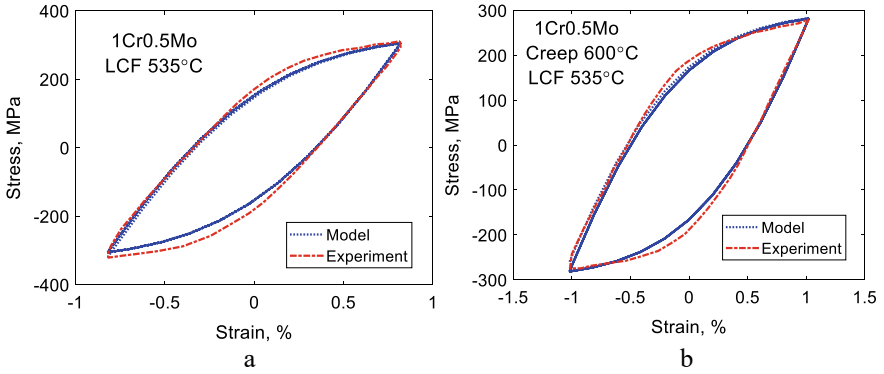

Fig. 11.9 Hysteresis loop for low cycle fatigue (LCF) of the ferritic-bainitic steel 1Cr0.5Mo at 535 °C. Experimental data from [17] are compared with the model in Eq. (11.24). **a** Tempered condition; **b** pre-crept to 5% strain at 600 °C. Redrawn from [18] with permission of Taylor & Francis

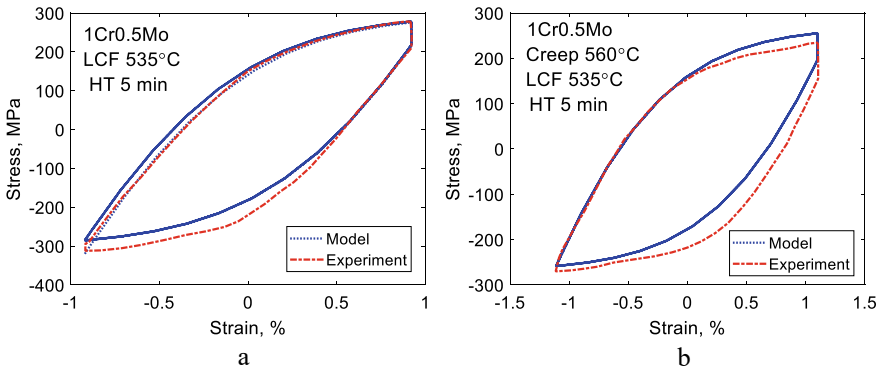

Fig. 11.10 Hysteresis loop for low cycle fatigue (LCF) of the bainitic steel 1Cr0.5Mo at 535 °C with a hold time of 5 min. Experimental data from [17] are compared with the model in Eq. (11.24). **a** Tempered condition; **b** pre-crept to 5% strain at 560 °C. Redrawn from [18] with permission of Taylor & Francis

and lower parts of the loops. The high temperature is the origin of the strong role of creep. The creep strain is of importance at lower stresses. This means that the vertical parts of the loops are controlled by the initial straighter part of the work hardening. The main effect of the lower strain rate in Fig. 11.11b is that it reduces the stress range somewhat.

In Fig. 11.12 a loop for thermo-mechanical fatigue (TMF) is presented. The thermal cycling is between 800 and 1200 °C with strain and temperature in phase, i.e. the maximum strain and temperature appear together. This is quite a severe test of the model in Eq. (11.24). The upper and lower parts of the loop are again controlled by creep. Since the temperature is increasing in parallel to the increasing strain in

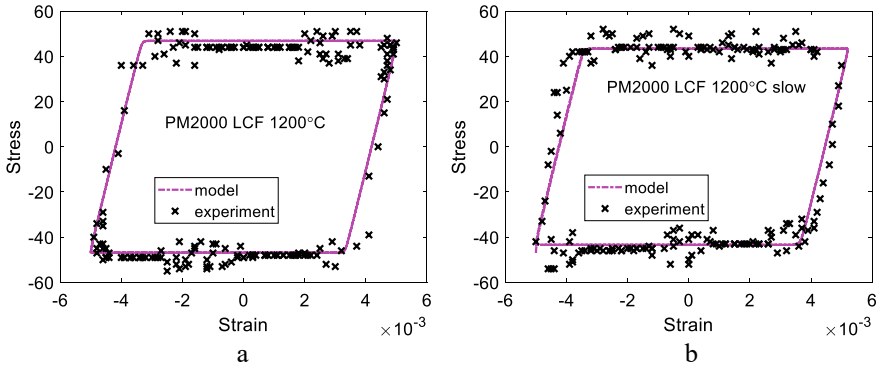

Fig. 11.11 Hysteresis loop for low cycle fatigue (LCF) of the ferritic ODS alloy at 1200 °C. Experimental data from [31] are compared with the model in Eq. (11.24); **a** strain rate 7×10^{-4} 1/s; **b** strain rate 5×10^{-5} 1/s. Reprinted from [5] with permission of Springer

the upper part of the loop, the stress is gradually decreasing. For the same reason the absolute value of the creep stress increases with decreasing strain in the lower part of the loop when the temperature is reduced.

Previously, the loops in Figs. 11.11 and 11.12 have been represented with an empirical model involving a number of adjustable parameters [31]. Such analysis is restricted to measured loops, and generalizing the results, for example, for computation of the fatigue and creep damage is difficult to manage in a safe way. However with the basic model for the hysteresis loop, the situation is different. It has been demonstrated that the model can handle different cases without using adjustable parameters. The possibility to extrapolate the results to new situations is then dramatically improved. In the past it has often been assumed that the shape of the hysteresis loops is due to the presence of a complex state of residual stresses that can be described with the Masing model or a distribution of yield strengths [23]. However, the results

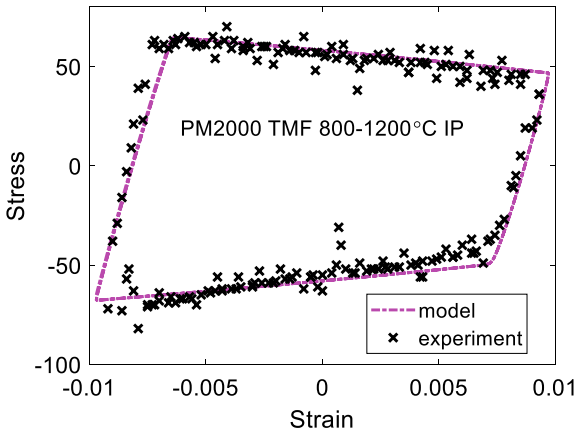

Fig. 11.12 Hysteresis loop for thermo-mechanical fatigue (TMF) of the ferritic ODS alloy PM2000 between 800 and 1200 °C in phase. Strain rate 5×10^{-5} 1/s. Experimental data from [31] are compared with the model in Eq. (11.24). Reprinted from [5] with permission of Springer

in this section demonstrate that monotonous and cyclic loading can be handled in the same way just by modifying the value of the dynamic recovery constant.

11.4 Cavitation

11.4.1 Nucleation of Cavities

The basic principles for nucleation of creep cavities are assumed to be the same in cycling and monotonous loading. Basic mechanisms for nucleation are discussed in 10.4 and in [6]. Although a number of mechanisms for nucleation have been proposed in the literature, the experimental data are fully consistent with the starting point that cavities are formed by grain boundary sliding (GBS). Cavities open up at particles or at subboundary—grain boundary junctions in sliding grain boundaries. The amount of GBS u_{GBS} is proportional to the creep strain, Eq. (9.11)

$$u_{\mathrm{GBS}} = C_{\mathrm{s}}\varepsilon \tag{11.29}$$

The value of the proportionality constant C_{s} has been determined with the help of FEM modeling [32], Eq. (9.12)

$$C_{\mathrm{s}} = \dot{u}_{\mathrm{GBS}}/\dot{\varepsilon} = \frac{3\phi}{2\xi} d_{\mathrm{g}} \tag{11.30}$$

where d_{g} is the grain size, $\phi = 0.15$–0.33 (the value increases with the creep stress exponent) and $\xi \approx 1.4$ are constants. With the help of the so called double ledge model, the nucleation rate can be related to the amount of creep strain [10]. According to this model, nucleation is assumed to take place when a subboundary on one side of a sliding grain boundary meets a subboundary on the other side or a particle. The result is the following nucleation rate, Eq. (10.8)

$$\frac{dn_{\mathrm{cav}}}{dt} = \frac{0.9C_s}{d_{\mathrm{sub}}}\left(\frac{g_{\mathrm{sub}}}{d_{\mathrm{sub}}^2} + \frac{g_{\mathrm{part}}}{\lambda^2}\right)\dot{\varepsilon} = B_{\mathrm{s}}\dot{\varepsilon} \tag{11.31}$$

where n_{cav} is the number of cavities nucleated per unit grain boundary area, and d_{sub} is the subgrain diameter. d_{sub} is inversely proportional to the dislocation stress that is in general close to the applied stress. λ is the interparticle spacing in the grain boundary. g_{part} and g_{sub} are the fractions of particles and subboundary junctions where cavitation takes place. The averaging over different orientations gives the factor 0.9. Equation (11.31) has been verified successfully by comparison to experiments for austenitic stainless steels [11] and copper [33].

A 1Cr0.5Mo ferritic-bainitic steel will be used to illustrate cavitation during LCF [17, 18]. Some of the specimens were creep tested before the LCF to study the

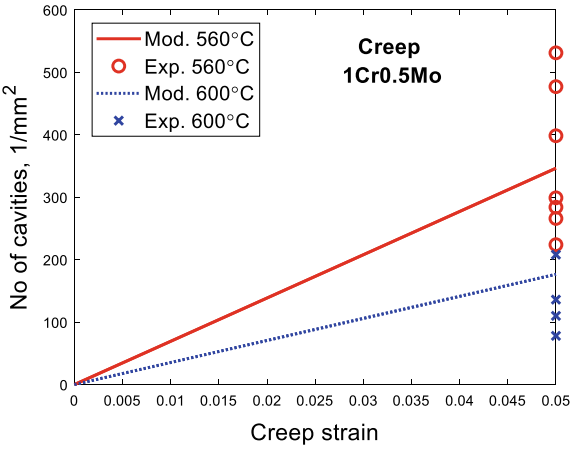

Fig. 11.13 Number of cavities versus creep strain for specimens later used in LCF testing. Experimental data from [17] are compared with the model in Eq. (11.31). Redrawn from [18] with permission of Taylor & Francis

combined influence of creep and cycling. The creep testing was performed at a stress of 100 MPa and was terminated when a creep strain of 5% was reached. The creep testing temperatures were 560 and 600 °C. The amount of cavitation is illustrated in Fig. 11.13.

The cavities are assumed to be nucleated around the carbides in the grain boundaries. By comparing the distribution of cavities and particles in the grain boundaries at 560 °C where micrographs are available, it turns out that one particle out of 5 initiated a cavity. This means that g_{part} is 0.2. It is not possible to predict the value of g_{part}. The grain size d_{grain} was 12 μm and the creep exponent $n_N = 4.4$. Equation (11.30) then gives a C_s value of 2.5×10^{-6} m. These parameter values are used in the modeling also for LCF.

The nucleation rate at 600 °C is clearly lower than at 560 °C. This has been interpreted as a result of particle coarsening. Since no basic creep model is available for the 1Cr0.5Mo steel, the amount of coarsening has to be estimated indirectly. With the help of Norton equations, the creep rates $\dot{\varepsilon}_{560}$ at 560 and $\dot{\varepsilon}_{600}$ at 600 °C can be expressed as

$$\dot{\varepsilon}_{560} = A_N \exp(-Q_{creep}/R_G T_{560})(\sigma - \sigma_{p560})^{n_N} \tag{11.32}$$

$$\dot{\varepsilon}_{600} = A_N \exp(-Q_{creep}/R_G T_{600})(\sigma - \sigma_{p600})^{n_N} \tag{11.33}$$

Since the creep rates have been measured, their ratio 21.3 is known. Since also the activation energy $Q_{creep} = 290$ kJ/mol and the stress exponent $n_N = 4.4$ are known, the ratio between the particle strengths σ_{p560} and σ_{p600} at 560 and 600 °C can be determined from Eqs. (11.32) and (11.33). It is found that the particle strengthening at 600 °C is 70% of that at 560 °C. Assuming that this is a consequence of differences in particle spacing according to model in Sect. 7.3, the corresponding differences in nucleation rate can be estimated. These results are applied in Fig. 11.13. It can be

seen that the observations for a creep strain of 0.05 can be reproduced in a reasonable way.

In [17] LCF tests with and without a hold time in tension were carried out at 535 °C. The length of the hold time was 5 min. Some of the tests were exposed to static creep before LCF as described above. The number of cavities was recorded before and after LCF. Only tests with a hold time significantly influenced the number of creep cavities. For this reason, the analysis will be focused on the tests with hold times. Seven such tests were performed. Some data for these tests can be found in Table 11.1.

The six left most columns in Table 11.1 give experimental data for the tests: total strain range ε_{tot}, stress range σ_{range}, number of cycles to failure N_{cycl}, number of cycles to crack initiation N_{init}, and the number of measured cavities per unit area n_{cav} after the test. Properties for the loops have been computed with the model in Sect. 11.3.1. Results are presented in the four right most columns in Table 11.1: stress drop due to relaxation during the hold time $\Delta\varepsilon_{hold}$, amount of creep strain during the hold time $\Delta\varepsilon_{hold}$, amount of creep strain during the tension going part of the cycle $\Delta\varepsilon_{cr\_tens}$ (excluding the strain during the hold time), and amount of creep strain during the compression going part of the cycle $\Delta\varepsilon_{cr\_cmpr}$. The stress relaxation during the hold time varies from 50 to 90 MPa. The corresponding creep strain lies between 0.00038 and 0.00067. The amounts of creep strain in the compression and tension going part of the cycle are almost two orders of magnitude smaller. Only the first of these four quantities can be compared with the experimental data. It was demonstrated in Sect. 11.3.2 that this could be accomplished in a successful way.

It is assumed that amount of cavitation during cycling can be based on Eq. (11.31), i.e. on the total creep strain. The total creep strain is the amount of creep strain in each cycle multiplied by the number of cycles N_{cycl}. There are three contributions to the creep strain in each cycle: (i) during the hold time $\Delta\varepsilon_{hold}$, (ii) during the compression going part of the cycle $\Delta\varepsilon_{cr\_cmpr}$ and (iii) during the tension going part $\Delta\varepsilon_{cr\_tens}$. These contributions are directly added. The result is the following expression for the number of cavities n_{cav}

$$n_{cav} = B_s(1 - f_{close})(\Delta\varepsilon_{hold} + \Delta\varepsilon_{cr\_tens} + \Delta\varepsilon_{cr\_cmpr})N_{cycl} \tag{11.34}$$

The total creep strain in each cycle is the expression within brackets in Eq. (11.34). The main part of the creep strain appears during the hold time. $\Delta\varepsilon_{cr\_tens}$ and $\Delta\varepsilon_{cr\_cmpr}$ are much smaller. In addition they have opposite signs so they cancel each other to a significant extent. In cycles with hold time in tension, the absolute value of $\Delta\varepsilon_{cr\_cmpr}$ is larger than that of $\Delta\varepsilon_{cr\_tens}$ so the overall effect is that the creep during the hold time is marginally reduced in the remainder of the cycle. The creep strain is multiplied by the B_s constant, Eq. (11.31). Some cavities may close during the compression going part of the cycle. This is taken into account with the help of the constant f_{close} which is the fraction of cavities that are closed in each cycle. The value of f_{close} will be estimated in Sect. 11.4.2.

Table 11.1 Data for hysteresis loops with hold time for 1Cr0.5Mo (Reprinted from [17] with permission of Taylor & Francis)

Pre-creep	ε_{tot}, %	σ_{range} MPa	N_{cycl}	N_{init}	n_{cav} 1/mm^2	$\Delta\sigma_{hold}$ MPa	$\Delta\varepsilon_{hold} \times 10^{-2}$%	$\Delta\varepsilon_{cr\_tens} \times 10^{-4}$%	$\Delta\varepsilon_{cr\_cmpr} \times 10^{-4}$%
No	0.92	590	720	540	905	62	4.5	6.2	−8.2
No	0.64	559	1590	1283	1097	52	3.8	2.8	−4.4
No	1.2	655	490	348	173	86	6.3	9.7	−13
No	1.53	669	409	334	1156	91	6.7	14	−18
Yes	0.55	447	1710	1489	3202	60	4.4	4.3	−6.5
Yes	0.83	494	671	568	3359	79	5.8	9.1	−14
Yes	1.11	502	576	517	2233	82	6.0	15	−21

The application of Eq. (11.34) is compared to experimental data in Figs. 11.14 and 11.15. The difference between the Figures is that in Fig. 11.15, the specimens were exposed to creep before the LCF testing.

For the modeling the same values as in Fig. 11.13 have been used with $C_s = 2.5\ \mu m$ and $d_{grain} = 12\ \mu m$. The subgrain size d_{sub} was determined at the average stress in the tension and compression going part of the cycles. The resulting values

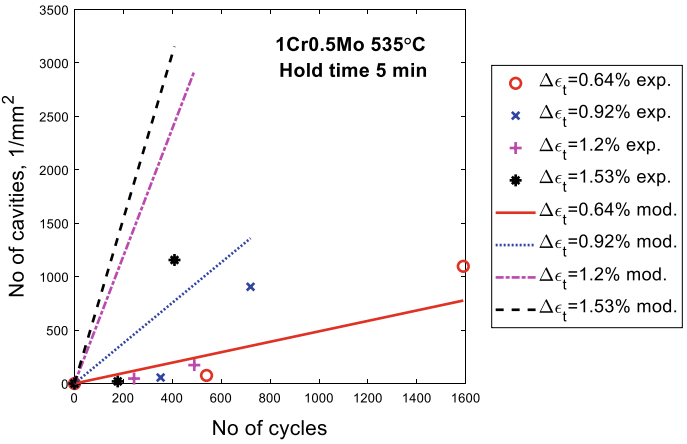

Fig. 11.14 Number of cavities versus number of cycles after LCF testing of 1Cr0.5Mo steels at 535 °C with 5 min hold time in the cycle. Total strain ranges between 0.64 and 1.53%. Experimental data from [17] are compared with the model in Eq. (11.34). Redrawn from [18] with permission of Taylor & Francis

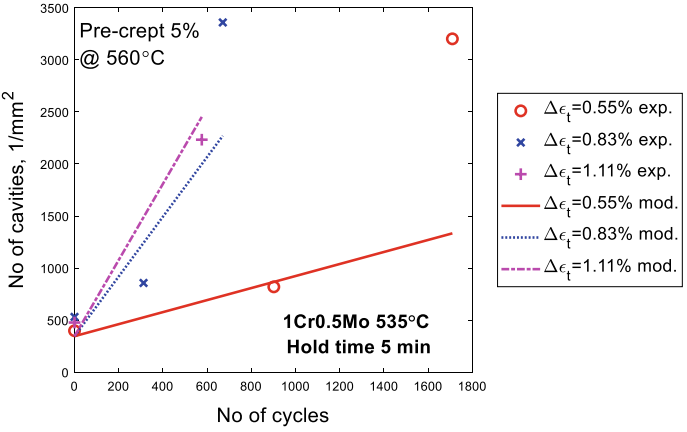

Fig. 11.15 Number of cavities versus number of cycles after LCF testing of 1Cr0.5Mo steels at 535 °C with 5 min hold time in the cycle. Total strain ranges between 0.55 and 1.11%. The specimens were exposed to 5% creep strain before the LCF testing. Experimental data from [17] are compared with the model in Eq. (11.34). Redrawn from [18] with permission of Taylor & Francis

are about $d_{sub} = 2$ μm. In Fig. 11.15, the number of cavities from the pre-creep in Fig. 11.13 has been added to the results. It seems that the cavitation model gives an acceptable result for most of the specimens.

11.4.2 Cavity Growth

Already in the 1950ties, Hull and Rimmer derived an expression for diffusion controlled growth of creep cavities. The expression was later modified by several authors to give it a more practical form. For example, Beere and Speight [34] derived the following formula that is of the form commonly used today, Eq. (10.11)

$$\frac{dR_{cav}}{dt} = 2D_0K_f(\sigma - \sigma_0)\frac{1}{R_{cav}^2} \tag{11.35}$$

where R_{cav} is the cavity radius in the grain boundary plane, dR_{cav}/dt its growth rate, σ_0 the sintering stress, $2\gamma_s \sin(\alpha)/R_{cav}$, where γ_s is the surface energy of the cavity per unit area and α the cavity tip angle. If the cavities are sufficiently small, they will shrink rather than grow after nucleation. The sintering stress avoids that the formula predicts growth in such cases. D_{GB} the grain boundary self-diffusion coefficient, and Ω_a the atomic volume are combined into a grain boundary diffusion parameter D_0, $D_0 = \delta D_{GB}\Omega_a/k_BT$. k_B is the Boltzmann's constant and T the absolute temperature. $K_f \approx 0.1$ is approximately a constant.

As discussed in Sect. 10.5, Eq. (11.35) typically overestimates the growth rates during creep. This problem was solved by introducing the requirement that the growth rate should not be higher than the creep rate of the surrounding matrix. This is referred to as constrained growth [12]. This means that equilibrium is established between the cavity growth and the creep deformation. Without this condition, the growth is referred to as unconstrained, and the growth rate in this case is given by Eq. (11.35). However, it is difficult to imagine that equilibrium can be established during the short cycle time and the small creep strain in common LCF tests. As illustrated in Table 11.1, the creep strains in each cycle are quite small. It must be assumed that unconstrained growth applies in LCF.

In addition for diffusion, plastic deformation can also give rise to growth of creep cavities. This was discussed in Sect. 10.5.3. A model where the cavity growth is proportional to the amount of grain boundary sliding (GBS) will be used [5], Eq. (10.24)

$$R_{cav} = C_s\varepsilon \tag{11.36}$$

Again the constant C_s is given by Eq. (11.30). After nucleation for example around particles, the cavities can continue to expand due to GBS. Elongated creep cavities in grain boundaries are often observed. It was demonstrated in Fig. 10.10

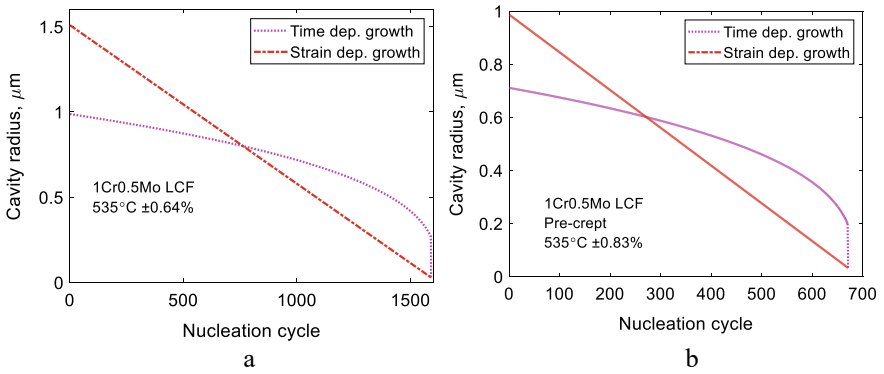

Fig. 11.16 Cavity radius versus the cycle where the cavity was nucleated. Two examples from the tests in Table 11.1 for 1Cr0.5Mo steel. Model values for diffusion controlled growth according to Eq. (11.35) and strain controlled growth, Eq. (11.36). Redrawn from [18] with permission of Taylor & Francis

that Eq. (11.36) could describe cavity growth for a 12CrMo steel and an austenitic stainless steel TP347 (17Cr12NiNb).

Equations (11.35) and (11.36) are applied in Fig. 11.16 to two cases in Table 11.1 for the 1Cr0.5Mo steel.

Figure 11.16 illustrates how a distribution of cavity sizes is obtained. The cavities that are nucleated early are larger since they are more exposed to growth processes. The two types of growth mechanisms give different behavior as a function of initiation cycle. Diffusion growth shows a rapid increase in cavity radius initially and a slower growth later. Strain controlled growth on the other hand has a constant increase with cycle number. No detailed measurement of the cavity size was performed in [17]. This would have been difficult anyway since the specimens were etched. Taking this into account, the computed cavity radii are consistent with the observations.

In the case of constrained growth, the values from diffusion and strain controlled growth should definitely not be added since the two mechanisms give each the maximum possible growth rates. This was discussed in Sect. 10.5.3. However, for unconstrained growth this conclusion is no longer self-evident. However, it turns out in the studied cases for 1Cr0.5Mo that if the two contributions are added quite large cavity radii of up to 10 μm are obtained which is not in agreement with observations. Adding the two contributions should therefore be avoided.

Equation (11.35) should in principle be possible to use to estimate the fraction of cavities that are closed during the compression going part of the LCF cycle. If it is applied directly it does not work. This can be seen in the following way. According to Eq. (11.36), in the first cycle a cavity with a radius of about 1×10^{-9} m is formed. With Eq. (11.35), such a cavity would disappear in fractions of a second. As a consequence, no cavities would be formed contrary to the observations. To make the result sensible, another case has to be considered. It is possible that the GBS does not take place in each cycle but occurs stepwise. It has been shown for copper during

static creep that the nucleated cavity size is in accordance with [33]

$$R_{\text{cavmin}} = 2\gamma_s \sin(\alpha)/\sigma \tag{11.37}$$

This relation is obtained by putting $\sigma = \sigma_0$ in Eq. (11.35). For the 1Cr0.5Mo steel, R_{cavmin} is about 1.5×10^{-8} m. With a strain rate of 0.003/s, in the compression part the cycle time is about 3 s. Using Eq. (11.35) one can derive that cavities that are smaller than about $R_{\text{cavmin}}/2.5$ are dissolved during this time. If it is assumed that the formed cavities have initially a size in the interval 0–2 R_{cavmin}, about a fifth of the cavities are closed during the compression part of the cycle. If this value is representative, f_{close} in Eq. (11.34) would be 0.2. However, this value is uncertain and it has not been applied in the computation of the nucleation rate in Figs. 11.14 and 11.15.

11.5 Summary

- Many plants that are operating at high temperatures are exposed to both creep and fatigue. A number of fossil-fired plants are running under intermittent loading while in the past they were adapted to base loading. The reason is that renewable sun and wind units do not supply power continuously and have to be backed up by conventional plants. As a consequence, fossil-fired power plants experience often combined creep and fatigue loading nowadays.
- Numerous empirical methods are available for assessing the material damage in plants. The classical Robinson's and Miner's damage summation rules have been extensively tested. Some results suggest that the damage typically can vary from being underestimated by a factor of three to being overestimated by the same factor. From a practical point of view such a large uncertainty is not acceptable. To base damage assessment just on mechanical properties is consequently difficult. It is also important to analyze the changes in the microstructure such as particle and substructure coarsening and formation of creep cavities and compare these findings with models. In this respect continuum damage mechanics can be quite useful.
- Many empirical models for damage assessment can predict both the development of mechanical properties and the microstructure. However, as for all empirical models, they have to be adapted to specific cases to give meaningful results. The alternative is to use basic models for both mechanical properties and microstructure. Such models are readily available also for the development of the microstructure as described in this book. Although basic models are somewhat more complex to program, the predictions are far safer.
- For analyzing creep damage, the assessment of cavitation has been quite useful. In recent years basic quantitative models for cavitation have been established that are directly applicable in this context. However, the situation has been different for cyclic loading. Two essential features have been missing. Prediction of stress

strain loops has been based on empirical approaches meaning that the results are restricted to the experimental case(s) under investigation. It is demonstrated in this chapter that many of the basic models applied in non-cyclic situations can be transferred to cyclic cases. The main parameter that has to be changed is the dynamic recovery constant. The reason for this is simple. During cyclic deformation dislocations encounter each other much more frequently than in monotonous cases and it increases the rate of recovery. Therefore, the recovery constant must take a higher value.

- The other missing feature has been the absence of models for the development of cavitation. It is expected that cavitation plays the same important role during creep-fatigue interaction as during plain creep. With the help of the models for the stress strain loops, the amount of creep strain in each cycle can be computed. By applying this in the formula for cavity nucleation, the number of cavities after LCF and after combined creep and LCF for a 1Cr0.5Mo steel have been possible to compute in an acceptable way.
- The cavity growth rate for the 1Cr0.5Mo steel has also been analyzed. Both models for diffusion controlled and strain controlled growth have been considered. Since quite small creep strains appear in each cycle unconstrained diffusion growth has been used. The reason is that it is assumed to be unrealistic that equilibrium between the cavity growth and the creep deformation could be established. The strain controlled growth is based on the assumption that the amount of growth is equal to the amount of grain boundary sliding. This assumption has previously worked well for two steels during creep where data are available. Although the diffusion growth is faster initially, the total growth is about the same as for strain controlled growth of the 1Cr0.5Mo steel. The final cavity size is in the interval from 0.1 to 1 μm, which seems reasonable. These results should be considered as tentative since detailed experiments are not available.
- It is often assumed that some closure of cavities takes place during the compression part of the load cycle. With the help of the model for diffusion controlled growth, it should in principle be possible to predict the amount of closure. Unfortunately, meaningful results are not obtained unless special assumptions are made. Therefore, the amount of cavity closure remains an open issue. In the prediction of cavity nucleation for 1Cr0.5Mo, no account of cavity closure has been taken into account. Satisfactory predictions have been obtained anyway indicating that the amount of cavity closure must be limited.

References

1. D.A. Miller, R.H. Priest, E.G. Ellison, Review of material response and life prediction techniques under fatigue-creep loading conditions. High Temp. Mater. Process. (London) **6**, 155–194 (1984)
2. S. Holdsworth, Creep-fatigue interaction in power plant steels. Mater. High Temp. **28**, 197–204 (2011)

3. L. Lundberg, R. Sandstrom, Application of low cycle fatigue data to thermal fatigue cracking. Scand. J. Metall. **11**, 85–104 (1982)
4. J.J. Moverare, A. Sato, S. Johansson, M. Hasselqvist, R.C. Reed, J. Kanesund, K. Simonsson, On localized deformation and recrystallization as damage mechanisms during thermomechanical fatigue of single crystal nickel-based superalloys, in *Advanced Materials Research* (2011), pp. 357–362
5. R. Sandström, Basic creep-fatigue models considering cavitation. Trans. Indian Natl. Acad. Eng. **7**(2), 583–591 (2021)
6. R. Sandström, J. He, Survey of creep cavitation in fcc metals, in *Study of Grain Boundary Character* (inTech, 2017), pp. 19–42
7. S.R. Holdsworth, Creep-fatigue properties of high temperature turbine steels. Mater. High Temp. **18**, 261–265 (2001)
8. L.C. Lim, Cavity nucleation at high temperatures involving pile-ups of grain boundary dislocations. Acta Metall. **35**, 1663–1673 (1987)
9. D. McLean, M.H. Farmer, The relation during creep between grain-boundary sliding, subcrystal size, and extension. J. Inst. Met. **85**, 41–50 (1957)
10. R. Sandström, R. Wu, Influence of phosphorus on the creep ductility of copper. J. Nucl. Mater. **441**, 364–371 (2013)
11. J. He, R. Sandström, Formation of creep cavities in austenitic stainless steels. J. Mater. Sci. **51**, 6674–6685 (2016)
12. B.F. Dyson, Constraints on diffusional cavity growth rates. Metal Sci. **10**, 349–353 (1976)
13. J.R. Rice, Constraints on the diffusive cavitation of isolated grain boundary facets in creeping polycrystals. Acta Metall. **29**, 675–681 (1981)
14. J. He, R. Sandström, Creep cavity growth models for austenitic stainless steels. Mater. Sci. Eng. A **674**, 328–334 (2016)
15. R. Sandström, J.-J. He, Prediction of creep ductility for austenitic stainless steels and copper. Mater. High Temp. **39**(6), 427–435 (2022)
16. J. He, R. Sandström, Basic modelling of creep rupture in austenitic stainless steels. Theoret. Appl. Fract. Mech. **89**, 139–146 (2017)
17. J. Storesund, R. Sandstrom, Interaction of creep damage and low cycle fatique damage in a 1Cr0.5Mo steel. Isij Int. **30**, 875–884 (1990)
18. R. Sandström, Cavitation during creep-fatigue loading. Mater. High Temp. **40**, 174–183 (2023)
19. D.R. Hayhurst, Creep rupture under multi-axial states of stress. J. Mech. Phys. Solids **20**, 381–382 (1972)
20. J.-F. Wen, S.-T. Tu, F.-Z. Xuan, X.-W. Zhang, X.-L. Gao, Effects of stress level and stress state on creep ductility: evaluation of different models. J. Mater. Sci. Technol. **32**, 695–704 (2016)
21. F.K.G. Odqvist, *Mathematical Theory of Creep and Creep Rupture* (Clarendon Press, 1966)
22. J.-F. Wen, S.-T. Tu, A multiaxial creep-damage model for creep crack growth considering cavity growth and microcrack interaction. Eng. Fract. Mech. **123**, 197–210 (2014)
23. R.P. Skelton, H.J. Maier, H.J. Christ, The Bauschinger effect, Masing model and the Ramberg-Osgood relation for cyclic deformation in metals. Mater. Sci. Eng. A **238**, 377–390 (1997)
24. S.R. Holdsworth, Creep-fatigue crack growth from a stress concentration. Mater. High Temp. **15**, 111–116 (1998)
25. R. Sandström, Fundamental models for the creep of metals, in *Creep* (inTech, 2017)
26. R. Sandström, J. Hallgren, The role of creep in stress strain curves for copper. J. Nucl. Mater. **422**, 51–57 (2012)
27. R. Sandstrom, Basic model for primary and secondary creep in copper. Acta Mater. **60**, 314–322 (2012)
28. F. Sui, R. Sandström, Basic modelling of tertiary creep of copper. J. Mater. Sci. **53**, 6850–6863 (2018)
29. H.C.M. Andersson, R. Sandstrom, D. Debord, Low cycle fatigue of four stainless steels in 20% CO-80% H-2. Int. J. Fatigue **29**, 119–127 (2007)
30. Data sheets on the elevated-temperature properties of normalized and tempered 1Cr-0.5Mo steel plates for pressure vessels (SCMT 2 NT) National Research Institute for Metals Tokyo, Japan (2002)

31. R. Sandstrom, H.C.M. Andersson, Modelling of hysteresis loops during thermomechanical fatigue, in *ASTM Special Technical Publication* (2003), pp. 31–44
32. F. Ghahremani, Effect of grain boundary sliding on steady creep of polycrystals. Int. J. Solids Struct. **16**, 847–862 (1980)
33. Y. Das, A. Fernandez-Caballero, E. Elmukashfi, H. Jazaeri, A. Forsey, M.T. Hutchings, R. Schweins, P.J. Bouchard, Stress driven creep deformation and cavitation damage in pure copper. Mater. Sci. Eng. A **833** (2021)
34. W. Beere, M.V. Speight, Creep cavitation by vacancy diffusion in plastically deforming solid. Metal Sci. **21**, 172–176 (1978)

Chapter 12
Tertiary Creep

Abstract In the tertiary stage, the creep rate is continously increasing eventually leading to rupture. Many mechanisms can contribute to the increasing creep rate such as particle coarsening, substructure coarsening, cavitation, changes in the dislocation density and necking. A large number of empirical models exist for the description of tertiary creep and the development of creep damage not least in the context of continuum damage mechanics (CDM). However, there are also basic models. An equation is presented that can describe the whole creep strain versus time curve. Only parameters that are already defined for secondary creep are needed. During the tertiary stage the true applied stress increases rapidly and faster than the counteracting dislocation strength, which is one main reason for the increase in the creep rate during the tertiary stage. Cavitation is of importance, but the cavitation is often local and therefore gives a modest contribution to the creep rate. According Hart's criterion, necking starts right at the beginning of the tertiary stage. But the necking is not fully developed until close to rupture. This is demonstrated both by uniaxial and multiaxial models and it is also consistent with available experimental data.

12.1 General

Most creep tests are performed as tensile tests at constant load or stress. In a creep strain test the strain is recorded as a function of test time, and the result is referred to as a creep strain curve. As discussed in detail in Chap. 4, the common form of the creep strain curves is that the slope decreases in the primary stage, reaches a minimum in the secondary stage and increases in the tertiary stage. In the secondary stage the microstructure is assumed to be essentially constant. Changes in the microstructure contribute to the increase in the creep rate that is observed in the tertiary stage. These changes will be analyzed in this chapter.

In the scientific literature, much focus has been on secondary creep, primarily because that data have been used to identify the operating creep mechanisms. However, primary and tertiary creep are technically also of major importance, but the number of systematic studies is much more limited. A significant fraction of the

R. Sandström, *Basic Modeling and Theory of Creep of Metallic Materials*, Springer Series in Materials Science 339,
https://doi.org/10.1007/978-3-031-49507-6_12

creep strain in fcc alloys occurs in the primary stage. The key to the understanding of creep rupture is the behavior during the tertiary stage.

The changes in the microstructure that give rise to the acceleration of the creep rate in the tertiary stage are traditionally referred to as creep damage [1]. Many mechanisms are known that contribute to the creep damage [2]. The most discussed ones are particle coarsening and dissolution, formation of creep cavities, recovery of dislocations and subgrain growth. In creep resistant martensitic steels microstructure degradation has often been observed to induce creep rupture. Fine carbonitrides (e.g. MX) coarsen and dissolve during long-term creep. New brittle phases can be created (e.g. Z-phase, Laves phase, M_6X carbides). The fine particles give a significant contribution to the creep strength which is reduced when their number decreases. The creep strength and in particular the creep ductility are lowered further when new coarse phases are present and act as crack nucleation sites [3–5].

Basic models for particle coarsening [6] and subgrain growth have been available for a long time. This includes the effect of Zener pinning of subboundaries [7]. This is of importance for stabilizing the substructure in martensitic creep resistant steels. For cavitation the situation has been less satisfactory. A basic model for cavity nucleation has only appeared recently [8, 9]. The models for cavity growth needed improvement to describe experimental data, Chap. 10 [10]. Also the dislocation models were necessary to extend and take substructure into account to understand why essentially the same creep strain behavior is observed at low and high temperatures, Sect. 8.4 [11, 12].

There is extensive literature on modeling of creep damage, not least in the connection of continuum damage mechanics (CDM) where the models are used to analyze the behavior of components. Reviews are given in [13, 14]. Practically all commonly used models are empirical or partially based on physical principles with a number of adjustable parameters involved. It is important to recognize the limitations with the use of adjustable parameters. Empirical models for tertiary creep were analyzed in [15]. Only two adjustable parameters were needed for some models to represent tertiary creep data in a satisfactory way and with three or four parameters almost any of the available models can give a good fit, Sect. 4.2. The important conclusion is that a good description with an empirical model does not ensure physical significance and does not make the model predictable. An empirical model can be used to identify operating mechanisms only if the same parameter values are used to get a good fit for a number of curves that is much larger than the number of adjustable parameters. A brief summary of CDM is given in Sect. 12.2.

Spent nuclear fuel in Finland and Sweden will be placed in copper canisters 500 m down in the bedrock for permanent disposal. Oxygen free copper alloyed with 50 ppm P has been selected as canister material because of its creep properties and its corrosion resistance in the environment. The copper will be exposed to creep deformation due to the hydrostatic pressure and the swelling pressure from the surrounding bentonite clay at temperatures up to 100 °C. The canisters should stay intact for 100000 years until radiation has declined to a low level. The creep properties of the canister must be possible to predict for such an extended time. This is only possible with fundamental creep models. It has been verified that the creep model

discussed in this book actually can cope with the required extended extrapolation, Sect. 14.4.6 [15].

Changes in the dislocation structure could generate microstructure degradation. A reduction in the dislocation density due to accelerated recovery has been found both experimentally [4, 16] and by computation [17]. Creep failure can also be induced by nucleation and growth of cavities [9, 10], Chap. 10. Also small defects can induce localized deformation if the material is plastically unstable which can result in necking [18]. During tensile creep testing at some stage, localized straining and necking occur. The role of the size of the initial defect has been studied [19–22].

Creep rupture is divided according to the type of failure. It is referred to ductile and brittle rupture if the creep ductility is high and low, respectively. There is no clear separation between these two types, but a rupture elongation above 30% is in general considered as high and an elongation below 10% as low. Brittle rupture is more crack sensitive since the creep cavities are more readily created. For brittle rupture the failure is primarily controlled by the formation of cavities, and when the cavitation is extensive enough, rupture occurs. Ductility exhaustion is assumed to initiate failure during ductile rupture. When the creep strain is sufficiently high, a plastic instability takes place and the component collapses. From a design point of view ductile rupture is preferred since more straining can take place before failure. The material is said to be more forgiving.

It will be assumed that tertiary creep is primarily controlled by the dislocation structure. The main mechanism for the increase in the creep rate in the tertiary stage has only recently been established [23]. The changes in the dislocation structure during a creep test can be quite complex. Modern 9Cr steel is a good example of that. To describe the creep deformation no less than three types of dislocation densities must be considered: mobile and immobile dislocations in the subgrain interiors and dislocations in the subgrain walls [24]. These complications will not be covered here. However, the general principles are expected to be the same. Instead, the analysis will be restricted to cases where only one type of dislocation controls the main behavior that is typical for example for fcc alloys. In this type of material there is generally a rapid increase in the dislocation density during primary creep. Contrary to what is stated in many places, there is slow continuous increase in the secondary stage in load controlled tests. During a creep test, there is a gradual reduction in the specimen cross section and for tests at constant load, this means that the true stress is increasing. During the secondary creep, this increase is matched by a corresponding increase in the dislocation density and thereby also the dislocation stress, Sect. 8.4. The rate of increase in the dislocation density is continuously reduced and in the tertiary stage this increase cannot keep up with the increase in the true stress and the creep rate is raised, Sect. 12.4.

There are other possible contributions to the increase in the creep rate in the tertiary stage. Cavitation plays a role in particular in creep brittle materials. However, extensive cavitation is typically strongly localized and does not appear over the whole material [25]. This means that cavitation gives a modest contribution to the increase in the creep rate. Particle coarsening is another effect. If particle coarsening takes place the internal stress from the particles is reduced and thereby an additional increase

in the creep rate is obtained [26]. Particle coarsening is considered in Sect. 12.3. Coarsening of the substructure also takes place, but that is considered to be a part of the changes in the dislocation structure mentioned above, Sect. 12.4. Finally, necking and other forms of plastic instabilities are of importance. The few systematic studies on necking in creep specimens that exist suggest that necking takes place close to rupture. This will be further discussed in Sect. 12.5 [23, 27].

12.2 Empirical Models for Tertiary Creep and Continuum Damage Mechanics

12.2.1 Models for Tertiary Creep

In this section a division is made between models that only aim to describe tertiary creep and those to attempt to model the development of the creep damage as well. The first type of models was analyzed in Sect. 4.2, and the analysis will not be repeated here. It was found that the Omega model [28, 29] could represent the creep rate in tertiary creep quite well with only two adjustable parameters in the considered cases for modified 9Cr steel, Fig. 4.4, and austenitic stainless steel, Fig. 4.8. If more adjustable parameters are involved, many models can be used to describe the tertiary stage, for a review, see [30, 31].

12.2.2 Continuum Damage Mechanics (CDM)

In continuum damage mechanics (CDM), the changes in the microstructure during creep is described with one or more damage parameters representing cavitation, particles coarsening, etc. Equations for the development of the damage parameters are formulated. When one of the damage parameters has reached the value of unity, crack initiation is assumed to take place and failure is close. Most models consider in reality cavitation to be the main damage mechanism. This is natural since extensive cavitation is closely related to crack initiation. There is a vast literature on CDM. For reviews, see [14, 32–34]. The models in general start with some basic concepts that are combined with empirical approaches. The number of adjustable parameters is often as high as 6–8 [13].

The work of CDM was initiated by Kachanov and Rabotnov. They considered the following types of model

$$\dot{\varepsilon} = A\left(\frac{\sigma}{1-\omega_1}\right)^n \qquad \dot{\omega}_1 = B\frac{\sigma^m}{(1-\omega_1)^\chi} \tag{12.1}$$

where $\dot{\varepsilon}$ is the creep rate, σ the applied stress, and ω_1 a damage parameter. A, B, m, n and χ are adjustable parameters. The new idea was the introduction of the damage parameter. It was assumed to have the value 0 at the start of the creep test and 1 at rupture. Although it is rarely stated in the literature, it is obvious that the equations are based on the assumption that the damage is due to cavitation. If the cavitation gives a reduction in the load bearing area, the modified Norton equation in (12.1) is obtained. In Eq. (12.1) an equation for the development of the creep damage is also given. With 5 adjustable parameters there is no difficulty in describing almost any creep curve in the tertiary stage.

As mentioned above there are numerous empirical CDM models in the literature. Two examples will be mentioned here because they seem to be still used frequently. The first one is due to Othman et al. [35]. The creep rate is given by

$$\dot{\varepsilon} = \frac{A}{(1-\omega_1)(1-\omega_2)^n}\sinh(B\sigma) \qquad \dot{\omega}_1 = C(1-\omega_1)^2\dot{\varepsilon} \tag{12.2}$$

$$\omega_1 = 1 - \frac{\rho_1}{\rho} \qquad \dot{\omega}_2 = \frac{\dot{\varepsilon}}{3\varepsilon_u}\left(\frac{\sigma_1}{\sigma_e}\right)^{\nu} \tag{12.3}$$

In Eqs. (12.2) and (12.3) there are two damage parameters ω_1 and ω_2. ω_1 takes into account the role of the increasing dislocation density ρ during creep. ρ_1 is the initial mobile dislocation density. Equation (12.2) gives a very rapid increase in the dislocation density close to rupture. The damage due to the cavitation is described by ω_2. It is supposed to take both the effect of nucleation and growth into account. ω_2 is proportional to the creep strain that is well established for nucleation, Eq. (10.8) and at least for some materials can describe growth as well, Eq. (10.24). σ_1 is the maximum principal stress and σ_e the effective stress. A, B, C, n, ν and ε_u are constants.

The second model that will be mentioned is due to Perrin et al. [36]. They give the following equations

$$\dot{\varepsilon}_{ij} = \frac{3s_{ij}}{2\sigma_e}A\sinh\left(\frac{B\sigma_e(1-H)}{(1-\Phi)(1-\omega_2)}\right) \qquad \dot{H} = \left(\frac{h\dot{\varepsilon}_e}{\sigma_e}\right)\left(1-\frac{H}{H^*}\right) \tag{12.4}$$

$$\dot{\Phi} = \left(\frac{K_c}{3}\right)(1-\Phi)^4 \qquad \Phi = (1-\lambda_i/\lambda) \tag{12.5}$$

To show that the CDM equations are straight forward to transfer to multiaxial stress states, Eqs. (12.4) and (12.5) are given in this form. $\dot{\varepsilon}_{ij}$ is the strain tensor and s_{ij} the stress deviator, and $\dot{\varepsilon}_e$ the effective strain rate. H is a damage parameter that is intended to take into account primary creep. Φ considers the effect of particle coarsening. λ is the particle spacing and λ_i the corresponding initial value. A, B, h, H^*, K_c are constants. Including the temperature dependence, no less than 12 constants is listed in [36].

The two models in Eqs. (12.2) and (12.3) as well as in (12.4) and (12.5) represented the state of the art when the papers were written. Unfortunately, not much of the modeling can be considered basic today.

12.3 Particle Coarsening

During later stages of the creep life, precipitates are often coarsening due to Ostwald ripening. The driving force for the coarsening is the reduction of the surface energy of the particles. For a given volume fraction, a distribution of coarser particles has a lower total surface energy than one with smaller particles. The coarsening takes place by diffusion of elements between the particles. Coarsening is believed to degrade creep properties in 9–12%Cr steels. Typically, there are two main types of particles in these steels: $M_{23}C_6$ and MX. In $M_{23}C_6$, M represents Cr, Fe, Mo or W. For MX, M stands for V and Nb and X for C or N. The distribution of the two types of particles is different. $M_{23}C_6$ are mainly found in the subgrain boundaries where they are nucleated during tempering. MX particles on other hand are more homogeneously distributed in the steel. The distribution of $M_{23}C_6$ is generally coarser than that of MX. As a consequence the two particle types have different roles during creep. $M_{23}C_6$ slows down or prevents the coarsening of the substructure. In this way the total dislocation density can be kept at a high level, which is most important for the creep strength. The MX particles on the other hand give precipitation hardening and in this way contribute directly to the creep strength.

If only a single particle type is involved and the coarsening is controlled by lattice diffusion, the coarsening can be described by Ostwald ripening

$$r_j^3 = r_{0,j}^3 + k_j t \tag{12.6}$$

where r_j is the average particle radius for type j and $r_{0,j}$ the corresponding initial value. k_j is the coarsening rate constant. For a system with N elements, k_j is given by [6]

$$k_j = \frac{8}{9} \frac{\Gamma_{\text{surf}} V_{\text{m}}^j}{\sum_{k=1}^{N} \frac{(x_k^j - x_k^{\alpha/j})^2}{x_k^{\alpha/j} D_k^\alpha / R_{\text{G}} T}} \tag{12.7}$$

where Γ_{surf} is the particle interfacial energy per unit area, V_{m}^j is the molar volume of the particle type j, R_{G} the gas constant, and T the absolute temperature. The denominator is a sum in k over the elements involved in the diffusion, D_k^α is the diffusion coefficient, as well as x_k^j and $x_k^{\alpha/j}$ the equilibrium mole fraction in the particle respectively the matrix at particle/matrix interface. Equation (12.7) is complex but the value of k_j can often be obtained directly from thermodynamic software.

From Eq. (12.6), it is evident that the average volume of the particles increases linearly with time, so it is quite a simple dependence. The presence of particle in the subgrain walls slows down the growth of the subgrain and sets a limit to the maximum subgrain size. This is described by the following equation [7]

$$\frac{dd_{\text{sub}}}{dt} = \frac{3M_{\text{climb}}\tau_{\text{L}}}{2d_{\text{sub}}} \cdot \left[1 - \left(\frac{d_{\text{sub}}}{d_{\text{sub lim}}}\right)^2\right]^2 \tag{12.8}$$

d_{sub} is the subgrain diameter and $d_{\text{sub lim}}$ the limiting subgrain size due to the retarding force from the particles, which is referred to as Zener drag. The limiting subgrain size is given by [7]

$$d_{\text{sub lim}} = \frac{\pi r_{\text{p}}}{\gamma f_{\text{p}}} \tag{12.9}$$

r_{p} is the radius of particles at subgrain boundaries, and f_{p} their volume fraction. The constant γ has a value of about 0.5 [37].

As was described in Sect. 2.6, creep strain can generate a large number of vacancies. This means that phenomena that are diffusion controlled can also be strain controlled. Diffusion requires the presence of vacancies. An equilibrium amount of vacancies C_{Va} is formed due to thermal activation. C_{Va} can be represented with an Arrhenius expression

$$C_{\text{Va}} = c_0 = \exp\left(\frac{S^{\text{F}}_{\text{Va}}}{k_{\text{B}}} - \frac{H^{\text{F}}_{\text{Va}}}{k_{\text{B}}T}\right) \tag{12.10}$$

where S^{F}_{Va} and H^{F}_{Va} are the entropy and the enthalpy for vacancy formation, and k_{B} Boltzmann's constant. The corresponding formula for the diffusion coefficient D_{Va} is

$$D_{\text{Va}} = A^{\text{D}}_{\text{Va}} \exp\left(-\frac{H^{\text{F}}_{\text{Va}} + H^{\text{M}}_{\text{Va}}}{k_{\text{B}}T}\right) \tag{12.11}$$

where H^{M}_{Va} is the enthalpy for vacancy migration and A^{D}_{Va} a constant. Diffusion depends on both formation and migration of vacancies, but the vacancy concentration is only a function of the formation energy. The part of the diffusion coefficient that depends on the vacancy concentration can be extracted

$$D_{\text{Va}} = A^{\text{D}}_{\text{Va}} \exp\left(-\frac{H^{\text{M}}_{\text{Va}}}{k_{\text{B}}T} - \frac{S^{\text{F}}_{\text{Va}}}{k_{\text{B}}}\right)c_0 \tag{12.12}$$

The corresponding amount of vacancies generated by straining is given by Eq. (2.37)

$$\Delta c = 0.5 c_0 \frac{\sqrt{2} K_{sub}^2 \dot{\varepsilon} b^2}{D_{self}} \frac{G}{\sigma} \tag{12.13}$$

It can be assumed that straining gives rise to coarsening in the same way as Ostwald ripening in Eq. (12.6)

$$\frac{dV_p}{d\varepsilon} = k_\varepsilon \tag{12.14}$$

where V_p is the average particle volume and k_ε a constant. The value of k_ε can be derived from Eq. (12.7) by replacing c_0 in the expression for the diffusion coefficient by Δc using Eq. (12.12).

For homogeneously distributed particles, coarsening of the particles implies that their contribution to the creep strength is reduced. This is described by Eq. (7.17). When coarsening takes place, the critical spacing between particles λ_{crit} increases.

12.4 Dislocation Strengthening During Tertiary Creep

12.4.1 The Role of Substructure During Tertiary Creep

During deformation a cell structure is formed in most alloys. Already after 10% strain the majority of the dislocations can be found in the cell boundaries [38]. After 20% deformation practically all dislocation are located in the cell boundaries [39]. As will be demonstrated below the cell structure plays an important role during tertiary creep. To simplify the analysis the role of dislocations in the cell interiors will be neglected. This has been justified experimentally. For example, Straub et al. showed with X-ray techniques that the dislocations in cell interiors in copper only contributed 10 MPa to the strength [40].

As was introduced in Sect. 8.1, there are two sets of dislocations in the cell walls: balanced and unbalanced. This is a direct consequence of the basic nature of dislocations. The dislocations are initially randomly distributed in the cells. If there are dislocations in the cell interior with burgers vector **b** and opposite burgers vector −**b** on a given slip plane, they would move in opposite directions under stress. The effect is that dislocations with one sign end up at one side of the cells and the ones with the opposite sign on the other side. This means that the dislocations have different signs on the two sides of a cell wall in the stress direction. Such a set of dislocations are called polarized or unbalanced. The term unbalanced is due to the fact that all the dislocations in the neighborhood have the same sign. At other regions of the cells, the dislocations with both types of burgers vectors are present. These sets of dislocations are referred to as balanced.

That the dislocations in the cell walls are divided into two sets, balanced and unbalanced is therefore natural. It is well documented experimentally that the dislocations in cell walls can be statistically distributed and polarized [41]. The central and main part of the cell walls is found to consist of balanced dislocations, whereas the outer layers are polarized. The polarized dislocations cannot move through the walls due to the large number of dislocations in the cell walls [12]. Argon has proposed that the balanced dislocations in the cell walls to a significant extent are dislocation locks [42]. To understand tertiary creep and some other properties, the distinction between balanced and unbalanced dislocation is of importance.

Equations for the dislocation densities of the balanced and unbalanced types as well as for locks were given in Eqs. (8.17)–(8.19). The dislocation densities satisfy the following equations [11, 12]

$$\frac{d\rho_{\text{bnd}}}{d\varepsilon} = k_{\text{bnd}} \frac{m\rho_{\text{bnd}}^{1/2}}{bc_L} - \omega\rho_{\text{bnd}} - 2\tau_{\text{L}} M\rho_{\text{bnd}}^2/\dot{\varepsilon} \tag{12.15}$$

$$\frac{d\rho_{\text{bnde}}}{d\varepsilon} = k_{\text{bnde}} \frac{m(\rho_{\text{bnd}}^{1/2} + \rho_{\text{bnde}}^{1/2})}{bc_L} - \omega\rho_{\text{bnde}} \tag{12.16}$$

$$\frac{d\rho_{\text{lock}}}{d\varepsilon} = k_{\text{lock}}\omega(\rho_{\text{bnd}} + \rho_{\text{bnde}}) - \omega\rho_{\text{lock}} - 2\tau_{\text{L}} M\rho_{\text{lock}}^2/\dot{\varepsilon} \tag{12.17}$$

ρ_{bnd}, ρ_{bnde} and ρ_{lock} are the balanced, unbalanced and lock dislocation density in the cell walls, which are defined as the total length of the dislocations divided by the cell volume. ε is the strain, m_{T} the Taylor factor, b Burger's vector, c_{L}, k_{bnd} and k_{bnde} are work hardening constants, ω the dynamic recovery constant, τ_{L} the dislocation line tension, $\dot{\varepsilon}$ the strain rate and M the creep climb mobility. In Eq. (12.15) the three terms on the right hand side represent work hardening, dynamic recovery and static recovery in the same way as in the basic Eq. (2.17). Since the unbalanced dislocations cannot meet a dislocation with opposite sign, there is no static recovery term in Eq. (12.16). Both unbalanced and balanced dislocations are subjected to dynamic recovery. The dislocation locks cannot generate dislocations, but instead they obtain an input of dislocation due to dynamic recovery of balanced and unbalanced dislocations. As a consequence the first term in Eq. (12.17) has a different appearance in comparison to Eqs. (12.15) and (12.16). It is important to understand the difference between static and dynamic recovery. Static recovery occurs when dislocations of opposite signs meet and annihilate. Dynamic recovery takes place through the formation of dislocation configurations with lower energy [43]. A contributing factor has been suggested by Argon [42]. It is well documented that when dislocations are released during plastic straining they move through one or more cell boundaries. When this happens a fraction of the dislocation in the boundaries is removed, giving rise to a recovery effect. Both dynamic recovery and static recovery should be considered when describing tertiary creep as will be discussed below. Dynamic recovery requires straining [44] while static recovery is a time dependent process [45]. In the analysis

below the dislocation locks will be considered to be a part of the balanced density in the cell walls.

Since the unbalanced dislocations in the cell walls are not exposed to static recovery they give rise to an extra hardening that is referred to as a back stress [11]. The increase in the true applied stress $\sigma = \sigma_0 e^{\varepsilon}$ during creep under constant load is compensated by the back stress, where σ_0 is the applied nominal stress. The magnitude of the back stress equals the dislocation stress plus other strengthening contributions σ_i minus the nominal applied stress

$$\sigma_{\text{back}} = \sigma_{\text{disl}} + \sigma_i - \sigma_0 \tag{12.18}$$

where σ_{disl} is given by (cf. Eq. (8.3))

$$\sigma_{\text{disl}} = \frac{m_T \alpha G b}{2} \sqrt{\rho_{\text{bnd}} + \rho_{\text{bnde}}} \tag{12.19}$$

where α is a constant in Taylor's equation, and G the shear modulus. The effective creep stress is obtained as the true applied stress minus the back stress

$$\sigma_{\text{creep}} = \sigma - \sigma_{\text{back}} \tag{12.20}$$

From Eq. (12.15), an expression for the secondary creep rate can be obtained

$$\dot{\varepsilon}_{\text{sec}} = 2\tau_L M(T, \sigma_{\text{creep}}) \rho_{\text{bnd}}^2 / \left(k_{\text{bnd}} \frac{m \rho_{\text{bnd}}^{1/2}}{b c_L} - \omega \rho_{\text{bnd}} \right) \tag{12.21}$$

where the effective creep is inserted. It is now assumed that Eq. (12.21) it is not just applicable to secondary creep but it describes the influence of the changes of the dislocation density on the whole creep curve [12]

$$\dot{\varepsilon} = 2\tau_L M(T, \sigma_{\text{creep}}) \rho_{\text{bnd}}^2 / \left(k_{\text{bnd}} \frac{m \rho_{\text{bnd}}^{1/2}}{b c_L} - \omega \rho_{\text{bnd}} \right) \tag{12.22}$$

This model suggests that if the stress dependence of the secondary creep rate is known, the influence of the dislocation density on the whole creep curve can be derived. Primary creep was dealt with in Sect. 8.2.

The variation of the stress components is illustrated for copper in Fig. 12.1. At the start of the creep test, the dislocation is low and the effective creep stress is high. But already after a short time they are of about the same magnitude. The dislocation stress then balances the true applied stress quite well in the secondary stage giving almost overlapping curves. This means that the creep stress is approximately constant in the secondary stage. Finally in the tertiary stage the increase of the applied stress is faster than that of the dislocation stress. Thus, there is an increase in the creep stress and thereby in the creep rate.

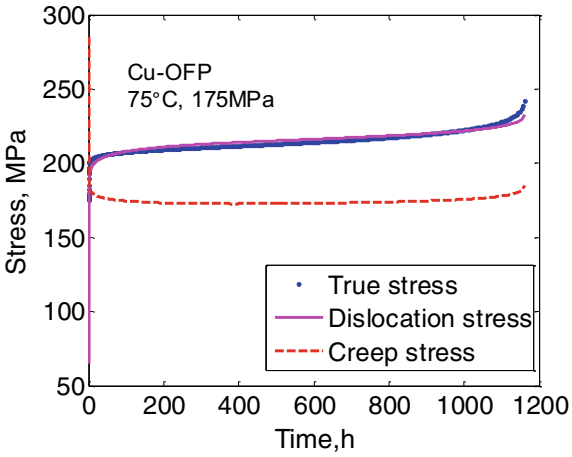

Fig. 12.1 Evolution of dislocation stress, true applied stress and effective creep stress as a function of time for Cu-OFP at 75 °C with an applied stress of 175 MPa. Redrawn from [23] with permission of Springer

By integrating Eq. (12.22) together with (12.15) and (12.16), creep strain versus time curves can be obtained. Two examples for Cu-OFP at 75 °C are given in Fig. 12.2. The experimental curves show distinct primary, secondary and tertiary creep in spite of the low temperature. An extended secondary stage is found in spite of a stress exponent that exceeds 50. How this is possible was explained in Sect. 8.4. The substructure plays an important role in this respect and that is taken into account in Eq. (12.22). There are steps in the experimental curves due to the necessity of reloading the creep when a certain creep strain was reached. No attempts have however been made to try to compensate for the reloading of the creep machine. The experimental creep curves can be reproduced in a reasonable way. Some of the differences can be accounted for by taking necking into account which is analyzed in Sect. 12.5.

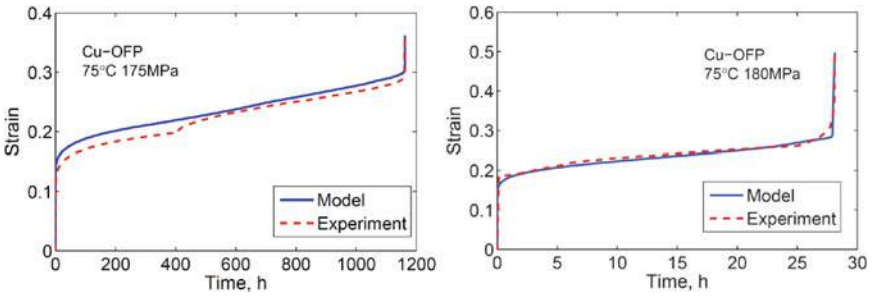

Fig. 12.2 Comparison of experimental creep curves with the model in Eq. (12.22) for Cu-OFP, **a** 75 °C, 175 MPa; **b** 75 °C, 180 MPa. Redrawn from [23] with permission of Springer

12.4.2 Accelerated Recovery Model

During later stages of creep there is often a degradation of the creep strength. This degradation is often referred to as creep damage. Important examples of creep damage are cavitation and particle coarsening. The latter effect was analyzed in Sect. 12.3. Particle coarsening gives rise to a reduction of the precipitation hardening. In addition, subgrain coarsening can take place if the distance between particles in the boundaries is increased.

Particle coarsening is usually represented with a time dependence described by Ostwald ripening in Eq. (12.6). However, tertiary creep shows more typically strain dependence. This is illustrated in Sect. 4.2. The strain rate in the tertiary stage increases exponentially with strain. This is referred to as the Omega model, which was discovered during work with estimates of residual life time of fossil fired power plants. For this reason it is natural to consider strain dependent processes. One such process is the strain dependent coarsening given in Eq. (12.14). A strain dependent process is also present for static recovery. Time dependent static recovery has been the basis of many derivations in this book. Its basic form is given in Eq. (2.17)

$$\frac{d\rho}{dt} = -2\tau_L M\rho^2 \tag{12.23}$$

However, strain dependence is also possible to consider in the same way as for particle coarsening

$$\frac{d\rho}{d\varepsilon} = -2\tau_L M_\varepsilon \rho^2 \tag{12.24}$$

In the modified version of the climb mobility M_ε in Eq. (12.24), the diffusion constant has to be replaced by the expression given in Eq. (12.12). The principles for the derivation of Eqs. (12.16) and (12.24) are straightforward, but the expressions have not yet been verified experimentally. By taking also Eq. (12.24) into account, Eq. (2.17) takes the form

$$\frac{d\rho}{d\varepsilon} = \frac{m_T}{bc_L}\rho^{1/2} - \omega\rho - 2\tau_L(M/\dot{\varepsilon} + M_\varepsilon)\rho^2 \tag{12.25}$$

From Eq. (12.25), an expression for the creep rate can be derived in the same way as in Sect. 8.2.2

$$h(\sigma) = 2\tau_L M(T,\sigma)\frac{\sigma^3}{(\alpha m_T G b)^3}\Big/\left(\frac{m_T}{bc_L} - \omega\frac{\sigma}{\alpha m_T G b} - 2\tau_L M_\varepsilon \frac{\sigma^3}{(\alpha m_T G b)^3}\right) \tag{12.26}$$

$$\dot{\varepsilon} = h(\sigma_{creep}) \tag{12.27}$$

The effective creep stress σ_{creep} is given by Eq. (12.20). With the help of Taylor's Eq. (2.29), Eq. (12.25) can be expressed in term of the dislocation stress σ_{disl}

$$\frac{d\sigma_{disl}}{d\varepsilon} = \frac{\alpha m_T^2 Gb}{2bc_L} - \frac{\omega}{2}\sigma_{disl} - 2\tau_L(f_M M/h(\sigma_{creep}) + M_\varepsilon)\frac{\sigma_{disl}^3}{(\alpha m_T Gb)^2} \qquad (12.28)$$

Since the value of M_ε is unknown, it has been assumed that its stationary value is that of $M/h(\sigma_{creep})$, i.e. that the two types of static recovery give about the same contribution.

The use of Eqs. (12.27) and (12.28) in Fig. 12.3 is illustrated for Sanicro 25. A comparison is made with the same experimental data set as in Fig. 4.8. In Fig. 12.3a, the dislocation stress is shown as a function of creep strain. There is initially a rapid increase in the dislocation density. When the stress touches the true stress curve and the secondary stage is reached, the increase in the stress continues but at a much lower rate. The difference between the sum of the true stress and the nominal stress on one hand and the dislocation stress on the other is the effective creep stress, Eq. (8.29). Considering the difference between the true stress and any of the dislocation stresses, it is evident from Fig. 12.3a that the creep rate is higher in the tertiary stage than in the secondary stage but lower than in the primary stage.

In Fig. 12.3a, the dislocation stress is compared with the true applied stress. Most creep models are based on the nominal stress, so also in this book. However, to describe tertiary creep, the true stress plays an important role, and Eqs. (12.26)–(12.28) are based on the true stress. To take the true stress into account instead of the nominal one, some adjustments of the model must be made. For example, the secondary stress to give the creep rate in the secondary stress is slightly higher when the true stress is used. This is covered with the constant f_M in Eq. (12.28). f_M is close

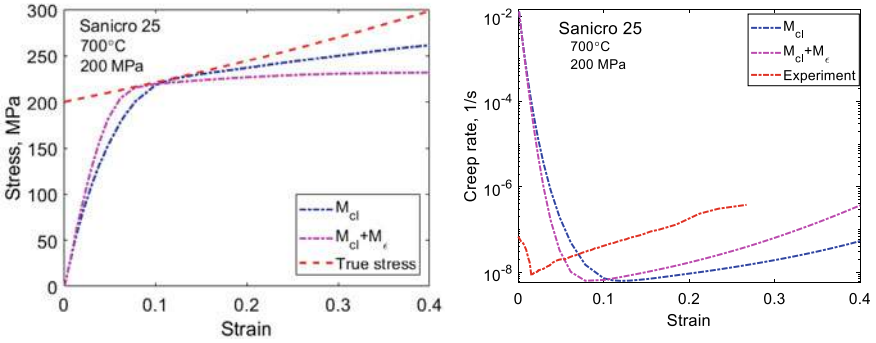

Fig. 12.3 **a** Dislocation stress according Eq. (12.28) with $(M_{cl} + M_\varepsilon)$ and only with (M_{cl}). M_ε and M_{cl} are the strain and time dependent climb mobility, respectively. The true stress is also shown; **b** creep rate from Eq. (12.27) for the same cases as in a). A comparison with experiment is included. Sanicro 25 at 700 °C, 200 MPa

to unity. This can also be seen in Fig. 12.3a, where the stresses in the secondary stage are slightly higher than the nominal value of 200 MPa.

In Fig. 12.3, a comparison is made between the case when only the time dependent static recovery and the case when both the time and strain dependent types are included. In the first case only the time dependent climb mobility M is taken into account and in the second case both M and M_ε. The difference between the two cases is clearly observed in Fig. 12.3b where the creep rate is plotted versus strain. The creep rate drops rapidly in the primary stage. The position of the minimum creep rate does not agree with the observations. The reason is most likely that the strain on loading is included in the modeling but not in the experiments. In the tertiary stage the logarithm of the creep rate increases linearly as a function of strain. This is the characteristic feature of the Omega model as was discussed in detail in Sect. 4.2. The slope of the experimental curve in the tertiary stage Fig. 12.3b is $n_\Omega = 14$. The creep stress exponent at 700 °C for the material is $n_\mathrm{N} = 7$. At 725 and 750 °C the corresponding values are $n_\Omega = 11$ and 9 and $n_\mathrm{N} = 6$ and 5, respectively. If only M is taken into account in the model the slope is close to the n_N value whereas a higher value close to n_Ω is obtained when also M_ε is involved.

For P91 that is also studied in Sect. 4.2, the difference between n_Ω and n_N is even larger. The experimental data in [46] is for 600 °C. The n_N value at this temperature is 12 whereas n_Ω takes the values 28, 39, 65 and 95 for applied stresses of 180, 150, 130 and 110 MPa, respectively. That n_Ω increases with decreasing applied stress is also found for Sanicro 25 although the effect is less dramatic. The fact that n_Ω is significantly larger than n_N clearly shows that degradation of the microstructure takes place. It is natural that the degradation increases with decreasing stress since there is more time for microstructural changes to take place. The degradation is larger for P91 than for Sanicro 25. This is also expected since P91 has a martensitic structure that is prone to changes at high temperatures. The model including M_ε describes how the recovery is accelerated during the tertiary stage, which is a direct consequence of microstructural degradation.

12.5 Necking

12.5.1 Hart's Criterion

During tensile creep testing a plastic instability develops towards the end of the experiment. A waist is formed around the specimen that grows until the specimen fails. This phenomenon is usually referred to as necking. It is assumed that it is initiated due to the presence of a geometric imperfection or a material inhomogeneity. The continued growth of the waist does not depend on how it was initiated.

Hart proposed a criterion for the initiation of necking during creep [47]. The initiation is assumed to be due to area fluctuations. The deformation is stable provided that the variation at a particle point is larger than zero. From the relation between the

area reduction and the strain a stability criterion can be derived

$$\ddot{\varepsilon}/\dot{\varepsilon}^2 \leq 1 \tag{12.29}$$

where $\dot{\varepsilon}$ is the strain rate, and $\ddot{\varepsilon}$ is strain acceleration, the second time derivative of the strain. One can expect that when this stability criterion fails, necking would be initiated in the same way as for Considère's criterion during tensile testing at ambient temperatures.

12.5.2 Use of Omega Model

The implications of Hart's criterion can be illustrated with the help of the Omega (Ω) model. It was illustrated in Sect. 4.2 that primary creep often follows the phi (ϕ) model and tertiary creep the Omega model. As was demonstrated in Sect. 4.2, it is not necessary to have a separate term for secondary creep. Then according to Table 4.1, the creep rate can be expressed as

$$\dot{\varepsilon} = \phi_1 \varepsilon^{-\phi_2} + \Omega_3 \exp(n_\Omega \varepsilon) \tag{12.30}$$

where the first and second term on the RHS refers to primary and tertiary creep. ϕ_1, ϕ_2, Ω_3 and n_Ω are adjustable parameters. Ω_4 in Table 4.1 has been replaced by n_Ω since that designation was used above. According to Sect. 4.2, tertiary creep can be represented by the second term in Eq. (12.30) over a fair strain range. Consequently, it is of interest to analyze that term separately.

$$\dot{\varepsilon} = \Omega_3 \exp(n_\Omega \varepsilon) \qquad \ddot{\varepsilon} = \Omega_3 n_\Omega \dot{\varepsilon} \exp(n_\Omega \varepsilon) \tag{12.31}$$

By combing the two equations in (12.31), we find that

$$\ddot{\varepsilon}/\dot{\varepsilon}^2 = n_\Omega \tag{12.32}$$

Since n_Ω is typically much larger than unity, the stability criterion in (12.29) is very far from satisfied in the tertiary stage. In the primary stage $\ddot{\varepsilon}$ is negative and in the secondary stage zero, so in these stages the stability criterion is fulfilled. To satisfy it also in the tertiary stage, there must be a large contribution from the primary creep term in (12.30). This is only possible at the start of the tertiary stage. One can conclude that Eq. (12.29) implies that an instability is formed when tertiary creep is initiated. Similar results have been found when testing the criterion on experimental creep curves that do not follow the Ω model.

Burke and Nix [48] studied necking by analyzing the deformation in a cylindrical bar with an imperfection. They assumed a cross section that varied with a smooth sinusoidal function

$$A(x,0) = A_0 - \frac{\Delta A}{2}\cos\frac{2\pi x}{L_i} \qquad (0 \le x \le L_i) \tag{12.33}$$

where A_0 is the original cross section area of specimen, and L_i the length of the specimen with the defected part. ΔA represents the changes of the initial cross section area. They considered that the development of the imperfection could be described by a uniaxial model. The shape of the initial imperfection is then not so important, only the initial reduction of the cross section.

It is possible to estimate the growth of the imperfection. As was discussed above, Eq. (12.29) suggests that an instability is formed shortly after the start of tertiary. Only then an imperfection can grow. It is thus possible to use the tertiary part of Eq. (12.30) to estimate the amount of necking.

$$\dot{\varepsilon} = \Omega_3 \exp(n_\Omega \varepsilon) \qquad \varepsilon_\mathrm{bar} = -\frac{1}{n_\Omega}\log(\exp(-n_\Omega\varepsilon_0) - n_\Omega\Omega_3 t) \tag{12.34}$$

The integrated solution is given in the second member. ε_0 is the starting strain of tertiary and t is the time. Following Eq. (12.33), the imperfection has a reduced cross section by a factor f_red. The solution of the equation in the presence of an imperfection is

$$\varepsilon_\mathrm{waist} = -\frac{1}{n_\Omega}\log\left(\exp(-n_\Omega\varepsilon_0) - \frac{n_\Omega\Omega_3 t}{f_\mathrm{red}^{n_\mathrm{N}}}\right) \qquad f_\mathrm{red} = 1 - \Delta A/A_0 \tag{12.35}$$

The solutions of Eqs. (12.34) and (12.35) are illustrated in Fig. 12.4 for Sanicro 25 and P91. The cases are the same as the ones in Figs. 4.4 and 4.8.

Solutions with and without waist are given in (12.34) and (12.35). The difference between the strain in the waist and in the unaffected bar $\varepsilon_\mathrm{diff}$ gives the depth of the waist and this difference is shown in the Figure. Thus, we have the following simple

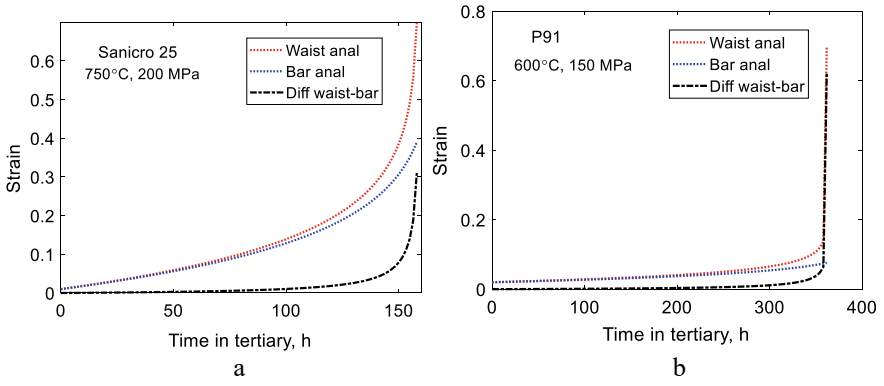

Fig. 12.4 Strain versus time for the solutions in Eqs. (12.34) and (12.35) for **a** Sanicro 25, 750 °C, 200 MPa and **b** P91, 600 °C, 150 MPa. **a** Redrawn from [49] with permission of Taylor & Francis

relation

$$\varepsilon_{\text{waist}} = \varepsilon_{\text{bar}} + \varepsilon_{\text{diff}} \tag{12.36}$$

The influence of the waist is only significant late in the creep life. It is evident that when this strain difference exceeds 0.2, rupture is close. By assuming an $\varepsilon_{\text{diff}}$ value larger than 0.2 a criterion for rupture can be obtained. By combing the equations for ε_{bar} (12.34), for $\varepsilon_{\text{waist}}$ (12.35) and Eq. (12.36), and expression for the rupture time can be derived

$$t_{\text{R}} = \frac{e^{-n_\Omega \varepsilon_0}}{\Omega_3 n_\Omega} \frac{1 - e^{-n_\Omega \varepsilon_{\text{diff}}}}{(1/f_{\text{red}}^{n_{\text{N}}} - e^{-n_\Omega \varepsilon_{\text{diff}}})} \qquad \Omega_3 = \dot{\varepsilon}_{\text{min}} \exp(\varepsilon_0) \tag{12.37}$$

In Eq. (12.37), an expression for Ω_3 has been given in terms of the minimum creep rate. The latter quantity may be easier to find. Assuming $f_{\text{red}} = 0.99$ which is often done, Eq. (12.37) gives a rupture time of 51, 75, 144 and 244 h for Sanicro 25 for the four curves in Fig. 4.8 that are in reasonable accordance with the observed values 51, 63, 148 and 244 h. The corresponding values for P91 in Fig. 4.4 are 62, 357, 1787, 10800 h that should be compared with the observed ones 101, 546, 3650 and 13940 h. The predicted values clearly underestimate the experimental ones in this case. An equation for the rupture elongation ε_{R} can also be obtained. The same three Eqs. (12.34)–(12.36) are combined and this time the time t and $\varepsilon_{\text{waist}}$ are eliminated

$$\varepsilon_{\text{R}} = \frac{1}{n_\Omega} \frac{(1/f_{\text{red}}^{n_{\text{N}}} - e^{-n_\Omega \varepsilon_{\text{diff}}})}{(1/f_{\text{red}}^{n_{\text{N}}} - 1) e^{-n_\Omega \varepsilon_0}} \tag{12.38}$$

For the same four curves in Fig. 4.8, Eq. (12.38) yields 0.31, 0.38, 0.31, and 0.34 that should be compared with the experimental values 0.24, 0.22, 0.36 and 0.43. The predicted values are of the right order of magnitude but they do not reproduce the observed values more precisely. For the curves for P91 in Fig. 4.4, the predicted values are 0.095, 0.078, 0.053, 0.034 and the experimental ones 0.17, 0.15, 0.19 and 0.072. The predicted values are about half the observed ones. The reason why the values for the martensitic steel are underpredicted is not known.

12.5.3 Basic Dislocation Model

More detailed comparisons will now be made with experimental data for P alloyed pure copper Cu-OFP [23]. Distinct necking was observed on the ruptured specimens, which emphasizes the importance of necking in tertiary creep. To describe the deformation, the dislocation model in Eq. (12.27) is used. Again uniaxial behavior will be assumed for assessing the influence of necking. Influence of multiaxial stress states will be considered in Sect. 12.5.4. The starting imperfection is given by Eq. (12.33)

with a 1% reduced cross section ($f_{\text{red}} = 0.99$) and a half length of the imperfection of $L_{\text{i}} = 5$ mm. With the formulae in Chap. 10, the amount of cavitation can be estimated. For the cases considered in [23], the local values of the cavitated grain boundary area were found to be about 2% which is consistent with observations on the specimens. However, as discussed in Sect. 12.1, the average amount is much lower. As a consequence the influence of cavitation on the creep curves is small and is not noticeable at the scale of the Figures. The initiation of the instability is assumed to follow Hart's criterion (12.29). In Fig. 12.5b the position of this initiation point is marked. It is again evident that the point appears very early in the tertiary stage.

Modeled creep curves are compared with experiments for three stresses at 75 °C for Cu-OFP in Fig. 12.5. The dislocation model in Eq. (12.27) takes primary, secondary and tertiary creep into account. The dislocation model gives only a modest contribution to tertiary creep, but the effect is clearly visible. There are other cases where the influence is much more pronounced. Examples are shown in Fig. 8.12 for cold worked copper.

The rise of the creep strain at the end of the creep life is due to necking. Obviously the uniaxial creep model can reproduce the sharp increase quite well. The model clearly demonstrates that the necking takes place late in the creep life.

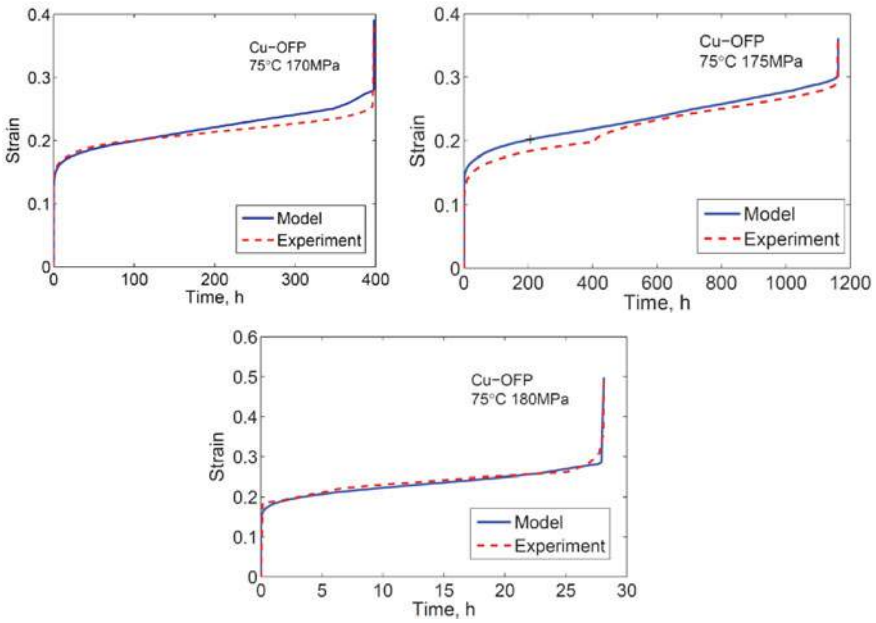

Fig. 12.5 Comparison of experimental creep curves with necking model results for Cu-OFP, **a** 75 °C, 170 MPa; **b** 75 °C, 175 MPa, plus marker indicating necking starting point according to Hart's criterion (12.29), **c** 75 °C, 180 MPa. Redrawn from [23] with permission of Springer

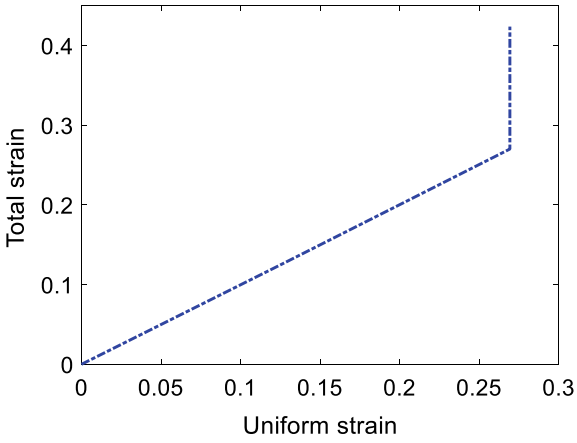

Fig. 12.6 Total strain versus uniform strain for the FEM model in Fig. 12.7. Redrawn from [23] with permission of Springer

12.5.4 Multiaxial Stress States

The formation of a waist clearly takes place under multiaxial stress states. For this reason finite element analysis (FEM) has been performed [23]. Unfortunately, special FEM software is required that can handle creep deformation with large strains. It should also allow for a plastic instability to occur, which makes the analysis sensitive. At this stage it is difficult to consider it for routine applications.

The dislocation model in Eqs. (12.15), (12.16), (12.22), etc. is implemented in the FEM program. The parameters used are the same as in the uniaxial case in 12.5.3. A creep test of Cu-OFP at 75 °C and 175 MPa was simulated, i.e. the same case as the one shown in Fig. 12.5a. The necking appeared at a uniform strain of 0.27. Then all the subsequent strain took place in the waist. This is illustrated in Fig. 12.6.

The strain in the neck is as high as 2. This is not shown in Fig. 12.6 but this is clearly evident in Fig. 12.7, where the final strain distribution and profile of the specimen is shown.

That the high strain value is in accordance with the experiment that is illustrated in Fig. 12.8, where the observed and modeled specimen profiles are shown. The experimental values are reproduced within about 10%.

According to the FEM modeling, the necking develops quite slowly and only appears close to rupture. This has also been observed for the martensitic 9Cr1Mo steel P91 [27]. Once the necking has started to form, the strain in the neck increases rapidly. The results of the uniaxial and the multiaxial computations are obviously fairly consistent. Also the uniaxial modeling of necking gives a significant necking strain only close to rupture.

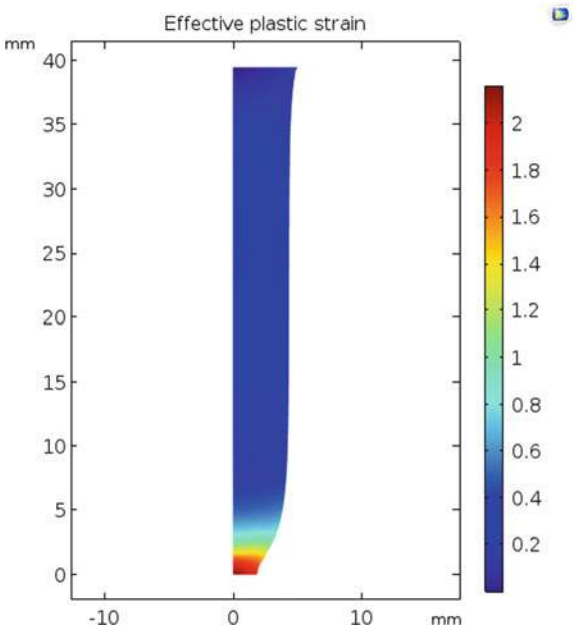

Fig. 12.7 FEM results of profile strain distribution along a creep specimen of Cu-OFP at 75 °C with an applied stress of 175 MPa. Redrawn from [23] with permission of Springer

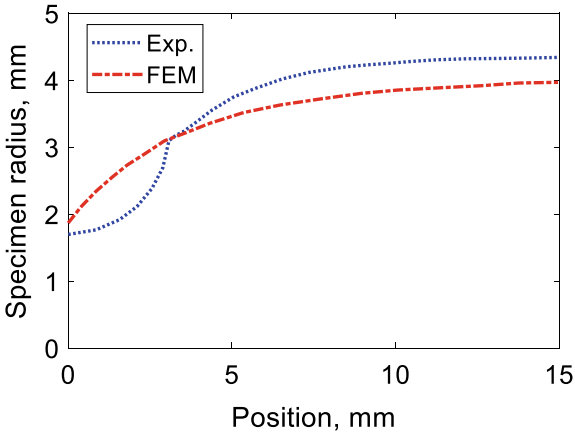

Fig. 12.8 Specimen radius versus axial coordinate at the necking position. Comparison of experimental necking profile with FEM results for Cu-OFP at 75 °C with an applied stress of 175 MPa. Redrawn from [23] with permission of Springer

12.6 Summary

Many mechanisms that contribute to tertiary creep are well known such as particle coarsening, substructure coarsening, cavitation, changes in the dislocation density and necking. In the literature these mechanisms have mainly been modeled with empirical approaches not least in the context of continuum damage mechanics.

However, due to the complexity of the phenomena empirical methods give unsafe predictions.

- A basic dislocation model for the whole creep curve is described. The model extends results from previous chapters to tertiary creep. The model is formulated in such a way that if the stress dependence of the secondary creep rate is known, tertiary as well as primary creep rate can be computed. This is done by introducing an effective creep stress that takes the changes in the dislocation density into account.
- In the secondary stage there is a balance between the applied stress and the stress from the dislocations plus contributions from other strengthening mechanisms. In the tertiary stage the dislocation strength continues to increase but the true stress increases faster. This means that the effective stress is raised and thereby the creep rate. This simple concept is proposed to be the main mechanism behind tertiary creep.
- For copper it is essential to take the substructure into account when modeling tertiary creep. A distinction is made between balanced and unbalanced dislocations in the cell walls. The main difference between balanced and unbalanced dislocations is that the former type is exposed to static recovery but not the latter. The unbalanced dislocations provide a counteracting stress against the rapidly increasing true stress at lower temperatures, which makes it possible to explain the observed creep rates.
- In steels there is often a very rapid increase in the creep rate in the tertiary stage that can be represented by a linear increase in the logarithm of the creep rate with strain (Omega model). To explain this behavior, the degradation mechanisms in the microstructure must be strain dependent. This applies in particular to particle and substructure coarsening. Quantitative models have been proposed for these mechanisms but the models have not yet been verified experimentally.
- With models presented in Chap. 10, the influence of cavitation on tertiary creep can directly be derived. However, pronounced cavitation typically occurs quite locally. This means that the overall effect on tertiary creep is limited.
- Necking is assumed to be initiated when Hart's stability criterion fails which takes place at the very beginning of tertiary creep. Although necking is initiated early in the creep process, both uniaxial and multiaxial models suggest that significant necking takes place only close to rupture but then necking is progressing very rapidly. These results are fully consistent with available experimental data.

References

1. B.J. Cane, K.R. Williams, K.J. Miller, R.F. Smith, Creep damage accumulation and life assessment of a ½Cr½Mo¼V steel, in *Mechanical Behaviour of Materials* (Pergamon, 1980), pp. 255–264
2. M.F. Ashby, B.F. Dyson, S.R. Valluri, D.M.R. Taplin, P.R. Rao, J.F. Knott, R. Dubey, Creep damage mechanics and micromechanisms, in *Fracture*, vol. 84 (Pergamon, 1984), pp. 3–30
3. J. Vanaja, K. Laha, R. Mythili, K.S. Chandravathi, S. Saroja, M.D. Mathew, Creep deformation and rupture behaviour of 9Cr–1W–0.2V–0.06Ta reduced activation ferritic-martensitic steel. Mater. Sci. Eng. A **533**, 17–25 (2012)
4. A. Aghajani, C. Somsen, G. Eggeler, On the effect of long-term creep on the microstructure of a 12% chromium tempered martensite ferritic steel. Acta Mater. **57**, 5093–5106 (2009)
5. F. Abe, Bainitic and martensitic creep-resistant steels. Curr. Opin. Solid St. M **8**, 305–311 (2004)
6. J. Agren, M.T. Clavaguera-Mora, J. Golcheski, G. Inden, H. Kumar, C. Sigli, Application of computational thermodynamics to phase transformation nucleation and coarsening. Calphad: Comput. Coupling Phase Diagrams Thermochem. **24**, 41–54 (2000)
7. R. Sandstrom, Subgrain growth occurring by boundary migration. Acta Metall. Mater. **25**, 905–911 (1977)
8. R. Sandström, J. He, Survey of creep cavitation in fcc metals, in *Study of Grain Boundary Character* (inTech, 2017), pp. 19–42
9. J. He, R. Sandström, Formation of creep cavities in austenitic stainless steels. J. Mater. Sci. **51**, 6674–6685 (2016)
10. J. He, R. Sandström, Creep cavity growth models for austenitic stainless steels. Mater. Sci. Eng. A **674**, 328–334 (2016)
11. R. Sandström, Formation of a dislocation back stress during creep of copper at low temperatures. Mater. Sci. Eng. A **700**, 622–630 (2017)
12. R. Sandström, The role of cell structure during creep of cold worked copper. Mater. Sci. Eng. A **674**, 318–327 (2016)
13. Q. Meng, Z. Wang, Creep damage models and their applications for crack growth analysis in pipes: a review. Eng. Fract. Mech. **205**, 547–576 (2019)
14. J. Lemaître, R. Desmorat, *Engineering Damage Mechanics: ductile, Creep, Fatigue and Brittle Failures* (Springer, Berlin, 2010)
15. R. Sandstrom, Basic model for primary and secondary creep in copper. Acta Mater. **60**, 314–322 (2012)
16. B.K. Choudhary, Microstructural degradation and development of damage during creep in 9% chromium ferritic steels. Trans. Indian Inst. Metal **69**, 189–195 (2016)
17. A. Vinogradov, I.S. Yasnikov, H. Matsuyama, M. Uchida, Y. Kaneko, Y. Estrin, Controlling strength and ductility: dislocation-based model of necking instability and its verification for ultrafine grain 316L steel. Acta Mater. **106**, 295–303 (2016)
18. S.D. Antolovich, R.W. Armstrong, Plastic strain localization in metals: origins and consequences. Prog. Mater. Sci. **59**, 1–160 (2014)
19. J.W. Hutchinson, K.W. Neale, Influence of strain-rate sensitivity on necking under uniaxial tension. Acta Metall. **25**, 839–846 (1977)
20. U.F. Kocks, J.J. Jonas, H. Mecking, The development of strain-rate gradients. Acta Metall. **27**, 419–432 (1979)
21. A.J. Levy, The tertiary creep and necking of creep damaging solids. Acta Metall. **34**, 1991–1997 (1986)
22. I.H. Lin, J.P. Hirth, E.W. Hart, Plastic instability in uniaxial tension tests. Acta Metall. **29**, 819–827 (1981)
23. F. Sui, R. Sandström, Basic modelling of tertiary creep of copper. J. Mater. Sci. **53**, 6850–6863 (2018)
24. H. Magnusson, R. Sandstrom, Creep strain modeling of 9–12 pct Cr steels based on microstructure evolution. Metall. Mater. Trans. A **38A**, 2033–2039 (2007)

25. S. Majumdar, Relationship of creep, creep-fatigue, and cavitation damage in type 304 austenitio stainless steel. J. Eng. Mater. Technol. Trans. ASME **111**, 123–131 (1989)
26. H. Magnusson, R. Sandstrom, The role of dislocation climb across particles at creep conditions in 9–12 pct Cr steels. Metall. Mater. Trans. A **38A**, 2428–2434 (2007)
27. R. Lim, M. Sauzay, F. Dalle, I. Tournie, P. Bonnaillie, A.F. Gourgues-Lorenzon, Modelling and experimental study of the tertiary creep stage of Grade 91 steel. Int. J. Fract. **169**, 213–228 (2011)
28. R. Sandstrom, A. Kondyr, Creep deformation, accumulation of creep rupture damage and forecasting of residual life for three Mo- and CrMo-steels. VGB Kraftwerkstechnik **62**, 802–813 (1982)
29. R. Sandstrom, A. Kondyr, Model for tertiary-creep in Mo and CrMo-steels, in *Mechanical Behaviour of Materials* (Pergamon press, Oxford, 1979), pp. 275–284
30. S. Holdsworth, The European creep collaborative committee (ECCC) approach to creep data assessment. J. Press. Vessel Technol. Trans. ASME **130**, 0240011–0240016 (2008)
31. S.R. Holdsworth, Constitutive equations for creep curves and predicting service life, in *Creep-Resistant Steels* (2008), pp. 403–420
32. D. Krajcinovic, Damage mechanics. Mech. Mater. **8**, 117–197 (1989)
33. T.H. Hyde, W. Sun, J.A. Williams, Creep analysis of pressurized circumferential pipe weldments—A review. J. Strain Anal. Eng. Des. **38**, 1–30 (2003)
34. H.-T. Yao, F.-Z. Xuan, Z. Wang, S.-T. Tu, A review of creep analysis and design under multi-axial stress states. Nucl. Eng. Des. **237**, 1969–1986 (2007)
35. A.M. Othman, D.R. Hayhurst, B.F. Dyson, Skeletal point stresses in circumferentially notched tension bars undergoing tertiary creep modelled with physically based constitutive equations. Proc. R. Soc. Lond. **441**, 343–358 (1993)
36. I.J. Perrin, D.R. Hayhurst, Creep constitutive equations for a 0.5Cr–0.5Mo–0.25V ferritic steel in the temperature range 600–675 °C. J. Strain Anal. Eng. Des. **31**, 299–314 (1996)
37. L.M. Brown, R.K. Ham, Strengthening methods in crystals, in *Applied Science Publisher Ltd.*, p. 9 (1971)
38. R. Wu, N. Pettersson, A. Martinsson, R. Sandstrom, Cell structure in cold worked and creep deformed phosphorus alloyed copper. Mater. Charact. **90**, 21–30 (2014)
39. H. Mughrabi, T. Ungár, W. Kienle, M. Wilkens, Long-range internal stresses and asymmetric X-ray line-broadening in tensile-deformed [001]-orientated copper single crystals. Philos. Mag. A: Phys. Condens. Matter Struct. Defects Mech. Prop. **53**, 793–813 (1986)
40. S. Straub, W. Blum, H.J. Maier, T. Ungar, A. Borbély, H. Renner, Long-range internal stresses in cell and subgrain structures of copper during deformation at constant stress. Acta Mater. **44**, 4337–4350 (1996)
41. D.A. Hughes, N. Hansen, D.J. Bammann, Geometrically necessary boundaries, incidental dislocation boundaries and geometrically necessary dislocations. Scripta Mater. **48**, 147–153 (2003)
42. A. Argon, *Strengthening Mechanisms in Crystal Plasticity* (Oxford University Press, Oxford, 2008)
43. U.F. Kocks, H. Mecking, Physics and phenomenology of strain hardening: the FCC case. Prog. Mater. Sci. **48**, 171–273 (2003)
44. W.D. Nix, J.C. Gibeling, D.A. Hughes, Time-dependent deformation of metals. Metall. Trans. A **16**, 2215–2226 (1985)
45. E. Nes, Modelling of work hardening and stress saturation in FCC metals. Prog. Mater Sci. **41**, 129–193 (1997)
46. R. Wu, R. Sandstrom, F. Seitisleam, Influence of extra coarse grains on the creep properties of 9% CrMoV (P91) steel weldment. J. Eng. Mater.-T ASME **126**, 87–94 (2004)
47. E.W. Hart, Theory of the tensile test. Acta Metall. **15**, 351–355 (1967)
48. M.A. Burke, W.D. Nix, Plastic instabilities in tension creep. Acta Metall. **23**, 793–798 (1975)
49. R. Sandström, J.-J. He, Prediction of creep ductility for austenitic stainless steels and copper. Mater. High Temp. **39**, 427–435 (2022)

Chapter 13
Creep Ductility

Abstract For a number of creep resistant steels, the creep ductiliy decreases with increasing temperature and time. As a function of stress, the ductiity is often describe with an S-shaped curve with an upper and a lower shelf level. As a function of time, the S-shape is inverted. If the ductility is high, the rupture is referred to as ductile, and for low ductility levels as brittle. Ductile rupture is believed to be due to a plastic instability such as necking. Brittle rupture on the other hand is controlled by the nucleation, growth and linkage of creep cavities. With the help of the basic models for creep deformation and cavitation, the rupture stress and ductility can be predicted. Several models exist for the influence of multiaxiality on the creep ductility. Although the models are based on different principles, they predict approximately the same behavior, which is verified by comparison to rupture data for notched bars.

13.1 Introduction

In creep tests, the ductility is commonly measured in two ways: as creep elongation and reduction of area, both at rupture. The creep ductility influences several properties. With a low ductility cracks are more easily formed and the risk for failure is higher than when the ductility is high. This is not least the case for cyclic loading. The reason is that creep cavities are more readily formed when the ductility is low. Cavities grow and link which results in initiation sites for cracks. For materials with low ductility, the risk is obviously higher that the strain allowance is exceeded in notches and at inhomogenieties like in welds. Materials with high creep ductility are considered to be more forgiving.

As a consequence it is desirable to select a material with high creep ductility. Unfortunately that is not easy. Most creep resistant alloys loose ductility with increasing rupture time. In addition, there can be a large cast to cast difference in the ductility. It was demonstrated early on that the 17Cr–12Ni–2Mo steel 316 showed such a variation [1]. The rupture elongation was observed to vary between 2 and 120%. Also for the martensitic 9Cr1Mo steel P91, low ductility is often found. In a larger investigation it was recorded that about 10% of the casts had a reduction

R. Sandström, *Basic Modeling and Theory of Creep of Metallic Materials*, Springer Series in Materials Science 339,
https://doi.org/10.1007/978-3-031-49507-6_13

of area below 20% [2]. It can be concluded that also for materials that have a long successful operation record, the ductility can frequently be low.

There are many mechanisms that are known to influence the ductility. A coarse grain size often reduces the ductility. This is natural since the amount of grain boundary sliding and thereby the cavitation increases with the grain size. This is evident from Eq. (9.12). Particles that are present in the grain boundaries act as nucleation sites for cavitation. With increasing number of particles, more cavities are formed, see Eq. (10.8). It is known that the presence of coarse particles in the grain boundaries increases the risk for crack initiation. Impurity elements P and S can lower the ductility in steels. It is suspected that the presence of impurity elements is the cause of low creep ductility in many casts but the number of systematic studies is limited [2]. It is a common experience for steels that if the creep strength is raised, the ductility is often reduced. Some of the mentioned effects can be modeled but not all of them. In particular, the observed cast to cast variation is difficult to explain. One reason is that some mechanisms can be both positive and negative. One example is particles in grain boundaries. As mentioned they can act as nucleation sites for cavitation but they can probably also limit the amount of grain boundary sliding and thereby resist cavitation, but that does not seem to have been verified. The limitation concerning the understanding of the controlling mechanisms must be considered when modeling creep ductility. In most cases only a general description of influencing factors can be obtained, not a detailed computation.

To illustrate the influence of parameters on the creep ductility, schematic diagrams are often used. Such diagrams are shown in Fig. 13.1.

At high stresses and short rupture times the ductility is high and approximately constant. This is referred to as the upper shelf or regime I. When the stress is reduced, the ductility drops to much lower values over a fairly narrow range of stresses and rupture times. This is regime II. At low stresses or long rupture times the ductility takes very low values. In this range the ductility is again approximately constant. It

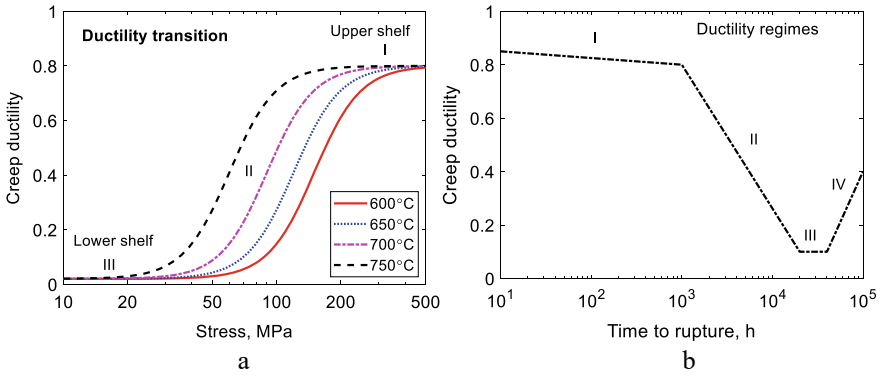

Fig. 13.1 Schematic diagram of the creep ductility; **a** as a function of stress at a few temperatures typical for austenitic stainless steels; **b** as a function of time to rupture for 9–12%Cr steels

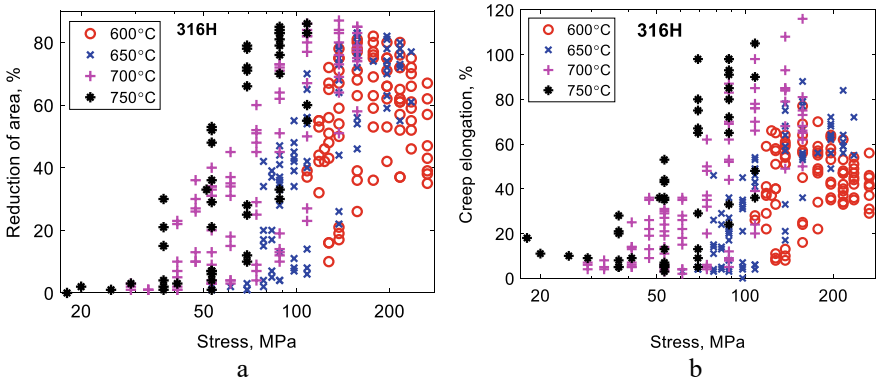

Fig. 13.2 Creep ductility as a function of stress for the 17Cr12Ni2Mo austenitic stainless steel 316H at 600–750 °C. Data from NIMS [5]; **a** reduction of area; **b** elongation at rupture

is called the lower shelf or regime III. In some materials for example 9%Cr steel [3] and CrMoV steels [4], the ductility can increase again at very long rupture times. The curves in Fig. 13.1 move to the left with increasing temperature.

To illustrate how the schematic curves in Fig. 13.1a, look for observed values, results for 17Cr12Ni2Mo (316H) are given in Fig. 13.2 for the reduction of area and for the elongation at rupture.

Although the tests have been performed under well controlled conditions there is a large scatter in the data. In fact, the scatter in creep ductility values is typically much larger than for creep strength values. A difference in comparison with Fig. 13.1 is that the upper shelf ductility in Fig. 13.2 varies somewhat with temperature in particular for the creep elongation. It should be noticed that the ductility can take very low values.

It is also instructive to plot the creep ductility as a function of rupture time. This is shown in Fig. 13.3.

Both the reduction in area and the creep elongation decrease with increasing rupture time and increasing temperature. For reduction of area an upper shelf is apparent at shorter rupture times. This is only evident for the elongation at lower temperatures. Except at the lowest temperature, the ductility values at long times can be quite low. This demonstrates that a low ductility shelf is present. The ductility versus rupture time can also be represented with an S-shape curve as in Fig. 13.1 but with inverted S curves. Nice S-shaped curves can be found in the literature with much less scatter than in Figs. 13.2 and 13.3 [6].

Many attempts have been made in the past decades to model creep ductility. With few exceptions, empirical approaches have been used. One important method to assess the remaining life of plants operating at high temperature, where creep has been the life controlling mechanism, has involved ductility exhaustion. With the help of continuum damage mechanics (CDM) [7–9], the creep strain in critical components is computed to ensure that it does not exceed the ductility values. In

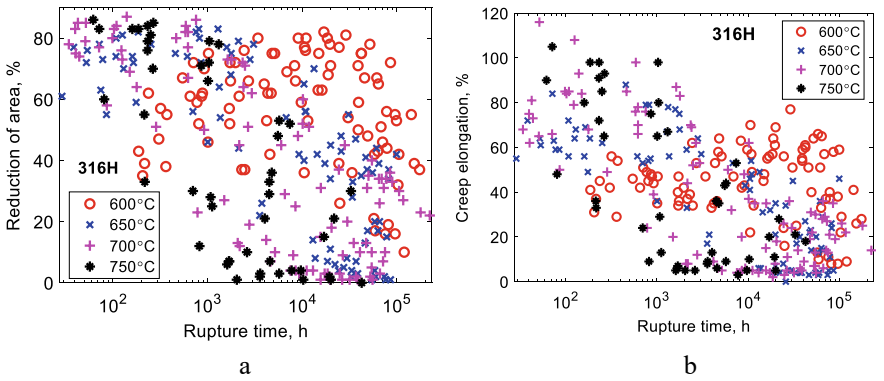

Fig. 13.3 Creep ductility as a function of rupture time for the 17Cr12Ni2Mo austenitic stainless steel 316H at 600–750 °C. Data from NIMS [5]; **a** reduction of area; **b** elongation at rupture

this process some observed microstructural changes have been recorded and then been the basis in the modeling. In the literature there are a large number of papers discussing this type of analysis. The mentioned volumes on CDM can serve as a starting point in this respect.

In the present chapter empirical models for the creep ductility will be discussed in Sect. 13.2. These models are mainly statistical. In statistical methods mathematical expressions are chosen and fitted to the experimental data. The choice of expression is merely for numerical convenience to get a good fit to the data. The approaches involve a number of adjustable parameters that are fitted to the data. The reason for developing these models has in general been to use them in design or in residual life assessment. To meet this aim, it must be possible to generalize the data for example to longer times. This requires that the models are trained against a large set of data. In particular, the number of independent experimental data points must be very much larger than the number of adjustable parameters involved.

To avoid these limitations basic models based on physical principles and without the use of adjustable parameters have been developed. Such models will be presented in Sect. 13.3.

Failures that are associated with low and high creep ductility are referred to as brittle and ductile rupture, respectively. As was illustrated in Figs. 13.1, 13.2 and 13.3, brittle rupture occurs primarily at low stress, long rupture times and high temperatures, whereas the conditions for ductile rupture are opposite, i.e. it takes place at high stresses, low temperatures and short rupture times. Brittle rupture is assumed to be initiated by the nucleation, growth and linkage of creep cavities. Cavitation models for the creep ductility will be presented in Sect. 13.3.1. Such models have turned out to give successful results in a number of cases. Much less work has been carried out for ductile rupture. For a number of steels and copper it has been demonstrated that necking controls the failure during ductile rupture. This approach will be discussed in Sect. 13.3.2. To study the necking, creep strain

data must be available. However, also a ductility corresponding to the upper shelf in Fig. 13.1 can be used to predict ductile rupture.

13.2 Empirical Ductility Models

Creep strength data have been analyzed with statistical methods for a long time. The European Collaborative Creep Committee (ECCC) has developed suitable procedures that ensure that the statistical analysis is performed in a good way and that the results behave in a physically correct way. There is a large number of methods available analyzing and extrapolating creep strength data and practically all are empirical. In spite of this, the methods can provide quite valuable information due to the large number of data points.

ECCC have also proposed procedures for assessment of creep ductility values [10]. A number of different expressions for the ductility are suggested [11]. Various combinations of constants, stress and temperature dependencies are used such as

$$\log(\varepsilon_R) = \log(\beta_0) + \beta_1 \log(T) + \beta_2 \log(\sigma) + \beta_3/T + \beta_4\sigma/T \tag{13.1}$$

where ε_R is the rupture ductility, T the absolute temperature, σ the stress and β_0–β_4 constants. Analyses with such expressions have for example been performed by Spindler for austenitic stainless steels [12], by Payten et al. for 9Cr1Mo steels [13], and by Holdsworth and co-workers for 1CrMoV rotor steel [4, 14]. Many alternative expressions have also been considered; see for example [15, 16].

Other types of analyses have also been performed. Lai collected a large database for the austenitic stainless steel 316H. He made a regression analysis to determine the influence of the composition and some microstructure parameters on the ductility [1, 17]. Wilshire used creep data from NIMS to generate master curves for high Cr-steels. The principle was to use an activation energy to make ductility values at different temperatures merge to a single curve [18]. Xu and Hayhurst used continuum damage mechanics (CDM) to assess the creep ductility of 316H [19]. Low alloy rotor steels were studied by Singh and Kamaraj, again with a CDM approach [20].

The complexity and variability of creep ductility data were illustrated in Figs. 13.2 and 13.3. The cast to cast differences have rarely been possible to model. One notable exception is the paper by Binda and Holdsworth [14], where the influence of composition on 1CrMoV steel was analyzed. However, in most cases it is beneficial to concentrate the modeling to the most essential features. From a technical point, the start and level of the lower shelf are the most important aspects in general. For this purpose, the variation of the ductility can be described by a step function. A suitable step function is the sigmoid function that has a characteristic S-shape.

$$f_{\text{sigm}}(x) = 1/(1 + \exp(-x)) \tag{13.2}$$

With the help of the sigmoid function, curves of the form in Fig. 13.1 can be generated

$$\varepsilon_{f\sigma} = L_{\text{shelf}} + (U_{\text{shelf}} - L_{\text{shelf}})\, f_{\text{sigm}}((\log \sigma e^{Q/R_G T} - \log \sigma_0)/\log \sigma_{\text{rng}}) \tag{13.3}$$

$$\varepsilon_{ft_R} = L_{\text{shelf}} + (U_{\text{shelf}} - L_{\text{shelf}})\, f_{\text{sigm}}\left(-\left(\log t_R e^{Q/R_G T} - \log t_{R0}\right)/\log t_{R\text{rng}}\right) \tag{13.4}$$

where σ and t_R are the creep stress and rupture time and $\varepsilon_{f\sigma}$ and ε_{fR} rupture ductilities. L_{shelf} and U_{shelf} are the lower and upper shelf energies. The parameters with index 0 and rng indicate the central position of the curve and the size of the transition range, respectively. An activation Q is introduced to represent curves at different temperatures. With the help of Eqs. (13.3) and (13.4), it should be straightforward to generate curves describing the influence of parameters on the ductility. Ductility curves as a function of stress and rupture time have been presented above. In the literature, other parameters are also considered. Use of the strain rate or normalized stress are often applied, see for example [6, 11].

13.3 Basic Ductility Methods

13.3.1 Brittle Rupture

The main mechanism for brittle rupture is the nucleation and growth of cavities. When a critical cavitated area fraction in the grain boundaries is reached failure occurs. A combination of nucleation and growth of cavities must take place. A model for nucleation of cavitation based on grain boundary sliding was presented in Eq. (10.8)

$$\frac{dn_{\text{cav}}}{dt} = \frac{0.9C_s}{d_{\text{sub}}}\left(\frac{g_{\text{sub}}}{d_{\text{sub}}^2} + \frac{g_{\text{part}}}{\lambda^2}\right)\dot{\varepsilon} = B_s\dot{\varepsilon} \tag{13.5}$$

where n_{cav} is the number of cavities, d_{sub} the subgrain size, $\dot{\varepsilon}$ the creep strain rate, λ the interparticle spacing in the grain boundary and C_s a constant. The factors g_{sub} and g_{part} are the fraction of active nucleation sites at sub-boundary junctions and particles.

Diffusion controlled growth of cavities is described by Eqs. (10.15) and (10.18)

$$\frac{dR_{\text{cav}}}{dt} = 2D_0K_f(\sigma_{\text{red}} - \sigma_0)\frac{1}{R_{\text{cav}}^2} \tag{13.6}$$

$$2\pi D_0K_f(\sigma_{\text{red}} - \sigma_0)n_{\text{cav}}R_{\text{cav}} + \dot{\varepsilon}(\sigma_{\text{red}}) = \dot{\varepsilon}(\sigma) \tag{13.7}$$

where R_{cav} the cavity radius in the grain boundary plane, σ_0 the sintering stress. The grain boundary diffusion parameter D_0 is equal to $\delta D_{GB}\Omega/k_B T$ where δ is the grain boundary width, D_{GB} the grain boundary self-diffusion coefficient, and Ω the atomic volume. k_B is the Boltzmann's constant and T the absolute temperature. The factor K_f is given in Eq. (10.12).

Equations (13.6) and (13.7) model constrained cavity growth. Constrained growth is essential to take into account to avoid overestimating the growth rate. σ_{red} is a reduced stress that is lower than the applied stress σ. $\dot{\varepsilon}(\sigma_{red})$ and $\dot{\varepsilon}(\sigma)$ are the creep rates at the reduced and applied stress, respectively. σ_{red} is found by solving Eq. (13.7).

Grain boundary decohesion is the main mechanism for brittle rupture. Due to both cavity nucleation and growth, there is a gradual increase of the cavitated grain boundary area fraction during creep. When this fraction reaches a critical value, failure takes place. It is fairly well established that this critical area fraction is about 0.25 [21]. The cavitated grain boundary area fraction A_{cav} can be calculated from [22]

$$A_{cav} = \int_0^t \frac{dn_{cav}}{dt_1}(t_1)\pi R_{cav}^2(t, t_1)dt_1 \tag{13.8}$$

The nucleation rate and the cavity radius in Eq. (13.8) are given by Eqs. (13.5) and (13.6). The resulting time dependence of these quantities is illustrated in Fig. 13.4. In this Figure the number of cavities, the average cavity radius, the cavitated area fraction, and the creep strain are given as a function of time in a common diagram. Ductile rupture occurs when the creep strain reaches a fixed elongation value of 0.2. Brittle rupture takes place when the cavitated area fraction gets a value of 0.25. These levels are marked in the diagram. The condition that is first satisfied controls the type of failure. Thus, if the creep strain reaches 0.2 before the cavitated area fraction is 0.25, the rupture is ductile but if cavitated area fraction takes its critical value first, the rupture is brittle.

Two cases for the austenitic stainless steel 316H are considered in Fig. 13.4a at a relatively high stress and low temperature and in Fig. 13.4b at a low stress and high temperature. The number of cavities increases at the same rate as the creep strain. This is a direct consequence of Eq. (13.5). Since a constant creep rate is assumed, both the creep strain and the number of nucleated cavities are linear in time. For unconstrained growth the cavity volume is linear in time, cf. Eq. (10.11). This means that the cavity radius is proportional to $t^{1/3}$ where t is the time. For constrained growth, the growth rate is lower. Since the cavitated area fraction in the grain boundaries increases both with the number of cavities and the cavity radius, it shows a faster increase than the two contributing processes. In Fig. 13.4a, the strain criterion is met first. Consequently the rupture is ductile. On the other hand in Fig. 13.4b, the criterion for the cavitated area fraction is satisfied first. The rupture is brittle.

An early example of the application of Eqs. (13.5), (13.6) and (13.8) was for pure oxygen free copper with 50 ppm P (Cu-OFP) and without P. The difference in

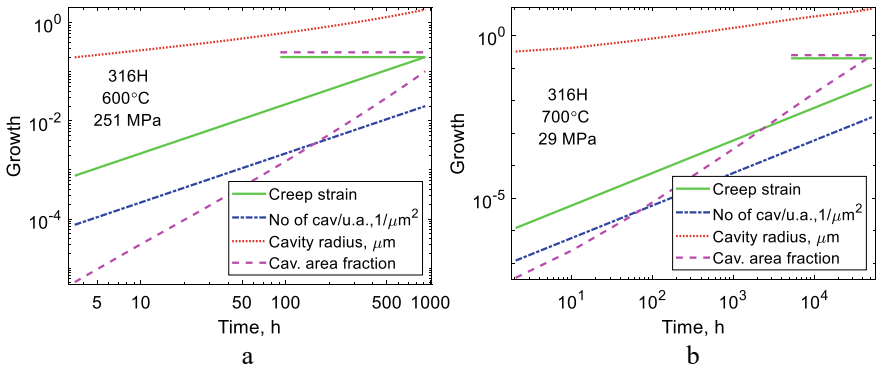

Fig. 13.4 Modeled time dependence of cavity evolution for the austenitic stainless steel 17Cr12Ni2Mo (316H). The number of nuclei, the cavity radius, the area fraction of cavities in the GBs, and the creep strain are shown as a function of time on a common scale; **a** 600 °C, 251 MPa (ductile rupture); **b** 700 °C, 29 MPa (brittle rupture)

cavitation between these two types of alloys has been possible to model in detail, see Sect. 10.4. The predicted rupture elongation as a function of temperature is shown in Fig. 13.5.

The influence of P in Fig. 13.5 is striking. With 50 ppm P the rupture is ductile and this is modeled with ductility exhaustion. In contrast, Cu without P can have very low creep ductility values (brittle rupture) that can be fully described by the model.

With the help of Eqs. (13.5), (13.6) and (13.8), predicted creep ductility values for brittle rupture are given as a function of rupture time for two austenitic stainless steel 321H and 316H in Fig. 13.6.

The computed ductility values decrease with increasing temperature and rupture time. This is regime II in Fig. 13.1. The upper shelf regime I appears at higher ductility

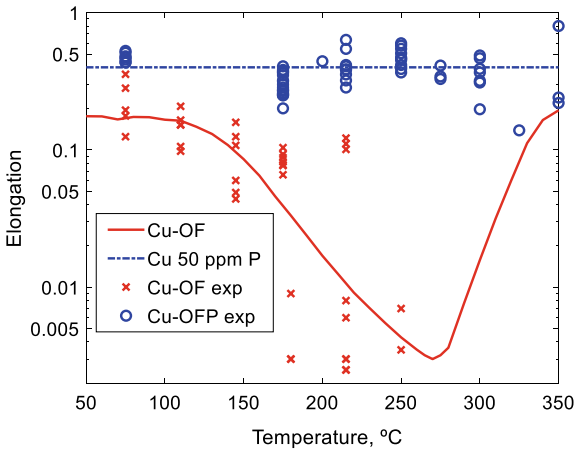

Fig. 13.5 Comparison of modeled and experimental rupture elongation for oxygen free copper with and without 50 ppm P. Cu-OF is exposed to brittle rupture (Cu-OF) whereas the rupture is ductile for Cu-OFP. The rupture time is of the order of 10000 h for the tests. Redrawn from [22] with permission of Elsevier

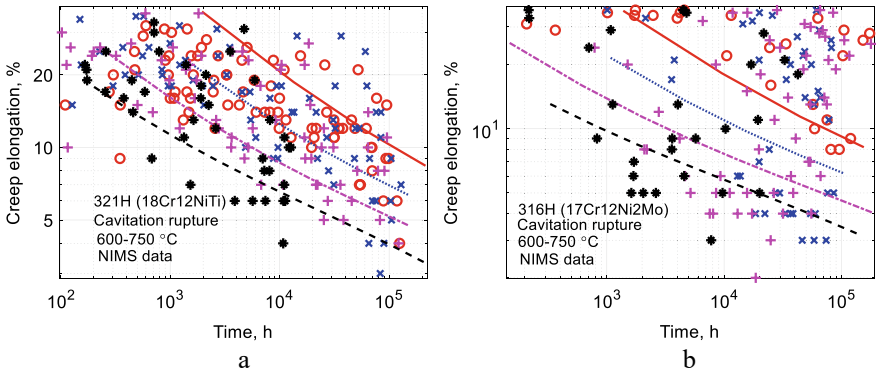

Fig. 13.6 Comparison of modeled and experimental creep elongation values for brittle rupture for two austenitic stainless steels at four temperatures 600, 650, 700, 750 °C (from top to bottom). The predicted and observed values at a given temperature are shown in the same colour; **a** 18Cr12NiTi (321H); **b** 17Cr12Ni2Mo (316H). Creep data from NIMS [5, 23]. Redrawn from [24] with permission of Taylor & Francis

values, see Fig. 13.3. In Fig. 13.6 there is no direct evidence of a lower shelf regime III. The modeling can only describe the general behaviour of the ductility, not the cast to cast variation as explained in Sect. 13.1.

13.3.2 Ductile Rupture

Ductile creep rupture of tensile creep specimen is believed to be initiated by necking, i.e. the plastic instability that forms a waist around the specimen. That was demonstrated for creep of copper in Sect. 12.4.1. In addition, when tertiary creep can be described with the Omega model, the necking takes place very close to the rupture and can be assumed to start the rupture, Sect. 12.5.2. For a number of steels that follow the Omega model including many low alloy steels, 9 and 12%Cr steels and austenitic stainless steels, ductile rupture can be considered to be controlled by necking. Since necking and the associated ductility values are fully described in Sect. 12.5, the results will not be repeated here.

13.4 The Role of Multiaxiality

In the literature there has been considerable interest in the effect of multiaxiality on the creep ductility. One of the main reasons is that creep ductility exhaustion is an important method for residual life assessment of components operating at high temperatures. For surveys on the role of multiaxiality, see [6, 11].

13.4.1 Diffusion Controlled Growth

Giessen and Tvergaard has proposed that Eq. (10.8) for cavity nucleation should be modified by including the ratio between the stress normal to the grain boundary σ_n and the effective stress σ_e to take into account the effect of the stress state [25]

$$\frac{dn_{cav}}{dt} = \frac{0.9C_s}{d_{sub}}\left(\frac{g_{sub}}{d_{sub}^2} + \frac{g_{part}}{\lambda^2}\right)\left(\frac{\sigma_n}{\sigma_e}\right)^2 \dot{\varepsilon} = B_s\left(\frac{\sigma_n}{\sigma_e}\right)^2 \dot{\varepsilon} \tag{13.9}$$

Gonzales and Cocks have taken the average of this expression over all contributing grain boundaries and found the following result for the multiaxiality factor [26]

$$\frac{dn_{cav}}{dt} = Bf_{MA}\dot{\varepsilon} \text{ where } \quad f_{MA} = \frac{4}{9} + 5\left(\frac{\sigma_h}{\sigma_e}\right)^2 \tag{13.10}$$

σ_h is the hydrostatic stress and σ_e the effective stress.

$$\sigma_h = (\sigma_1 + \sigma_2 + \sigma_3)/3; \quad \sigma_e = \sqrt{((\sigma_1 - \sigma_2)^2 + (\sigma_2 - \sigma_3)^2 + (\sigma_3 - \sigma_1)^2)/2} \tag{13.11}$$

σ_1, σ_2 and σ_3 are the principal stresses.

The derivation of the expression for diffusion controlled growth Eq. (10.11) has the form that it is natural to assume the following effect of the stress state [27]

$$\frac{dR_{cav}}{dt} = 2D_0K_f\sigma_e\frac{1}{R_{cav}^2}\frac{\sigma_n}{\sigma_e} \tag{13.12}$$

where σ_n and σ_e have the same interpretation as in Eq. (13.9). For simplicity the role of the sintering stress is neglected since it is small anyway. Thus, the influence of the stress state has a similar form as for the nucleation rate in Eq. (13.9). If the averaging over grain boundary orientation is made in the same way as in Eq. (13.10), the following result is obtained

$$\frac{dR_{cav}}{dt} = 2D_0K_f\sigma_e\frac{1}{R_{cav}^2}f_{MA}^{1/2} \tag{13.13}$$

If a constant stress is assumed, Eqs. (13.10) and (13.12) can be integrated directly

$$n_{cav} = B_sf_{MA}\dot{\varepsilon}t; \quad R_{cav} = (R_{cav0}^3 + 6D_0K_f\sigma_ef_{MA}^{1/2}(t - t_0))^{1/3} \tag{13.14}$$

where t is the time. These expressions can be inserted in Eq. (13.8) for the cavitated area fraction

$$A_{\text{cav}} = \pi B_{\text{s}} f_{\text{MA}}^{4/3} \dot{\varepsilon} (6 D_0 K_f \sigma_{\text{e}})^{2/3} \int_0^t (t - t')^{2/3} dt'; \quad \int_0^t (t - t')^{2/3} dt' = \frac{3}{5} t^{5/3} \tag{13.15}$$

In this equation the rupture time t_{R} for t is introduced. With a constant stress and only secondary creep $\varepsilon_{\text{R}} = \dot{\varepsilon} t_{\text{R}}$.

$$A_{\text{cav}} = \frac{3\pi}{5} B_{\text{s}} f_{\text{MA}}^{4/3} \dot{\varepsilon}^{-2/3} (6 D_0 K_f \sigma_{\text{e}})^{2/3} \varepsilon_R^{5/3} \tag{13.16}$$

From Eq. (13.16), the rupture ductility can be obtained if A_{cav} is taken as its critical value A_{crit}

$$\varepsilon_R = (A_{\text{crit}} \dot{\varepsilon}^{2/3} / \left(\frac{3\pi}{5} B_{\text{s}} f_{\text{MA}}^{4/3} (6 D_0 K_f \sigma_{\text{e}})^{2/3} \right)^{3/5}) \quad \text{(Diffusion control)} \tag{13.17}$$

Since the expression is based on unconstrained rather than constrained growth is cannot be used to predict the uniaxial ductility. However, the effect of the stress state is expected to be the same for unconstrained and constrained growth. The influence of multiaxiality can now be extracted

$$\varepsilon_{\text{R}} = \varepsilon_{\text{R}}^0 / f_{\text{MA}}^{4/5} \quad \text{(Diffusion control)} \tag{13.18}$$

where ε_{R}^0 is the uniaxial ductility.

13.4.2 Strain Controlled Growth

There are several expressions for strain control of cavity growth that are properly derived. The one due to Cocks and Ashby [28] was discussed in Sect. 10.5.3. Wen and Tu has improved one expression in Cocks and Ashby's derivation and proposed a new formula [29]. Another result was derived by Rice and Tracey [30]. It gives a cavity growth rate of the form

$$\frac{1}{R_{\text{cav}}} \frac{dR_{\text{cav}}}{dt} = \dot{\varepsilon} \frac{1}{2} \sinh \frac{3\sigma_{\text{h}}}{2\sigma_{\text{e}}} \tag{13.19}$$

where σ_{h} is the hydrostatic stress and σ_{e} the effective stress. This equation was derived for plastic deformation. Hellan transferred the equation to creep conditions [31]

$$\frac{1}{R_{\text{cav}}} \frac{dR_{\text{cav}}}{dt} = \alpha_{\text{H}} \dot{\varepsilon} \sinh \frac{\beta_{\text{H}} \sigma_{\text{h}}}{\sigma_{\text{e}}} \tag{13.20}$$

where

$$\alpha_H = 3\text{arcsinh}(2(n_N - 1)/n_N); \quad \beta_H = 2(n_N - 1)/n_N) \tag{13.21}$$

n_N is the creep rate stress exponent. Equation (13.20) can be combined with Eq. (13.10) for the nucleation rate to derive the cavitated area fraction. But Eq. (13.8) must first be transformed from time to strain dependence

$$A_{cav} = \int_0^{\varepsilon} \frac{dn_{cav}}{d\varepsilon_1}(\varepsilon_1)\pi R_{cav}^2(\varepsilon, \varepsilon_1)d\varepsilon_1 \tag{13.22}$$

The nucleation rate Eq. (13.10) can directly be expressed as

$$\frac{dn_{cav}}{d\varepsilon} = B_s f_{MA} \tag{13.23}$$

Equation (13.20) can also easily be transformed to strain dependence and integrated

$$\frac{1}{R_{cav}}\frac{dR_{cav}}{d\varepsilon} = \alpha_H \sinh\frac{\beta_H\sigma_h}{\sigma_e}; \; R_{cav} = R_{cav}^0 \exp(\alpha_H \sinh\frac{\beta_H\sigma_h}{\sigma_e}(\varepsilon - \varepsilon_0)) \tag{13.24}$$

where R_{cav}^0 is the initial cavity radius when a cavity starts to grow at the strain ε_0. Inserting Eqs. (13.23) and (13.24) into (13.22) gives

$$A_{cav} = B_s f_{MA}\pi(R_{cav}^0)^2 \int_0^{\varepsilon} \exp(2\alpha_H \sinh\frac{\beta_H\sigma_h}{\sigma_e}(\varepsilon - \varepsilon_1))d\varepsilon_1 \tag{13.25}$$

The integral in Eq. (13.25) is elementary

$$A_{cav} = B_s f_{MA}\pi(R_{cav}^0)^2 \frac{\exp\left(2\alpha_H \sinh\frac{\beta_H\sigma_h}{\sigma_e}\varepsilon\right)}{2\alpha_H \sinh\frac{\beta_H\sigma_h}{\sigma_e}} \tag{13.26}$$

By replacing A_{cav} by its critical value A_{crit} the rupture ductility is obtained

$$\varepsilon_R = \frac{1}{2\alpha_H \sinh\frac{\beta_H\sigma_h}{\sigma_e}} \log\left(\frac{A_{crit}2\alpha_H \sinh\frac{\beta_H\sigma_h}{\sigma_e}}{B_s f_{MA}\pi(R_{cav}^0)^2}\right) \quad \text{(Hellan)} \tag{13.27}$$

One uncertainty in Eq. (13.27) is the initial value of the cavity radius. Another limitation is the absence of significant temperature dependence. These problems seem to be common for many strain controlled growth mechanisms. The equation

is consequently difficult to use to predict the uniaxial rupture ductility. The main influence of the stress state is in the sinh function outside the logarithm.

13.4.3 Growth Due to Grain Boundary Sliding (GBS)

In Sect. 10.5.3 a model for cavity growth due to GBS was presented in Eq. (10.24)

$$R_{\text{cav}} = C_{\text{s}}\varepsilon \tag{13.28}$$

If this expression together with Eq. (13.10) for the nucleation rate are inserted in Eq. (13.22) the cavitated area fraction in the grain boundaries is found

$$A_{\text{cav}} = Bf_{\text{MA}}\pi C_{\text{s}}^2\varepsilon^2/2 \tag{13.29}$$

This gives the following rupture ductility

$$\varepsilon_{\text{R}} = (2A_{\text{crit}}/Bf_{\text{MA}}\pi C_{\text{s}}^2)^{1/2} \quad \text{(GBS growth)} \tag{13.30}$$

13.4.4 Comparison of Models

In Fig. 13.7 the multiaxial creep ductility factor for the diffusion controlled growth model, Eq. (13.18), is shown as a function the stress triaxiality ratio $\sigma_{\text{h}}/\sigma_{\text{e}}$. Also results for Hellan's model in Eq. (13.27) are illustrated. A comparison is made to experimental data for notched bars. Values for Durehete 1055 (1Cr1Mo), 2.25Cr1Mo (P22), 9Cr1Mo, 9Cr1Mo mod. (P91) and the stainless steel 316H (17Cr12Ni2Mo) are included.

A comparison is also made to the models of Cocks and Ashby [28] and of Wen and Tu [29]

$$\varepsilon_{\text{R}} = \sinh\left(\frac{2}{3}\frac{(n_{\text{N}}-0.5)}{(n_{\text{N}}+0.5)}\right)/\sinh\left(\frac{2(n_{\text{N}}-0.5)}{(n_{\text{N}}+0.5)}\frac{\sigma_{\text{h}}}{\sigma_{\text{e}}}\right) \quad \text{(Cocks and Ashby)} \tag{13.31}$$

$$\varepsilon_{\text{R}} = \exp\left(\frac{2}{3}\frac{(n_{\text{N}}-0.5)}{(n_{\text{N}}+0.5)}\right)/\exp\left(\frac{2(n_{\text{N}}-0.5)}{(n_{\text{N}}+0.5)}\frac{\sigma_{\text{h}}}{\sigma_{\text{e}}}\right) \quad \text{(Wen and Tu)} \tag{13.32}$$

The five models in Fig. 13.7a are in reasonable agreement with the observations. The GBS growth model is in the upper end of the data range. For small stress triaxiality values, the models fall in two groups. The diffusion controlled and GBS growth models are close to that of Wen and Tu [29]. They derived a model that corrected an approximation in the Cocks and Ashby model improving the model at

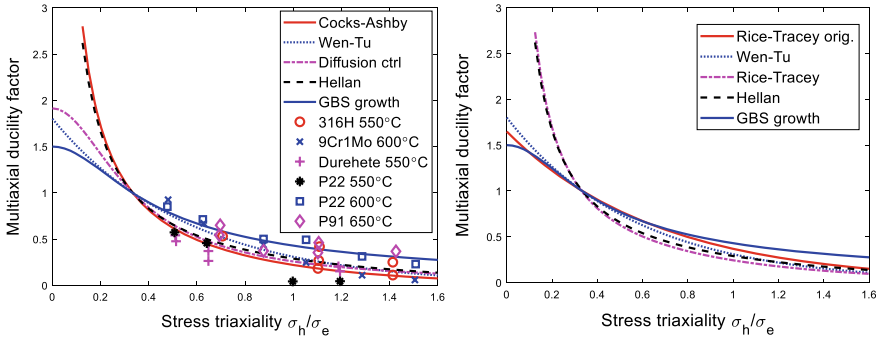

Fig. 13.7 Effect of stress triaxiality σ_h/σ_e on the multiaxial creep ductility factor $\varepsilon_R/\varepsilon_R^0$ for round notched bar specimens where ε_R^0 is the uniaxial creep ductility; **a** model values are compared to experimental data from [6]; **b** values for strain controlled growth models

low triaxiality stresses [6]. Hellan's and Cocks and Ashby's models give results that are quite similar. The parts in their expressions for the influence of the stress states are also close.

In spite of the fact that the models tend to give similar results when compared to observations, they are based on quite different principles. The diffusion control and GBS growth models are based on expressions for nucleation and growth of creep cavities that are verified experimentally. For both models the nucleation plays an important role. For the strain governed models only the derivation of Hellan's model takes nucleation into account but the nucleation has only a smaller effect on the results. The other two models for strain controlled growth, Cocks and Ashby as well as Wen and Tu do not involve nucleation. All the strain controlled models suffer from the limitation that there is no direct temperature or stress dependence in the models, which is not consistent with data for uniaxial creep ductility. The starting value of the cavity radius for growth in these models is not defined except for the GBS growth models. These facts imply that it is difficult to make direct comparisons to observed growth rates. If these limitations affect the multiaxial ductility factor is not known.

The derivation (13.27) based on Hellan's model is new. In the past, most researches have started directly from Rice and Tracey's Eq. (13.19) ignoring the transformation to creep. In the literature the multiaxial ductility in Eq. (13.33) is assumed to be derived from Rice and Tracey's equation.

$$\varepsilon_R = \varepsilon_R^0 \exp\left(\frac{1}{2} - \frac{3}{2}\frac{\sigma_h}{\sigma_e}\right) \quad \text{(Rice and Tracey orig.)} \tag{13.33}$$

Further comparisons between models are given in Fig. 13.7b. The transformation to creep in Hellan's equation seems to have only a modest effect. This can be seen by comparing the curves for Hellan's and Rice and Tracey's models. However, the

usual expression referred to as Rice and Tracey's original equation is quite different to that of Hellan.

A number of empirical models for the multiaxial ductility factor exist. Wen et al. have given of survey of them [6]. Since several models derived from basic principles are available and they give results that are often not very different from the empirical models, the incentive to use the latter type must be limited in particular since the expressions for the basic models are not very complex.

13.5 Summary

- For a number of creep resistant steels the creep ductility decreases with increasing rupture time and temperature. Sometimes an upper shelf level is observed at short rupture times and a lower shelf level at longer rupture times. For martensitic steels an increase in the ductility can be found at still longer times.
- Creep ductility is traditionally modelled with empirical mathematical expressions describing an S or an inverted S-shaped curve depending on the variables used.
- Basic expressions for cavity nucleation and diffusion controlled growth can be used to describe the ductility during brittle failure. For steels only general predictions are possible due to the complex cast to cast variation that is not fully understood at present.
- The ductility during ductile rupture has been demonstrated to be controlled by necking for the investigated steels and copper alloys. Since necking occurs very close to the rupture, modeling of necking can be used to predict the creep ductility.
- Several derivations for the influence of multiaxiality on the creep ductility are presented. In spite of the fact that they are based on many principles, the results are in general close to observations for notched bars.

References

1. J.K.L. Lai, Creep rupture ductility variations in AISI type 316 stainless steel. Mater. Sci. Eng. A **104**, L7–L9 (1988)
2. J.A. Siefert, J.D. Parker, Evaluation of the creep cavitation behavior in Grade 91 steels. Int. J. Pres. Ves. Pip. **138**, 31–44 (2016)
3. F. Abe, Influence of boron nitride inclusions and degradation in creep rupture strength on creep rupture ductility of Gr.122. Mater. High Temp. **38**, 197–210 (2021)
4. S. Holdsworth, Creep ductility of 1CrMoV rotor steel. Mater. High Temp. **34**, 99–108 (2017)
5. Data Sheet on the Elevated-Temperature Properties of 18Cr–8Ni–Mo Stainless Steel Tubes for Boiler and Heat Exchangers (SUS 316H TB), National Research Institute for Metals Tokyo, Japan, Report No. 6B (2000)
6. J.-F. Wen, S.-T. Tu, F.-Z. Xuan, X.-W. Zhang, X.-L. Gao, Effects of stress level and stress state on creep ductility: evaluation of different models. J. Mater. Sci. Technol. **32**, 695–704 (2016)
7. D. Krajcinovic, Damage mechanics. Mech. Mater. **8**, 117–197 (1989)

8. T.H. Hyde, W. Sun, J.A. Williams, Creep analysis of pressurized circumferential pipe weldments—A review. J. Strain Anal. Eng. Des. **38**, 1–30 (2003)
9. H.-T. Yao, F.-Z. Xuan, Z. Wang, S.-T. Tu, A review of creep analysis and design under multi-axial stress states. Nucl. Eng. Des. **237**, 1969–1986 (2007)
10. S. Holdsworth, Developments in the assessment of creep strain and ductility data. Mater. High Temp. **21**, 25–32 (2004)
11. S. Holdsworth, Creep-ductility of high temperature steels: a review. Metals **9** (2019)
12. M.W. Spindler, The multiaxial creep ductility of austenitic stainless steels. Fatigue Fract. Eng. Mater. Struct. **27**, 273–281 (2004)
13. W.M. Payten, D. Dean, K.U. Snowden, Analysis of creep ductility in a ferritic martensitic steel using a hybrid strain energy technique. Mater. Des. **33**, 491–495 (2012)
14. L. Binda, S.R. Holdsworth, E. Mazza, The exhaustion of creep ductility in 1CrMoV steel. Int. J. Pres. Ves. Pip. **87**, 319–325 (2010)
15. Y. Takahashi, Modelling of rupture ductility of metallic materials over wide ranges of temperatures and loading conditions, part II: comparison with strain energy-based approach. Mater. High Temp. **37**, 340–350 (2020)
16. Y. Takahashi, Modelling of rupture ductility of metallic materials for wide ranges of temperatures and loading conditions, part I: development of basic model. Mater. High Temp. **37**, 357–369 (2020)
17. J.K. Lai, A set of master curves for the creep ductility of type 316 stainless steel. J. Nucl. Mater. **82**, 123–128 (1979)
18. B. Wilshire, P.J. Scharning, Creep ductilities of 9–12% chromium steels. Scripta Mater. **56**, 1023–1026 (2007)
19. Q. Xu, D.R. Hayhurst, The evaluation of high-stress creep ductility for 316 stainless steel at 550 °C by extrapolation of constitutive equations derived for lower stress levels. Int. J. Pres. Ves. Pip. **80**, 689–694 (2003)
20. K. Singh, M. Kamaraj, Creep ductility of 1Cr1Mo1/4V low alloy forging and casting steels. Mater. Sci. Eng. A **510–511**, 51–57 (2009)
21. J. He, R. Sandström, Creep cavity growth models for austenitic stainless steels. Mater. Sci. Eng. A **674**, 328–334 (2016)
22. R. Sandström, R. Wu, Influence of phosphorus on the creep ductility of copper. J. Nucl. Mater. **441**, 364–371 (2013)
23. Data Sheet on the Elevated-Temperature Properties of 18Cr–10Ni–Ti Stainless Steel for Boiler and Heat Exchanger Seamless Tubes (SUS 321H TB), National Research Institute for Metals Tokyo, Japan, Report No. 5B (1987)
24. R. Sandström, J.-J. He, Prediction of creep ductility for austenitic stainless steels and copper. Mater. High Temp. **39**, 427–435 (2022)
25. E. van der Giessen, V. Tvergaard, Interaction of cavitating grain boundary facets in creeping polycrystals. Mech. Mater. **17**, 47–69 (1994)
26. D. Gonzalez, A.C.F. Cocks, T. Fukahori, T. Igari, Y. Chuman, Creep failure of a P91 simulated heat affected zone material under multiaxial states of stress, in *ECCC2014 3rd International ECCC Conference* (2014)
27. W. Beere, M.V. Speight, Creep cavitation by vacancy diffusion in plastically deforming solid. Metal Sci. **21**, 172–176 (1978)
28. A.C.F. Cocks, M.F. Ashby, Intergranular fracture during power-law creep under multiaxial stresses. Metal Sci. **14**, 395–402 (1980)
29. J.-F. Wen, S.-T. Tu, A multiaxial creep-damage model for creep crack growth considering cavity growth and microcrack interaction. Eng. Fract. Mech. **123**, 197–210 (2014)
30. J.R. Rice, D.M. Tracey, On the ductile enlargement of voids in triaxial stress fields*. J. Mech. Phys. Solids **17**, 201–217 (1969)
31. K. Hellan, An approximate study of void expansion by ductility or creep. Int. J. Mech. Sci. **17**, 369–374 (1975)

Chapter 14
Extrapolation

Abstract The extrapolation of creep data to longer times is technically very important. The traditional way of extrapolating creep rupture data is to use time temperaturer parameters (TTPs). In this way data from several test temperatures are combined to a single master curve that can be used to assess rupture strengths at long times. Recently, there is much focus on machine learning techniques (neural networks, NNs). Both types of procedures can generate accurate results, but a detailed analysis is required. A good way to assess the quality of the results is to use the post assessment tests (PATs) developed by ECCC. Without such tests arbitrary results can be obtained. They are important for both TTPs and NNs. It has been shown that by putting requirements on the derivatives of the creep rupture curves, the PATs can more or less automatically be satisfied. In addition, the error in the extrapolated values should be estimated. Using the basic creep models presented in this book, prediction of rupture strength and ductility can be made in a safer way. It is demonstrated for Cu that accurate extrapolation of many order of magnitude in the creep rate can be made, which is never possible with empirical models.

14.1 Introduction

Many types of high temperature plants have a long design life. Modern fossil fired power plants are designed for 20–40 years of operation and nuclear power plants for 60–80 years. To ensure safe operation accurate creep data and other time dependent material property values must be available that cover such long design lives. Direct measurement of creep data for these extended times is not practical for several reasons. It is expensive and technically complicated to perform long term creep tests. Disturbances can take place that destroy the test results. In addition the material being tested can be outdated before the test is finished. Instead numerical time extrapolation of the experimental results must be carried out. Extrapolation of creep rupture data have been performed for many years. Long term values have been predicted from shorter time experimental data. It should be emphasized that systematic procedures must be applied in order to obtain accurate results.

R. Sandström, *Basic Modeling and Theory of Creep of Metallic Materials*, Springer Series in Materials Science 339,
https://doi.org/10.1007/978-3-031-49507-6_14

The most common approach is to use time-temperature parameters (TTPs). With the help of a TTP, creep rupture data at several temperatures are combined to a single master curve, where the creep stresses are shown as a function of the TTP. From the master curve, time extrapolated values at lower temperatures can be derived from master curve values at higher temperatures. In this way, extrapolated values at most temperatures can be found by interpolation from the master curve. By being able to interpolate reduces the error in the analysis significantly. Many different TTPs exist, see [1]. It started with the Larson-Miller method in the 1950ties. Some TTPs will be listed in Sect. 14.2. Although many adjustable parameters are typically involved in the fit of the creep rupture data to the master curve, the TTPs are in general simple to use since the adjustable parameters can be obtained with linear algebra. The application of TTPs will be demonstrated in Sect. 14.2.

There are other types of methods than TTPs for extrapolation of creep rupture data. Two methods can be mentioned where also the form of the TTP is adjustable. The minimum commitment method [2] and the free temperature model [3]. In general it is difficult to reach more than a factor of three in time for accurate extrapolation with statistical methods like TTPs. With the free temperature model a factor of ten can be reached in many cases. This has been demonstrated for austenitic stainless steels. Other approaches for extended extrapolation also exist [4, 5]. Two other groups of methods should also be mentioned. With algebraic methods a creep stress versus rupture time equation is the starting point. This type of approach was popular in the former Soviet Union [6]. The German graphical techniques have successfully been used to perform accurate extrapolations [7]. Another graphical method is a former ISO-standard [8]. A more recent method that is popular is due to Wilshire [9]. In this approach the creep data is normalized with the tensile strength. This is valuable if the amount of scatter in the creep data can be reduced in this way.

It was recognized a long time ago that the extrapolation results significantly depended on the chosen TTP and on the degree of the polynomial used in the fit of the master curve [10]. Since different analysts often have different opinions about the choice of method, it means that the results are operator dependent and this was not considered to be an acceptable situation. For this reason, the European Collaborative Creep Committee (ECCC) was initiated. Within ECCC, a framework of systematic procedures has been developed that generate more consistent results. The ECCC program started in 1992 and is still ongoing in 2022. It has been known that it is not possible to pin point a specific TTP to be more advantageous than others. Instead, post assessment tests (PATs) have been formulated that are used to check that the applied method does not show unphysical behavior and that the extrapolated creep rupture strength values are not sensitive to limited changes in the input data. Due to the flexibility of the polynomial fit to the master curve, unphysical behavior often appears. The PATs represented a major step forward when they were introduced [11, 12]. Creep rupture data for many steels and alloys proposed by ECCC are now in European standards. However, there are still short comings of the proposed procedures and PATs. None of them are based on derivations from physical principles and in the past there has been no way of estimating the error in the results.

To improve the situation for these remaining limitations, two things have recently been proposed [13]. The first one is to put requirements on the first and second derivatives of the predicted creep rupture curve. The derivatives should be negative. In this way a correct physical behavior is often automatically achieved and the flexing of creep rupture curves is avoided. The second item is that principles for estimating the extrapolation error have been proposed. The use of these findings will be discussed in Sect. 14.3.

The use of a Neural Network (NN) is an alternative to TTP. NN is also called Artificial Neuron Network and is a part of deep learning. NNs are extensively applied in the development of Artificial Intelligence (AI). NNs are used in a large number of industrial applications such as autonomous driving, signal processing, risk assessment, pattern recognition of images, missile control, autopilots, etc. [14]. In contrast to TTP no basic parameter model is chosen. NNs consist of a number of functions, neurons, with adjustable parameters. NNs are sufficiently flexible that they can adapt to many types of functional dependence. Fitting of data with empirical models has found new interest with the wide spread use of NNs. NNs are in principle limited to interpolation of data. However, in practice they are used for extrapolation as well.

Complicated creep rupture behavior can be simulated with NNs even when special degradation mechanisms are present [15, 16]. The fit of the functional dependence implies that the number of adjustable parameters is larger than when using TTPs, often much larger. Liang et al. [17] have analyzed the creep rupture life of 9–12%Cr steels with NN; Ghatak et al. have modeled the creep rupture curve of HP40Nb steels with NN successfully [15]. Adductive NN has also been suggested for creep rupture prediction of 9–12%Cr steels by Wang et al. [18].

In fact, the debate for the extrapolation capability of NN has lasted for a long time. Including physical principles in the common NN is a good way to improve the extrapolation. This is called physics-constrained [19] or physics-informed NN [20] (PCNN or PINN). The extrapolation can be safely conducted by adding constraints or prior knowledge to the common NN.

Extrapolation from NN results must be common in industry. In spite of this it is difficult to find procedures for error analysis in the literature. The common method is to make a regression analysis between the predicted values and the source data and to determine the standard deviation between predictions and the observations. As will be shown in Sect. 14.3, this is not adequate at all for creep rupture data and probably not for many other types of applications either. For this reason new types of error analysis have been formulated recently, Sect. 14.3.

As was mentioned above, the introduction of requirements on the first and second derivative of the creep rupture curves can significantly simplify and improve the results of the extrapolation analysis with TTPs. For example, many of the ECCC PATs were found to be automatically satisfied if these requirements were introduced. It will be shown in Sect. 14.2 that these requirements are equally essential when NN-based modeling is carried out. This will be demonstrated in Sect. 14.3.

The methods discussed above are all empirical models. None of TTPs commonly used have been derived from basic physical principles. Both TTPs and NNs are just flexible expressions that can easily be fitted to the observations. Empirical models

have the drawback that a large amount of data must be available to make safe predictions. Unless the amount of data is sufficient, the models cannot be used to identify the operating mechanisms [21–23]. To fully understand the underlying mechanisms, fundamental models should be applied where the contributions from different mechanisms are derived from basic physical principles. Such models have been derived for dislocation strengthening as well as precipitation and solid solution hardening. They have been used to predict the creep rate of austenitic stainless steels [21, 22, 24, 25]. Fundamental models have also been formulated for cavity nucleation and growth. By applying these models, brittle rupture can be modeled. Both creep rupture strength and ductility have successfully been computed for copper and austenitic stainless steels [22, 23, 26–28]. Some of these models will be discussed in Sect. 14.4. Fundamental models are of importance for example to meet the full design life of modern nuclear reactors with a planned design life of 60–80 years.

14.2 Empirical Extrapolation Analysis

14.2.1 Basic TTP Analysis

Extrapolation from a single curve gives quite an uncertain result in particularly if there are no requirements on the derivatives. It was recognized long ago that by combining creep data from several temperatures, the accuracy could be much improved. The size of the improvement will be analyzed in Sect. 14.3. The classical approach is to use a time temperature parameter (TTP). It is a function of absolute temperature and time. A polynomial in the logarithm of the creep stress is fitted to the TTP in such a way that the creep rupture data fall on a single curve, the master curve. A logarithm with the base 10 is most frequently used in studies on extrapolation and that practice will be followed in this chapter. The coefficients in the polynomial and a few constants in the TTP represent the adjustable parameters involved. For many TTPs the adjustable parameters can be determined with the help of linear algebra and are consequently easy to find. Many TTPs are available. Sources were given in Sect. 14.1. Examples of TTPs are listed in Table 14.1.

Table 14.1 Examples of time-temperature parameters (TTPs)

Larson-Miller (LM)	$\mathrm{TTP_{LM}} = T[\log(t) + C_{\mathrm{LM}}]$
Manson-Haferd (MH)	$\mathrm{TTP_{MH}} = \frac{\log(t)-\log(t_a)}{T-T_a}$
Manson-Brown (MB)	$\mathrm{TTP_{MB}} = \frac{\log(t)-\log(t_a)}{(T-T_a)^r}$
Orr-Sherby-Dorn (OSD)	$\mathrm{TTP_{OSD}} = \log(t) + C_{\mathrm{OSD}}/T$
Manson-Succop (MS)	$\mathrm{TTP_{MS}} = \log(t) + C_{\mathrm{MS}} \cdot T$
Sud aviation (SA)	$\mathrm{TTP_{SA}} = \log(t) + C_{\mathrm{SA}} \cdot \log(T)$
Goldhoff-Sherby (GS)	$\mathrm{TTP_{GS}} = \frac{\log(t)-\log(t_a)}{1/T-1/T_a}$

For the listed TTPs, T is the temperature, t the time, and C_{NN} and $\log(t_a)$ are adjustable parameters. The parameters T_a and r are given predefined values in general.

The TTPs in Table 14.1 have been used for a number of decades. References to the original sources of the TTPs can be found in [1, 29, 30]. The extrapolation results depend on the chosen TTP and the degree of the polynomial that is used to fit the master curve. Consequently, it is critical how these quantities are selected. There is general experience that it is not possible to find the optimal TTP for a given analysis in advance [10]. Instead, a number of TTPs and polynomial degrees have to be tested to find a satisfactory solution.

With an example it will be shown how extrapolation with a TTP can be performed and how the result is checked and analyzed. A creep resistant 17Cr12NiTi austenitic stainless steel with the common designation 321H will be studied. The experimental data are taken from NIMS' large collection. The studied creep data are shown in Fig. 14.1. Larson-Miller TTP is applied and the polynomial degree is selected to 6. The fitted master curve is shown in Fig. 14.2.

The model values in Fig. 14.1 are taken directly from the master curve in Fig. 14.2. The part of the master in the range of the data is used for all temperatures except the highest one where it is necessary to take into account the extrapolated part of the master curve for large TTP values. The advantage of using a TTP is already obvious from this description. The extrapolated values at all temperatures except the highest one can be determined by interpolation along the master curve. This gives a more accurate result than when being forced to extrapolate from single curves. As a consequence the extrapolated values at the highest temperature involve a potentially

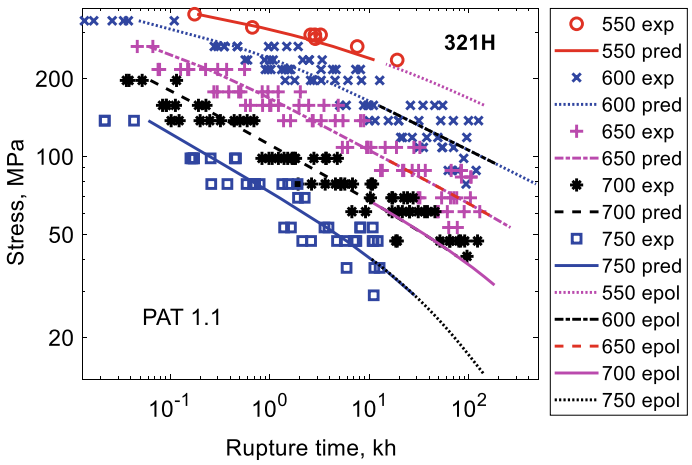

Fig. 14.1 Comparison of experimental and modeling (interpolated and extrapolated) values for creep rupture of the 17Cr12NiTi austenitic stainless steel (321H); Larson-Miller TTP model is used; 'pred' represents the interpolated values, 'epol' the extrapolated values, and 'exp' the experimental data at five test temperatures from 550 to 750 °C. Experimental data from NIMS [31]

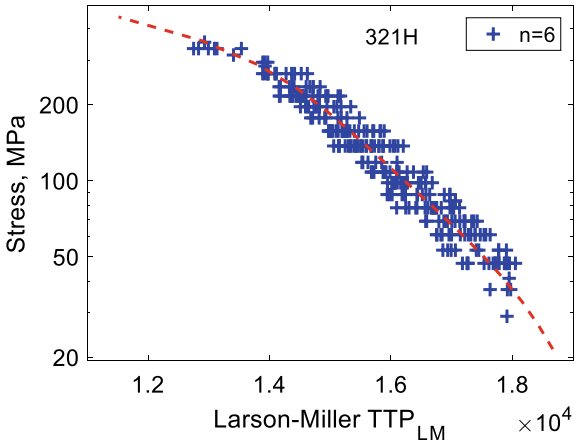

Fig. 14.2 Master curve for the creep rupture data in Fig. 14.1. A polynomial of degree 6 in $\log(\sigma_{creep})$ versus TTP (dashed curve --) is fitted to the experimental data (pluses +) at the five test temperatures 550–750 °C

higher error than the predicted values at other temperatures. The first requirement of a successful analysis is that good fit to the data is obtained, which should be directly evident from the comparison with source data (Fig. 14.1) and for the master curve (Fig. 14.2).

In many cases the analysis is performed without additional requirements. This often means that a number of attempts have to be made before smooth curves and a good fit can be obtained. However, the results in Figs. 14.1 and 14.2 have been determined with additional requirements. All creep strength versus rupture time representations with double logarithmic scale (which are referred to as creep rupture curves) must have a non-positive derivative, in practice a negative derivative. Otherwise the rupture time would not increase with decreasing creep strength which is unphysical. In addition, the absolute slope is not arbitrarily large.

The second derivative of creep rupture curves is in most cases negative, i.e. the absolute value of their slope increases with rupture time. The reason is that there is microstructural degradation for example through coarsening of precipitates. The exception is so-called sigmoidal behavior with a slightly S-shaped curve. Such rupture curves are typically the result of complex precipitation during the creep tests and there is a time period when the strength is not degrading but increasing. It is quite unusual that the sigmoidal appearance has a temperature dependence that is consistent with the creep rupture and can be described with a TTP so this case is not considered here. In fact, sigmoidal forms are suitable to handle with the type of basic models that are presented in Sect. 14.4. As a consequence it can be assumed that also the second derivative of the rupture curve is negative.

When computing the results in Fig. 14.1 and in Fig. 14.2, constraints on the creep rupture curves have been taken into account. The conditions are formulated as

$$-m = \frac{d \log t_R}{d \log \sigma} \leq -1.5; \quad \frac{d^2 \log t_R}{d \log \sigma^2} \leq 0 \tag{14.1}$$

$$\frac{d\log t_R}{d\log T} \leq 0 \tag{14.2}$$

As pointed out above it is a physical requirement that the first derivative of creep rupture curves is negative

$$\frac{d\log \sigma}{d\log t_R} < 0 \tag{14.3}$$

$\frac{d\log t_R}{d\log \sigma}$ is the inverse of $\frac{d\log \sigma}{d\log t_R}$, and consequently the former derivative is also negative.

In Eq. (14.1) the second derivative can be expressed as the second derivative of the rupture curve

$$\frac{d^2\log t_R}{d\log \sigma^2} = -\frac{d^2\log \sigma}{d\log t_R^2} \Big/ \left\{\frac{d\log \sigma}{d\log t_R}\right\}^3 \tag{14.4}$$

Equation (14.4) can be obtained with elementary calculus. Since the first derivative is assumed to be negative it follows that the two second derivatives have the same sign. Thus, the second criterion in Eq. (14.1) is verified. This ensures that the creep rupture curves have a negative second derivative. The second derivative of the rupture time is somewhat easier to compute than the second derivative of the creep stress.

With a Norton type of approach both the creep rate $\dot{\varepsilon}_{sec}$ and the rupture time t_R can be represented with stress exponents (power-law creep)

$$\dot{\varepsilon}_{sec} = A_N \sigma^{n_N};\ t_R = B_R \sigma^{-m} \tag{14.5}$$

The constant m is the inverse slope of the flow curve with a minus sign, see Eq. (14.1). The Modified Monkman-Grant equation relates the rupture strain ε_R to the strain rate and the rupture time [32]

$$\dot{\varepsilon}_{sec} t_R = C_{MMG} \varepsilon_R \tag{14.6}$$

Sundararajan lists values of C_{MMG} for a number of materials [33]. The values lie in the interval 0.1–0.64. If only secondary creep contributed to the rupture strain the constant C_{MMG} would be equal to unity. Another constant, the rupture ductility factor λ_R, is often used

$$\lambda_R = \frac{\varepsilon_R}{\dot{\varepsilon}_{sec} t_R};\ \lambda_R = 1/C_{MMG} \tag{14.7}$$

By comparing the definition of λ_R with the modified Monkman-Grant equation, it is evident that λ_R is just the inverse of the modified Monkman-Grant constant C_{MMG}. The value of the rupture ductility factor has been analyzed in more detail for modern 9Cr1Mo steels. The result is that $\lambda_R \approx 5$ and increases with rupture time [34].

By combining Eqs. (14.5)–(14.7) and taking the logarithmic derivative, one finds that

$$m - n_N = \frac{d \log \lambda_R}{d \log \sigma} - \frac{d \log \varepsilon_R}{d \log \sigma} \tag{14.8}$$

Since the rupture strain often increases with stress and λ_R decreases with stress for some alloys, the m value is smaller than the n_N value at least at lower stresses. ECCC has suggested a lower limit of m of 1.5, cf. Eq. (14.1). This is a characteristic feature of creep resistant steels. If the absolute value of the slope would be still higher and the m value lower, the steel would not be safe to use.

If the Omega model is satisfied for tertiary creep, the following relation is available from Eq. (12.37) if the reasonable assumption that ε_{diff} is large is made

$$t_R \dot{\varepsilon}_{min} = \frac{e^{-n_\Omega \varepsilon_0} f_{red}^{n_N}}{n_\Omega} \tag{14.9}$$

If this equation is combined with the expression for the rupture strain, Eq. (12.38), one finds that

$$t_R \dot{\varepsilon}_{min} = \varepsilon_R f_{red}^{n_N} (1 - f_{red}^{n_N}) \tag{14.10}$$

This recovers obviously the modified Monkman-Gran relationship (14.6) with a constant that depends on the size of the imperfection of the specimen. Since ε_0 is about 0.01 and $f_{red} \approx 0.99$, the right hand side of Eq. (14.9) is often close to $1/n_\Omega$. From Eqs. (14.6), (14.7) and (14.9) one then finds that

$$\frac{1}{n_\Omega} \approx C_{MMG} \varepsilon_R = \frac{\varepsilon_R}{\lambda_R} \tag{14.11}$$

This provides another way of estimating the slope n_Ω of log(strain rate) versus strain curves in the tertiary stage. This result is consistent with the finding that n_Ω increases with increasing rupture time for modified 9Cr1Mo steels (end of Sect. 12.4.2) in the same way as ε_R/λ_R does [34].

The first and second derivatives for the predicted rupture curves in Fig. 14.1 are illustrated in Fig. 14.3. The first derivative is given as the m value, Eq. (14.1).

The conditions in Eq. (14.1) require that the m value is larger than 1.5 and that the second derivative is not positive. These conditions are obviously fulfilled. The criterion in Eq. (14.2) ensures that the creep rupture curves at different temperatures do not cross. This criterion is usually not difficult to meet.

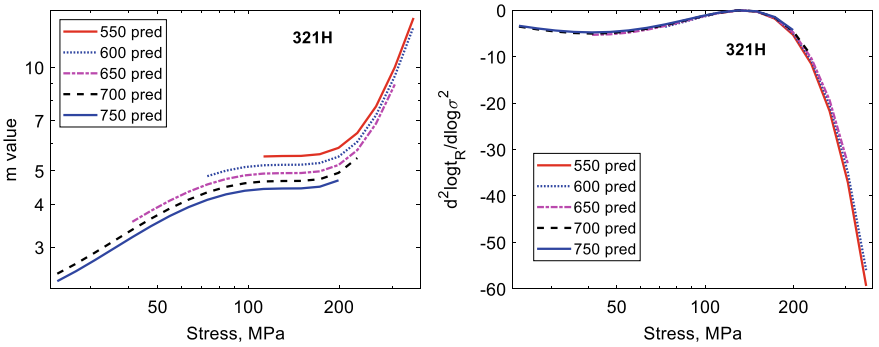

Fig. 14.3 The first **a** and second **b** derivatives of the rupture time as a function of creep stress for the creep rupture curves at the five test temperatures 550–750 °C in Fig. 14.1. The *m*-value is minus the inverse of the first derivative (PAT 1.3)

14.2.2 The ECCC Post-assessment Tests

As mentioned above the results of the extrapolation analysis depend on the chosen TTP and degree of the polynomial that is used to fit the master curve. The European Creep Collaborative Committee (ECCC) recognized that additional tools are needed to improve the possibility to select amongst all the alternatives. They proposed a number of Post Assessment Tests (PATs) that should be applied when the predicted rupture strengths have been generated. There are three sets of PATs [11, 12, 35]. The PATs are listed in Table 14.2. PATs 1.1–1.3 check the physical realism of the predicted creep rupture curves. A good fit to the data is required, and the derivative of the rupture curve should follow the measured values. PATs 2.1 and 2.2 assess that the result is uniform and unbiased and that data at specific stresses, temperatures, or casts do not behave in a different way from the rest of the prediction. The analysis is repeated in PATs 3.1 and 3.2 with some of the long term data removed to verify the stability of the prediction.

Table 14.2 ECCC post-assessment tests (PATs) for creep rupture data extrapolation (reproduced from [36] with permission from Elsevier)

PAT 1.1 Visibility check that the model has given a good fit to data
PAT 1.2 Physical behavior of the rupture curve over an extended range of temperatures and stresses
PAT 1.3 First derivative of rupture curves to check that the slope is not too steep
PAT 2.1 Regression of predicted vs. experimental rupture times to avoid bias
PAT 2.2 Analysis of individual casts
PAT 3.1 Reanalysis with 50% of the longest time data removed
PAT 3.2 Reanalysis with 10% of the lowest stress data at each temperature removed

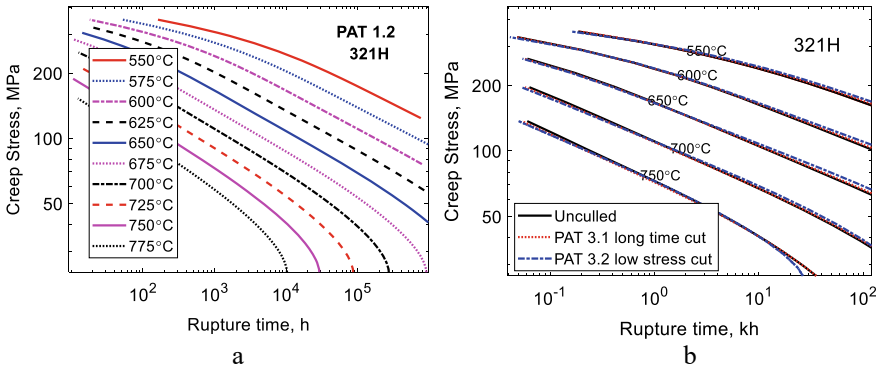

Fig. 14.4 **a** Representation of predicted creep rupture curves over an extended range of rupture times for a fine distribution of temperatures (PAT 1.2); **b** influence of culling of data on the predicted rupture curves; According to PAT 3.1 long term data are removed in the analysis, and in PAT 3.2 the data points with the lowest stresses at each temperature are not included

The match of the predicted to the experimental data is illustrated in Figs. 14.1 and 14.2. The fit is fine which means that PAT 1.1 is satisfied. In Fig. 14.3, $m > 1.5$ and consequently PAT 1.3 is fulfilled.

In Fig. 14.4 the results of PAT 1.2 and PAT 3 are shown. In Fig. 14.4a there is no bending back or crossing of curves in spite of the wide range of stresses and rupture times and the fine temperature spacing. PAT 1.2 is verified. It should be demonstrated that the results are not sensitive to the data for the longest test times. This is studied with the help PAT 3.1 and PAT 3.2. In PAT 3.1 the same analysis is performed again but with 50% of the data points with rupture time larger than a tenth of the maximum observed rupture time randomly removed (culled). In PAT 3.2, the analysis is repeated again but this time with 10% of the data points with the lowest stresses culled. As can be seen in Fig. 14.4b only at the highest temperature there is a significant difference between the culled and the unculled curves. The difference should be less than 10% according to the ECCC recommendation and this is satisfied.

In Fig. 14.5 regression plots between the experimental and the predicted rupture times are shown. The purpose of this type of diagram is to demonstrate that the predicted values are close to the observed ones at both low and high stresses. Otherwise the regression line would deviate from the 1:1 line. Two sets of border lines are marked in the Figure. There are lines a factor of 2 above and below the 1:1 line. If there is limited scatter in the data set, the result would fall inside these lines, but that is typically not the case. The second set is located 2.5 σ_{std} above and below the 1:1 line. If the data show a normal distribution, no more than 2% of the data should fall outside these lines. This is obviously fulfilled in Fig. 14.5. The regression coefficient should be higher than 0.78 (0.92 in Fig. 14.5a). The regression plots are used to estimate the regression error. This will be further discussed in Sect. 14.3.

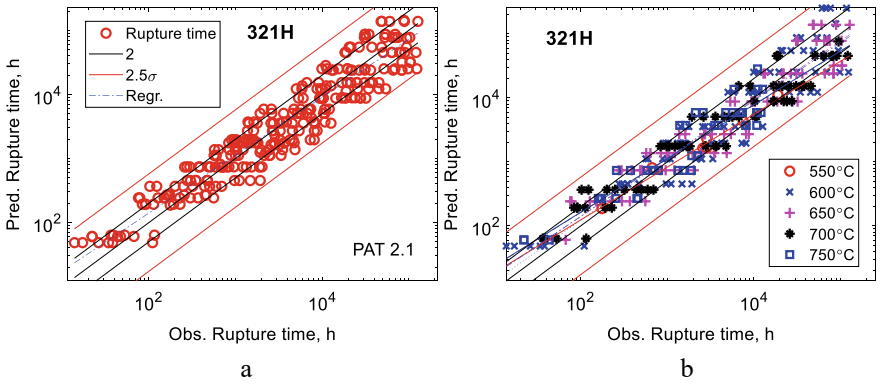

Fig. 14.5 Regression plots between observed and predicted rupture times. The regression line is marked. The black line represents a factor of 2 above and below the mean line. The red line describes a factor of 2.5 times the standard deviation above and below the mean line; **a** all temperatures (PAT 2.1); **b** Regression plots for individual temperatures

14.2.3 Use of Neural Network (NN)

Creep rupture data can be analyzed with a neural network [37]. It is sufficient to use a simple NN. The NN that has been applied is illustrated in Fig. 14.6. There are a hidden layer and an output layer. In the hidden layer there are 3–10 neurons (3 in the Fig. 3) and in the output layer one.

Each neuron represents transfer functions, one for each input and one for each output. The type of transfer function is sigmoidal in the input layer and linear in the output layer. There are weight and base parameters in the transfer functions. They are used as adjustable parameters in the fitting process. Well established procedures for finding the values of the adjustable parameters are available [14]. The fitting process for NNs is usually called training. Of the experimental data 70% were set for training, 15% for testing, and 15% for validation. The Levenberg-Marquardt back propagation method was applied in the training of the network to minimize the Mean Squared Error (MSE). A random number stream was used in the NN fitting process to fix the output.

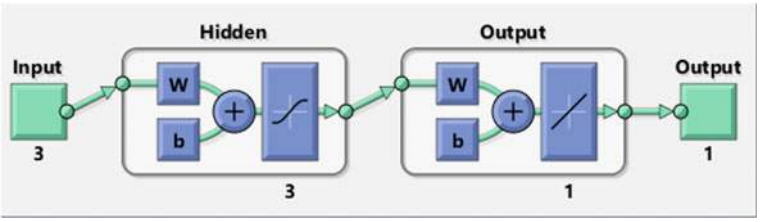

Fig. 14.6 Schematic structure of the neural network used to fit the creep rupture data (with Matlab)

With n_{input} inputs, n_{out} outputs, and n_{neur} neurons in the hidden layers, the number of adjustable parameters (weight and base parameters) n_{adj} is

$$n_{\text{adj}} = (n_{\text{input}} + 1 + n_{\text{out}})n_{\text{neur}} + 1 \tag{14.12}$$

For creep rupture, the test temperatures and the stresses are the two inputs and the rupture times the output. The flexible NN model should give a good representation of the rupture times. According to Eq. (14.12), there are 13 adjustable parameters with 3 neurons in the hidden layer; and there are 41 with 10 neurons. In the framework of creep rupture, 13 adjustable parameters is already a large number [12]. With more neurons the fitting of the data is improved but overfitting may quickly be the result.

For precisely the same reasons as in the TTP analysis, the requirements on the derivatives in (14.1) and (14.2) should be fulfilled. This ensures that flexing and other unphysical behavior of the predicted creep rupture curves are avoided. Unfortunately expressions for the derivatives are not readily available in NN software. For this reason expressions for derivatives have been derived. Since the expressions are complex, the derivation has been placed in an Appendix (Sect. 14.6). An alternative is to repeat the computations many times until the constraints and other requirements are fulfilled. This is referred to as soft constrained machine learning [38].

The application of a NN model is illustrated in Fig. 14.7 for the austenitic stainless 18Cr10NiCu steel Super304H. It has also the common designation 304HCu. The predicted rupture strengths are compared with the observations.

A good fit was possible to obtain in Fig. 14.7. It should be emphasized that many runs with different stream numbers were needed before a satisfactory result was obtained. The stream number fixes the random number generator so the same run can be repeated. In this way the adjustable parameters in the NN model are initiated

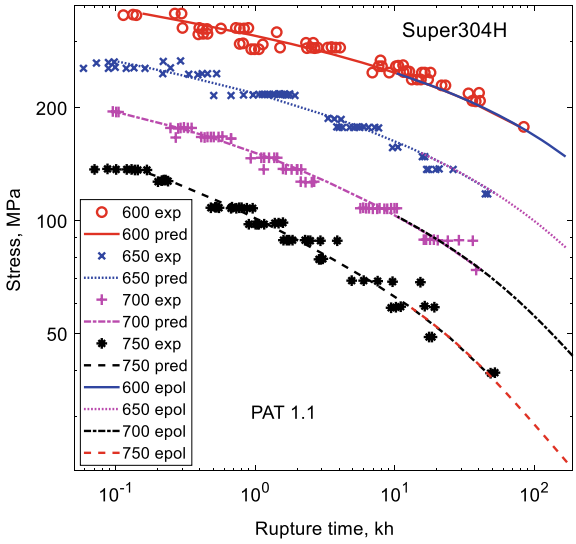

Fig. 14.7 Comparison between observed and predicted rupture times for the creep-resistant austenitic stainless steel Super304H at four test temperatures from 600 to 750 °C. The prediction of the rupture times was made with a constrained NN model. "pred" is the modeling results within the experimental range; "epol" is the extrapolated results; "exp" is the experimental data of Super304H taken from [39]. Reproduced from [37] with the permission of Taylor & Francis

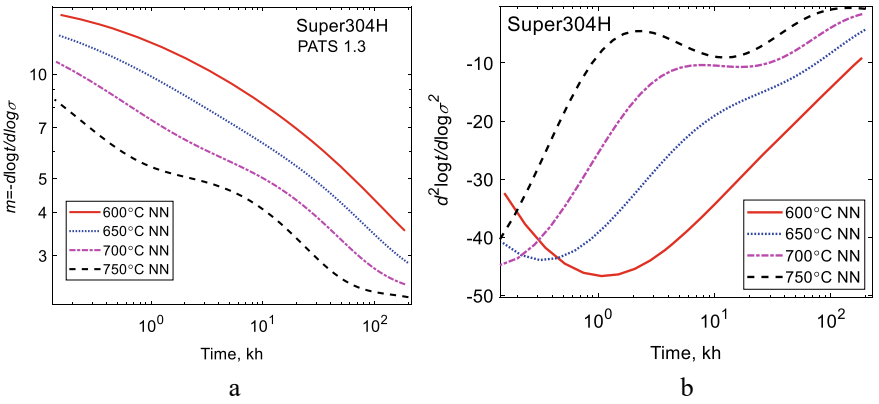

Fig. 14.8 The first and second derivatives of rupture time with respect to the creep stress for the rupture curves in Fig. 14.7; **a** the *m* value and **b** the second derivative both as a function of rupture time. Reproduced from [37] with the permission of Taylor & Francis

with the same values. The initial values have obviously a significant effect on the result. The requirements on the derivatives simplify the search for a good fit that behaves in a physical correct way.

The derivatives of the rupture curves are presented in Fig. 14.8. In this case the derivatives are given as a function of rupture time instead of stress as in Fig. 14.3. But the same message is provided. The derivatives are negative and the *m* value is larger than 1.5 so the conditions in Eqs. (14.1) and (14.2) are satisfied.

The regression plot in Fig. 14.9 shows a narrower scatter band than in Fig. 14.5 for 321H. Most of the data fall inside the band for a factor of 2. The reason is most likely that the data for Super304H come from just one cast whereas the 321H data are from 9 casts. Only single points are outside the 2.5 σ_{std} limit in Fig. 14.9. PAT 2.1 is fulfilled since the regression line is close to the 1:1 line. An even distribution is shown for the extended curves in Fig. 14.9b. No crossing of curves and no bending back verify that PAT 1.2 is satisfied.

Studies on several materials show that the PATs play an equally important role for NN models as in TTP analysis. That the results have a physical correct behavior cannot be ascertained without the application of the PATs. The use of constrained optimization with conditions on the derivatives of the creep rupture curves makes it much more straightforward to fulfill the requirements of the PATs.

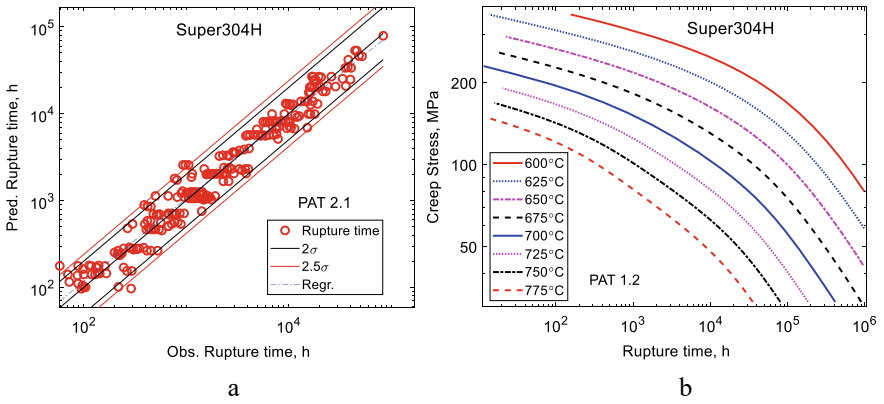

Fig. 14.9 Regression plot of predicted rupture time versus observed rupture time for Super304H with a regression line (dashed line) close to the 1:1 line. Two bands are given: ±2.5 times the standard deviation and a factor of ±2; **b** predicted rupture times over a wide range of stresses and rupture times to demonstrate that the curves are not bending back in an unphysical way. Reproduced from [37] with the permission of Taylor & Francis

14.3 Error Analysis in Extrapolation

14.3.1 Model for Error Analysis

Fitting a model to the observed creep rupture data is the start of all empirical models. The model must give a good fit to the data. This means that the model must be able to interpolate accurately between the data points. If TTPs are used the fit is to a single curve, the master curve. The deviation between the interpolated values and experimental data gives the first contribution to the extrapolation error.

A schematic creep rupture curve is shown in Fig. 14.10. The creep stress is plotted versus rupture time. The data points are scattered around a source curve with a random scatter of 50%. The curve will be used to estimate the interpolation error.

The data is fitted with a polynomial of degree 5. To simulate the situation for a creep rupture curve, the condition for the first derivative is taken into account according to the first criterion in Eq. (14.1). The polynomial lies well inside the scatter band but it is moving from one side of the source curve to the other side. This means that the second derivative changes sign. In the curve designated fit with constraints the second derivative is also assumed to be negative according to the second criteria in Eq. (14.1). Since this condition is fulfilled for most rupture curves, see Sect. 14.2, the focus will be on this case. It will be referred to as the constrained one (although the pure polynomial fit is also constrained to some degree).

The average error σ_{devcon} in the fit with the constraints can be estimated from basic principles in statistics [40]

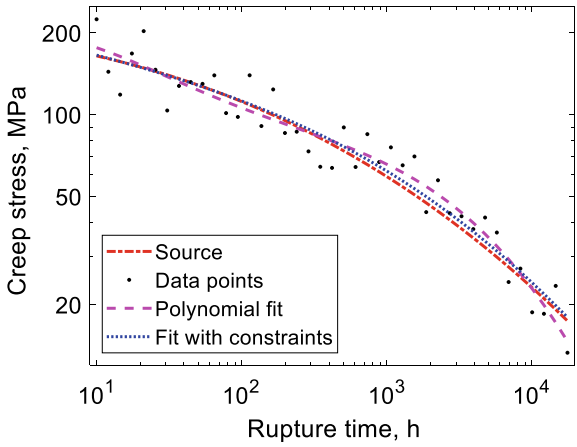

Fig. 14.10 Schematic creep rupture curve with the creep stress as a function of the rupture time in a double logarithmic diagram

$$\log \sigma_{\text{dev con}} = \log \sigma_{\text{rnd}} / \sqrt{n_{\text{d}}} \tag{14.13}$$

n_{d} is the number of data points. σ_{rnd} the amount of scatter in the data points measured as the deviation of the difference between the data points and the source curve.

$$\log \sigma_{\text{rnd}} = \sqrt{\sum_i (\log \sigma_i - \log \sigma_{\text{source}})^2 / (n_{\text{d}} - 1)} \tag{14.14}$$

A polynomial fit is flexing around the source up to n_{p} times, where n_{p} is the degree of the polynomial. Within each range of flexing the principles of Eq. (14.13) can be applied. The average error σ_{devuncon} becomes

$$\log \sigma_{\text{devuncon}} = \log \sigma_{\text{rnd}} / \sqrt{n_{\text{d}} / n_{\text{p}}} \tag{14.15}$$

Consequently, the error is raised by a factor of $\sqrt{n_{\text{p}}}$ in relation to Eq. (14.13). The derived errors in Eqs. (14.13) and (14.15) have been verified with thousands of test runs. Logarithms are used in Eqs. (14.13) and (14.15), which shows that relative errors are derived.

In Fig. 14.11a it is illustrated what happens if one tries to extrapolate the curves in Fig. 14.10. For the polynomial fit a partially unphysical result is obtained and the curve is almost bending upwards. This is avoided in the constrained fit. In Fig. 14.11b another case is illustrated for the same source curve but with a new set of randomly generated data points. It is evident that extrapolation from a single curve can give significant variations.

When a significant extrapolation is made, the result is controlled by the highest order term in the polynomial. In the error analysis, this part is taken into account. It can be expressed as

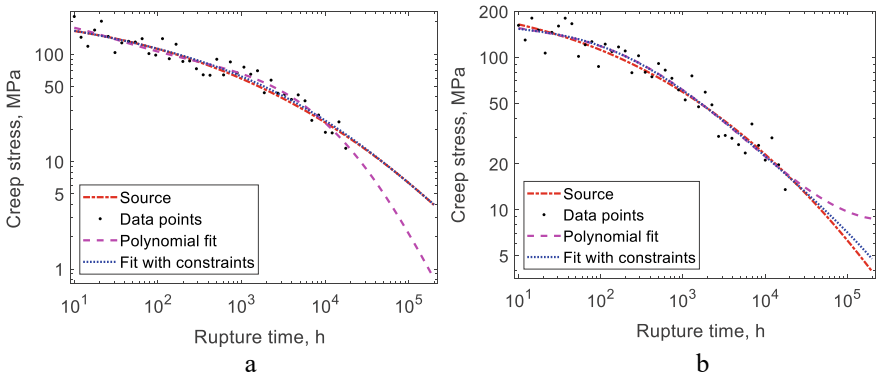

Fig. 14.11 Schematic creep rupture curve with the creep stress as a function of the rupture time in a double logarithmic diagram; **a** extrapolated from Fig. 14.10; **b** parallel example from the same source curve

$$\log e_{\text{ext}} = A(\log(t_{\text{ext}}/t_{\text{ref}}))^{n_{\text{p}}} \tag{14.16}$$

where t_{ext} is the extrapolated rupture time. The reference time t_{ref} is chosen as the minimum rupture time t_{min} included in the analysis. A is a constant that is a function of the degree n_{p} of the polynomial, the number of data points n_{d}, and the half-width of scatter band σ_{rnd}. The value of A has been determined with the help of a large number of test runs. The following expressions have been found for the constrained and unconstrained cases

$$A_{\text{con}} = \frac{a_0 \log \sigma_{\text{rnd}}}{\sqrt{n_{\text{d}}}(\log(t_{\text{max}}/t_{\text{min}}))^{n_{\text{p}}}};\ A_{\text{uncon}} = \frac{a_0 \log \sigma_{rnd}}{\sqrt{n_d/n_p}(\log(t_{\text{max}}/t_{\text{min}}))^{n_p}} \tag{14.17}$$

t_{min} and t_{max} are the minimum and maximum rupture times in the analysis. a_0 is an empirical factor that has been found to be about unity. A safety factor of 2.5 in the width of the scatter band is included in the value of a_0.

The constant A and consequently the error from Eq. (14.17) are directly proportional to the logarithm of the half-width of the scatter band and inversely proportional to the square root of the number of data points. For the unconstrained case the error is higher by a factor that is equal to the square root of the degree of the polynomial. These basic factors are the same as in Eqs. (14.13) and (14.15).

In Fig. 14.12 an example is given for how the error increases with rupture time. There is a rapid increase. If extrapolation by a factor of 3 in time is assumed which is a common requirement, it can be seen from the Figure that this corresponds to an error of 20% in the constrained case and 50% in the unconstrained case. It is obvious that extrapolation from a single curve can generate large errors.

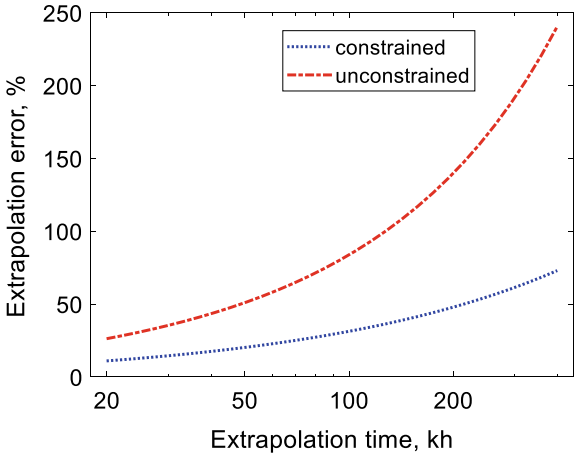

Fig. 14.12 Error in stress after extrapolation. Results for extrapolation with constrained derivatives are compared with unconstrained ones. $t_{min} = 0.01$ kh and $t_{max} = 20$ kh. Redrawn from [36] with permission of Taylor & Francis

14.3.2 Error Analysis with PATs

The ECCC PATs are valuable tools to assess if the analysis has worked in a satisfactory way and the predicted values show a correct physical behavior. However, they do not give a direct measure of the accuracy even if all PATs are satisfied. However, with the help of the analysis above this can be achieved. The interpolation error e_{interp} from the master curve can be expressed as

$$\log e_{interp} = \frac{\log \sigma_{rnd}}{m(\sigma)} \sqrt{\frac{n_{temp}}{n_d}} \tag{14.18}$$

Logarithms are used in Eq. (14.18), since the modeling of the creep rupture curves is usually analyzed in log scales. The error in stress is requested, whereas σ_{rnd} gives the scatter in the time direction. To take this into account, the $m(\sigma)$ value is introduced in Eq. (14.18). As marked the m value is stress dependent, see Fig. 14.3. The number of temperatures in the analysis n_{temp} is included for the same reasons as the degree of the polynomial in Eq. (14.15).

The regression lines in Fig. 14.5 do not follow the 1:1 line precisely. This deviation results in an error that can be expressed as

$$\log e_{regr} = b_0 + (b_1 - 1) \log t_R \tag{14.19}$$

where b_0 and b_1 are adjustable parameters describing the regression line. In Fig. 14.5b, the regression lines are evaluated at each temperature. This means that b_0 and b_1 are temperature dependent. As can be seen the regression line at individual temperatures can deviate from the 1:1 line much more than the mean line.

The expressions for the errors e_{interp} and e_{regr} in Eqs. (14.18) and (14.19) are often close to unity. The corresponding differences from unity E_{interp} and E_{regr} and their

sum are therefore introduced

$$E_{\text{interp}} = e_{\text{interp}} - 1; \quad E_{\text{regr}} = e_{\text{regr}} - 1 \tag{14.20}$$

$$E_{\text{tot}} = e_{\text{interp}} e_{\text{regr}} - 1 \tag{14.21}$$

For the case in Fig. 14.1 the three types of errors are given for 321H in Table 14.3.

The interpolation error in Table 14.3 is between 4 and 6%. The error due to bias in the prediction is referred to as the regression error which takes values from 7 to 10%. The total error is between 12 and 18%. The strength values are multiplied by the total relative errors to find the uncertainties in the stress values that are given as plus-minus additions.

To find the extrapolated values at the highest temperature, it is necessary to extrapolate from the master curve. The error in this case is given by Eqs. (14.13) and (14.14)

$$\log e_{\text{extrap}} = \frac{a_0 \log \sigma_{\text{rnd}}}{\sqrt{n_{\text{d}}}} \left[\frac{\log(t_{\text{ext}}/t_{\text{ref}})}{\log(t_{\max}/t_{\min})} \right]^{n_{\text{p}}} \tag{14.22}$$

t_{ext} is the extrapolated rupture time, and $t_{\min}$ and $t_{\max}$ the range of experimental rupture times. $a_0 = 1$ and $t_{\text{ref}} = t_{\min}$ are chosen as explained above. The relative error E_{extrap} is obtained as in Eq. (14.20) from

$$E_{\text{extrap}} = e_{\text{extrap}} - 1 \tag{14.23}$$

The regression error is determined in the same way as for the other temperatures and the total error from Eq. (14.21). The results are shown in Table 14.4.

Table 14.3 Error estimates for values interpolated from the master curve in Fig. 14.2

Temperature, °C	Rupture time, h	Stress, MPa	Rel. interpolation error E_{interp}, %	Rel. regression error E_{regr}, %	Rel. total error E_{tot}, %
550	100000	177.6 ± 21.6	4.3	7	12.1
600	100000	112.6 ± 14.9	4.7	7.5	13.2
650	100000	70.6 ± 10.2	5.2	8.2	14.5
700	100000	42 ± 6.8	5.8	9	16.3
550	200000	167.1 ± 22	4.4	7.7	13.2
600	200000	105.2 ± 15.1	4.8	8.4	14.3
650	200000	65.5 ± 10.3	5.2	9.1	15.8
700	200000	38 ± 6.8	5.9	10.2	17.9

Table 14.4 Error estimates for values extrapolated from the master curve (321H)

Polynomial degree	Temperature, °C	Rupture time, h	Stress, MPa	Rel. extrapolation error E_{extrap}, %	Rel. regression error E_{regr}, %	Rel. total error E_{tot}, %
4	750	70000	20.1 ± 8.2	27.2	9.7	40.9
4	750	100000	17 ± 8.2	33.6	9.7	48.0
6	750	70000	20.1 ± 13.2	49.5	9.7	65.7
6	750	100000	17 ± 15.1	70.1	9.7	88.5

The total errors are larger in Table 14.4 than in Table 14.3. This is precisely as expected since at the highest temperature there is extrapolation from the master curve. The degree of the polynomial plays an important role. The extrapolation error is significantly increased when the degree of the polynomial is raised from 4 to 6. The corresponding effect is small in Table 14.3. The absolute error for the strength is obtained in the same way as in Table 14.3, i.e. by multiplying the relative total error by the stress value and giving the result as a plus-minus addition.

The errors in Table 14.4 are so large that the extrapolated values are of little technical value. The reason for the large values is that the data range at the highest temperature is quite limited. That this gives a large error is directly evident from Eq. (14.22). In addition the longest test duration at the highest temperature is fairly short, see Fig. 14.1. The case demonstrates the value of the error estimates, although already from Fig. 14.1 it is evident that the accuracy would be lower at the highest temperature. However, not until the error has been computed, one can draw the conclusion that the error is so large that the extrapolated results at the highest temperature are not very useful.

A comparison between different TTPs is made in Table 14.5 to further investigate extrapolation errors. The study is for the austenitic stainless steel Sanicro 25 and is taken from [36]. The results for five TTPs are shown at 700 °C for two rupture times 100000 and 200000 h. The abbreviations of the five methods can be found in Table 14.1.

The predicted strengths vary from 92 to 97 MPa at 100000 h and from 78 to 84 MPa at 200000 h. The five methods are associated with fairly similar error estimates. Two of the methods (Larson-Miller and Manson-Succop) give slightly higher predicted stresses. From the generated PATs for the TTPs (not shown) one finds that

- For these two methods, the fit at low stresses to the master curve results in a slight over-prediction of the stresses.
- The m-value at low stresses is about 4 for the two methods and 3 for the others.
- At low stresses the second derivative of the rupture time is about -2 at low stresses for the two methods instead of -5 for the others.

These three sets of observations are not unrelated. They simply show that the rupture curves bend down slightly less for Larson-Miller and Manson-Succop

Table 14.5 Error estimates for values interpolated from the master curve with different TTPs for the austenitic stainless steel Sanicro 25 (22Cr25Ni4W1.5Co3CuNbN). Reproduced from [36] with permission of Taylor & Francis

Method	Temperature, °C	Rupture time, h	Stress, MPa	Rel. interpolation error E_{interp}, %	Rel. regression error E_{regr}, %	Rel. total error E_{tot}, %
OSD	700	100000	91.7 ± 6.8	3.1	4.0	7.4
	700	200000	78.3 ± 6.8	3.2	5.0	8.6
LM	700	100000	95.6 ± 7.4	3.2	4.2	7.7
	700	200000	83.6 ± 7.4	3.3	5.2	8.9
MS	700	100000	97.1 ± 8	3.0	4.8	8.2
	700	200000	84.5 ± 8.1	3.1	5.9	9.6
SA	700	100000	95.2 ± 6.1	3.0	3.1	6.4
	700	200000	82.5 ± 6	3.1	3.9	7.3
GS	700	100000	93.2 ± 6.6	3.2	3.6	7.0
	700	200000	80.5 ± 6.5	3.3	4.5	8.1

methods at low stresses than the other methods. The error analysis indicates that all the five methods give acceptable results but one of the OSD, SA and GS methods should be chosen if conservative values are desirable.

It has been assumed indirectly in the error analysis that the TTPs are valid also for extrapolated values. Some support for this assumption is that PAT 1.3 is satisfied when some of the long term or low stress points from the data set are removed and predicted values can be repeated, see Fig. 14.4.

14.3.3 Error Analysis with NN

In Table 14.6 some of the creep data for the investigated cast of Super304H are given that are essential for the error analysis. The shortest and longest rupture time at each temperature as well as an approximate strength value at the longest rupture time are provided. In addition the relative regression error is shown.

Contrary to the case for TTPs, the creep rupture curves at different temperatures must be considered as individuals. Thus, each temperature must be analyzed as a single curve when the extrapolation error should be estimated with Eq. (14.22). The extrapolation error is multiplied by the regression error in the same way as in the TTP analysis. The total errors in the strength are listed in Table 14.7 as plus-minus additions. When the errors are very large, no decimal is given in the error because it does not have any significance. In some cases the errors are close or even exceeding the values they are associated with. In that case no values are given. The error depends on the number of adjustable parameters n_{adj}. When using Eq. (14.22) the polynomial

Table 14.6 Some creep properties of Super304H (reproduced from [37] with permission of Taylor & Francis)

Temperature, °C	Stress at start, MPa	Shortest rupture time, h	Longest rupture time, h	Regression error, %
600	194.1	113	83985	12.5
650	133.4	59	46324	1.5
700	84.1	95	38293	2.7
750	42.3	70	52178	2.5

degree n_p is assumed to correspond to $n_p = n_{adj} - 2$ since that is the case in the TTP analysis. Naturally, the error increases with extrapolated rupture time. In many cases the estimated error also increases rapidly with the number of adjustable parameters. This is an indication that the number of neurons in the hidden layer should be kept as low as possible. It is not common to use networks with smaller n_{adj} values than 13. This is an important observation because the number of adjustable parameters can easily become quite large in NN analyses. The total error is often quite large and typically larger than in a TTP analysis. The reason is that the extrapolation occurs from single curves with the NN method whereas at most temperatures the extrapolated values can be found from interpolation along the master curve with a TTP method.

Table 14.7 Error analysis for creep rupture prediction with the constrained NN model for Super304H. Reproduced from [37] with permission of Taylor & Francis

No of parameters	Temperature, °C	Predicted creep rupture strength, MPa		
		70000 h	100000 h	200000 h
9	600	187.4 ± 30	174.6 ± 30.3	149.2 ± 30
9	650	110.1 ± 5.6	101.1 ± 6.6	84.5 ± 9.3
9	700	64.9 ± 4.8	59.2 ± 5.6	49.1 ± 7.9
9	750	39.3 ± 2.2	35.7 ± 2.5	29.5 ± 3.3
13	600	187.4 ± 30	174.6 ± 30	149.2 ± 36
13	650	110.1 ± 6.6	101.1 ± 9.4	84.5 ± 20
13	700	64.9 ± 6.2	59.2 ± 9	49.1 ± 20
13	750	39.3 ± 2.5	35.7 ± 3.3	29.5 ± 6.4
21	600	187.4 ± 30	174.6 ± 32	149.2 ± 65
21	650	110.1 ± 9.8	101.1 ± 21	–
21	700	64.9 ± 11.6	59.2 ± 29	–
21	750	39.3 ± 3.1	35.7 ± 6.1	–

14.4 Basic Modeling of Creep Rupture Curves

14.4.1 General

To predict and extrapolate creep rupture data, empirical models have been used for many years. Such models are described in Sect. 14.2. Many such models are well established. They are in principle easy to use. However, if precise results are needed they have to be combined with post assessment tests and error analysis. These additions require a significant computational effort. This has the consequence that it is tempting to ignore these additions but then the results would be quite uncertain.

Nowadays it is possible to model and describe the development of the microstructure during high temperature service. There are also basic models for mechanical properties available. By combining these two types of models the mechanical properties including creep can be predicted.

Empirical models require large data set in order to be used for predictions of properties. With just a limited data set the models act as more or less arbitrary mathematical expressions that are fitted to the data. In such cases it would be very risky to generalize and extrapolate the results. An empirical model with say three or more adjustable parameters can represent many sets of experimental observations. It is very unlikely that a good fit to the data ensures that the model describes the physics of the observations.

To avoid these problems several steps must be taken:

- The models must be derived from basic physical principles.
- All the parameters in the models should be well defined and it should be specified how they should be determined.
- No adjustable parameters should be involved that are fitted to the mechanical properties.

There are many models in the creep literature that are derived from basic principles but with some parameters that are fitted to the data. It is not quite as risky to apply such models as fully empirical ones, but numerous examples exist in the literature where such models have been applied and questionable or incorrect results have been obtained. Further analysis of this issue can be found in Chap. 1. A summary of basic models that can be used for creep rupture is given below. Most of these models are derived in other parts of the book.

14.4.2 Secondary Creep Rate

The main contribution to the creep strength comes from the dislocation density. An accurate description of the dislocation density is therefore essential. Equation (2.17) describes the development of the dislocation density ρ

$$\frac{d\rho}{d\varepsilon} = \frac{m_\mathrm{T}}{bc_L}\rho^{1/2} - \omega\rho - 2\tau_\mathrm{L} M_\mathrm{climb}\rho^2/\dot{\varepsilon} \tag{14.24}$$

ε is the strain, m_T the Taylor factor, b Burger's vector, c_L a constant and L_s the "spurt" distance which the dislocation moves in each elementary release during deformation for example from a Frank-Read source. ω is the dynamic recovery constant, τ_L the dislocation line tension, and $\dot{\varepsilon}$ the creep strain rate. M_climb the dislocation mobility is given by Eq. (2.34)

$$M_\mathrm{climb}(T,\sigma) = \frac{D_{\mathrm{s}0}b}{k_\mathrm{B}T} e^{\frac{\sigma b^3}{k_\mathrm{B}T}} e^{-\frac{(Q_\mathrm{self}+Q_\mathrm{sol})}{R_G T}} f_\mathrm{clglide}(\sigma) \tag{14.25}$$

where T is the absolute temperature, σ the applied stress, $D_{\mathrm{s}0}$ the pre-exponential coefficient for self-diffusion, Q_self the activation energy for self-diffusion, k_B Boltzmann's constant, and R_G the gas constant. Q_sol the contribution to the activation energy from solid solution hardening has been added to Eq. (14.25). Q_sol is equal to the maximum interaction energy between solute atoms and dislocations, Eq. (6.10)

$$Q_\mathrm{sol} = U_i^\mathrm{max} = \frac{1}{\pi}\frac{(1+\nu_\mathrm{P})}{(1-\nu_\mathrm{P})} G\Omega_0\delta_i \tag{14.26}$$

where G is the shear modulus, ν_P the Poisson's ratio of the material, Ω_0 the atomic volume of the parent metal, and δ_i the linear misfit of the element i. M_climb has a strong temperature dependence from the activation energies. M_climb can also have strong stress dependence in particular in the power-law break down regime. This was explained in Sect. 2.6.4. This stress dependence is described with the function f_clglide, Eq. (2.50)

$$f_\mathrm{clglide}(\sigma) = \exp\left(\frac{Q}{R_\mathrm{G}T}\left(\frac{\sigma}{R_\mathrm{max}}\right)^2\right) \tag{14.27}$$

The name of the factor f_clglide is somewhat misleading. Earlier it was thought that the factor was due to the influence of glide. However, the factor is now derived only assuming climb, see Sect. 2.6.4.

The secondary creep rate can be obtained from Eq. (14.24) directly since the dislocation density is constant in that stage and consequently its strain derivative vanishes.

$$\dot{\varepsilon}_\mathrm{sec} = 2\tau_\mathrm{L} M_\mathrm{climb}\rho^{3/2}/\left(\frac{m_\mathrm{T}}{bc_\mathrm{L}} - \omega\rho^{1/2}\right) \tag{14.28}$$

Taylor's Eq. (2.29) gives the contribution σ_disl from the dislocation to the strength

$$\sigma_\mathrm{disl} = \alpha m_\mathrm{T} G b\rho^{1/2} = \sigma - \sigma_\mathrm{i} \tag{14.29}$$

where σ is the applied stress and α ≈ 0.19 a constant. σ_i represents other strength contributions than from the dislocations. They will be exemplified below. Using Taylor's Eq. (2.29), Eq. (14.28) can be formulated in terms of the applied stress which is the common way of expressing the creep rate

$$\dot{\varepsilon}_{\text{sec}} = h_{\text{sec}}(\sigma - \sigma_i); \quad h_{\text{sec}}(\sigma) = 2\tau_L M_{\text{climb}}(T,\sigma)\frac{\sigma^3}{(\alpha m_T G b)^3}\Big/\left(\frac{m_T}{bc_L} - \omega\frac{\sigma}{\alpha m_T G b}\right) \tag{14.30}$$

This can be considered as a Norton equation where the stress dependence of the creep rate is given. At low stresses the stress dependence is from the σ^3 factor but at the high stresses the main contribution is from the f_{clglide} factor, Eq. (14.27), in the expression for M_{climb}.

Practically all high temperature alloys have contributions from solid solution hardening (SSH) and/or precipitation hardening (PH) to the creep strength. SSH enters the equation in two ways. It gives a contribution Q_{sol} to the activation energy for the creep rate, Eq. (14.26). The other part gives a drag stress that contributes to σ_i. This depends on if slowly or fast diffusion elements are involved. The case with slowly diffusing solute will be covered first. There are several expressions for the drag stress in Sect. 6.4. The one that is most commonly valid is Eq. (6.20)

$$\sigma_i^{drag} = \frac{v_{\text{climb}} c_{i0}\beta^2}{bD_i k_B T} I(z_0) \tag{14.31}$$

c_{i0} is the average concentration of solute i, and D_i the diffusion constant for solute i. $I(z_0)$ is an integral of $z_0 = b/r_0 k_B T$ where r_0 is the dislocation core radius. $I(z_0)$ is given by Eq. (6.21). The climb velocity v_{climb} and the strength parameter σ_i are found from, Eqs. (6.14) and (6.15)

$$v_{\text{climb}} = M_{\text{climb}} b\sigma; \quad \beta_i = bU_i^{\max} \tag{14.32}$$

For fast diffusion elements, the solute must break away from the dislocations. The necessary stress is, Eq. (6.28)

$$\sigma_{\text{break}} = \frac{U_i^{\max}}{b^3}\int c_i^{\text{dyn}} dz \tag{14.33}$$

c_i^{dyn} describes the distribution of solutes around the dislocations, Eq. (6.13).

The validity of the expressions (14.31) and (14.33) for SSH have been demonstrated in Sects. 6.4 and 6.5. The influence of Mg on creep rate in Al–Mg alloys is illustrated in Fig. 6.4 and the effect of P on the creep rate of Cu in Fig. 6.6.

The starting point for the precipitation hardening is the Orowan strength, Eq. (7.3)

$$\sigma_O = \frac{m_T C_O G b}{\lambda_s} \tag{14.34}$$

where λ_s is the mean particle spacing, Eq. (7.4) and $C_O = 0.8$ a constant. Equation (14.33) gives the contribution from particles at ambient temperatures. At elevated temperatures small particles can be climbed across without contributing to the strength. Only particles larger than a critical radius r_{crit} give an addition to the strength

$$\sigma_{part} = \frac{C_O G b m_T}{\lambda_{crit}} = \sigma_O e^{-k(r_{crit}-r_0)/2} \tag{14.35}$$

where λ_{crit} is the mean spacing between the particles larger than r_{crit}, $k \approx 1/\overline{r}$ is the slope of the particle size distribution and $\overline{r}$ is the mean particle size. r_{crit} is given as, Eq. (7.9)

$$r_{crit} = M_{climb}(T, \sigma) b^2 \sigma \lambda_F \frac{\rho}{\dot{\varepsilon}_{sec} m_T} \tag{14.36}$$

The Friedel particle spacing λ_F can be determined from Eqs. (7.6) and (7.14)

$$\left(\frac{\lambda_s}{\lambda_F}\right)^3 = \frac{\alpha_{cl}}{\alpha_{cl} + 2C_O}; \quad \alpha_{cl} = \frac{2\overline{r}}{3\lambda_s} = \sqrt{\frac{2 f_V}{3\pi}} \tag{14.37}$$

f_V is the volume fraction of all particles.

The applicability of Eq. (14.35) has been demonstrated in Sect. 7.4.3 for Cu–Co alloys. This is shown in Figs. 7.5 and 7.8. Cu–Co is a suitable system to analyze the effect of particles on the creep strength, since well-defined particles can be formed and the influence of SSH is quite small.

14.4.3 Creep Strain Curves

In the literature much focus has been placed on the prediction and analysis of the creep rate in the secondary stage. However, both primary and tertiary creep is of importance in many applications. It has been demonstrated in Sect. 12.4 that the whole creep strain versus time curves (creep strain curves) can be derived from the creep rate in the secondary stage. It is possible to simplify this approach somewhat [36]. The creep rate for the whole creep curve can then be expressed by using Eq. (14.30)

$$\dot{\varepsilon} = h_{sec}(\sigma_{creep}); \quad \sigma_{creep} = \sigma_{true} + \sigma_{nom} - \sigma_{disl} - \sigma_i \tag{14.38}$$

The only difference in comparison with Eq. (14.30) is that an effective creep stress, Eq. (12.19), is introduced. σ_{true} and σ_{nom} are the true and nominal applied stress. It is essential to take the true stress into account because otherwise there would be no

tertiary creep. The nominal creep stress must also be included. Otherwise the creep curves close to ambient temperatures could not be explained. They have the same form as at elevated temperatures in spite of the fact that stress exponent can be as high as 50. This is further discussed in Sect. 8.4. During primary creep, the dislocation density increases and thereby the dislocation strength σ_{disl}. When the secondary stage is reached, the stresses balance and σ_{creep} is equal to the true stress and Eq. (14.30) is recovered.

In the book there are several models for primary and tertiary creep. For example, there are more advanced models taking the substructure into account. However, the principles are the same. Examples of computed creep strain curves can be found in Sect. 12.5.3.

14.4.4 Cavitation

Basic models for nucleation and growth of creep cavities have been presented in Chap. 10 and summarized in Sect. 13.3.1. The cavity nucleation rate can be expressed as, Eq. (13.5)

$$\frac{dn_{cav}}{dt} = \frac{0.9C_s}{d_{sub}}\left(\frac{g_{sub}}{d_{sub}^2} + \frac{g_{part}}{\lambda^2}\right)\dot{\varepsilon} = B_s\dot{\varepsilon} \tag{14.39}$$

n_{cav} is the number of cavities, d_{sub} the subgrain size, $\dot{\varepsilon}$ the creep strain rate, λ the interparticle spacing in the grain boundaries and C_s a constant. The fraction of active nucleation sites is given by the factors g_{sub} and g_{part}. The main feature of Eq. (14.39) is that the nucleation rate is proportional to the creep strain rate, which has been observed for many materials.

Two types of growth of cavities are considered: diffusion controlled and strain controlled. It was early on recognized that for diffusion control, the growth rate cannot be faster than creep deformation of the matrix. This is referred to as constrained growth. The general equation for constrained growth is, Eq. (13.6)

$$\frac{dR_{cav}}{dt} = 2D_0K_f(\sigma_{red} - \sigma_0)\frac{1}{R_{cav}^2} \tag{14.40}$$

R_{cav} is the cavity radius in the grain boundary plane and σ_0 the sintering stress. The grain boundary diffusion parameter D_0 is equal to $\delta D_{GB}\Omega/k_BT$ where δ is the grain boundary width, D_{GB} the grain boundary self-diffusion coefficient, and Ω the atomic volume. k_B is the Boltzmann's constant and T the absolute temperature. The factor $K_f \approx 0.2$ is given in Eq. (10.12). The reduced stress σ_{red} can be determined from Eq. (13.7)

$$2\pi D_0K_f(\sigma_{red} - \sigma_0)n_{cav}R_{cav} + \dot{\varepsilon}(\sigma_{red}) = \dot{\varepsilon}(\sigma) \tag{14.41}$$

$\dot{\varepsilon}(\sigma_{\text{red}})$ and $\dot{\varepsilon}(\sigma)$ are the creep rates at the reduced and applied stress.

Equations (14.39) and (14.40) have been applied successfully to model cavity nucleation and growth in austenitic stainless steels. This is illustrated in Figs. 10.5 and 10.8.

There are several derived expressions for strain controlled growth. The most well-known ones are due to Rice and Tracey and to Cocks and Ashby modified by Wen and Tu, see Sect. 13.4.2. Unfortunately, these expressions are difficult to use for predictions. The start value for the cavity size has a large effect on the results but there is no obvious way of selecting the value. Furthermore, the model by Rice and Tracey gives quite a limited growth rate in the uniaxial case and the Cocks and Ashby model does not fulfill the criterion for constraint growth. A model based on grain boundary sliding, Eq. (10.24) avoids these problems but it needs further experimental verification for general use.

14.4.5 Rupture Criteria

A distinction is made between brittle and ductile rupture. Brittle rupture is assumed to occur when the cavitated grain boundary area reaches a sufficient fraction. The cavitated grain boundary fraction A_{cav} can be computed from the expression for cavity nucleation and growth, Eqs. (14.39) and (14.40). The result is given in Eq. (13.8)

$$A_{\text{cav}} = \int_0^t \frac{dn_{\text{cav}}}{dt'}(t')\pi R_{\text{cav}}^2(t,t')dt' \tag{14.42}$$

Several studies indicate that the local critical value for brittle rupture is $A_{\text{cav}} \approx 0.25$.

The results in Sect. 12.5 suggest that a plastic instability initiates ductile rupture, for tensile specimens necking. Only very close to the rupture a fully developed waist is formed. The prediction of necking requires creep strain data. If creep strain curves are not available, they could be predicted with the help of Eq. (14.38). Unfortunately, the applicability of this equation has been documented mainly for Cu. The alternative is to assume ductility exhaustion, and use a fixed creep rupture elongation value as failure criterion. As will be seen below, this seems to work well.

14.4.6 Extensive Extrapolation of the Creep Rate for Cu

In the present book it has been emphasized that basic models can improve the possibility to predict and extrapolate results. This was illustrated for Al in Sect. 5.7 and for Cu-OFP in Sect. 5.8.1. Another example will be given here for Cu-OFP where this capability of extrapolation in time is also demonstrated in a dramatic way. The

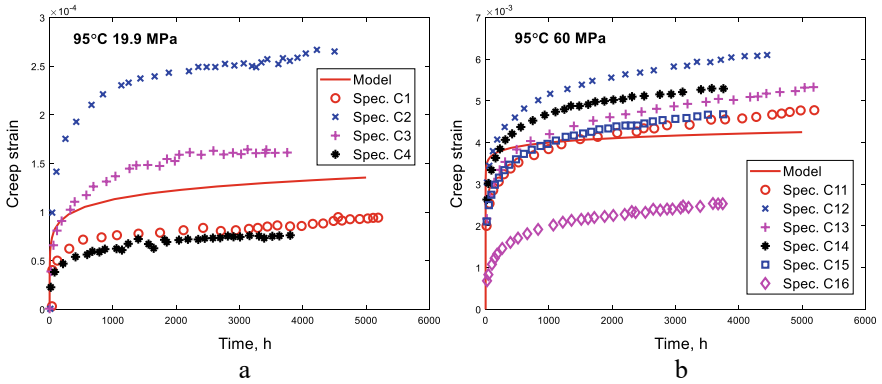

Fig. 14.13 Creep strain versus testing time for Cu with 50 ppm P (Cu-OFP) at 95 °C. The creep strain according to Eq. (5.32) is compared to experimental data from Ho [43]; **a** 19.9 MPa; **b** 60 MPa. Redrawn from [42] with permission of Elsevier

case was originally presented in [41], but it is reanalyzed here with the primary creep model in Sect. 5.5 [42].

With conventional creep testing techniques creep rates down to about 1×10^{-12} 1/s can be measured. This requires for example that the testing temperature in the laboratory is controlled within 2 °C. Ho carried out creep tests at much lower stationary creep rates for Cu-OFP [43]. Tests were performed at 20–100 MPa at 95 °C, at 20–60 MPa at 125 °C and at 20–40 MPa at 150 °C. The model in Sect. 5.5 can at least approximately describe all the experimental results. The parameter value σ_y/K is taken from the room temperature data in [41], and the ω value is computed from Eq. (5.35). It is checked that the criterion in Eq. (5.36) is fulfilled. Two examples are given in Fig. 14.13. Four tests were performed at 19.9 MPa and six tests at 60 MPa. In spite of the low stresses, creep is clearly present in all the tests.

From Fig. 14.13 one might think that creep is approaching the secondary stage. But that is not at all the case. The lowest creep rates in Fig. 14.13a are about 1×10^{-12} 1/s and in Fig. 14.13b about 3×10^{-11} 1/s. From Eq. (14.30), the stationary creep rate can be estimated to 1.3×10^{-22} and 1.4×10^{-19} 1/s in Fig. 14.13a, b, respectively. Such creep rates are far outside the interval where they can be measured. For a specimen with a gauge length of 50 mm, 1.3×10^{-22} 1/s represents a displacement of less than one lattice spacing in a million years. The basic stationary creep model can obviously handle creep rates at least from 180 MPa at 75 °C of 1.4×10^{-7} (Fig. 6.6) to 20 MPa at 95 °C of 1.3×10^{-22} 1/s. This represents a range of validity of 15 orders of magnitude. It clearly demonstrates the value of the basic creep model.

In Fig. 12.1 the stress exponent is about $n_N = 60$ deep in the power-law break down regime. In Fig. 14.13a, the stress exponent is $n_N = 3.3$ and in Fig. 14.13b $n_N = 8.3$. Thus, the model provides valuable information even when there is a transfer from one creep regime to another. These results have profound implications.

- Basic models have the potential to extrapolate results by orders of magnitude in time. This should be compared with empirical statistical methods where a factor of 3 typically can be reached and in special cases a factor of 10.
- Meaningful results can be obtained even when there is a transfer from one testing regime to another. With basic models it is much safer to generalize and extrapolate findings.
- The technical consequences are of immense significance. Cu-OFP will be used in canisters for disposal of spent nuclear fuel in Finland and Sweden. The canisters have a design life of 100000 years. Cu-OFP has been creep tested for up to 3 years. An extrapolation by almost 5 orders of magnitude is required. The results above demonstrate that the basic creep model is valid for such a time extrapolation factor with a good margin and that the model can safely be used to predict the creep properties of the canisters.

14.4.7 Creep Rupture Predictions for Austenitic Stainless Steels

With the equation in Sects. 14.4.2–14.4.5 the rupture time can be predicted. This has been applied to austenitic stainless steels in several papers [21, 25, 44]. Ductile rupture is handled with ductility exhaustion. A constant elongation at rupture of 0.2 is assumed. This value is lower than the observed values for ductile rupture. On the other hand the strain computation is based on the secondary creep rate, Eq. (14.30) that underestimates the total strain. At present there is not sufficient data available to take primary and tertiary creep into account as well.

Brittle rupture is based on the cavitated area fraction in the grain boundaries A_{cav}, Eq. (14.41). When A_{cav} reaches 0.25, brittle rupture is assumed to occur. The criterion for ductile or brittle rupture that is met first is considered to control the type of rupture that takes place.

Results for the 18Cr12NiNb steels (347H) are shown in Fig. 14.14. In Fig. 14.14a only ductile rupture is taken into account but in Fig. 14.14b both types of rupture are included.

The difference between the two types of rupture is not very large. Only at low stresses and long times there is a significant difference. Cavitation reduces the rupture times in that situation. The general behavior of the rupture curves can be seen to be represented in a reasonable way.

In Fig. 14.15, the corresponding results for the 17Cr12Ni2Mo steel 316H are illustrated. The influence of ductile and brittle rupture is much the same as for 347H. The experimental data is represented quite well in particular at long times.

The variation of the slope in Figs. 14.14 and 14.15 follows the observations well. The absolute value of slope was designated m in Eq. (14.1). The m value is given in Fig. 14.16a for the curves in Fig. 14.14 for 347H.

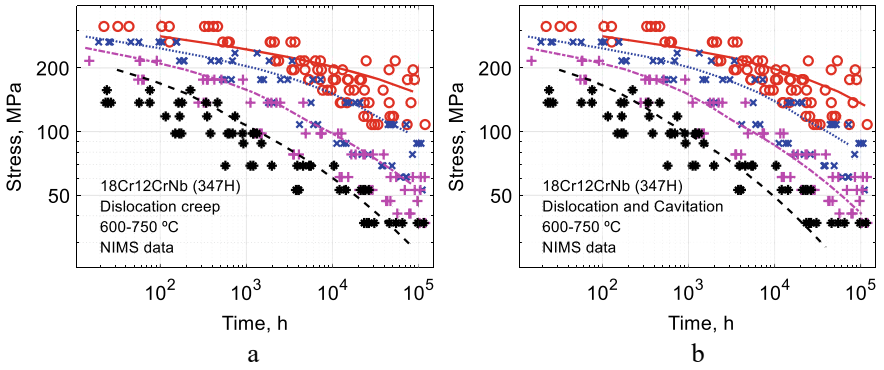

Fig. 14.14 Creep rupture strength values as a function of rupture time for the austenitic stainless steel 18Cr12NiNb (347H); **a** ductile rupture based on ductility exhaustion, Eq. (14.30); **b** ductile rupture as in **a** and brittle rupture assuming a fixed cavitated area fraction at failure, Eq. (14.42). Experimental data from [45] at temperatures between 600 and 750 °C. Redrawn from [21] with permission of Elsevier

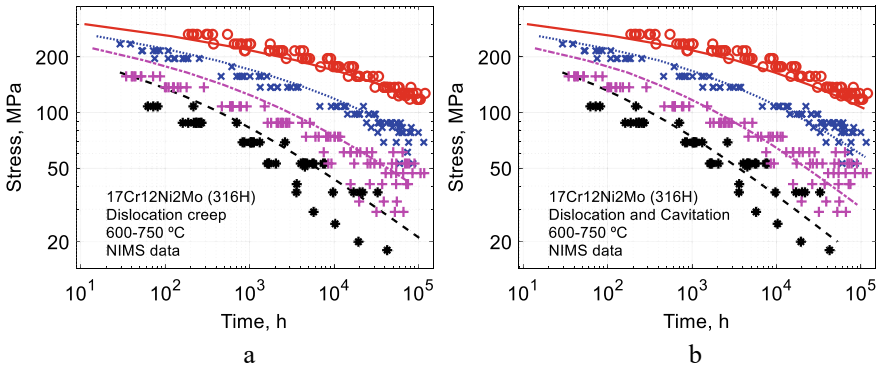

Fig. 14.15 Creep rupture strength values as a function of rupture time for the austenitic stainless steel 17Cr12Ni2Mo (316H); **a** ductile rupture based on ductility exhaustion, Eq. (14.30); **b** ductile rupture as in **a** and brittle rupture assuming a fixed cavitated area fraction at failure, Eq. (14.42) Experimental data from [45] at temperatures between 600 and 750 °C. Redrawn from [21] with permission of Elsevier

If the modified Monkman-Grant relation was strictly followed, m would be equal to the stress exponent for the creep rate n_N. However, m is typically larger than n_N at least for modest rupture times. Figure 14.16 illustrates the contributions to the rupture strength. For 347H, the dislocations give the largest contribution which is often the case. 347H is precipitation hardened with Nb(C, N). It clearly gives a significant contribution to the strength. From solid solution hardening, there is only a small effect.

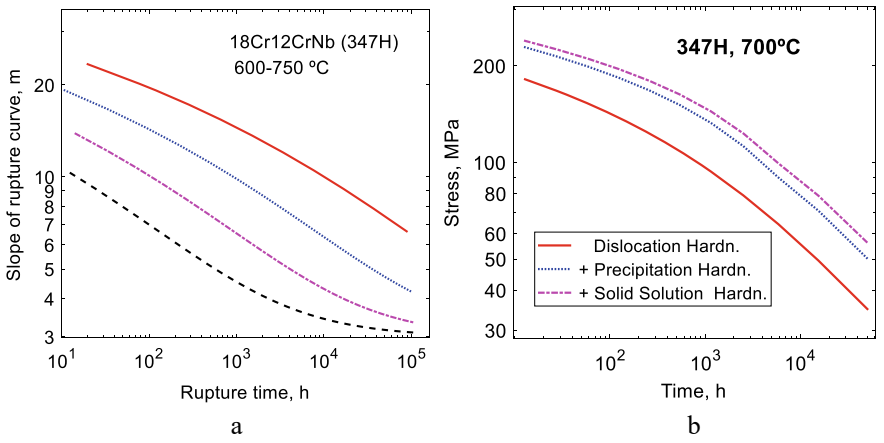

Fig. 14.16 Creep rupture behavior of the austenitic stainless 18Cr12NiNb steel 347H; **a** stress exponent m for creep rupture versus rupture time at the temperature 600 °C (top) to 750 °C (bottom); **b** contribution to the rupture strength from dislocations, precipitates and elements in solid solution. **b** Redrawn from [21] with permission of Elsevier

Successful predictions of the creep ductility taking both brittle and ductile rupture into account were presented in Sect. 13.3. For example, results corresponding to Fig. 14.15 were shown in Fig. 13.6. These results illustrate that the ductility is also possible to compute with basic models.

14.5 Summary

- The use of time-temperature parameters (TTPs) is the classical way to extrapolate creep rupture data to longer times. With the help of TTPs the rupture data are fitted to a single curve, the master curve. Extrapolation at most temperatures can be handled by interpolation along the master curve. In this way the extrapolation from single curves is avoided that gives a less accurate result. Only at the highest temperature this is necessary.
- An alternative to TTPs is to use a neural network (NN). It is necessary to choose a simple NN to minimize the number of adjustable parameters involved. The error can increase rapidly with the number of parameters.
- The ECCC post assessment tests (PATs) are quite valuable to show that an extrapolation analysis has worked and that the results show a correct physical behavior. This applies to both TTPs and NN.
- Creep rupture curves, i.e. creep stress versus rupture times show some characteristic features. Their first derivative is always negative. This applies also to the second derivative except for so-called sigmoidal behavior but that is not considered in this chapter. For empirical extrapolation, the creep data are fitted to a model

with a number of adjustable parameters. To improve the fit and the physical realism of the predicted rupture time, constrained optimization with conditions on first and second derivatives is recommended. It has been shown that many of the PATs are automatically satisfied in this way.

- Formulae for error estimates are presented. Expressions for the relative errors of interpolation, extrapolation and regression are given. These error estimates make it much simpler to assess the quality of an evaluation. Both interpolation and extrapolation from a master curve are covered as well as NN.
- Basic models for creep rupture have been presented throughout the book. The main equations for brittle and ductile rupture are summarized in Sect. 14.4.
- In principle, basic modeling should make it possible to significantly improve the possibility to generalize and extrapolate results. For Cu-OFP it has been possible to demonstrate that this is in fact the case. It was verified that meaningful extrapolation of many orders of magnitude in time is possible. This makes it possible to safely compute the creep properties over such extended periods as 100000 years, which has been fully utilized in canisters for disposal of spent nuclear waste.
- Basic creep rupture predictions for austenitic stainless are summarized. It is demonstrated that experimental creep rupture can be well reproduced.

Appendix: Derivatives in Neural Network Models (Reproduced from [37] with Permission)

The rupture curves, i.e., the creep stress plotted versus the observed rupture time, must show the same behavior as described for the TTP analysis, the first and second derivative must fulfill the requirements in Eqs. (14.1) and (14.2). If the criteria in these equations are satisfied unphysical flexing of the predicted rupture curve is prevented. The criteria are of the same importance when NN models are used.

The derivatives of predicted curves are not available in general in NN programs, so expressions for the derivatives are derived below. The NN model is represented with the matrix formalism given by Hagan et al. [14]. The input $\mathbf{p}$ to output $\mathbf{a}^1$ from the first layer in the network is given by

$$\mathbf{v}_k^1 = \sum_i \mathbf{W}_{ki}^1 \mathbf{p}_i + \mathbf{b}_i^1 \tag{14.43}$$

$$\mathbf{a}_k^1 = \varphi^1(\mathbf{v}_k^1) \tag{14.44}$$

$\mathbf{p}$ has components corresponding to the number of inputs n_{input}. There is a weight factor $\mathbf{W}^1$ to each neuron for each input. Thus, the matrix $\mathbf{W}^1$ has the dimension $n_{\text{neuron}} \times n_{\text{input}}$ where n_{neuron} is the number of neurons in the first layer. For each neuron there is also a component in the base vector $\mathbf{b}^1$. The linear combination in Eq. (14.43), the transfer input $\mathbf{v}^1$ is fed into the transfer function φ^1, which results

in the output $\mathbf{a}^1$ from the first layer. φ^1 is a scalar function. The output from the first layer is the input to the next layer. The qth layer in the network can be expressed as:

$$\mathbf{v}_k^q = \sum_i \mathbf{W}_{ki}^q \mathbf{a}_i^{q-1} + \mathbf{b}_k^q \tag{14.45}$$

$$\mathbf{a}_k^q = \varphi^q(\mathbf{v}_k^q) \tag{14.46}$$

The superscript refers to the number of the layer in the network. Thus the output from layer $q-1$ namely $\mathbf{a}^{q-1}$ is the input to layer q. This generates a transfer input $\mathbf{v}^q$, which is then used to form the output from layer q.

The formalism set up in Eqs. (14.43)–(14.46) will now be employed to derive the expression for derivatives with respect to the input variables in the vector $\mathbf{p}$. An iterative procedure will be considered in the sense that if the parameters for one layer are known the parameters in the next layer can be derived. The derivative of the transfer input in the first layer can be obtained from Eq. (14.43)

$$\frac{d\mathbf{v}_j^1}{d\mathbf{p}_m} = \mathbf{W}_{jm}^1 \tag{14.47}$$

Equation (14.45) gives the transfer input from layer $q-1$ to layer q

$$\frac{d\mathbf{v}_k^q}{d\mathbf{p}_m} = \sum_i \mathbf{W}_{ki}^q \frac{d\mathbf{a}_i^{q-1}}{d\mathbf{p}_m} \tag{14.48}$$

The derivative of the output $\mathbf{a}^q$ from layer q takes the form

$$\frac{d\mathbf{a}_k^q}{d\mathbf{p}_m} = \frac{d\varphi^q}{dv}(\mathbf{v}_k^q)\frac{d\mathbf{v}_k^q}{d\mathbf{p}_m} \tag{14.49}$$

Notice that there is a summation over index i in Eq. (14.48) but no summation over the repeated index k in Eq. (14.49). The rule of automatic summation over repeated indices is not applied. When there is a summation, it is explicitly indicated. If Eqs. (14.48) and (14.49) are combined, an expression is obtained where the derivative of the transfer input in one layer is directly related to transfer input in the previous one.

$$\frac{d\mathbf{v}_k^q}{d\mathbf{p}_m} = \sum_i \mathbf{W}_{ki}^q \frac{d\varphi^{q-1}}{dv}(\mathbf{v}_i^{q-1})\frac{d\mathbf{v}_i^{q-1}}{d\mathbf{p}_m} \tag{14.50}$$

With the Eqs. (14.47), (14.49) and (14.50) the derivatives of transfer input and output can be computed for a layer from the corresponding values in the previous layers.

The second derivatives can be derived in a similar way. From Eq. (14.43), it is evident that the second derivative of the transfer input vanishes in the first layer.

$$\frac{d^2\mathbf{v}_j^1}{d\mathbf{p}_m d\mathbf{p}_n} = 0 \tag{14.51}$$

Derivating Eq. (14.50) gives the following result

$$\frac{d^2\mathbf{v}_k^q}{d\mathbf{p}_m d\mathbf{p}_n} = \sum_i \left\{ \mathbf{W}_{ki}^q \frac{d^2\varphi^{q-1}}{dv^2}(\mathbf{v}_i^{q-1}) \frac{d\mathbf{v}_i^{q-1}}{d\mathbf{p}_m} \frac{d\mathbf{v}_i^{q-1}}{d\mathbf{p}_n} + \mathbf{W}_{ki}^q \frac{d\varphi^{q-1}}{dv}(\mathbf{v}_i^{q-1}) \frac{d^2\mathbf{v}_i^{q-1}}{d\mathbf{p}_m d\mathbf{p}_n} \right\} \tag{14.52}$$

The second derivative of the output from layer q can be obtained from Eq. (14.49)

$$\frac{d^2\mathbf{a}_j^q}{d\mathbf{p}_m d\mathbf{p}_n} = \frac{d^2\varphi^q}{dv^2}(\mathbf{v}_j^q) \frac{d\mathbf{v}_j^q}{d\mathbf{p}_m} \frac{d\mathbf{v}_j^q}{d\mathbf{p}_n} + \frac{d\varphi^q}{dv}(\mathbf{v}_j^q) \frac{d^2\mathbf{v}_j^q}{d\mathbf{p}_m d\mathbf{p}_n} \tag{14.53}$$

Since NN software where conditions on the derivatives could be introduced was not found, a new NN program was written from scratch. The network consists of layers of neurons. The number of neurons in each layer could be chosen. The values of the weights and bases were determined with the help of an algorithm for back propagation. A contribution Δerr to the mean square error was added

$$\Delta\text{err} = c_1 \varphi_{\text{logsig}}\left(\frac{da^Q}{dp_m}\right) + c_2 \varphi_{\text{logsig}}\left(\frac{d^2 a^Q}{dp_n^2}\right) \tag{14.54}$$

where Q is the final layer in the network, and c_1 and c_2 are constants. φ_{logsig} is a logsig function. If the derivatives are positive, there is a contribution to the error function that the training of the network will try to remove.

In the NN models for the prediction of the creep rupture times, two layers were used. The first hidden layer contained 3–10 neurons with a logsig transfer function for φ^1. The second output layer with one output had one neuron with a linear transfer function φ^2. With a final linear transfer function, the first term in Eq. (14.53) vanishes in this case. With one output, a^{Q} becomes a scalar as indicated in Eq. (14.54).

References

1. J. Bolton, A visual perspective of creep rupture extrapolation. Mater. High Temp. **30**, 87–98 (2013)
2. M. Prager, S.S. Manson, U. Muralidharan, Analysis of creep-rupture data for five multi-heat alloys by the minimum-commitment method using double heat-term-centering technique. Final report; Metal Properties Council, Inc., New York (USA); Case Western Reserve Univ., Cleveland, OH (USA) (1983), pp. Medium: X; Size: Pages: 65
3. R. Sandstrom, A procedure for extended extrapolation of creep rupture data. J. Test. Eval. **31**, 58–64 (2003)

4. W.-G. Kim, J.-Y. Park, S.-J. Kim, E.-S. Kim, J. Jang, Improvement of long-term creep life extrapolation using a new master curve for Grade 91 steel. J. Mech. Sci. Technol. **32**, 4165–4172 (2018)
5. J. Bolton, Reliable analysis and extrapolation of creep rupture data. Int. J. Pres. Ves. Pip. **157**, 1–19 (2017)
6. I.I. Trunin, N.G. Golobova, E.A. Loginov, New method of extrapolation of creep test and long time strength results, in *4th International Symposium on Heat-Resistant Metallic Materials* (1971), p. 168
7. J. Granacher, M. Monsees, P. Hillenbrand, C. Berger, Software for the assessment and application of creep and rupture data. Nucl. Eng. Des. **190**, 273–285 (1999)
8. ISO 6303: Pressure vessel steels not included in ISO 2604, Parts 1–6-Derivation of long-time stress rupture properties, Annex: "Methods of Extrapolation Used in Analyses of Creep Rupture Data.", in *ISO Standard* (1981), p. 5
9. B. Wilshire, P.J. Scharning, Extrapolation of creep life data for 1Cr–0.5Mo steel. Int. J. Pres. Ves. Pip. **85**, 739–743 (2008)
10. B. Ivarsson, Evaluation of different methods for extrapolation of creep rupture data, Swedish Institute for Metals Research, report IM-1794 (1983)
11. Generic recommendations and guidance for the assessment of full size creep rupture datasets, ECCC Recommendations, Volume 5 Part Ia (2008)
12. G. Merckling, Long-term creep rupture strength assessment: development of the European collaborative creep committee post-assessment tests. Int. J. Pres. Ves. Pip. **85**, 2–13 (2008)
13. R. Sandström, J. He, Error estimates in extrapolation of creep rupture data: applied to an austenitic stainless steel, in *ASME 2021 Pressure Vessels & Piping Conference* (2021)
14. H.B. Demuth, M.H. Beale, O.D. Jess, M.T. Hagan, in *Neural Network Design*, ed. by M. Hagan (2014)
15. A. Ghatak, P.S. Robi, Prediction of creep curve of HP40Nb steel using artificial neural network. Neural Comput. Appl. **30**, 2953–2964 (2018)
16. C.-Y. Lai, S. Santos, M. Chiesa, Machine learning assisted quantification of graphitic surfaces exposure to defined environments. Appl. Phys. Lett. **114**, 241601 (2019)
17. T. Liang, X. Liu, P. Fan, L. Zhu, Y. Bi, Y. Zhang, Prediction of long-term creep life of 9Cr–1Mo–V–Nb steel using artificial neural network. Int. J. Press. Vessels Pip. **179**, 104014 (2020)
18. N. Wang, S.-T. Tu, F.-Z. Xuan, A novel prediction method of creep rupture life of 9–12% chromium ferritic steel based on abductive network. Eng. Fail. Anal. **31**, 302–310 (2013)
19. Y. Zhu, N. Zabaras, P.-S. Koutsourelakis, P. Perdikaris, Physics-constrained deep learning for high-dimensional surrogate modeling and uncertainty quantification without labeled data. J. Comput. Phys. **394**, 56–81 (2019)
20. G.E. Karniadakis, I.G. Kevrekidis, L. Lu, P. Perdikaris, S. Wang, L. Yang, Physics-informed machine learning. Nat. Rev. Phys. **3**, 422–440 (2021)
21. J. He, R. Sandström, Basic modelling of creep rupture in austenitic stainless steels. Theoret. Appl. Fract. Mech. **89**, 139–146 (2017)
22. R. Sandström, J. He, Survey of creep cavitation in fcc metals, in *Study of Grain Boundary Character* (InTech, 2017), pp. 19–42
23. J. He, R. Sandström, Brittle rupture of austenitic stainless steels due to creep cavitation. Procedia Struct. Integr. **2**, 863–870 (2016)
24. J. He, High temperature performance of materials for future power plants (KTH Royal Institute of Technology, Stockholm, 2016), p. 55
25. J. He, R. Sandström, Application of fundamental models for creep rupture prediction of Sanicro 25 (23Cr25NiWCoCu). Crystals **9** (2019)
26. J. He, R. Sandström, Formation of creep cavities in austenitic stainless steels. J. Mater. Sci. **51**, 6674–6685 (2016)
27. J. He, R. Sandström, Modelling grain boundary sliding during creep of austenitic stainless steels. J. Mater. Sci. **51**, 2926–2934 (2016)
28. J. He, R. Sandström, Creep cavity growth models for austenitic stainless steels. Mater. Sci. Eng. A **674**, 328–334 (2016)

29. R. Viswanathan, *Damage Mechanisms and Life Assessment of High-Temperature Components* (ASM International, Metals Park, Ohio, 1989)
30. S.R. Holdsworth, Recent developments in the analysis of creep rupture data. Key Eng. Mater. **171–174**, 1–8 (1999)
31. Data Sheet on the Elevated-Temperature Properties of 18Cr–10Ni–Ti Stainless Steel for Boiler and Heat Exchanger Seamless Tubes (SUS 321H TB), National Research Institute for Metals Tokyo, Japan, Report No. 5B (1987)
32. F. Dobeš, K. Milička, The relation between minimum creep rate and time to fracture. Metal Sci. **10**, 382–384 (1976)
33. G. Sundararajan, The Monkman-Grant relationship. Mater. Sci. Eng. A **112**, 205–214 (1989)
34. F. Abe, Influence of boron nitride inclusions and degradation in creep rupture strength on creep rupture ductility of Gr.122. Mater. High Temp. **38** 197–210 (2021)
35. S. Holdsworth, The European creep collaborative committee (ECCC) approach to creep data assessment. J. Press. Vessel Technol.-Trans. ASME, **130**, 6 (2008)
36. R. Sandström, J.-J. He, Error estimates in extrapolation of creep rupture data and its application to an austenitic stainless steel. Mater. High Temp. **39**, 181–191 (2022)
37. J. He, R. Sandström, Creep rupture prediction using constrained neural networks with error estimates. Mater. High Temp. **39**, 239–251 (2022)
38. J.-J. He, R. Sandström, J. Zhang, H.-Y. Qin, Application of soft constrained machine learning algorithms for creep rupture prediction of an austenitic heat resistant steel Sanicro 25. J. Mater. Res. Technol. **22**, 923–937 (2023)
39. M. Igarashi, 18Cr–9Ni–3Cu–Nb–N steel: datasheet from Landolt-Börnstein—Group VIII advanced materials and technologies Volume 2B: "Creep Properties of Heat Resistant Steels and Superalloys", in *SpringerMaterials* eds. by K. Yagi, G. Merckling, T.U. Kern, H. Irie, H. Warlimont (Springer, Berlin, Heidelberg)
40. A.A. Borovkov, *Probability Theory* (Springer, London, 2013)
41. R. Sandstrom, Basic model for primary and secondary creep in copper. Acta Mater. **60**, 314–322 (2012)
42. R. Sandström, Primary creep at low stresses in copper. Mater. Sci. Eng.: A **873**, 144950 (2023)
43. E.T.C. Ho, A study of creep behaviour of oxygen-free phosphorus-doped copper under low-temperture and low-stress test conditions, Ontario Power Technologies Report No: 06819-REP-01200-10031-R00 (2000)
44. Data Sheet on the Elevated-Temperature Properties of 18Cr–12Ni–Nb stainless steel tubes for boilers and heat exchangers (SUS 347H TB), National Research Institute for Metals Tokyo, Japan, Report No. 28B (2001)
45. Data Sheet on the Elevated-Temperature Properties of 18Cr–8Ni–Mo stainless steel tubes for boiler and heat exchangers (SUS 316H TB), National Research Institute for Metals Tokyo, Japan, Report No. 6B (2000)